Neuro-inspired photonics for telecommunication applications

Jeremy Vatin

NNT : 2020CSUP0004

CentraleSupélec

Ecole Doctorale C2MP

« Chimie Mécanique. Matériaux Physique » - n° 606

Laboratoire Matériaux, Optique, Photonique et Système LMOPS EA-4423
Chaire Photonique

THÈSE DE DOCTORAT

Spécialité de doctorat : Physique

Soutenue le 22 octobre 2020

par :

Jérémy Vatin

Photonique neuro-inspirée pour des applications télécoms

Composition du jury :

Directeur de thèse :	Marc Sciamanna	Professeur (CentraleSupélec)
Co-directeur de thèse :	Damien Rontani	Maître de conférences (CentraleSupélec)
Président du jury :	Sylvain Barbay	Directeur de recherche CNRS (C2N)
Rapporteurs :	Daniel Brunner	Chargé de recherche CNRS (Femto ST)
	Serge Massar	Professeur (Université libre de Bruxelles)
Examinateurs :	Sylvain Barbay	Directeur de recherche CNRS (C2N)
	Cristina Masoller	Professeur (Universitat Politecnica de Catalunya)

CentraleSupélec

C2MP

Neuro-inspired photonics for telecommunication applications

CentraleSupélec

Ecole Doctorale C2MP

Chimie Mecanique Materiaux Physique

Chaire Photonique

Laboratoire MOPS

Matériaux Optique Photonique et Systèmes

Philosophiæ Doctor Thesis

Specilisation : Physics

Jérémy Vatin

Jury members

Ph. D. supervisor:	Prof. Marc Sciamanna	CentraleSupélec
Ph. D. co-supervisor:	Asst. Prof. Damien Rontani	CentraleSupélec
Rapporteur:	Daniel Brunner	Femto-ST
Rapporteur:	Prof. Serge Massar	Université libre de Bruxelles
Examiner:	Sylvain Barbay	C2N
Examiner:	Prof. Cristina Masoller	Universitat Politecnica de Catalunya

Defended the : 22/10/2020

Acknowledgements

Is it possible to write acknowledgements without forgetting someone? A PhD is such an incredible experience during which we meet such incredible people. For my part, the benefits and the impact of my thesis were not bounded the university sphere.

But let us begin with the laboratory in which I worked over the last 3 years. I realized my thesis in the LMOPS (Laboratoire Matériaux, Optique, Photonique et Système) which is a joint research unit between CentraleSupélec and Université de Lorraine. I would like to first of all to thank Prof Marc Sciamanna and Dr. Damien Rontani who gave me the opportunity to work on this topic. They have accompanied me all along this thesis and helped in the hardest moment. But on top of the rest, they have also believed in me and in my choices, letting me explore some part of my subject that was not certain to achieved something.

I would also like to thank Dr. Piotr Antonik for all the discussion we had, especially at the beginning of my thesis. He helped me to understand a lot in my topic, not only in the theory, but also in the experimental realization of my setup.

And I would like to thank all the post-doctoral fellows and PhD students that I worked with, and the ones that I met during the conferences for all the nice moment we shared together, the drinks we had, the game we played, and the fruitful philosophical discussions.

The organization of my thesis would not have been possible without all the administration staff of CentraleSupélec. That is why I would like to thank them for their help, and more specifically Maryvonne and Fabienne for their great work. I would also like to thank Mario, the mechanic of the lab for his kindness and his incredible help in designing mechanical pices to solve my very specific problems.

I also thank the head of the doctoral school Prof Dominique Daloz, and his assistant Christine Sartori for their help during this last three years. They have always done their best to make the administrative work as simple as possible.

I would like to give a special thank to the member of the jury who made them available for my defense, specifically because they have done their utmost to come to the defense despite the Covid-19.

Finally, I would never thank enough my family and all my friends that back me up during all my PhD. They have been here to cheer me up in the hardest moment, they trusted me when I was not myself, and they always remind me to keep my feed on the ground.

And I would like to specifically thank my parents that have always been here for me, and who made all of this possible.

Abstract:

We produce everyday thousands of gigabits of data, exchanged over the internet network. These data are processed thanks to computation clusters, which are responsible of the large amount of energy consumed by the internet network. In this work, we study an architecture made of photonic components, to get rid of electronic components that are power consuming. Thanks to components that are currently used in the internet network, we build an artificial neural network made of a VCSEL and a feedback loop that can process telecommunication data. The complex behavior of this system is used to feed the artificial neurons that are distributed along the fiber.

We first present the basics of the physics of semiconductor lasers. We first briefly remind the principle of the lasing effect. A laser can be realized with semiconductor materials, and we can distinguish lasers emitting light from the edge (EEL) and lasers emitting from the surface (VCSEL). This last kind of laser has several advantages which makes it largely used in different fields, such as telecommunication networks, in biology or in smartphones. A semiconductor laser can exhibit different complex dynamics while submitted to feedback or injection for instance. This complex dynamics is already used, to mimic natural phenomena, or to process signals for instance.

We secondly present the basic knowledge of reservoir computing. We first introduce the artificial neural network, and two topologies of network: the feedforward and the recurrent neural network. Reservoir computing paradigm has been proposed to simplify training procedure, and consists in using a fixed recurrent neural network, and training only a readout layer thanks to simple regression algorithm. In reservoir computing, we focused more specifically on the time-delay reservoir computing. This architecture is composed of a single physical neuron with a feedback loop, along which virtual neurons are distributed. We also present examples of reservoir computing device. We finally present the tasks we use to benchmark our reservoir computing device. After introducing the basic knowledge required to understand our work, we present the performance on single task processing of our reservoir computing device made of a VCSEL and single mode silica fiber, based on time-delay reservoir computing paradigm. We used the spin-flip model (SFM) to simulate the system and explore the space of parameters of the system by either injecting the input electrically or optically. We also explore the influence of the polarization of the optical feedback. We draw two main conclusions: the input injected optically leads to better and faster performance and using polarization-rotated optical feedback allows doubling the memory capacity of the reservoir computer, hence potentially reaching better performance on applied tasks. The experimental confirmation of this last observation is detailed, after presenting the experimental setup. We finally compare the numerical and experimental performance of our device.

We finally explore the performance of our proposed architecture processing two tasks simultaneously. We adapt the model to be able to inject two tasks: each task is injected in a different polarization mode of the VCSEL. We test the influence of some internal parameters of the VCSEL on the memory capacity of the reservoir, and on its performance when processing telecommunication tasks, and we also prove that the ratio of the injection power between the two polarization modes can be used to tune the splitting of performance between the two processed tasks. This last conclusion is also demonstrated experimentally. We finally compare experimental results with numerical simulations.

Résumé:

Nous produisons chaque jour de grandes quantités de données, que nous échangeons grâce à Internet. Ces données sont traitées grâce à des clusters de calcul, responsables de la consommation énergétique d'internet. Dans cette thèse, nous étudions une architecture faite de composants photoniques, pour se débarrasser des composants électroniques consommant de l'énergie. Grâce aux composants actuellement utilisés dans le réseau Internet (laser et fibre optique), nous réalisons un réseau neuronal artificiel capable de traiter les données de télécommunication. Le réseau de neurones artificiel est constitué d'un laser et d'une fibre optique qui renvoie la lumière dans ce laser. Le comportement complexe de ce système est utilisé pour alimenter les neurones artificiels qui sont répartis le long de la fibre.

Nous présentons d'abord les bases de la physique des lasers à semi-conducteurs. Nous rappelons le principe de l'effet lasant. Un laser peut être réalisé avec des matériaux semi-conducteurs, et nous pouvons distinguer les lasers émettant par la tranche (EEL) de ceux émettant par la surface (VCSEL). Ce dernier type de laser présente des avantages qui le rend largement utilisé dans différents domaines, tels que les réseaux télécom, la biologie ou dans les smartphones. Un laser à semi-conducteur peut révéler des dynamiques complexes lorsqu'il est soumis à rétroaction ou à injection par exemple. Cette dynamique est déjà utilisée entre autres pour imiter des phénomènes naturels ou pour traiter des signaux.

Nous présentons ensuite les bases du reservoir computing. Nous présentons d'abord le réseau de neurones artificiels, et deux topologies de réseau : le réseau de neurones à propagation avant et le réseau récurrent. Le reservoir computing, apparu pour simplifier la phase d'entrainement, consiste à utiliser un réseau récurrent fixe, et à entraîner uniquement une couche de lecture grâce à une régression. Au sein du reservoir computing, nous étudions plus particulièrement le réservoir à retard. Cette architecture est composée d'un seul neurone physique avec une boucle de rétroaction, le long de laquelle sont distribués des neurones virtuels. Nous présentons des exemples de reservoir, ainsi que les tâches que nous utilisons pour évaluer notre dispositif de calcul de réservoir.

Après les éléments de théorie, nous présentons les performances de notre reservoir computer composé d'un VCSEL et d'une fibre de silice monomode, basé sur le principe du reservoir à retard. Nous avons utilisé le modèle de spin-flip (SFM) pour simuler le système et explorer l'espace des paramètres du système en injectant l'entrée soit électriquement soit optiquement. Nous explorons également l'influence de la polarisation de la rétroaction optique. Nous tirons deux conclusions principales : l'injection optique

de l'entrée conduit à des meilleures performances et l'utilisation de la rétroaction optique à rotation de polarisation permet de doubler la mémoire du système, permettant d'atteindre potentiellement de meilleures performances. Nous détaillons la confirmation expérimentale de cette dernière observation, après avoir présenté l'expérience. Nous comparons enfin les performances numériques et expérimentales de notre dispositif.

Enfin, nous testons les performances de notre système pour le traitement deux tâches simultanées. Nous adaptons le modèle pour pouvoir injecter deux tâches : chaque tâche est injectée dans un mode de polarisation différent du VCSEL. Nous testons l'influence de certains paramètres internes du VCSEL sur la capacité mémoire du réservoir, et sur ses performances lors du traitement de tâches télécom, et nous prouvons également que le rapport de puissances d'injection entre les deux modes de polarisation peut être utilisé pour régler la répartition de performances entre les deux tâches traitées. Cette dernière conclusion est également démontrée expérimentalement, avant de comparer les performances des systèmes numériques et expérimentaux.

Contents

List of Figures **ix**

1 Background and Motivation **1**

2 Physics of semiconductor lasers **9**

2.1 Semiconductor lasers . . . 10
2.1.1 Basic principle of lasing effect . . . 10
2.1.2 Semiconductor edge-emitting laser (EEL) . . . 12
2.1.3 Verical-cavity surface emitting laser (VCSEL) . . . 15
2.2 The use of VCSELs today . . . 16
2.2.1 Industrial advantages of the VCSEL . . . 16
2.2.2 VCSELs in telecommunication system . . . 18
2.2.3 VCSELs in biology . . . 19
2.2.4 VCSELs in our everyday life . . . 20
2.3 Complex Dynamics of lasers . . . 20
2.3.1 Laser submitted to feedback . . . 21
2.3.2 Laser submitted to injection . . . 24
2.3.3 Laser submitted to modulated injection . . . 25
2.3.4 Specific properties of VCSELs . . . 27
2.4 Use of complex waveforms . . . 29
2.4.1 To mimic . . . 29
2.4.1.1 Rogue waves . . . 29
2.4.1.2 Chimera . . . 30
2.4.1.3 Spiking dynamics . . . 30
2.4.2 To process information . . . 32
2.4.2.1 Cryptography . . . 32
2.4.2.2 Random number generation . . . 32
2.4.2.3 Sensors . . . 33
2.5 Conclusion . . . 33

3 Theory of artificial neural network and reservoir computer **35**

3.1 The artificial neural network . . . 36
3.1.1 Different models of neuron . . . 36
3.1.2 Feedforward neural network . . . 37
3.1.3 Recurrent neural network . . . 38
3.1.4 Network of spiking neurons . . . 39

3.2 Reservoir computing . . . 40
3.2.1 What is reservoir computing? . . . 40
3.2.2 Time-delay reservoir computing . . . 43
3.2.2.1 Single node reservoir computer . . . 43
3.2.2.2 Pre-processing: the masking procedure . . . 44
3.2.2.3 Training . . . 46
3.3 Examples of physical reservoir computing . . . 47
3.3.1 Physical reservoir computing . . . 48
3.3.2 Photonic reservoir computing . . . 48
3.3.2.1 Spatial reservoir computing . . . 48
3.3.2.2 Time-delay reservoir computing . . . 49
3.4 Tasks and metrics . . . 51
3.4.1 Computational ability . . . 52
3.4.1.1 Kernel quality . . . 52
3.4.1.2 Generalization property . . . 53
3.4.1.3 Computational ability . . . 53
3.4.2 Memory capacity . . . 54
3.4.3 The Sante Fe time series prediction . . . 54
3.4.4 The Nonlinear channel equalization task . . . 56
3.4.4.1 WI-FI channel . . . 57
3.4.4.2 Single mode optical fiber . . . 58
3.5 Conclusion . . . 60

4 Performance of VCSEL-based time-delay reservoir computing device on single task processing 61
4.1 Current performance of time-delay reservoir computing . . . 62
4.2 Numerical simulations . . . 63
4.2.1 Presentation of the model . . . 64
4.2.2 Reservoir with an electric input . . . 67
4.2.2.1 Raw performance of the system . . . 68
4.2.2.2 Applied performance of the system on the Santa-Fe prediction task . . . 70
4.2.3 Reservoir with an optical input . . . 71
4.2.3.1 Dependence of the intrinsic performance of the system on operating parameters . . . 71
4.2.3.2 Dependence of the memory capacity on VCSELs parameters . . . 76
4.2.3.3 Applied performance of the system . . . 79

4.3 Experimental results 86
4.3.1 Presentation of the experimental setup 86
4.3.2 Finding the operating point of the reservoir 89
4.3.3 Performance of the experimental system 91
4.3.4 Link between numerical and experimental results 98
4.4 Conclusion 99

5 Performance of VCSEL-based time-delay reservoir computing device on multi-task processing 101
5.1 Time-delay reservoir and dual task processing 102
5.2 Numerical simulations 103
5.2.1 Presentation of the new model 103
5.2.2 Memory properties of the system 106
5.2.3 Applied performance of the system 109
5.3 Experimental results 114
5.3.1 Presentation of the complete experimental setup 115
5.3.2 Preparing the setup to perform computation 119
5.3.3 Experimental performance 120
5.3.4 Comparison numerical and experimental results 126
5.4 Conclusion 126

6 Conclusion and perspectives 129
6.1 Summary of the dissertation 130
6.2 Perspective for future work 131

Bibliography 133

A Appendix 1: Code deployment on CPU cluster 145

B Appendix 2: Résumé de la thèse en français 147

List of Figures

1.1 Picture of a Google Data center 2

1.2 Processing signal with machine learning approach in case of supervised learning: the system is first trained. During this step, the system learns how to realize a task (here recognizing an apple). The system is then tested. During this step, other inputs are shown to the system and the system responds using the method learned during the training (here the system recognizes an apple as he has been trained to recognize apples). 3

2.1 The three interaction light-matter. An electron can get excited from the lower level of energy to the higher by absorbing the energy of a photon (a). An electron can relax from the higher level of energy E_2 to the lower one E_1 emitting a photon having an energy $E_2 - E_1$. This phenomenon can be spontaneous (b) or stimulated by another photon with the same energy $E_2 - E_1$ (c). In the second case, the emitted photon has the same properties as the stimulating photon. 11

2.2 Typical light pump curve of a laser. when the energy brought to the cavity is too low, the dominant effect is the spontaneous emission. After the threshold on the contrary, the losses are compensated, the dominant phenomenon is the stimulated emission, and the laser starts emitting light. 13

2.3 Energy diagram of the double heterostructure. The diagram shows the conduction band (higher level of energy) and the valence band of energy (lower level of energy). Thanks to diffusion (natural process) and drift (induced by the forward bias current), holes move from the p-doped layer to the middle layer, and electrons from the n-doped layer to the middle layer. Due to the double barrier of energy surrounding the middle layer, electrons and holes are trapped in this middle layer, allowing to reach population inversion. 14

2.4 Schematic of an edge emitting laser. The propagation in the active layer is achieved horizontally. The beam is emitted from the edge . . . 15

2.5 Schematic of a vertical-cavity surface-emitting laser. The active layer is surrounded by two distributed Bragg reflectors. The propagation of photons in the active layer is achieved vertically. The beam is emitted from the upper surface. 16

2.6 Pictures of the vertical-cavity surface-emitting laser used in our experimental work. Pictures provided by Raycan, seller of the VCSEL [34]. 17

2.7 Pictures of a wafer of vertical-cavity surface-emitting lasers. Picture provided by Raycan, seller of the VCSEL [34]. 17

2.8 Schematic of an optical telecommunication line. The signal is emitted thanks to a modulated laser diode. It is then transmitted through optical fiber and is amplified multiple times during the transmission. The signal is finally recorded at the output of the line thanks to photodiode to be interpreted. 18

2.9 Schematic of a laser diode with optical feedback (a) and of a laser diode with opto-electronic feedback(b). 21

2.10 The different regime of dynamics of a laser with feedback, depending on the length of the external cavity end the feedback ratio. Taken from [45] 22

2.11 Numerical examples of dynamics exhibited by a semiconductor laser with feedback (L = 20 cm): (a) steady-state for a feedback rate of 0.5 GHz, (b) periodic for a feedback rate of 1.5 GHz, (c) chaotic for a feedback rate of 2.5 GHz. (d) Bifurcation diagram of a semiconductor laser with feedback, while varying the feedback rate. 23

2.12 Schematic of laser injection. Laser diode b (slave laser) is injected optically by laser a (master laser) 24

2.13 Schematic of a Mach-Zehnder modulator. The phase of the light going through the bottom arm is modulated thanks to the two electrodes. The amplitude is modulated thanks to the interferences happening between the beams outing the two arms of the modulators. 25

2.14 Optical spectra of semiconductor laser externally modulated thanks to optical injection. (a) The slave laser is locked to the master laser. (b) the slave laser is not locked to the master laser 26

2.15 Experimental polarization properties of a VCSEL. (a) Optical spectrum of a free running VCSEL for a bias current close to the threshold current (1.5 × threshold current. (b) Optical power emitted by LP_X polarization mode (orange) and LP_Y polarization mode (blue) of a VCSEL. A polarization switching occurs for a bias current of 5 mA. . . 28

2.16 Pictures of rogue waves 29

2.17 Picture of the squid giant axon. Picture provided by the National Institute of Health. 31

2.18 Pictures of optical neurons 31

3.1 Schematic of a neuron, with transfer function f, weighted inputs $w_i x_i$ and output y_j 37

3.2 Topology of the feedforward neural network. The signal propagates from one layer to another from the input layer to the output layer, in only one (here forward) direction 38

3.3 Topology of the recurrent neural network. The loop in the network allows current signals crossing previous ones 39

3.4 Topology of the reservoir computing network. The topology of the reservoir is the same as the one of the recurrent neural network. We add an output layer to perform the training. 41

3.5 Example of linearly solved problem. Separating linearly gray and black points. The original problem (left) cannot be solved linearly. Adding one dimension allows finding linear solution. 42

3.6 Topology of the time-delay reservoir computing architecture. The neurons are distributed along a delay-line which has a length τ. They are separated by a length of θ. The input stream is pre-processed before sending the input signal in the nonlinear physical node. The training is realized once the signal has propagated in the delay-line thanks to the output layer. 43

3.7 Masking procedure. The input stream can be either a discrete time series $u(k)$ or a continuous signal discretized $u(t)$. The signal $v(t)$ is obtained by holding each value of the input data. $v(t)$ is then multiplied by a mask which has a total length of τ and in which each value is hold during θ. This gives the input signal $s(t)$ which is send in the nonlinear physical node. 44

3.8 Interconnection topology in case of large spacing between virtual neurons ($\theta \gg T$). The dashed red signal represents the driving input signal $s(t)$ and the blue line is the response of the physical node. The node is able to reach its steady state for each input value. Its response only depends on the instantaneous value of $s(t)$ and on the instantaneous state of the reservoir. There is no connection between the virtual neurons. Adapted from L. Appeltant *et al.* work [8] 45

3.9 Interconnection topology in case of small spacing between virtual neurons ($\theta < T$). The dashed red signal represents the driving input signal $s(t)$ and the blue line is the response of the linear node. The node does not have enough time to reach its steady state for each input value. Its response depends on the instantaneous value of s(t) and on the previous states of the reservoir. There are connections between the virtual neurons. Adapted from L. Appeltant *et al.* work [8] 46

3.10 Complete working principle of time-delay reservoir computing. The input stream is first pre-processed with the masking procedure. The signal is sent in the nonlinear node; once its response has propagated in the delay-line, the values of the neurons are collected to perform the training. 47

3.11 Scheme on the optoelectronic reservoir. taken from Y. Paquot *et al.* work [10] 49

3.12 Scheme of the photonic reservoir. Taken from F. Duport *et al.* work [11] 50

3.13 Scheme of the edge-emitting laser-based reservoir. Adapted from D. Brunner *et al.* work [136] 51

3.14 Scheme of the semiconductor ring laser-based reservoir. Adapted from R. Nguimdo *et al.* work [139] 51

3.15 Measuring procedure of the kernel quality. N different input streams are sent in the reservoir computer. The response of each last input is recorded in a matrix. Adapted from L. Appeltant Ph. D. thesis [143] . 52

3.16 Measuring procedure of the generalization property. N different input streams are sent in the reservoir computer, before sending a same input series. The response of each last input is recorded in a matrix. Adapted from L. Appeltant Ph. D. thesis [143] 53

3.17 Exemple of memory function for VCSEL-based time-delay reservoir computer (numerical results presented in Chap. 4). This curve displays the different value of the memory coefficients, depending on the delay i. 55

3.18 First thousand points of the Santa Fe time series 55

3.19 Principle of the nonlinear channel equalization task. The transmitted signal is distorted due to the nonlinear channel. This distorted signal is set as the input of the reservoir computer. The reservoir is trained to predict the original signal. 56

3.20 Example of wireless signal. The line in dotted blue is an example of signal at the input of the channel. The line in grey is the corresponding output of the channel. 57

3.21 Example of optical signals. (a) Signal sent at the input of the fiber. (b) Received signal after 25 km of fiber. (c) Received signal after 50 km of fiber. 59

4.1 Scheme of the VCSEL-based reservoir computer taken from [17] 64

4.2 The two configurations of feedback. For isotropic feedback, the main polarization mode of the VCSEL at the end of the feedback loop is injected parrallely to the main emitted polarization mode, and so is the depressed polarization mode. For polarization rotated feedback, the polarization orientation is rotated perpendicularly during the feedback: the dominant VCSEL polarization mode LP_x at the end of the feedback loop is injected parrallelly to the depressed polarization mode LP_y, and the depressed polarization mode LP_y is injected to the opposite of the dominant polarization mode $-LP_x$. 67

4.3 Temporal response of the system subitted to a step. The bias current is set at $\mu_0 = 1.5$ before $t = 0$ ns. At $t = 0$ ns, the bias current is set at $\mu = 1.55$. $\tau = 8$ ns, $\eta = 0.2$ GHz 68

4.4 Computational ability of the system with electrical input depending on (a) the scaling factor γ and the delay between nodes θ, and (b) on the feedback strength η and the bias current μ_0. Computational ability has been normalized by the number of nodes. 69

4.5 Memory capacity of the system with electrical input depending on (a) the scaling factor γ and the delay between nodes θ, and (b) on the feedback strength η and the bias current μ_0 70

4.6 NMSE on Santa-Fe prediction task of the system with electrical input depending on on the feedback strength η and the bias current μ_0 for (a) $\theta = 0.15$ ns and $\gamma = 0.05$ the scaling factor γ, and (b) $\theta = 0.25$ ns and $\gamma = 0.03$. 70

4.7 Temporal response of the system submitted to a step for the system with (a) isotropic feedback and (b) for the system with rotated feedback. The blue (red) line presents the power emitted by the dominant (depressed) polarization mode. There is no injected power before $t = 0$ ns. At $t = 0$ ns, the injected power is set at $P_{inj} = 0.1$ mW. $\tau = 8$ ns, $\eta = 30$ GHz. A zoom on the oscillating response is providing for both figures. 72

4.8 Bifurcation diagram of the reservoir computer with optical injection. The emitted power is measured while varying the feedback strength η. $P_{inj} = 0.1$ mW, $\tau = 8$ ns. 72

4.9 Computational ability plot as a function of the injection current μ, the node inter-delay θ for an injection power $P_{inj} = 0.1$ mW, and a feedback strength $\eta = 10$ GHz. Adapted from [17]. 73

4.10 Computational ability as a function of the injection power P_{inj} and the feedback strength η. (a) Isotropic feedback configuration (b) Rotated feedback configuration. $\mu = 1.3$ and $\theta = 0.02$ ns. Adapted from [17]. . . 74

4.11 Memory capacity as a function of the injection power P_{inj} and the feedback strength η. (a) Isotropic feedback configuration (b) Rotated feedback configuration. $\mu = 1.3$ and $\theta = 0.02$ ns. Adapted from [17]. . . 75

4.12 Comparison between the dynamics of the reservoir and its (a) computational ability and (b) memory capacity in case of rotated feedback, depending on the injection power P_{inj} and the feedback strength η. $\mu = 1.3$ and $\theta = 0.02$ ns. The black line shows the border between stable and chaotic dynamics. 75

4.13 Memory capacity depending on the rotation of the feedback Θ and the feedback strength η. $P_{inj} = 0.1$ mW, $\mu = 1.3$ and $\theta = 0.02$ ns. 76

4.14 Memory capacity depending on the detuning $\Delta\nu$ and the injected power P_{inj}. $\eta = 10$ GHz, $\mu = 1.3$ and $\theta = 0.02$ ns. 77

4.15 Memory capacity depending on the injection power P_{inj} and the feedback strength η for (a) $\alpha = 1$, (b) $\alpha = 2$, (c) $\alpha = 3$, (d) $\alpha = 4$, (e) $\alpha = 5$, (f) $\alpha = 6$. $\mu = 1.3$ and $\theta = 0.02$ ns. 78

4.16 Memory capacity depending on the injection power P_{inj} and the feedback strength η for (a) $\gamma_a = -0.5$ GHz, (b) $\gamma_a = 0$ GHz, (c) $\gamma_a = 0.5$ GHz. $\mu = 1.3$ and $\theta = 0.02$ ns. (d) Best achievable memory capacity depending on γ_a 79

4.17 Memory capacity depending on the injection power P_{inj} and the feedback strength η for (a) $\gamma_p = 11$ GHz, (b) $\gamma_p = 21$ GHz, (c) $\gamma_p = 41$ GHz, (d) $\gamma_p = 50$ GHz, (e) $\gamma_p = 70$ GHz, (f) $\gamma_p = 87$ GHz. $\mu = 1.3$ and $\theta = 0.02$ ns. (f) Best achievable memory capacity depending on γ_p. The blue line corresponds to the real values, and the red dotted line corresponds to the moving average of the memory capacity. 80

4.18 Sante Fe time series prediction (a) NMSE after prediction for isotropic injection. (b) NMSE after prediction for rotated injection. (c) Example of prediction of chaotic signal: the original signal(blue) and the predicted signal (red crosses). From [20] 81

4.19 Nonlinear channel equalization. The performance of the reservoir is presented as a function of the feedback strength η and the injected power P_{inj} with (a) the isotropic feedback, (b) the rotated feedback configuration using the total emitted power $|E|^2$ as a node state, and (c) with the rotated feedback configuration using separately the emitted power of each polarization mode $|E_x|^2$ and $|E_y|^2$. (d) Symbol error rate for different signal-to-noise ratio. $\square$: single-mode system. $\diamond$: dual mode system using both $|E|^2$. $\triangle$: dual-mode system using $|E_x|^2$ and $|E_y|^2$. (e) Example of reconstruction of a signal with $SNR = 24$ dB: the signal sent in the channel (dotted blue), the non-linearly modified signal at the output of the channel (grey), the reconstructed signal (red). The arrow points to the single error in this data sequence. Adapted from [17] 83

4.20 Illustration of the preprocessing method for the optical channel equalization, using 5 consecutive bits. The signal at the output of the fiber is averaged at twice the frequency of the input data stream, giving symbols $b_n^{(1)}$ and $b_n^{(2)}$ for each bit b_n. Each symbols is hold during the duration of the delay line τ. The 10 values $b_{n-4}^{(1)}$, $b_{n-4}^{(2)}$, to $b_n^{(1)}$ and $b_n^{(2)}$ are masked with a 10 different masks of N values (resulting in a global mask $10 \times N$ values) and used as an input of the reservoir to reconstruct b_{n-2} 84

4.21 Nonlinear optical channel equalization. The BER of the reservoir is presented depending on the feedback strength η and the injected power P_{inj} with (a) the isotropic feedback configuration, (b) the rotated feedback configuration 85

4.22 Nonlinear channel equalization. The BER of the reservoir is presented depending on the feedback strength η and the injected power P_{inj} with (a) the isotropic feedback configuration, (b) the rotated feedback configuration 86

4.23 Pictures of the experimental setup 87

4.24 Scheme of the setup. The signal loaded in the AWG is made by multiplying the input signal by a mask. MZ: Mach-Zehnder madolator, P.C.: polarization Controller, AWG:Arbitrary Waveform Generator, att: attenuator, Oscillo: Oscilloscope, ampl: amplifier,PD: photodiode, BOSA: brilloin scattering optical spectrum analyser. Adaptated from [18] 88

4.25 Experimental optical spectra in different conditions. (a) free running VCSEL, (b) System with feedback and injection (0.3 mW injection, 18 dB attenuation), (c) VCSEL with parallel feedback, 10 dB attenuation, (d) VCSEL with rotated feedback, 10 dB attenuation. From [18] 90

4.26 Experimental signals. (a) masked signal for the input of the reservoir computer. (b) corresponding response of the reservoir. 92

4.27 Example of Santa Fe series prediction: the original Santa-Fe series (blue line and circles), and the predicted series (red line and crosses). Adapted from [18] 93

4.28 Histogram presenting the NMSE obtained with the reservoir with isotropic feedback configuration (blue) and rotated feedback configuration (red) on the Santa Fe prediction task over 50 repetitions. The mean values obtained with isotropic feedback ($\mu_{NMSE,IF}$) and with the rotated feedback ($\mu_{NMSE,RF}$) are represented with the thinner lines. . . 93

4.29 Results for channel equalization task. (a) Experimental results: The shortest strips shows the different SER obtained over different measurement series, the biggest strips shows the mean value, for the parallel feedback (blue) and the perpendicular feedback (red). (b) Experimental prediction for the channel equalization task: the target signal (blue lines and circles) and the predicted signal (red crosses) in case of polarization rotated feedback. arrow points out the error. Adapted from [18] 95

4.30 Histogram presenting the SER obtained with the reservoir with isotropic feedback configuration (blue) and rotated feedback configuration (red) on the wifi channel equalization task over 50 repetitions. The mean values obtained with isotropic feedback ($\mu_{SER,IF}$) and with the rotated feedback ($\mu_{SER,RF}$) are represented with the thinner lines. 96

4.31 Histogram presenting the BER obtained with the reservoir with isotropic feedback configuration (blue) and rotated feedback configuration (red) on the optical channel equalization task over 50 repetitions using (a) 25 km of fiber and (b) 50 km of fiber. The mean values obtained with isotropic feedback ($\mu_{BER,IF}$) and with the rotated feedback ($\mu_{BER,RF}$) are represented with the thinner lines. 97

4.32 Experimental prediction for the optical channel equalization task for a 25 km-long fiber: the target signal (blue lines and circles) and the predicted signal (red crosses) in case of polarization rotated feedback. . 97

4.33 Histogram presenting the SER obtained depending on the level of noise in the output layer of the reservoir with the reservoir with isotropic feedback configuration (purple) and rotated feedback configuration (yellow) on the wifi channel equalization task over 50 repetitions. The mean values obtained with isotropic feedback ($\mu_{NMSE,IF}$) and with the rotated feedback ($\mu_{NMSE,RF}$) are represented with the thinner lines. Adapted from [18] 98

5.1 Scheme of the setup. The dominant (depressed) polarization mode is represented by the blue (orange) arrow. The polarization controller in the feedback loop preserves the polarization state along the fiber. The ones in the input layer are used to align the polarization of both signals with the dominant and depressed polarizations of the VCSEL. MZ: Mach-Zehnder modulator, P.C.: polarization controller, att.: attenuator 103

5.2 Method used to produce the figures. For each value of the ratio of infected power $\frac{P_{inj_y}}{P_{inj_x}}$, we look for minimizing the mean of the BER of both tasks T_x and T_y. We take the values of the BER and report them in the next figures. 105

5.3 Memory capacity of (a) the task injected in the dominant polarization mode and (b) the task injected in the depressed polarization mode, provided by the system with isotropic feedback configuration plot as a function of the feedback strength η and the injected power in the dominant polarization mode P_{inj_x}. $P_{inj_x}/P_{inj_x} = 2$, $\gamma_s = 10$ GHz, $\gamma_p = 50$ GHz. 107

5.4 Best memory capacity of the system with isotropic feedback configuration plot as a function of the injection ratio between the two polarization modes, for different set of parameters of the VCSEL. The blue (orange) line corresponds to the memory of the task injected in the dominant (depressed) polarization mode of the VCSEL. The light color corresponds to the standard deviation. Parameters are (a) $\gamma_s = 10$ GHz,$\gamma_p = 6$ GHz, (b) $\gamma_s = \infty, \gamma_p = 6$ GHz, (c) $\gamma_s = 10$ GHz, $\gamma_p = 50$ GHz, (d) $\gamma_s = \infty, \gamma_p = 50$ GHz 108

5.5 Best memory capacity of the system with rotated feedback configuration plot as a function of the injection ratio between the two polarization modes, for different set of parameters of the VCSEL. The blue (orange) line corresponds to the memory of the task injected in the dominant (depressed) polarization mode of the VCSEL. Parameters are (a) $\gamma_s = 10$ GHz, $\gamma_p = 6$ GHz, (b) $\gamma_s = \infty, \gamma_p = 6$ GHz, (c) $\gamma_s = 10$ GHz, $\gamma_p = 50$ GHz, (d) $\gamma_s = \infty, \gamma_p = 50$ GHz 109

5.6 Example of performance on nonlinear channel equalization for two different signals injected in the two different polarization modes of the VCSEL. Parameters are $\gamma_p = 6$, $\gamma_s = \infty$, $P_{inj_y}/P_{inj_x} = 1$. (a)-(b) Example of symbols reconstruction on the task injected in the dominant polarization mode (a) and in the depressed polarization mode (b). The blue circles correspond to the original signal and the red crosses to the predicted signal. The arrows point out the errors. (c) confusion matrix of the task injected in the dominant polarization mode (LP_X). (d) confusion matrix of the task injected in the depressed polarization mode (LP_Y). 110

5.7 Best SER on the nonlinear channel equalization task of the system with isotropic feedback configuration plot as a function of the injection ratio between the two polarization modes, for different set of parameters of the VCSEL. The blue (orange) line corresponds to the SER of the task injected in the dominant (depressed) polarization mode of the VCSEL. The light color corresponds to the standard deviation. Parameters are (a) $\gamma_s = 10, \gamma_p = 6$, (b) $\gamma_s = \infty, \gamma_p = 6$, (c) $\gamma_s = 10, \gamma_p = 50$, (d) $\gamma_s = \infty, \gamma_p = 50$ 111

5.8 Best SER on the nonlinear channel equalization task of the system with rotated feedback as a function of the injection ratio between the two polarization modes, for different set of parameters of the VCSEL. The blue (orange) line corresponds to the SER of the task injected in the dominant (depressed) polarization mode of the VCSEL. Parameters are (a) $\gamma_s = 10, \gamma_p = 6$, (b) $\gamma_s = \infty, \gamma_p = 6$, (c) $\gamma_s = 10, \gamma_p = 50$, (d) $\gamma_s = \infty, \gamma_p = 50$ 113

5.9 Best BER on the nonlinear optical channel equalization task after 25 km of fiber as a function of the injection ratio between the two polarization modes, for different set of parameters of the VCSEL. The blue (orange) line corresponds to the BER of the task injected in the dominant (depressed) polarization mode of the VCSEL. Parameters are (a) $\gamma_s = 10$ GHz, $\gamma_p = 6$ GHz, (b) $\gamma_s = \infty, \gamma_p = 6$ GHz, (c) $\gamma_s = 10$ GHz, $\gamma_p = 50$ GHz, (d) $\gamma_s = \infty, \gamma_p = 50$ GHz 114

5.10 Best BER on the nonlinear optical channel equalization task after 50 km of fiber as a function of the injection ratio between the two polarization modes, for different set of parameters of the VCSEL. The blue (orange) line corresponds to the BER of the task injected in the dominant (depressed) polarization mode of the VCSEL. Parameters are (a) $\gamma_s = 10$ GHz, $\gamma_p = 6$ GHz, (b) $\gamma_s = \infty, \gamma_p = 6$ GHz, (c) $\gamma_s = 10$ GHz, $\gamma_p = 50$ GHz, (d) $\gamma_s = \infty, \gamma_p = 50$ GHz 115

5.11 Pictures of the experimental setup 117

5.12 Scheme of the experiment. The two masked signals are sent on the two modulators. Each input signal is aligned with a different polarization mode of the VCSEL. The blue and orange arrows show the polarization of the light in the setup. MZ: Mach-Zehnder modulator, P.C.: polarization controller, AWG: arbitrary waveform generator, Att: attenuator, Osc: Oscilloscope, ampl: amplifier, PD: photodiode. 118

5.13 Example of experimental signals. (a) Example of two input streams generated by the AWG. The blue line corresponds to the input stream injected in the dominant polarization mode (LP_x), and the red line to the stream injected in the depressed polarization mode (LP_y) of the VCSEL (b) Example of signals recorded at the output of the reservoir computing system. The blue line corresponds to the response of the dominant polarization mode (LP_x), and the red line to response of the depressed polarization mode (LP_y) of the VCSEL. 118

5.14 Optical spectra of the system under different operation conditions. LP_x: dominant polarization mode, LP_y: depressed polarization mode, ML: master laser. (a) VCSEL with isotropic feedback, $\eta = 17$ dB. (b) reservoir computer with optical injection on both polarization mode without modulation, $P_{inj_x} = P_{inj_y} = 0.08$ mW, $\eta = 17$ dB, (c) reservoir computer with optical injection on both polarization mode with modulation, $P_{inj_x} = P_{inj_y} = 0.08$ mW, $\eta = 17$ dB, (d) reservoir computer with optical injection on both polarization mode with modulation, $P_{inj_x} = 0.08$ mW, $P_{inj_y} = 0.4$ mW $\eta = 17$ dB. 120

5.15 Performance on wifi channel equalization task as a function of the injection power in the main polarization mode P_{inj_x} for a fixed ratio of injection power $\frac{P_{inj_y}}{P_{inj_x}}$ at 0.3. The blue curve corresponds to the performance of the task T_x and the red one to the performance of the task T_y. The dotted line corresponds to the choice of P_{inj_x} reported in figures 5.16 for this specific case. 121

5.16 Performance on wifi channel equalization task as a function of the ratio of injection P_{inj_y}/P_{inj_x}. The blue curve corresponds to the performance of the task T_x, and the red curves corresponds to the performance of the task T_y. The lighter area shows the standard deviation of the performance. The dotted line shows the performance of the reservoir performing the single task. 122

5.17 Performance on nonlinear optical channel equalization task as a function of the injection power in the main polarization mode P_{inj_x} for a fixed ratio of injection power $\frac{P_{inj_y}}{P_{inj_x}}$ at 0.3. (a) Performance for a distortion due to 25 km of optical fiber. (b) Performance for a distortion due to 50 km of optical fiber. The blue curve corresponds to the performance of the task T_x and the red one to the performance of the task T_y. The dotted line corresponds to the choice of P_{inj_x} reported in figures 5.18 and 5.19 for this specific case. 123

5.18 Performance on nonlinear optical channel equalization task after 25 km of optical fiber as a function of the ratio of injection P_{inj_y}/P_{inj_x}. The blue curves correspond to the performance of the task T_x, and the red curves corresponds to the performance of the task T_y for (a) the reservoir computer and (b) the linear classifier. The lighter area shows the standard deviation of the performance. The dotted line shows the performance of the reservoir performing the single task. 124

5.19 Performance on nonlinear optical channel equalization task after 50 km of optical fiber as a function of the ratio of injection P_{inj_y}/P_{inj_x}. The blue curves corresponds to the performance of the task T_x, and the red curves corresponds to the performance of the task T_y for (a) the reservoir computer and (b) the linear classifier. The lighter area shows the standard deviation of the performance. The dotted line shows the performance of the reservoir performing the single task. 125

A.1 Principle of the numerical simulation method. The C++ code is embedded in an Python environment. The same code is run on each CPU of the cluster using a different set of parameters 146

1

Background and Motivation

Alice: Would you tell me, please, which way I ought to go from here?
The Cheshire Cat: That depends a good deal on where you want to get to.
Alice: I don't much care where.
The Cheshire Cat: Then it doesn't much matter which way you go.
Alice: ...So long as I get somewhere.
The Cheshire Cat: Oh, you're sure to do that, if only you walk long enough.
Lewis Caroll, *Alice in Wonderland*

Thirty three billions of terabits. This is the amount of data produced by the whole world in 2018. These is the same amount of data contained in 660 billion of Blue-Ray disc. This data are produced by our computers, smartphones and other smart objects. The recent explosion of the number of this small computers in the network also led the explosion of data production. The new trends for home automation also tend to connect even more objects to the network, each producing data. This amount of data is forecasted to grow even more in the next few years with the upcoming 5G network used with the connected objects from Internet of Things [1].

All these data need to be processed, which often requires a high computing power due to the complexity of the related algorithms. These computational resources can be found in data centers. Data centers occupy huge building containing thousands of super computers, each composed of several central process unit (CPU), and each composed of several computational units (core).

Figure 1.1: Picture of a Google Data center

These data centers process data from everywhere to offer even more functionalities to the end user: Internet search (Google currently processes on average 70,000 searches/second), recover of the transmitted data over the internet network, helping industries with precise statistics and market prediction, weather forecasting, simulating complex physical problems (such as mapping the dark matter halo in the Milky Way), just to name a few.

However, Von Neumann architectures (classical computer performing algorithms) struggle with performing some tasks that are highly complex [2], such as decisional problems (e.g. is that object a pear or an apple? What should I do based on what I heard?). Our brain is however able to process such decisional tasks very efficiently while we are not able to execute efficiently algorithms, when compared to a computer. Our brain records and processes all the sensorial signals around us, which trigger a neuronal activity leading to a reaction. The efficiency of our brain is based on the nearly hundred billions of neurons that are all connected together. This internal brain

structure inspired a novel processing approach called artificial neural network, which is a concept of machine learning.

The data processing approach in machine learning is radically different from the Turing machine method. In the Turing machine, an analog signal to be processed is converted to a digital signal. The processing of this signal is predefined in an algorithm made of logical blocks. After processing, the resulting digital signal is converted back to an analog signal to be used in the physical world. Machine learning offers instead to process analog signals without coding explicitly the transformation that must be operated. The analog signal can be processed analogically or converted to a numerical signal depending on the architecture considered. Before processing signals, the system must be trained with examples, as a child is taught at school. This learning phase can be supervised or unsupervised. With supervised learning, the system learns the processing thanks to sets of examples of inputs and the corresponding target signals. With unsupervised learning, the system learns from a large number of examples to separate the input signals in classes, which groups similar inputs together. The system learns from the similarity that can exist between different input signals. Once the system is trained, it can process signals that have never been seen by the system, but that have the same properties. Machine learning is currently used to class images or

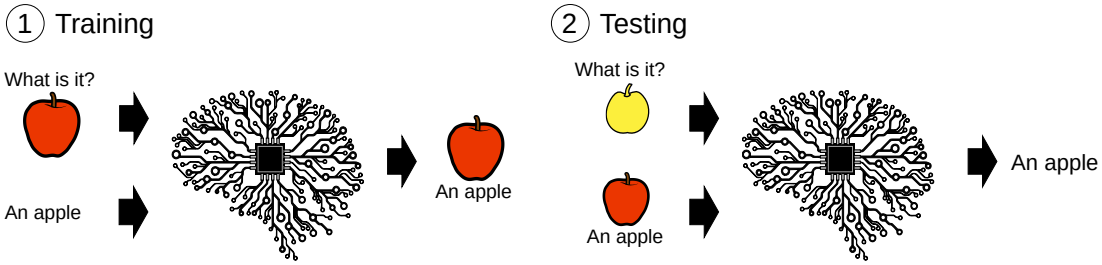

Figure 1.2: Processing signal with machine learning approach in case of supervised learning: the system is first trained. During this step, the system learns how to realize a task (here recognizing an apple). The system is then tested. During this step, other inputs are shown to the system and the system responds using the method learned during the training (here the system recognizes an apple as he has been trained to recognize apples).

recognize shapes [3], recognize spoken words [4], or even to translate texts [5]. Artificial neural network is one of the numerous machine learning technique. It is inspired from the architecture of the human brain, as it is composed of neurons that are linked together. The training consists of adapting the strength of the links between the neurons (similarly to the training phase of the human brain).

Another limitation encountered with data centers is the power consumption. A data

center use around 100 MW to work properly, which represent 10% of the energy production of a nuclear reactor. This high energy consumption is mainly due to the heat of electronic components, and the cooling systems used to evacuate this energy. Replacing electronic components with photonic components has thus been studied to perform some of the tasks in place of electronic devices. Photonic components such as semiconductor lasers require only low energy to work properly, and also suffer from lower loss, thanks to a better power efficiency. As a result, these semiconductor lasers do not require powerful cooling systems, which further contribute to a lower power consumption. Where a classical computer uses about 1 kW, a semiconductor laser-based system would require only few watts. Realizing computational system using photonic component has recently been proved to be feasible [6].

While thinking of photonic artificial neural network, one may think about a network of lasers connected together, each laser being a neuron. D. Brunner and I. Fischer realized experimentally such a network by coupling semiconductor lasers in a matrix thanks to a diffractive element [7]. However, coupling a large number of lasers remains a technical challenge. It is the reason why a new type of neural network, called time-delay reservoir computing came to birth. This new type of artificial neural network is made of one dynamics component (e.g. a laser) and a delay-line. The neurons are now virtual, distributed along the delay-line [8], and their number can be easily increased by lengthening the delay-line, or bringing the neurons closer together. L. Larger *et. al.* reported the first realization of such an architecture, using opto-electronic components [9], quickly followed by Y. Paquot *et. al.* [10]. However, the speed of such an architecture is limited by the length of the delay-line: the longer the delay-line is, the slower the neural network performs computation. A key issues is to find dynamical component allowing to bring closer the neurons. To this end, several architectures have been proposed, made of an optical amplifier [11], a semiconductor laser [12, 13, 14, 15], or an electro-optic modulator [16].

The goal of this thesis is thus to realize a computational device made of photonic components, which aims at being used for telecommunication applications, implying reaching fast computational speed. Our challenge will be to use mainly telecommunication components to realize this reservoir, such as vertical-cavity surface emitting laser (VCSEL), and single mode optical fiber. It appears that this specific laser exhibits an interesting polarization dynamics that we want to harness to achieve the best possible computational performance. We will realize the system on the basis of numerical simulation and experimental tests. Each concept is first explored numerically to choose the components properly and find the best set of parameters that leads to an efficient computational device. This allows exploring more parameters quickly, and to have an insight of the role of each parameter on the working properties of the system. The

relevant data found numerically are exploited to build the corresponding experimental setup, and to validate the numerical hypothesis experimentally. In this thesis, we do not aim at creating new dynamics but rather at exploiting these known dynamics to perform computation with optimal performance.

Outline

This dissertation is divided in four chapters.

In a first chapter, we present the basics about semiconductor lasers. We introduce the lasing effect and how to realize lasers with semiconductor materials. The structures of two different lasers are introduced: the conventional semiconductor laser so-called edge-emitting laser (EEL) and the vertical-cavity surface-emitting laser (VCSEL). VCSELs exhibit several advantages, which make them widely used in the industry. Some of their properties are presented in this chapter. We then present the main dynamics achievable with a system made of semiconductor lasers, and we introduce the specific polarization dynamics of VCSELs. We finally propose some examples of use of laser dynamics, including reservoir computing.

In a second chapter, we present the basic knowledge on artificial neural networks (ANN) and reservoir computing (RC). We introduce what is a feedforward neural network and a recurrent neural network (RNN), and we focus on a specific recurrent neural network called reservoir computing. We then introduce the concept of time-delay reservoir computing, which is a particular architecture to implement reservoir computing. We also provide several examples of ANN, before presenting the tasks we will use to benchmark our photonic architecture.

These two first chapters explain all the basic concepts required to understand our thesis work.

In a third chapter, we present our proposal for a reservoir computer architecture made of telecommunication components. The architecture is based on time-delay reservoir paradigm, using a VCSEL and single-mode optical fiber. In this chapter, we focus on the performance of the reservoir when processing a single task. We first explore numerically the performance of the system with electrical or optical input and describe the steps toward an experimental setup and test its performance. We finally compare the numerical and experimental results to assess on the validity of our theoretical model.

In a fourth chapter, we show how our architecture can be used to process two tasks simultaneously while exploiting multimode optical properties of a VCSEL. Two optical

signals linearly polarized are injected in each polarization mode of a VCSEL, and the response of the reservoir is used to train it to perform the two tasks corresponding to the inputs. As in the third chapter, we first present the adapted model and the results of the exploration of the parameter space. The numerical performance is then checked experimentally, and we finally compare the numerical predictions with the experimental performance.

We finally propose in the last chapter an overview of the thesis work and draw perspectives for future work.

Publications and conferences

The results found during this Ph. D. have been published in different articles and has been presented in different conferences.

Publications

- J. Vatin, D. Rontani, and M. Sciamanna, "Enhanced performance of a reservoir computer using polarization dynamics in VCSELs," *Opt. Lett.***43**, 4497–4500 (2018) [17].

- J. Vatin, D. Rontani, and M. Sciamanna, "Experimental reservoir computing using VCSEL polarization dynamics", *Opt. Exp.***27**, 18579–19584 (2019) [18].

- J. Vatin, D. Rontani, and M. Sciamanna, "Experimental realization of dual task processing with a photonic reservoir computing", *APL. Phot.***5**, 18579–19584 (2020) [19].

Conferences

- Vatin, Jeremy, Damien Rontani, and Marc Sciamanna. "High-Speed All-Optical Reservoir Computing Using VCSEL Polarization Dynamics." 2018 European Conference on Optical Communication (ECOC). IEEE, 2018. [20]

- Vatin, Jeremy, Damien Rontani, and Marc Sciamanna "Reservoir computing using VCSEL polarization dynamics" 2019 Conference on Laser and Electro-Optics (CLEO), IEEE, 2019 [21]

- J. Vatin, D. Rontani, and M. Sciamanna, "Photonic machine-learning using VCSEL polarization dynamics", Photorefractive Photonics and beyond 2019.

- J. Vatin, D. Rontani, and M. Sciamanna, “Polarization dynamics of VCSELs improves reservoir computing performance”, ICANN 2019: Workshop and Special Sessions. ICANN 2019. Lecture Notes in Computer Science, vol 11731. Springer, Cham [22]
- J. Vatin, D. Rontani, and M. Sciamanna, “VCSELs polarization dynamics for improved performance of photonic reservoir computing”, International Symposium on Physics and Applications of Laser Dynamics 2019.

2

Physics of semiconductor lasers

Highly organized research is guaranteed to produce nothing new.
Frank Herbert, *Dune*

Contents

2.1 Semiconductor lasers 10
2.1.1 Basic principle of lasing effect 10
2.1.2 Semiconductor edge-emitting laser (EEL) 12
2.1.3 Verical-cavity surface emitting laser (VCSEL) 15
2.2 The use of VCSELs today 16
2.2.1 Industrial advantages of the VCSEL 16
2.2.2 VCSELs in telecommunication system 18
2.2.3 VCSELs in biology 19
2.2.4 VCSELs in our everyday life 20
2.3 Complex Dynamics of lasers 20
2.3.1 Laser submitted to feedback 21
2.3.2 Laser submitted to injection 24
2.3.3 Laser submitted to modulated injection 25
2.3.4 Specific properties of VCSELs 27
2.4 Use of complex waveforms 29
2.4.1 To mimic 29
2.4.2 To process information 32
2.5 Conclusion 33

The massive use of optics in the telecommunication network has been made possible thanks to the development of the semiconductor laser. Compared to other light sources such as gas lasers or solid-state lasers, semiconductor lasers are very low cost and compact devices with a long life expectancy and a high efficiency. These advantages made this component suitable for an industrial use in telecommunication networks. More specifically, the work presented in this thesis is based on the use of a VCSEL.

Before presenting the use we are making of such components in the context of photonic computing, we will first introduce the physics underlying the semiconductor laser. In a first section 2.1, we present the basics about lasers, and how to achieve lasing with semiconductor lasers. In a second section 2.2, we focus on a specific type of semiconductor laser emitting light from the surface and called vertical-cavity surface-emitting laser. We then present how to achieve complex dynamics with semiconductor lasers 2.3, before presenting some applications of these dynamics 2.4.

2.1 Semiconductor lasers

The word "laser" is now approved in the dictionary. We can find for instance in the *Cambridge dictionary* that a laser is a "device that produces a powerful, narrow beam of light that can be used as a tool to cut metal, to perform medical operations, or to create patterns of light for entertainment" [23]. LASER is nevertheless in its first definition an acronym which stands for "light amplification by stimulated emission of radiation". Therefore, to understand how a laser works, we first need to understand the stimulated emission of light.

2.1.1 Basic principle of lasing effect

The stimulated emission of radiation was theoretically predicted by A. Einstein in 1916 [24]. However, the first component using this property came to birth in 1960 thanks to T. Maiman [25]. To briefly explain this effect, let us consider a system with two levels of energy E_1 and E_2 as depicted in Fig. 2.1. We also consider a particle which can exhibit one of the two energy states. The particle is said excited when it has the energy of the higher level E_2. We define the energy of the photon as $E_{phot} = h\nu$, where h is the Planck constant, and ν is the electromagnetic frequency of the photon. There are three different ways for this particle to interact with photons.

- The first phenomenon presented in Fig. 2.1.(a) is called *absorption*. The particle absorbs the energy of the photon, which allows it to reach its excited state.

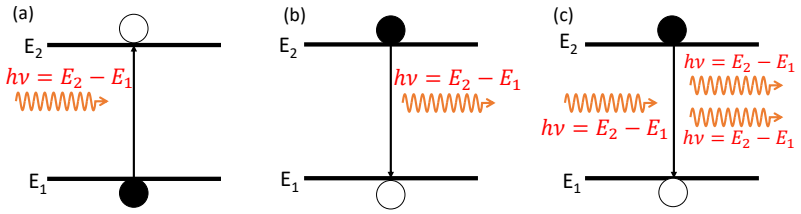

Figure 2.1: The three interaction light-matter. An electron can get excited from the lower level of energy to the higher by absorbing the energy of a photon (a). An electron can relax from the higher level of energy E_2 to the lower one E_1 emitting a photon having an energy $E_2 - E_1$. This phenomenon can be spontaneous (b) or stimulated by another photon with the same energy $E_2 - E_1$ (c). In the second case, the emitted photon has the same properties as the stimulating photon.

- The second one presented in Fig. 2.1.(b) is called *spontaneous emission*. The excited particle spontaneously relaxes from the upper level of energy E_2 to the lower level E_1. During this process, a photon is emitted which energy $h\nu = E_2 - E_1$ corresponds to the difference of energy between the two levels.

- The last possibility, depicted in Fig. 2.1.(c) is called *stimulated emission*. A photon with an energy $h\nu = E_2 - E_1$ is present in the system. This stimulates the transition of the particle from the upper level of energy to the lower level, creating another photon with the same energy. The newly created photon has therefore the same properties as the incoming photon (same energy, therefore same frequency or wavelength and the two photons exhibit the same phase). This incoming photon has then been amplified thanks to stimulated emission.

If we keep creating photons thanks to stimulated emission, and when the losses are compensated, we obtain light amplification, producing a gain in the medium. This phenomenon is the dominant process when most of the particles are excited. The configuration in which a maximum of particles are in the excited energy state is called *population inversion*, which can be obtained thanks to a process called *pumping*. Pumping can be achieved by sending a light source with an energy higher than $E_2 - E_1$ to the gain medium, which energy is absorbed, as for the first laser presented by T. Maiman, or by applying an electrical current to the active medium, as it is commonly done with helium-neon laser [26], or semiconductor lasers [27].

The energy $h\nu$ we presented can be either discrete (the number of reachable energies is countable) or continuous (a range of energies is achievable) depending on the considered materials. In case of semiconductors (presented in the next section), the reachable energies are continuous, allowing thus producing a continuous range of wavelengths (unless if the bulk semiconductor is replaced by quantum wells, dots, ...). However, a laser is wavelength-selective. This is done by placing the active medium in a resonant

cavity. The simplest one is a cavity made of two parallel mirrors, with the active layer in between. This is called the Fabry-Perot cavity. These mirrors impose boundary conditions. Only the electromagnetic waves satisfying these conditions can propagate in the cavity. These waves are called modes of the lasers. They are separated by a frequency difference $\Delta\omega$ such as:

$$\Delta\omega = \frac{c}{2Ln_g}, \tag{2.1}$$

with $c = 299792458$ m.s^{-1} the light velocity, L the length of the Fabry-Perot cavity, and n_g is the group velocity in the considered material. The two edge mirrors allow preserving part of the photons inside the cavity, which reduces the required pumping power to reach the population inversion state.

If stimulated emission is a mechanism creating more and more photons, Mechanisms for photon losses are inevitably created the cavity, for examples the natural absorption of the active medium, and the photons exiting the cavity. Because mirrors are partially reflective, we note indeed that the beam we are considering as an output of the laser is made of photons leaving the cavity, which are thus also considered as lost photons. The laser starts emitting a laser beam when the amplification effect of the cavity overcomes the losses. The specific point where the stimulated emission equals the losses is called laser threshold. Figure 2.2 shows a typical light-pump curve. When the energy brought to the cavity is too low, the dominant radiation effect is the spontaneous emission. After the threshold, the dominant radiation effect is the stimulated emission, and the laser starts emitting a powerful coherent light beam.

Three ingredients are thus required to have a laser:

- a gain medium in which gain results from stimulated emission
- a cavity to select frequencies and to control the losses
- a pump to provide energy for the gain and therefore to overcome the losses.

2.1.2 Semiconductor edge-emitting laser (EEL)

The lasing amplification effect can be obtained with semiconductor materials, which is rather convenient as it allows producing compact devices [28]. Moreover, semiconductors are largely used in electronic systems, and therefore the industrial process is well mastered. According to their name, semiconductors are neither conductors nor insulators. They can be both depending on their operating point. In terms of energy, electrons moving inside semiconductors can exhibit an energy inside the conduction

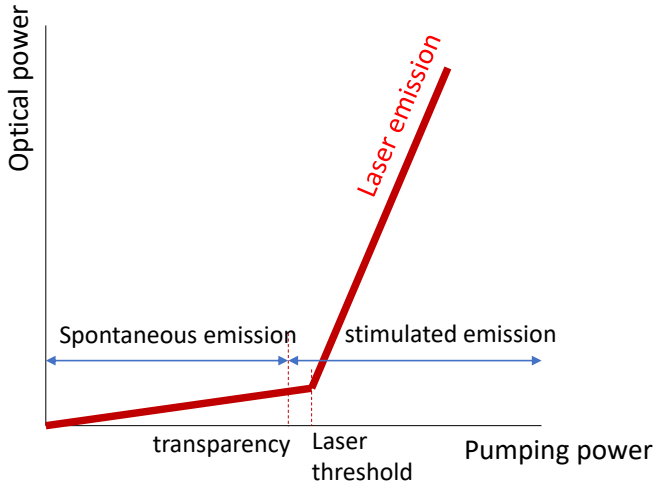

Figure 2.2: Typical light pump curve of a laser. when the energy brought to the cavity is too low, the dominant effect is the spontaneous emission. After the threshold on the contrary, the losses are compensated, the dominant phenomenon is the stimulated emission, and the laser starts emitting light.

band (high energy) or inside the valence band (low energy). These two bands of energy are separated by a band-gap in which no quantum state with such an energy can be found. When all the electrons have their energy in the valence band, the semiconductor behaves as an insulator. But thanks to the temperature, some electrons can get enough energy to access the conduction band, leaving a hole (a positive charge) in the valence band. Electrons and holes can be brought respectively in the conduction and valence band thanks to a bias electrical current. By combining different semiconductors, we can create what is called a double heterostructure [29], which energy diagram is depicted in Fig. 2.3. On both sides of the structure, the same semiconductor material is doped with donors on one side (n-doped) and with acceptors on the other side (p-doped). This allows changing the energy levels, keeping a constant energy band-gap. Between these two doped materials, a different semiconductor is introduced with a smaller band-gap. When the different semiconductors are in contact, a diffusion of carrier occurs, in which electrons move from the n-doped region to the middle layer, and the holes diffuse from the p-doped region to the middle layer. Applying a forward bias current brings a constant flow of electrons to the n-doped region, and of holes to the p-doped region. It also allows electrons to drift from the n-doped region to the middle layer, and holes to drift from the p-doped region to the middle layer. Once in this middle layer, electrons and holes are trapped due the double potential barrier. In the middle layer, population inversion ensures that a large number of energy states can be occupied by electrons in the conduction band and by holes in the valence

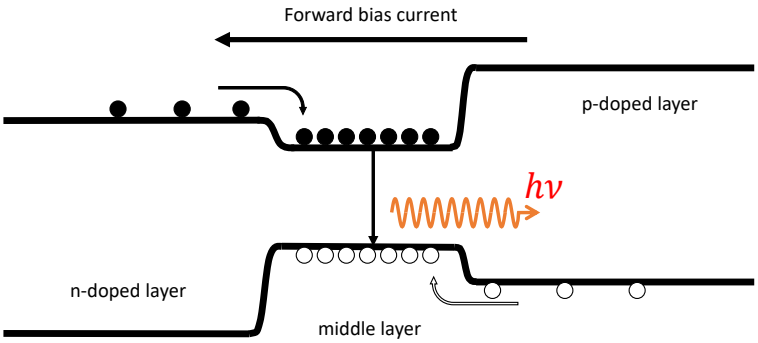

Figure 2.3: Energy diagram of the double heterostructure. The diagram shows the conduction band (higher level of energy) and the valence band of energy (lower level of energy). Thanks to diffusion (natural process) and drift (induced by the forward bias current), holes move from the p-doped layer to the middle layer, and electrons from the n-doped layer to the middle layer. Due to the double barrier of energy surrounding the middle layer, electrons and holes are trapped in this middle layer, allowing to reach population inversion.

band. Electrons can then relax from the conduction band to the valence band to recombine with holes. This can be achieved by a spontaneous or stimulated process, emitting photon during the transition. As the emission of photon happens in the middle material (with a smaller bang-gap), this region of the component is called active layer.

Although the double heterostructure is able to generate stimulated photons, a laser requires a large number of stimulating photons to emit radiation with enough power. This structure is achieved by adding mirrors that reinject enough photons in the active layer, so that enough power is achieved by stimulated emission. By cleaving the semiconductor material, one can easily build a cavity. The interface between the active layer and the air outside the structure acts as a semitransparent mirror that let some photons leaving the structure. This structure thus keeps enough photons in the active layer to encourage the stimulated emission. The photons leaving the structure by the edge are highly coherent, and thus provide radiation with a high-power density. This structure has been presented in 1970 by Z. Alferov [30] (cf Fig. 2.4) and is known as the double heterostructure edge-emitting laser, so-called since the laser beam is emitted from the edge.

The choice of the component of the active layer determines the wavelength of the laser, since photons have energy close to the band-gap energy. For instance, an active layer made of aluminum gallium arsenide (AlGaAs) will mainly emit light in red and near infra-red (between 630 nm and 900 nm). An active layer made of indium gallium arsenide phosphide (InGaAsP) mainly emits in middle infra-red (between 1000 nm

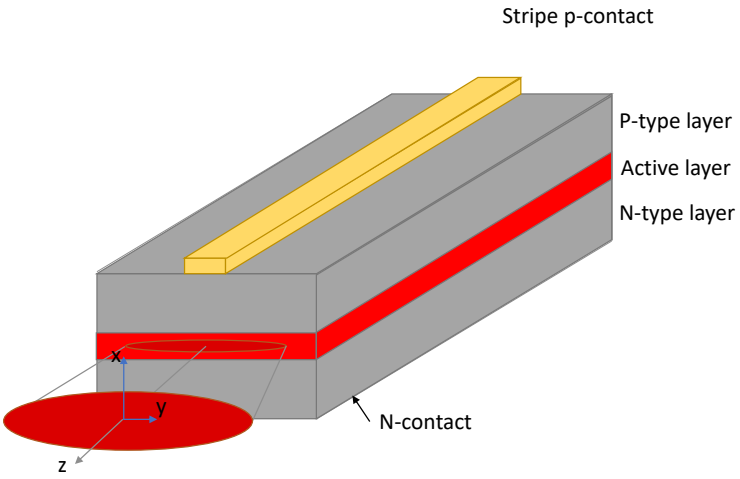

Figure 2.4: Schematic of an edge emitting laser. The propagation in the active layer is achieved horizontally. The beam is emitted from the edge

and 2100 nm).

2.1.3 Verical-cavity surface emitting laser (VCSEL)

The vertical-cavity surface-emitting laser (VCSEL) has been introduced in 1979 by Soda *et. al.* [31]. Contrary to the edge-emitting laser, the vertical-cavity surface-emitting laser emits light from its surface. The length of the active layer has been reduced from micrometers for the edge-emitting laser to few nanometers in the VCSEL, which leads to lower threshold current, but also to a smaller gain. To further decrease the loss, the active layer was placed between two gold mirrors. However, even if the reflectivity of such mirrors is rather high (95%) the threshold current remains high, around 900 mA.

Ogura *et al.* proposed in 1987 to replace the gold mirror with distributed Bragg reflectors (DBR) [32]. A DBR mirror is a superposition of thin layers of semiconductors. The constructive interference of light beam diffracting at the layer interfaces allows reaching reflective as high as 99%. Thanks to these new mirrors, Jewel *et al.* have been able to realize a VCSEL with a threshold current around 1 mA [33].

As the DBRs are made of semiconductor materials, they can be either p-doped or n-doped to conduct the carriers to the active layer, and to trap them in the active layer. A schematic of the structure of the VCSEL is presented in Fig. 2.5.

In addition to the low power consumption of the VCSEL, the specific geometry of the laser allows shaping the beam to be quasi circular, which optimizes the coupling

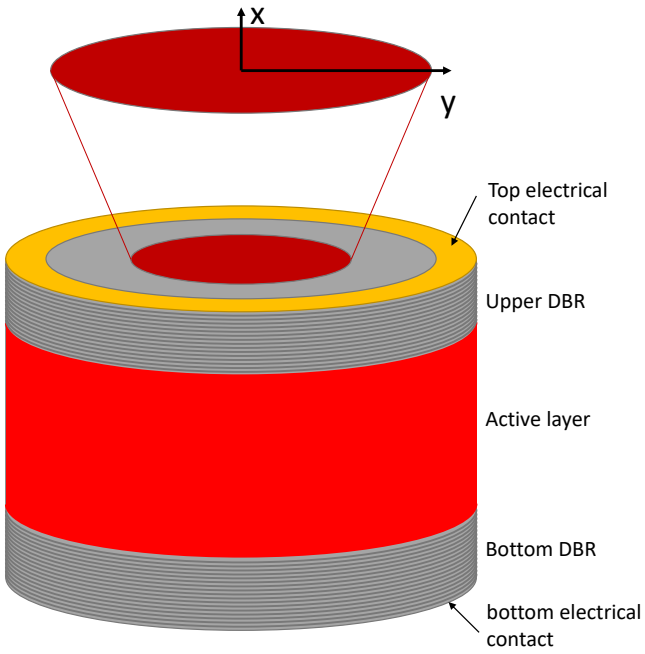

Figure 2.5: Schematic of a vertical-cavity surface-emitting laser. The active layer is surrounded by two distributed Bragg reflectors. The propagation of photons in the active layer is achieved vertically. The beam is emitted from the upper surface.

efficiency to optical fibers and also removes any polarization preference. This round shape also leads to interesting polarization properties that will be discussed later in this chapter.

The VCSEL we will use in this thesis emits light at 1550 nm. Its active layer is made of indium gallium arsenide (InGaAs). The two DBRs are a superposition of layers made of indium aluminum gallium arsenide (InAlGaAs) and indium aluminum arsenide (InAlAs). A picture of the structure of this VCSEL is presented in Fig. 2.6.

2.2 The use of VCSELs today

VCSELs are largely used, mainly due to their advantages in terms of laser properties and of manufacturing.

2.2.1 Industrial advantages of the VCSEL

The manufacturing of the VCSEL presents several advantages compared to the classical edge-emitting lasers. The light is emitted in a direction parallel to the growth direction, contrary to the EEL which emits light perpendicularly to the growth direction. This

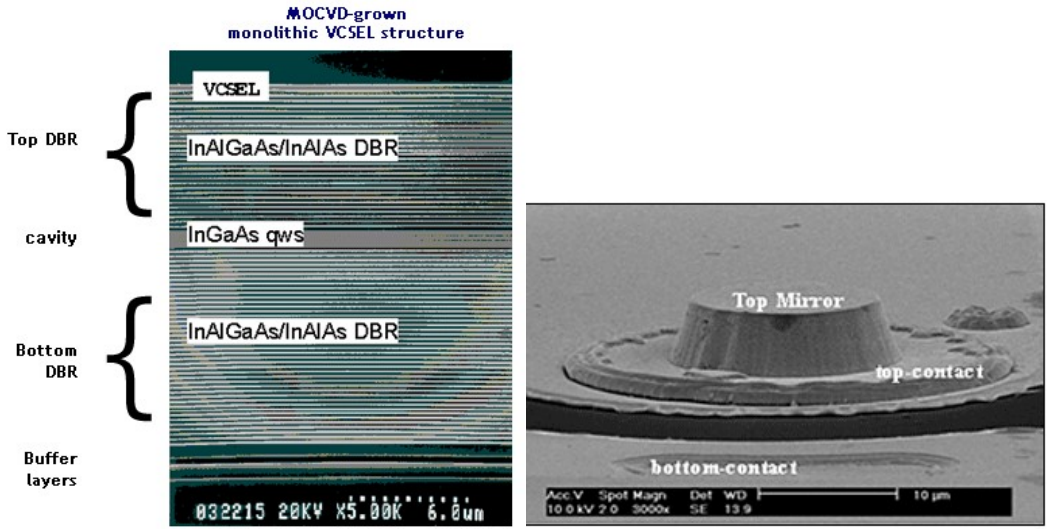

(a) Vertical cut **(b)** Microscopic picture

Figure 2.6: Pictures of the vertical-cavity surface-emitting laser used in our experimental work. Pictures provided by Raycan, seller of the VCSEL [34].

characteristic allows manufacturing 2D-wafers of lasers and testing each lasers directly on the wafer. A picture of such a wafer is presented in Fig. 2.7. Moreover, as presented in the previous chapter, the use of mirrors with higher reflectivity for VCSELs reduced its current threshold, allowing lowering its power consumption.

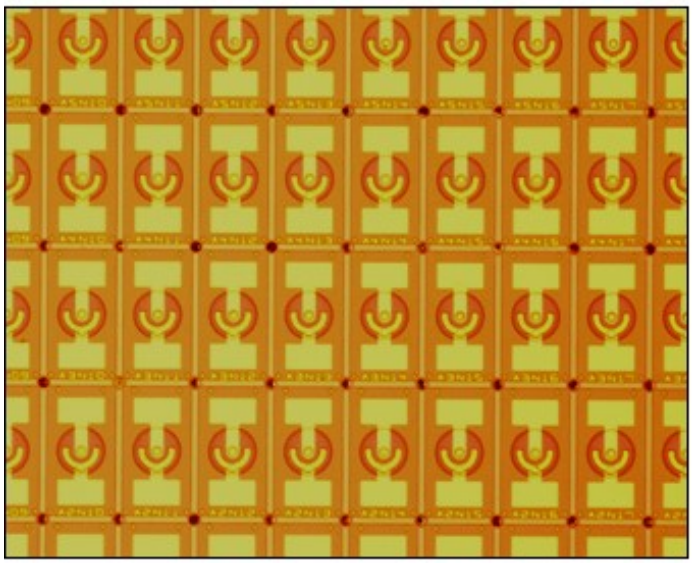

Figure 2.7: Pictures of a wafer of vertical-cavity surface-emitting lasers. Picture provided by Raycan, seller of the VCSEL [34].

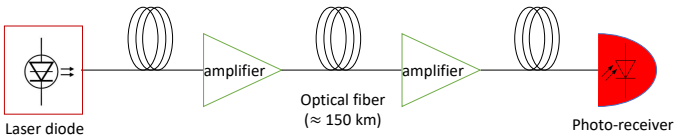

Figure 2.8: Schematic of an optical telecommunication line. The signal is emitted thanks to a modulated laser diode. It is then transmitted through optical fiber and is amplified multiple times during the transmission. The signal is finally recorded at the output of the line thanks to photodiode to be interpreted.

2.2.2 VCSELs in telecommunication system

One of the principal use of VCSELs today might be in optical communication networks. Optical communication is the core technology of today's internet network, allowing us to exchange more than 29 Pb each second. This network is based on four main components:

- a coherent light source
- a low loss optical channel
- an amplifier
- an optical receiver

The data exchanged thanks to internet are digital. That means they are encoded thanks as binary digits or bits (0 or 1). Bits are encoded in the light. This encoding is called modulation. We can think to the trivial modulation: we send a 1 by sending light, and a 0 by sending nothing. In order to reach higher transmission speed, the modulation is in fact more complex, to encode many bits at once. One of the most used modulation formats in the internet network is the quadratic amplitude modulation (QAM). These bits modulated together are called symbols. Thanks to this modulation format we are now able to reach transmission speed about terabits per seconds [35].

Using a semiconductor laser to transmit the bits shows several advantages. As we already explained, these light sources are power efficient, which allows transmitting signals at a low power cost. Moreover, the spectrum of a laser source is narrow thanks to the wavelength selectivity of the cavity, hence making possible to multiplex several wavelengths in one channel without overlapping the data. The discovery of VCSELs brought new advantages. The spectrum is even narrower allowing multiplexing more

wavelengths, and the typically circular aperture limits the divergence of the beam. This property leads to better coupling efficiency in the optical fiber.

The optical fiber is the key discovery that made the optical communication possible. Charles K. Kao has been awarded in 2009 the Nobel prize for discovering a low-loss optical fiber (0.2 dB/km) [36]. This fiber is made of silica, which is transparent for wavelengths between 500 nm and 1900 nm, with a minimum of attenuation around 1550 nm. This is specifically convenient as the manufacturing of VCSELs emitting in this range of wavelength is feasible, as presented previously, and inexpensive. Thanks to this fiber, the amplitude of the signal is divided by two after 15 km, which allows propagating the signals over 150 km before having to amplify the signal.

As the data have to be transmitted most of the time over thousands of kilometers, the signals have to be amplified in the line, each 150 km. The most used amplifier in telecommunication network is the erbium doped fiber amplifier (EDFA). This amplifier exploits nonlinear mechanisms of the erbium doped fiber. The system is pumped with a laser at 980 nm. This pumping stimulates the emission of photons at 1550 nm [37].

The optical signal is finally recorded with a photodiode. In a photodiode, the photons are absorbed to create pairs of electrons and holes, hence modifying the voltage at the output of the device.

2.2.3 VCSELs in biology

The specificities of the VCSEL also found applications in biology. For instance, A. Birbeck*et al.* published in 2003 a work showing that they have been able to use an array of VCSELs to manipulate cells [38]. They shape a Laguerre-Gaussian beam (in shape of a donut) to trap and manipulate cells. The advantage of the VCSEL in this application is that VCSEL is smaller than the other semiconductor lasers, and that arrays of VCSELs can easily be manufactured thanks to their growth direction, as presented in the previous section. Both compactness and ease of fabrication allows meeting the requirements of building microchips in biology applications.

Another example of the use of VCSELs in biology as been presented in 2008 by T. Svensson *et al.* [39]. In their work, they present how they use VCSELs to perform oxygen spectroscopy, and thus measure the porosity of biological tissues. The use of VCSELs simplifies the spectroscopy system by using a single laser diode to perform the measurement, instead of a dual laser system when using conventional semiconductor lasers. The resulting improvement is significant in terms of simplicity, robustness, cost and speed.

2.2.4 VCSELs in our everyday life

We can also find VCSELs in many devices we are using every day. The computer mouse is one of them. A VCSEL now substitutes the LED used to detect the displacement of the mouse [40]. The VCSEL brings several advantages to the manufacturing of computer mouse. The power efficiency of the VCSEL makes it specifically interesting for mouse working on batteries. Moreover, the movement detection with VCSELs provides a better accuracy.

Another application of VCSEL can be found in Apple Iphone, or other smartphones from Huawei or Xiaomi. In these smartphones, VCSELs are used to perform 3D sensing thanks to structured light [41]. For structured light, a light source emits a pattern on a surface. The distortion of this pattern while reflected toward the projecting device is recorded and helps deducing the 3D-shape of the observed object. This is used in smartphones mainly for face recognition and fingerprint detection. The advantage of VCSELs for this application is related to the better accuracy of the detection, and the low power consumption which makes the components suitable for embedded devices.

The accuracy of LIDAR has also been improved thanks to the use of VCSELs. LIDAR is the acronym for light detection and ranging. Short pulses at nanoseconds scales are emitted thanks to a light source. These pulses are reflected by an object. The distance between the light source and this object is calculated thanks to the delay between the emission and the reception of a pulse. The use of VCSEL allows not only improving the accuracy of the detection but also reducing the cost of the device [42]. LIDAR are used in a large range of application, such as threat detection for defense, detecting obstacles for robots and autonomous cars, or measuring the shape of the earth.

2.3 Complex Dynamics of lasers

Semiconductor lasers exhibit a rich dynamics as evidenced by an extensive research over the past 40 years [43]. We will briefly present the different dynamics that can be exhibited by a semiconductor laser in this section. This section does not aim at being exhaustive as this thesis is not focused on the study of the dynamics of the semiconductor laser, but rather at presenting the characteristics of the dynamics required to understand the observed phenomena in Chaps. 4 and 5.

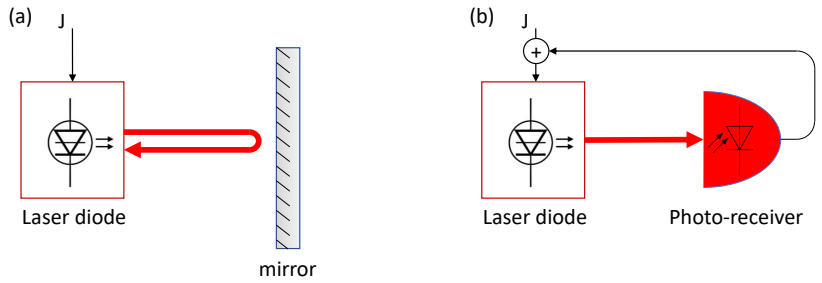

Figure 2.9: Schematic of a laser diode with optical feedback (a) and of a laser diode with opto-electronic feedback(b).

2.3.1 Laser submitted to feedback

Adding a feedback to a laser can unlock a rich dynamics, that would not be achieved with the free-running laser. There are two main configurations of feedback, that are depicted in Fig. 2.9:

- optical feedback: the light emitted by the laser is injected back in its cavity. This can be achieved deliberately with a mirror for instance, but also occurs spontaneously when coupling light into fiber. Fig. 2.9.(a)
- opto-electronic feedback: the light emitted be the laser is converted to an electrical signal thanks to a photodiode. This electronic signal is used to modulate the bias current of the laser. Fig. 2.9.(b)

Since the design of the system analyzed in this thesis is based on optical feedback, we will solely present the dynamics of the laser with optical feedback. We can define two parameters to measure the amplitude of the optical feedback: The feedback ratio (in %) which corresponds to the ratio of the emitted power that is reinjected in the laser cavity, and the feedback rate (in Hz) that is often used for numerical simulation. The feedback rate (noted η in this work) is defined as [44]

$$\eta = \frac{1 - r^2}{\tau_{in}} \frac{r_0}{r}, \tag{2.2}$$

with r the reflectivity of the of the facet of the cavity, r_0 is the reflectivity of the external mirror, and τ_{in} is the roundtrip time in the cavity.

Tkach and Chraplyvy has in 1986 analyzed the dynamics of such a setup [45]. Two parameters are considered: the length of the external cavity L, which is the distance travelled by light along the feedback, and the feedback ratio, which is ratio of optical power injected back to the cavity over the emitted optical power. When varying these parameters, different dynamical regimes are observed and presented in Fig. 2.10:

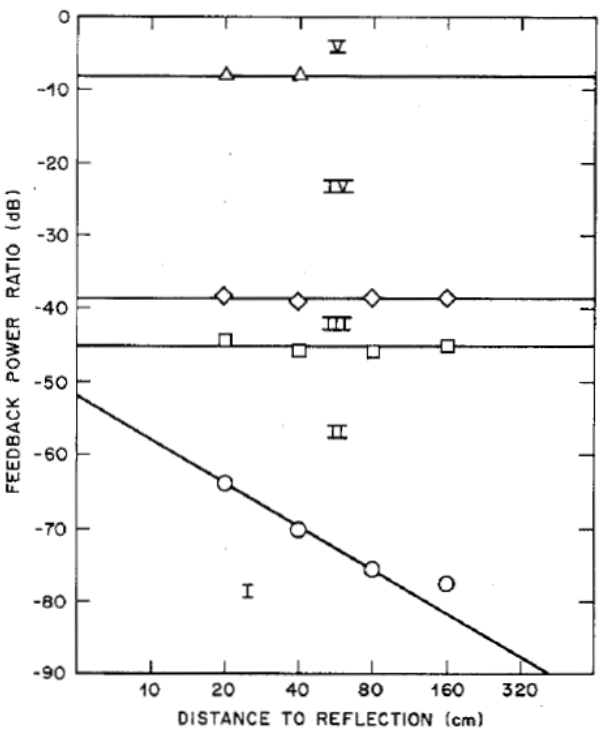

Figure 2.10: The different regime of dynamics of a laser with feedback, depending on the length of the external cavity end the feedback ratio. Taken from [45]

- Regime I (very weak feedback ratio, less than 0.001%): the spectrum of the laser broadens or narrows depending on the phase of the feedback.
- Regime II (weak feedback ratio, less than 0.01%): the laser exhibits external cavity modes. These modes are stationary solutions for which the wavelength of the laser is shifted by $n\frac{c}{2L}$, with n an integer. The laser can hop between the different solutions, which leads to a fluctuation of the output power of the laser.
- Regime III ($\sim 0.01\%$) the laser restabilizes, favouring one external cavity mode.
- Regime IV (moderate feedback ratio, about 1%), side peaks appear on the optical spectrum of the laser, separated from the emission peak by the relaxation oscillations. The laser exhibits chaotic dynamics while increasing the feedback.
- Regime V (strong feedback ratio, higher than 10%), the high feedback ratio makes the external cavity behaves as the internal laser cavity. The laser thus restabilizes and emits one laser mode.

The classification presented here does not provide a deep study of the different dynamics that a laser can exhibit. The regime that will be under interest in this manuscript is the third regime, when the first chaotic behavior appears. To present more in depth

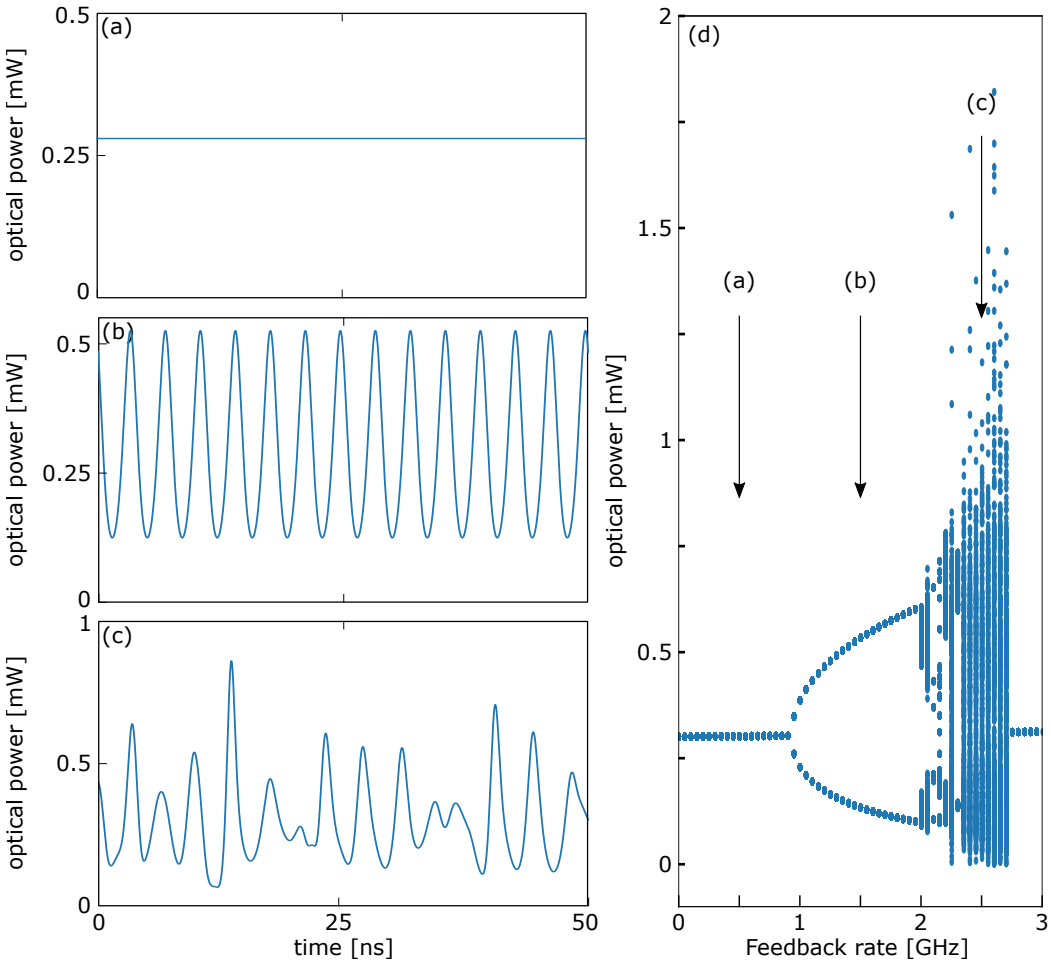

Figure 2.11: Numerical examples of dynamics exhibited by a semiconductor laser with feedback (L = 20 cm): (a) steady-state for a feedback rate of 0.5 GHz, (b) periodic for a feedback rate of 1.5 GHz, (c) chaotic for a feedback rate of 2.5 GHz. (d) Bifurcation diagram of a semiconductor laser with feedback, while varying the feedback rate.

that specific dynamics, we show in Fig. 2.11.(d) a typical bifurcation diagram obtained numerically for a semiconductor laser with feedback, while sweeping the feedback ratio. To realize this diagram, we used the same numerical model as the one used for numerical simulations in Chaps. 4 and 5. A bifurcation diagram shows the extrema of the temporal dynamics while varying a so-called bifurcation parameter. It is a useful tool for dynamics analysis. We observe on the bifurcation diagram that for low value of feedback rate, the system is in a steady state (Fig. 2.11.(a)), as demonstrated in the work of Tkach and Chraplyvy. The emitted power is constant. For a higher value of feedback rate (about 1 GHz), the emitted power begins oscillating. This specific point where the dynamics of the laser changes is called "bifurcation point". The laser exhibits periodic dynamics (Fig. 2.11.(b)). Keeping increasing the feedback rate leads to chaotic dynamics (Fig. 2.11.(c)): The power emitted by the laser oscillates irregularly and is highly sensitive to changes in the laser initial conditions. The dynamics that will

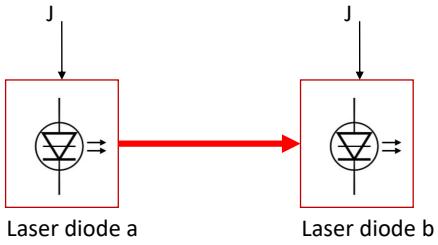

Figure 2.12: Schematic of laser injection. Laser diode b (slave laser) is injected optically by laser a (master laser)

be under consideration in the next chapters of this thesis is the steady state, just before the first bifurcation point. This dynamics is referred as edge of instabilities or edge of chaos, and it has been proved that it is suitable to perform computation with dynamical systems.

2.3.2 Laser submitted to injection

Complex dynamics can also be unlocked by injecting a semiconductor laser into another one (Fig. 2.12). The injecting laser is called master laser, and the injected laser is called slave laser. There are two parameters that drive the dynamics of the slave laser: The frequency detuning, which is the difference between the emission frequency of the master laser and the one of the slave laser, and the injection strength, which corresponds to the optical power emitted by the master laser, that is injected into the slave laser.

The dynamics of such a system has been largely studied since 1980, and a rich variety of dynamics has been documented [46]. One of them, called "injection locking" has drawn the interest of laser diode community as it allows enhancing the performance of a laser diode. In this specific dynamics, the frequency of the slave laser is locked to the one of the master laser [47]. Injection locking leads for instance to enhancement of the modulation bandwidth of the slave laser, and a reduction of its emission noise [48, 49].

A semiconductor laser can also exhibit much more complex dynamics, such as periodic and chaotic dynamics, due to optical injection [50]. The sequence of dynamics is very similar to the one presented with optical feedback. As for optical feedback, we can define the "edge of instabilities", which corresponds to the point just before the onset of oscillations of the optical power of the slave laser. The slave laser is thus still locked to the master laser. It is also important to note that if the detuning is too large, the slave laser can not be locked to the master laser and one cannot reach this "edge of instabilities" condition.

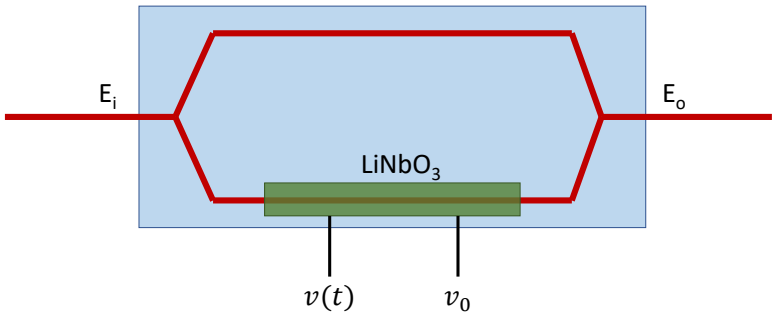

Figure 2.13: Schematic of a Mach-Zehnder modulator. The phase of the light going through the bottom arm is modulated thanks to the two electrodes. The amplitude is modulated thanks to the interferences happening between the beams outing the two arms of the modulators.

2.3.3 Laser submitted to modulated injection

We briefly explained previously that a laser diode can be directly modulated, by modulating the bias current of the laser. We can also modulate a laser diode by injecting a modulated laser in a slave laser. As we want in this work to reach high modulation frequency, we will present the Mach-Zehnder modulator, which allows modulating externally the optical power of a laser. A scheme of this kind of modulator is presented in Fig. 2.13. This modulator acts as an interferometer. We express the electrical field of the input beam as:

$$E_i = E_0 e^{i\omega_0 t}, \tag{2.3}$$

where $|E_0|^2$ is the optical power of the input beam, and ω_0 is the pulsation of the electro-magnetic field. This beam is split in two and propagates in two different arms. In the first arm, the beam simply propagates, and in the second arm, a delay is applied to the beam thanks to a specific crystal. The modulator we are using in this thesis uses a crystal of lithium niobate ($LiNbO_3$) as it acts on laser beam with a wavelength around 1550 nm. Two ports are present on the crystal to apply both a continuous bias voltage v_0 and a RF voltage $v(t)$. The beam at the end of this second arm can be expressed as:

$$E_m = \frac{E_0}{\sqrt{2}} e^{i\left(\omega_0 t + \frac{\pi v(t)}{2V_\pi} + \phi'\right)}, \tag{2.4}$$

where V_π corresponds to the voltage to apply in order to have a phase shift of π, and ϕ' the phase induced by the bias voltage. The output beam of the modulator is obtained

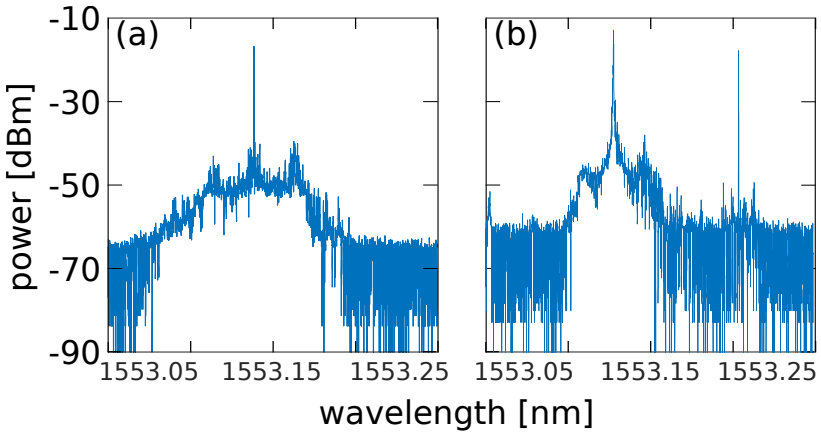

Figure 2.14: Optical spectra of semiconductor laser externally modulated thanks to optical injection. (a) The slave laser is locked to the master laser. (b) the slave laser is not locked to the master laser

by summing the two beams outing the two arms of the modulator.

$$E_o = \frac{E_0}{2} e^{i\omega_0 t} \left(1 + e^{i\left(\frac{\pi v(t)}{2V_\pi} + \phi'\right)}\right) \tag{2.5}$$

The crystals used to modulate the light act only along a preferential axis, that depends on the crystal used and on its crystallographic properties. This formula applies only if the polarization of the beam sent to the modulator is aligned with this preferential axis.

We can optically modulate a slave laser by injecting the modulated beam outing the modulator in the slave laser. We present two different cases:

- The slave laser is locked on the master laser which is modulated (Fig. 2.14.(a)). It thus emits light at the same wavelength as the one of the master laser. Due to the modulation, the spectrum of the slave lasers broadens. The frequency bandwidth equals the frequency of the modulation. As presented by T.B. Simpson, this configuration allows enlarging the modulation bandwidth of the slave laser [50].

- The slave laser is not locked to the master laser (Fig. 2.14.(b)). However, the spectral bandwidth of the master laser reaches and overlaps the optical frequency of the slave laser thanks to the modulation. In these conditions, the slave laser reacts to the modulation of the master laser, and its spectral bandwidth broadens. However, the enlargement of the spectrum is smaller than the one of the locked laser.

These two regimes are used in this work to inject data optically in our photonic computational device. We show in Chap. 4 that the first regime is suitable to perform computation and makes the photonic device produce an efficient response [51]. However,

in Chap. 5, we aim at injecting two input signals in two modes of a laser that are separated in frequency, and using only one modulated master laser. We thus use the second regime as a compromise to inject both modes of the laser at the same time.

2.3.4 Specific properties of VCSELs

VCSELs exhibit specific dynamics not found in conventional edge-emitting lasers. In most of the VCSELs, the polarization of the emitted beam is not pinned and depends on the laser parameters. Since its first study by Soda *et al.* [31], it appeared that the polarization of a VCSEL was hard to predict, and that the polarization properties of two VCSELs grown on the same wafer can differ [52]. Therefore, the polarization of the emission of one VCSEL can change by varying its operating parameters, such as the bias current or the temperature [53].

Two effects set the polarization of the emission in a VCSEL: the elasto-optic effect and the electro-optic effect [54]. The elasto-optic effect is responsible of creating electro-magnetic field at the different interfaces (due to growth-defects) existing in the cavity. These fields induce birefringence in the active region [55]. The electro-effect also induces birefringence, due to the voltage applied to the cavity [56].

This birefringence is typically linear and favors two main polarization axis. The two so-called polarization modes thus experience different refractive indices and are lasing at two different frequencies. These two modes are arbitrarily referenced as mode X (noted LP_x) and Y (noted LP_y). The mode X is often the mode that emits light when reaching the threshold. It is also called parallel or dominant polarization mode. The other mode is referred as orthogonal or depressed polarization mode. The two emitted polarization modes can be observed on the optical spectrum of a VCSEL from Raycan, used in this thesis (Fig. 2.15.(a)).

A free-running VCSEL mainly emits light along one of these two presented polarization axes. However, these axes can vary with the bias current as explained previously, and as presented in Fig. 2.15.(b). This is called polarization switching. The switching can take place between linear polarization modes or more complex polarization states [57].

Two different theories tend to explain this polarization selectivity. In 1994, Choquette *et al.* deduced that the two polarization modes do not experience the same gain due to the birefringence of the active layer [58]. His theory has been later completed by Ryvkin *et al.* [59]. The VCSEL emits solely the polarization mode that benefits from the higher gain to loss ratio. Changing the bias current or the temperature of the

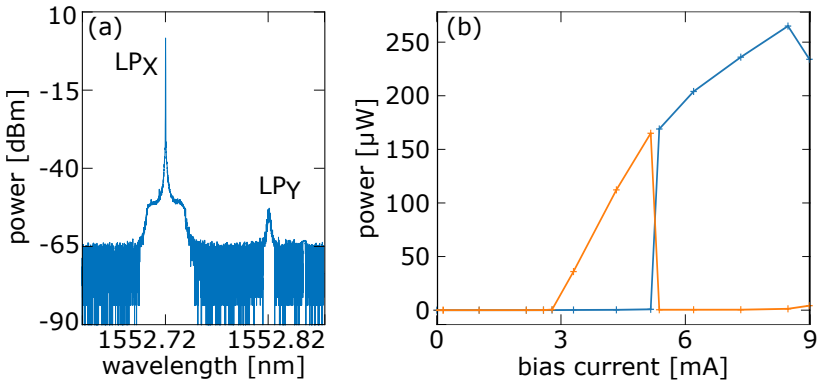

Figure 2.15: Experimental polarization properties of a VCSEL. (a) Optical spectrum of a free running VCSEL for a bias current close to the threshold current (1.5 × threshold current. (b) Optical power emitted by LP_X polarization mode (orange) and LP_Y polarization mode (blue) of a VCSEL. A polarization switching occurs for a bias current of 5 mA.

VCSEL modifies the gain to loss ratio relative to each polarization mode, and thus can change the polarization of the emitted light.

Another approach has been proposed by M. San Miguel *et al.* in 1995 with the spin-flip model [60]. This model suggests to account for the spin of the carriers in the active layer. There are thus 4 levels of energy instead of the only 2 considered in previously proposed model. The emission of photons can occur by either a recombination of electrons and holes of spin up, or of spin down. These two different recombinations emit photons with a different frequency, explaining the difference of wavelength between the two polarization modes. The two carrier populations with opposite spins are microscopic coupled thanks to spin-flip relaxation processes, which tend to equilibrate both populations. Moreover, due to the birefringence of the active layer, the two polarization modes do not experience the same amplification. The complex interplay between nonlinear coupling through carrier spin flip relaxations and linear birefringence explains then the polarization selectivity.

The two explanations of the polarization selectivity proposed by K. Choquette and M. San Miguel are complementary. They have both been observed in VCSELs [57]. Besides explaining polarization selectivity, the San Miguel-Feng-Moloney mechanism is also responsible for generating polarization chaos, as it has been recently observed experimentally [57].

(a) Picture of a rogue wave taken by the chief engineer of the Stolt Surf in 1977

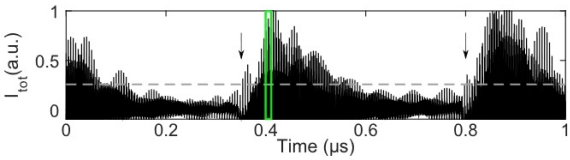

(b) Optical emission of a VCSEL with feedback. The dashed line coresponds to the detection threshold of a rogue wave. Taken from [62]

Figure 2.16: Pictures of rogue waves

2.4 Use of complex waveforms

We presented in the previous section that semiconductor lasers can exhibit complex dynamics resulting in different waveforms for the power emitted by the laser. These waveforms drew interest thanks to their possible applications. Some of these uses are presented in this section.

2.4.1 To mimic

The complex dynamics of laser allows reproducing behaviors observable in the nature. This is called biomimetics when it mimics living systems. This can be useful to study in a laboratory complex behaviors that are hardly analyzed in the nature directly, and that share some properties when analyzed in different physical systems.

2.4.1.1 Rogue waves

A first example can be found in extreme events such as rogue waves. Those waves are characterized by an enormous height and can appear in from calm and flat sea. The first reliable report of such a wave has been made in 1933 by the crew of an US tanker [61]: a wave with height of 34 m and a width between 300 and 450 m, for a total duration of 14.8 s. To be considered as a rogue wave, the amplitude of a wave should be twice higher than the so-called significant wave height, which is a statistical measure over a large number of observed waves. Due to their rarity, a rogue wave is hard to be observed.

Such behavior can be reproduced with photonic components. Solli *et al.* indeed demonstrated in 2007 that they have been able to observe rogue waves during the propagation of light in optical fiber [63]. Rogue waves have also been observed using laser diodes: an edge-emitting laser with either conventional feedback [64](using a

classical mirror), phase conjugated feedback [65](using a phase conjugated mirror), or optical injection. More recently, vectorial rogue waves, *i.e.* rogue wave that one observes only in polarized light, have also been observed in VCSELs with feedback [62], and in optical fibers [66].

2.4.1.2 Chimera

Another example is in the study of so-called chimera states. In physics a chimera is a group of identical coupled systems that experience at the same time coherent and incoherent dynamics. A set of coupled oscillators can synchronize after a certain time. One of the most striking natural example might be the flashing of fire flies [67]. However, with the right initial conditions, a set of coupled oscillators can reach state in which some oscillators are synchronized, and others are unsynchronized. The experimental observation of this behavior has been realized with either chemical oscillators [68] or opto-electronic oscillators [69]. This behavior has also been observed with two coupled set of coupled mechanical oscillators such as metronomes. One set was able to synchronize while the other one was exhibiting unsynchronized oscillations [70].

This behavior has been observed in an all-optical setup in 2019, by realizing simultaneously two feedbacks, one rotating the polarization of $pi/2$ along the feedback and one preserving the polarization along the feedback, on a laser diode [71]. This configuration allows periodical polarization switching of the laser between two states: one which is steady and the other one which is chaotic. The steady (chaotic) dynamics corresponds to synchronized (unsynchronized) virtual oscillators. The time spent in one of the two states and therefore the extension of the unsynchronized dynamics is controlled by the second feedback.

2.4.1.3 Spiking dynamics

We finally present a last example in biomimetics field which is related to the model of the biological neuron. The dynamics of a neuron is called "spiking". A neuron is an excitable system [72]. That means the response of the neuron is a spike if the input is higher than an activation threshold. Once the neuron has been activated, there is a relaxation period during which it cannot be trigger again, even if the input is higher than the threshold. Several models tend to reproduce this behaviour. One of the historical model is the Fitzugh-Nagumo model, which is based on the working properties of the squid giant axon [73] (cf Fig. 2.17). Other models have been proposed, such as the leaky integrate-and-fire model [74], which solves some memory problems.

This spiking dynamics has been successfully reproduced with a two-section DFB laser [75], which is composed of a smaller section with length 75 µm and larger section with

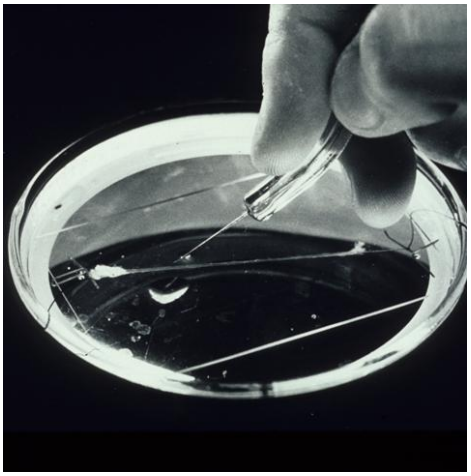

Figure 2.17: Picture of the squid giant axon. Picture provided by the National Institute of Health.

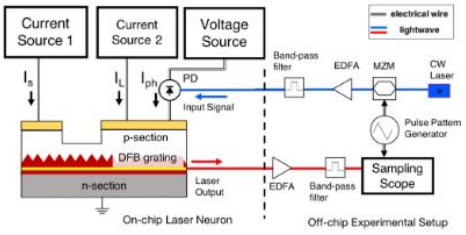

(a) Schematic of a optical neuron made with a DFB laser. The two electrical sources are used to bias the two parts of the laser. The input of the spikes is made electrically. The output of the neuron is optical. Taken from [75]

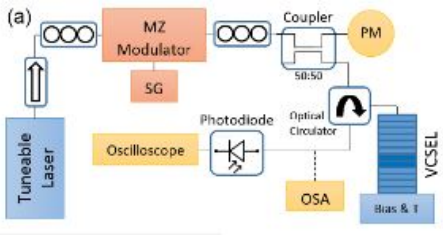

(b) Optical neuron made of a VCSEL. The input is made by injecting spikes in the orthogonal polarization mode of the VCSEL. Taken from [76]

Figure 2.18: Pictures of optical neurons

length 125 µm, optically coupled but electrically independent (cf Fig. 2.18.(a)). The input spikes are injected electrically in the larger part of the DFB laser.

The same behavior has been observed with VCSELs [77, 78, 76]. As presented in Fig. 2.18.(b), this dynamics can be achieved with VCSELs while injecting optically spikes to the orthogonal polarization mode of the VCSEL. We can also note that inducing a perturbation in a semiconductor laser with a saturable absorber also generate pulses with different amplitudes [79].

Realizing optical neurons has two advantages. If it can help studying the behavior of a biological neuron, it is currently mainly used to design fast artificial neural networks, since an optical neuron responds faster than the biological one.

2.4.2 To process information

In a more applied use, this complex dynamics can also be used to process information. We present some of these uses in this part.

2.4.2.1 Cryptography

As presented in the introduction, the growth of the amount of data requires new processing techniques, including new secured communication method. Solutions using the chaotic dynamics of semiconductor lasers to perform cryptography have been explored [80, 81]. The working principle is based on the synchronization of chaos in laser diodes [82, 83]. A transmitter laser diode is set in chaotic state. The chaotic signal emitted is used as a carrier to transmit a signal. At the receiver, another laser diode is synchronized with the transmitter laser diode. This synchronization is realized by injecting the transmitter laser to the receiver laser. Added to that, if both lasers are almost identical and operated in similar conditions (temperature, bias current), the receiver laser exhibits the same chaos as the one emitted by the transmitter laser. Having the transmitted signal and the chaotic carrier, a subtraction allows recovering the transmitted data. The operating data and the type of laser thus play the role of the private key, and the data cannot be recovered without these parameters. An experimental encrypted transmission has successfully been performed in Greece in 2005 using this method [84].

2.4.2.2 Random number generation

The random number generation is also a critical issue in secured communication. It is used to generate private keys to encrypt data. In 2008, A. Uchida *et. al.* realized a random bit generation at 1.7 Gb/s using semiconductor lasers [85]. The stream of random bit is generated thanks to two chaotic semiconductor lasers whose output beams are first recorded and converted to a bit stream separately. A final exclusive OR (XOR) logic operation recombines the two generated bits streams, into one random bits stream. In 2010, K. Hirano *et. al.* enhanced the random bits generation speed to 12.5 Gb/s thanks to an increase of the chaos bandwidth generated by the semiconductor laser. A first chaotic laser is injected in a second laser. The final bit stream is obtained by sampling the light emitted by the second laser and setting as an input of a XOR operation the signal of the second laser and the same signal delayed. Other architectures demonstrated interesting performance and simple implementation, such as an integrated semiconductor laser with external cavity allowing random bit generation up to 140 Gb/s [86], or a semiconductor laser with rotated optical feedback generating random bit stream at 4 Gb/s [87]. In 2014, M. Virte *et al.* proved that they were able to generate random numbers using a free-running VCSEL at 100 Gb/s

[88]. The generation of these numbers on a chaotic polarization switching exhibited by a quantum-dot VCSEL. More recently, G. Bouchez also proposed a system based on phase conjugated feedback generating wide-band chaos that extends over more than 40 GHz of bandwidth [89]. This wide band chaos can be used to generate a more complex series of random numbers, at a higher bit rate.

2.4.2.3 Sensors

There have been many reports of uses of the dynamical properties of semiconductor laser to performs sensing. For instance, erbium doped fiber lasers have been successfully applied for detection of intrusion [90], or gas detection [91]. These sensors are based on the high sensibility of the cavity of the laser. Small perturbations such as acoustic waves or the presence of gas can create transient dynamics in the cavity of this kind of laser, made of erbium doped fiber. The transient dynamics can be analyzed to perform sensing.

Laser diodes submitted to frequency shifted optical feedback have also been studied to perform small amplitude-vibration sensors[92]. By vibrating, an object is modifying the optical spectrum of the beam emitted by a laser which is injected back in the laser thanks to feedback. This modification of spectrum is extracted from the dynamics of the laser, which allows deducing the vibration frequency of the object.

2.5 Conclusion

In summary, we introduced in this chapter the basics of semiconductor lasers. We first presented that a laser is made of three main components: a gain medium, a cavity, and a pump. Lasers can be made of semiconductors. We presented two different semiconductor lasers, the edge-emitting laser, and the vertical-cavity surface emitting laser, both having their own properties. More specifically, VCSELs have several advantages that make them largely used today. We also presented briefly the different dynamical regimes that can exhibit a semiconductor laser in different configuration of feedback, injection or modulation. These different dynamical regimes are already in use, to mimic biological behavior, or to process data for instance.

As we presented in this chapter, the dynamical regime of a laser can be used in many different ways. In this thesis, we focus on how using this dynamics to perform reservoir computing: a machine learning technique that allows performing computation with dynamical system. Before presenting the system studied in the thesis, we present in the next chapter the basics of artificial neural networks, and more specifically reservoir computing, more in depth.

3

Theory of artificial neural network and reservoir computer

Smith yelled at the doctor, "What have you done to my boy? He's not flesh and blood, he's aluminium alloy!" The doctor said gently, "What I'm going to say will sound pretty wild. But you're not the father of this strange looking child. You see, there still is some question about the child's gender, but we think that its father is a microwave blender.

Tim Burton, *The Melancholy Death of Oyster Boy and Other Stories*

Contents

3.1 The artificial neural network 36

3.1.1 Different models of neuron 36

3.1.2 Feedforward neural network 37

3.1.3 Recurrent neural network 38

3.1.4 Network of spiking neurons 39

3.2 Reservoir computing 40

3.2.1 What is reservoir computing? 40

3.2.2 Time-delay reservoir computing 43

3.3 Examples of physical reservoir computing 47

3.3.1 Physical reservoir computing 48

3.3.2 Photonic reservoir computing 48

3.4 Tasks and metrics 51

3.4.1 Computational ability 52

3.4.2 Memory capacity 54

3.4.3 The Sante Fe time series prediction 54

3.4.4 The Nonlinear channel equalization task 56

3.5 Conclusion 60

As introduced in the general introduction, this thesis focuses on building a hardware VCSEL-based time-delay reservoir computer, based on the time-delay reservoir architecture proposed by L. Appeltant *et al.* [8]. Now that the different components and their properties have been presented, we will now focus on fundamental machine-learning part and shall introduce the mathematical formalism required to perform computation with photonic components.

We will first introduce the neural network in Sec. 3.1, before presenting the concept of reservoir computing, based on recurrent neural network in Sec. 3.2. Finally, in Secs. 3.3 and 3.4, we present some examples of time-delay reservoir computer using photonics with their specific properties as well as the different benchmark tasks we will use to assess the performance of our system in the next chapters.

3.1 The artificial neural network

An artificial neural network (ANN) is a system that is made of several small interconnected devices. Each of them has inputs and outputs, and computes a function of the input. The response of a network depends on the operation that each device realizes, and also to the way they are linked one with the others. One can "teach" the network how to perform a specific task by tuning the link between each neuron, like a real brain would basically do. This is called the training of the neural network.

3.1.1 Different models of neuron

The proposal to study neural networks has been first introduced in Ref. [93] with a simple model of a neuron, with several inputs x_i, entering the neuron through weighted connections of weights w_i. The response y of the neuron was considered as the sum of the weighted inputs combined with the heaviside transfer function, as follows:

$$y = h\left(\sum(w_i x_i)\right), \tag{3.1}$$

$$h(x) = \begin{cases} 0 & \text{if } x < 0, \\ 1 & \text{otherwise.} \end{cases} \tag{3.2}$$

However, such a mathematical description does not raise any explicit solution to train the system. Learning methods were proposed afterwards, leading to a trainable network.

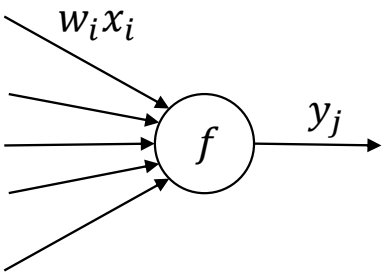

Figure 3.1: Schematic of a neuron, with transfer function f, weighted inputs $w_i x_i$ and output y_j

The model of a neuron can be generalized to any given transfer function f:

$$a_j = \sum_i w_i x_i + b, \tag{3.3}$$

$$y_j = f(a_j), \tag{3.4}$$

where the w_i are the weights applied to the inputs x_i. a_j is called the pre-activation of the j^{th} neuron. In the literature, we encounter very often the following transfer function:

- hyperbolic tangent: $f(a) = \tanh(a)$
- logistic function: $f(a) = \frac{1}{1+\exp(-a)}$
- rectified linear unit: $f(a) = \max(a, 0)$
- softmax: $f(a) = \log(1 + \exp(a))$

To create a neural network, we usually combine neurons with the same activation function. Different types of architecture can be distinguished, beginning with the feedforward neural network.

3.1.2 Feedforward neural network

The feedforward neural network (first introduced in [94]) is made of an input layer, one or several hidden layers, and an output layer, as presented in Fig. 3.2. In this architecture, the input signal enters in the network at the input layer, propagates in the system through the different layers, one after the other, until reaching the output layer. In this topology, there is no inner loop in the network, and the signal cannot go through a same neuron twice. All the connections are weighted and trainable. There are several ways to train such a system, but the historical method is the error backpropagation algorithm [95]: The error made by the network from the output to

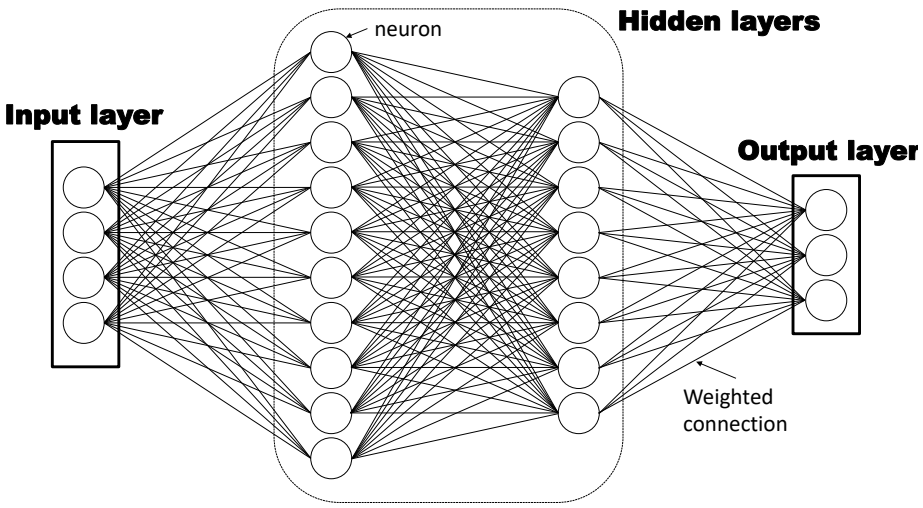

Figure 3.2: Topology of the feedforward neural network. The signal propagates from one layer to another from the input layer to the output layer, in only one (here forward) direction

the target is retro-propagated, and the weights are adjusted accordingly to reduce the error of the system. The algorithm stops when the error is smaller than a threshold defined at the beginning of the training process.
However, due to its topology, this kind of network is not the most suitable to process data with time dependence. At each processing step, the only data available in the output layer always corresponds to the last injected input. This architecture has been first used to process fixed patterns or images [96].

3.1.3 Recurrent neural network

Let us consider the problem of time-dependent information. We need to maintain the information corresponding to several inputs in the system. This can be done by creating loops inside the network. This allows creating a memory effect in the network. The output of the system then not only depends on the current input, but also on the previous inputs still present in the network. An example of such an architecture is presented in Fig. 3.3.
However, the recurrence of the system makes it harder to train: Training methods still exist, such as real-time recurrent learning (RTRL) or backpropagation through time (BPTT), but require a high computing power [97, 98]. Recurrent neural networks are specifically suitable to process data set that present a time dependency (such as speech signals). The neural network can learn the time dependency of the of the input data to generate the correct output.

Another paradigm recently appeared, allowing separating the recurrent network and

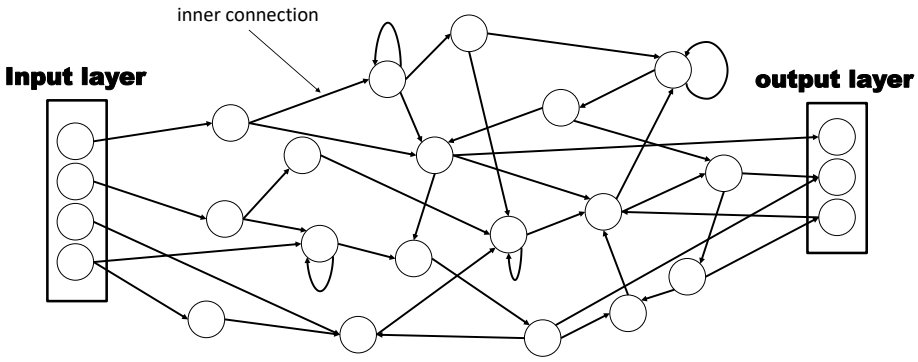

Figure 3.3: Topology of the recurrent neural network. The loop in the network allows current signals crossing previous ones

the trained layer. This new paradigm is called reservoir computing and will be discussed in Sec. 3.2.

3.1.4 Network of spiking neurons

Spiking neural networks considers neurons with an activation function different from the one presented in Sec. 3.1.1. In these networks, neurons communicate by sending spikes over the network, similar to biological neurons. Such a neuron produces a spike if the input is higher than a threshold and the the spike has the same amplitude as the input. Once the neuron has fired a spike, there is a relaxing time during which the neuron is not able to respond to any input. Such a dynamical behavior is called excitability [99]. Several models exist to reproduce excitability, such as the one presented by A. Hodgkin and A. Huxley, copying the giant squid axon properties [100].

As presented in the previous chapter, this excitability behavior can be produced with laser-based systems, such as graphene excitable lasers [101], DFB lasers [75] or VCSELs [76, 77, 78]. It has also been observed in micro-ring resonators [102], in some simple electronic circuits [103] or and with memristors [104]. Such neurons can then be coupled together in order to form a network [105, 106].

Spiking networks, which are explored to recognize pattern [107], require a totally different approach to be trained. A biological mechanism has been identified to adapt the synaptic weights in such a network, called spike-timing dependent-plasticity (STDP) (studied in [108]). Several training algorithms has been adapted from STDP, such as synaptic weight association training (SWAT) [109], or an adapted backpropagation

algorithm [110]. It will not be further explained in this thesis since this architecture is not used in the thesis work.

3.2 Reservoir computing

A solution to simplify the training of a recurrent neural network has been given by the framework of *reservoir computing*, which has been recently presented in [111, 112, 113].

3.2.1 What is reservoir computing?

Reservoir computing bring together two groups of recurrent neural networks, called echo state network (ESN) [114] and liquid-state machine (LSM) [111].

Echo state networks are a recurrent neural network, whose topology is randomly set, as well as the weights defining the connection between neurons. Input data are fed in the network, and the responses of the different neurons are transfered unidirectionally to an output layer. All the connections to this last layer are trainable with a regression algorithm. Nevertheless, we keep the ability of the network to mix the information from different inputs, responsible of the fading memory of the network, which means that the data relative to one input remains in the system a certain amount of time before vanishing. After this time, the network returns to its steady state.

Liquid state machines are similar to echo state networks in sense that they are also composed of a randomly defined network, and a unidirectional output layer in which the training is performed. The network is however a spiking neural network, as presented in Sec. 3.1.4. This system draws its performance from the separation property (different inputs are following different routes in the network) and the approximation property (different trajectories produce different outputs).

Reservoir computing thus extends echo state network and liquid state machine in a unified model. It maps an original problem to a higher dimensional space thanks to a fixed neural network. The training is realized in a unidirectional readout layer, meaning that there is no feedback connection from the readout layer to the network. As presented in Fig. 3.4, a reservoir computer is composed of an input layer in which the input signal is injected, a fixed neural network called "reservoir", and an output layer, also called readout layer, reading the state of the neuron of the neural network to perform the training.

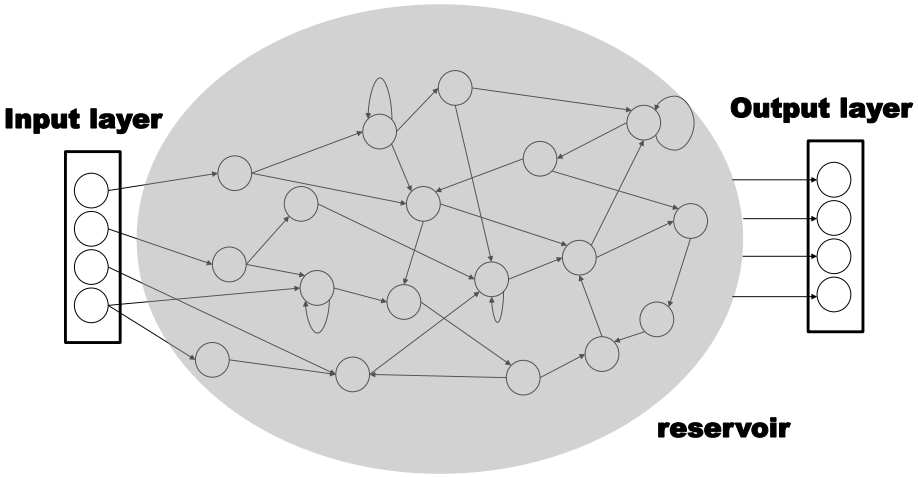

Figure 3.4: Topology of the reservoir computing network. The topology of the reservoir is the same as the one of the recurrent neural network. We add an output layer to perform the training.

According to the topology of the reservoir computing, we can express the state $x(k) \in \mathbb{R}^n$ of the reservoir at a discrete time step k when injected with an input $u(k) \in \mathbb{R}^p$ by:

$$\mathbf{x}(k) = f\left(W^{in}u(k-1) + Wx(k-1)\right), \tag{3.5}$$

and then express the value of the output of the reservoir $\hat{y}(k) \in \mathbb{R}^m$

$$\hat{y}(k) = W^{out}\begin{bmatrix} x(k) \\ u(k) \end{bmatrix} + b, \tag{3.6}$$

where $W^{in} \in \mathbb{R}^{n\times p}$ are the fixed input weights, $W \in \mathbb{R}^{n\times n}$ is the fixed matrix of weights applied to the linked between neurons, $W^{out} \in \mathbb{R}^{m\times(n+p)}$ are the output weights, and b is a bias. Training the reservoir is finding the coefficient of W^{out}, which translates into solving a linear optimization problem. This learning can be achieved online [115], meaning the weights in W^{out} are progressively adapted until reaching the desired output y, or offline, meaning the weights are calculated in one shot using a sufficient number l of input samples. We used in this work this last approach, which can be achieved in the simplest way by minimizing the mean square error $||W^{out}X - y||^2$, where X gather the states of the reservoir over l time steps. One can compute W^{out} using the Moore-Penrose pseudo-inverse of X which is defined as [116]:

$$X^{\dagger} = (XX^T)^{-1}X. \tag{3.7}$$

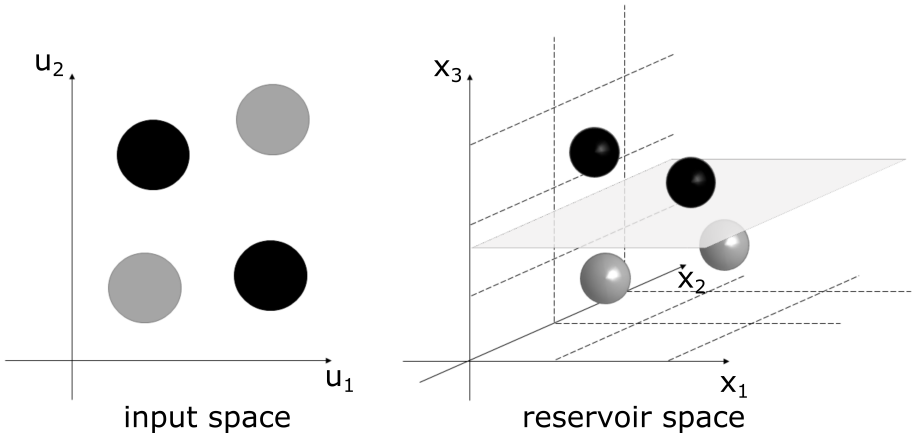

Figure 3.5: Example of linearly solved problem. Separating linearly gray and black points. The original problem (left) cannot be solved linearly. Adding one dimension allows finding linear solution.

We obtain:

$$W^{out} = X^{\dagger} y. \tag{3.8}$$

Reservoir computing with ESNs uses the nonlinear properties of the neurons to turn a low-dimensional linear or nonlinear problem into a high-dimensional one that can be solved linearly. Let us consider a problem in p dimensions. Once injected in the reservoir, each neuron responds differently, depending on the input. There is a nonlinear transformation from a vector space with p dimensions, to $n \gg p$ dimensions.

We can then draw benefits of these additional dimensions to solve linearly a problem, as shown by the example in Fig. 3.5. We cannot draw one line (hyper plane) to separate the gray and black balls. However, while adding one dimension to the problem, we can find a plane to separate those points. The same principle is applied by using a reservoir. In addition, we can easily design systems with a large number of neurons, therefore increasing the corresponding number of dimensions when compared to the original problem.

Reservoir computing is a suitable approach to apply machine learning techniques to hardware design. Designing a physical RNN with fixed topology and weights simplify considerably the implementation. The first reported system to apply this principle was a bucket of water and 8 mechanical actuators driving small weights [117]. These weights, when activating the corresponding actuators, produce ripples pattern at the surface of the water that can be used to calculate. The original problem has been changed (from eight punctual sources to water surface). These patterns have been used to solve different tasks, such as speech recognition task, or exclusive OR (XOR)

task. The small waves at the surface of the water are also a transient phenomenon, which would provide the fading memory.

However, designing an artificial neural network with a large number of nodes still remains a technical challenge. That is why another architecture has been proposed, in which only one physical node is used, but with a time-delay feedback, therefore generating so-called virtual nodes distributed in the feedback loop. This architecture is detailed in the next section.

3.2.2 Time-delay reservoir computing

3.2.2.1 Single node reservoir computer

The time-delay reservoir computing proposes to use only one physical device submitted to feedback. Its dynamics can be described with delay differential equation (DDE):

$$\frac{dx(t)}{dt} = F\left(t, x(t), x(t-\tau)\right), \tag{3.9}$$

with F a linear or nonlinear function describing the system, x the state variable and τ the time-delay. Such a system can exhibit the high dimensional attractors and fading memory [118], which can be exploited to perform reservoir computing.

Instead of having physical neurons spatially distributed, such an architecture uses *virtual neurons* timely spread along the delay line. It has been firstly introduced in [8] and further described in [119]. A scheme of this architecture is presented in Fig. 3.6.

This architecture provides the required properties to perform computation [8]. Added to that, the delay architecture can scale easily: Resizing the reservoir computer is now made by simply changing the length of the delay line. That is why such an architecture is highly suitable for experimental implementations.

3.2.2.2 Pre-processing: the masking procedure

Even if there is only one nonlinear device in the system, the training approach remains similar to the classical reservoir computer. The virtual neurons are N equidistant points, separated by an inter-delay of $\theta = \tau/N$, where τ is the propagation time in the delay-line. These virtual neurons are fed after a specific pre-processing of the input stream: Each value of the input stream (which can be a discrete time series $u(k)$ or a continuous input waveform discretized $u(t)$) is held during τ to feed the whole delay-line, giving the signal noted $u_{hold}(t)$. The resulting signal is then multiplied by a mask $m(t)$, a signal τ-periodic in which each value is held during θ, to create the

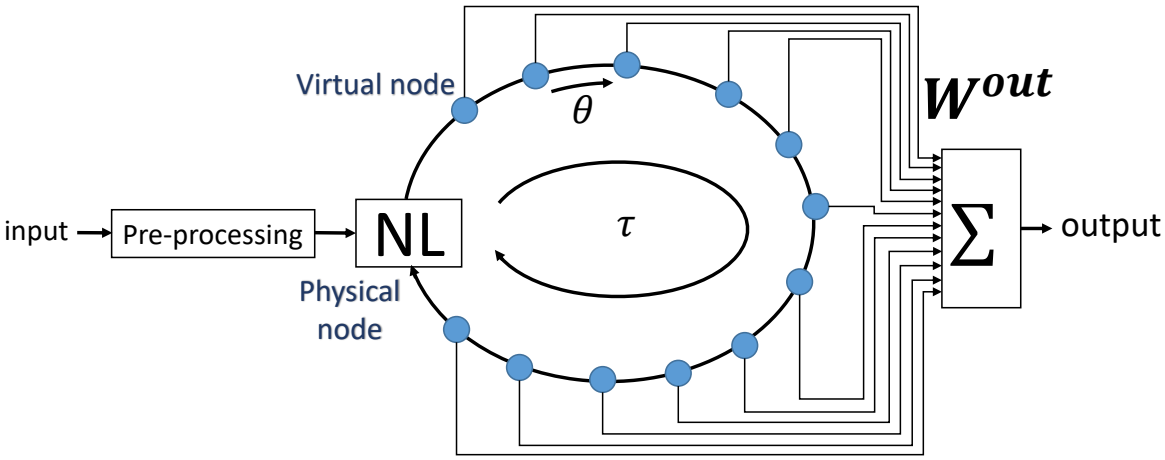

Figure 3.6: Topology of the time-delay reservoir computing architecture. The neurons are distributed along a delay-line which has a length τ. They are separated by a length of θ. The input stream is pre-processed before sending the input signal in the nonlinear physical node. The training is realized once the signal has propagated in the delay-line thanks to the output layer.

input signal of the reservoir $s(t)$, leading to $s(t) = u_{hold}(t) \cdot m(t)$. This procedure, called masking procedure, allows creating the virtual nodes and is presented in Fig. 3.7. The mask can take different shapes, which influences the processing performance of the reservoir [120]. The mask commonly used is the binary mask, made of 0 and 1 randomly taken. It can also have a more complex shape, such as a multi-level signal, a white noise or a chaotic signal. Adapting the values of the mask is similar to adapting the weights between an input layer and the virtual nodes.

The choice of θ is critical on the performance of the reservoir computer. We want to correctly chose this parameter to properly interconnect all the virtual neurons and draw benefits from the nonlinearity of the physical node. If we consider T the response (relaxation) time of the physical node, we can identify two different behavior.

First, if $\theta \gg T$, the physical node reaches its steady state for each virtual node. The response of the node is then only determined by the instantaneous value of the input signal $s(t)$ and the state of the physical node. The strength of the connection between the virtual nodes remains low, and a self-coupling effect is induced by the delayed feedback, as shown in Fig. 3.8.

The dashed red signal corresponds to the masked input stream $s(t)$, and the blue signal the response of the physical node. In this example, the driving input is held long enough to let the physical node reaching its steady state. The complexity of the response of the reservoir is then solely determined by the complexity of the mask.

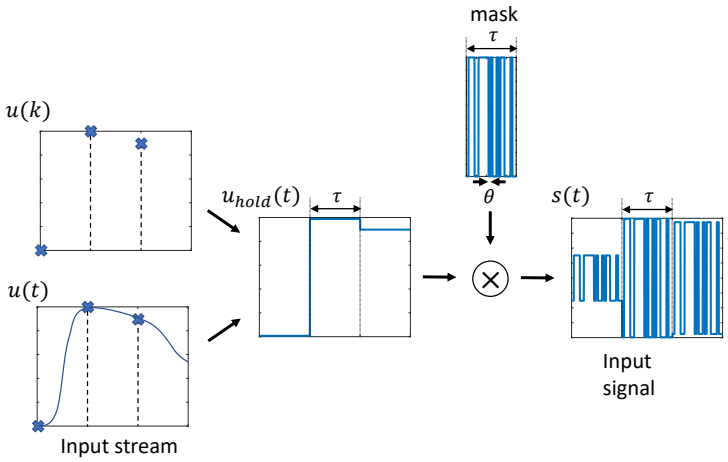

Figure 3.7: Masking procedure. The input stream can be either a discrete time series $u(k)$ or a continuous signal discretized $u(t)$. The signal $v(t)$ is obtained by holding each value of the input data. $v(t)$ is then multiplied by a mask which has a total length of τ and in which each value is hold during θ. This gives the input signal $s(t)$ which is send in the nonlinear physical node.

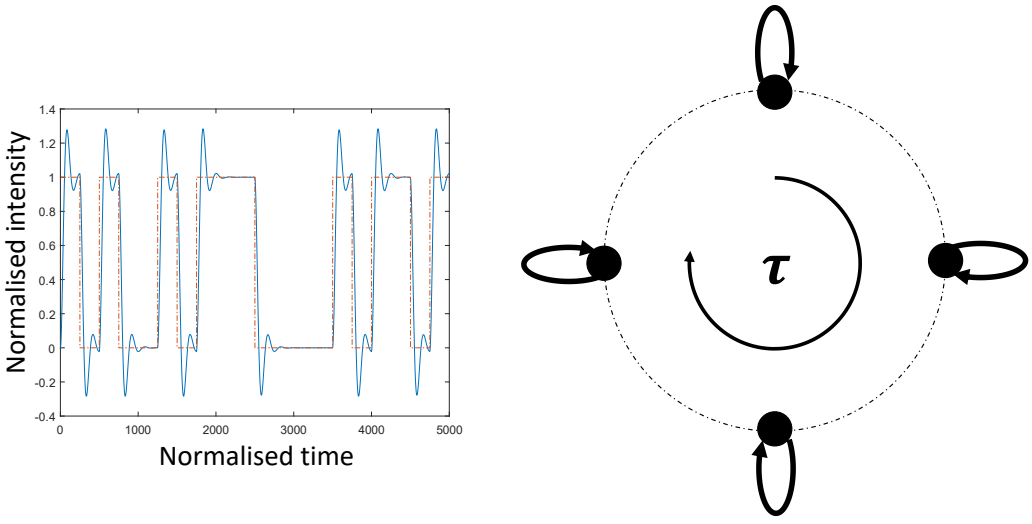

Figure 3.8: Interconnection topology in case of large spacing between virtual neurons ($\theta \gg T$). The dashed red signal represents the driving input signal $s(t)$ and the blue line is the response of the physical node. The node is able to reach its steady state for each input value. Its response only depends on the instantaneous value of $s(t)$ and on the instantaneous state of the reservoir. There is no connection between the virtual neurons. Adapted from L. Appeltant *et al.* work [8]

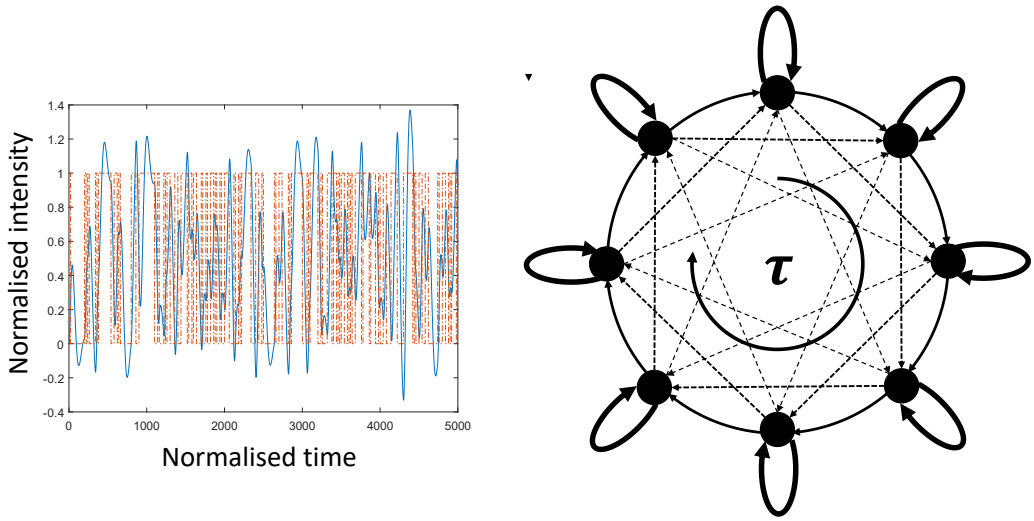

Figure 3.9: Interconnection topology in case of small spacing between virtual neurons ($\theta < T$). The dashed red signal represents the driving input signal $s(t)$ and the blue line is the response of the linear node. The node does not have enough time to reach its steady state for each input value. Its response depends on the instantaneous value of s(t) and on the previous states of the reservoir. There are connections between the virtual neurons. Adapted from L. Appeltant *et al.* work [8]

If $\theta < T$, the physical node does not have the time to reach its steady state before receiving the next driving input value. The response of the virtual neurons is then determined by the instantaneous value of the input signal $s(t)$, and the state of the previous virtual neurons as presented in Fig. 3.9. The complexity of the response of the reservoir computer draw benefits from the complexity of the nonlinearity arising from the physical node.

3.2.2.3 Training

To train a time-delay reservoir computer, we will process similarly to the classical reservoir computing system, based on Eq. (3.6):

$$\hat{y}(k) = W^{out} \begin{bmatrix} X(k) \\ u(k) \end{bmatrix}, \text{ with } X(k) = \begin{bmatrix} x(k\tau) \\ x\left(\left(k - \frac{1}{N}\right)\tau\right) \\ \vdots \\ x\left(\left(k - \frac{i}{N}\right)\tau\right) \\ \vdots \\ x\left((k-1)\tau\right) \end{bmatrix}, \tag{3.10}$$

as the nodes are temporally distributed. In practice, we will only use the states of the reservoir $X(k)$ and not the input $u(k)$ to train the reservoir. We can rewrite the training equation as follows:

$$\hat{y}(k) = \sum_{i=1}^{N} w_i x \left(k\tau - i\frac{\tau}{N} \right). \tag{3.11}$$

As previously, a weight is attributed to the state of each virtual neuron to build the desired output. This formula also shows the intrinsic speed limitation of such a system: Time-delay τ limits the speed of the system since the response of the physical node should propagate in the whole delay line before injecting new information. All the working steps are summarized in Fig. 3.10.

3.3 Examples of physical reservoir computing

As presented in the previous section, reservoir computing is specifically suitable to design neural network with physical components. We will present a non-exhaustive overview of reservoir computers in this section.

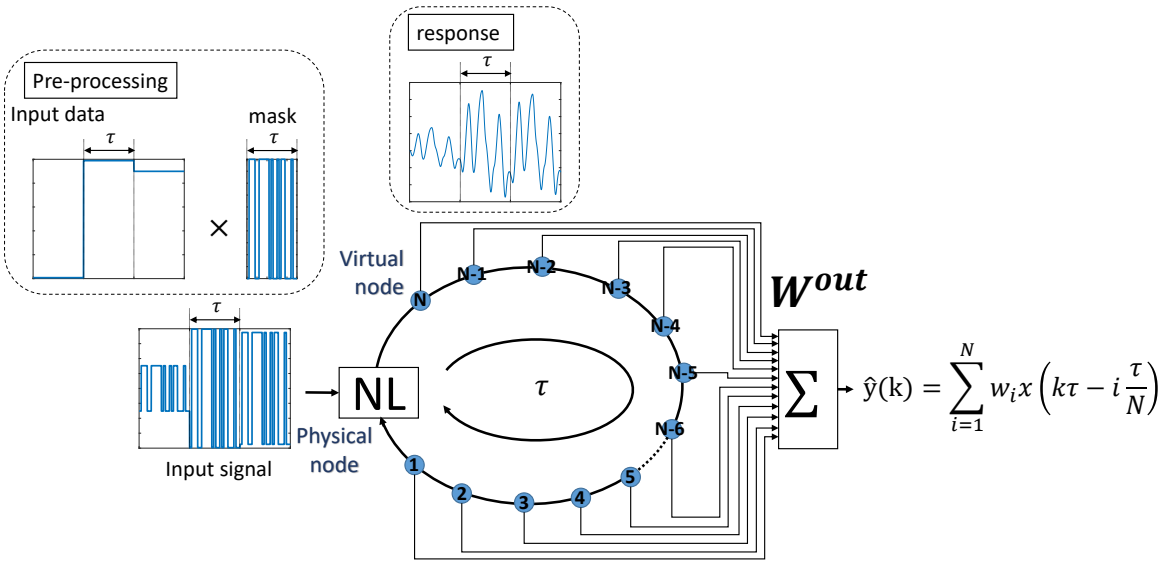

Figure 3.10: Complete working principle of time-delay reservoir computing. The input stream is first pre-processed with the masking procedure. The signal is sent in the nonlinear node; once its response has propagated in the delay-line, the values of the neurons are collected to perform the training.

3.3.1 Physical reservoir computing

The first experimental realization of a reservoir has been reported by C. Fernando *et. al.* in [117]. In this work the reservoir is made of a bucket full of water. The input of the reservoir is realized thanks to weights creating waves in the water. The output of the neurons is the pattern made at the surface of the water. This system exhibits the required properties to perform time-dependent tasks. The waves produced by the moving weights obviously depend on its location in the bucket. Moreover, once produced, the waves remain a small time at the surface and propagate, so that the different wave patterns are mixed, before vanishing. This creates the vanishing memory of the system. Other mechanical systems have been used to perform computation, such as a soft octopus robot [121], or a tensegrity structure [122]. Unfortunately, the working properties are based on mechanical behavior, which is rather slow. An original proposal considered using a cat brain [123] as physical device to prove its ability to perform computation. However, the performance was not has high as required. Other proposals use photonic components to build artificial neural networks because of their ability to perform fast computation thanks to their intrinsic short time constant.

Reservoir computers of different nature have also been proposed: electronic using for instance memristive components [124], spintronic using spin torque oscillators [125] or even biological, using the brain of a cat [123]. We can also note that L. Appeltant realized the first experimental time-delay reservoir computer with an electronic version of Mackey-Glass oscillator [8]. This list is non exhaustive, and the review of G. Tanaka *et. al.* present in more details all the recent works realized in the field of physical reservoir computing [126].

3.3.2 Photonic reservoir computing

The possibility to build small, cheap and fast components makes photonic components good candidates to explore new functionalities, and to some extend replace electronic devices. Different approaches exist to build reservoir computers: free space reservoir computer, fibered systems largely represented with time-delay architecture, and integrated on photonic chips.

3.3.2.1 Spatial reservoir computing

Building large reservoir computer based on the same principle as the one presented previously is possible with photonic components. The first reported architecture was an array of 8x8 VCSELs, coupled thanks to the diffraction realized by a spatial light modulator (SLM) that is also used to define the weights [7]. Similar work has been realized with an array of 9 by 9 neurons made of groups of pixels on a SLM [127].

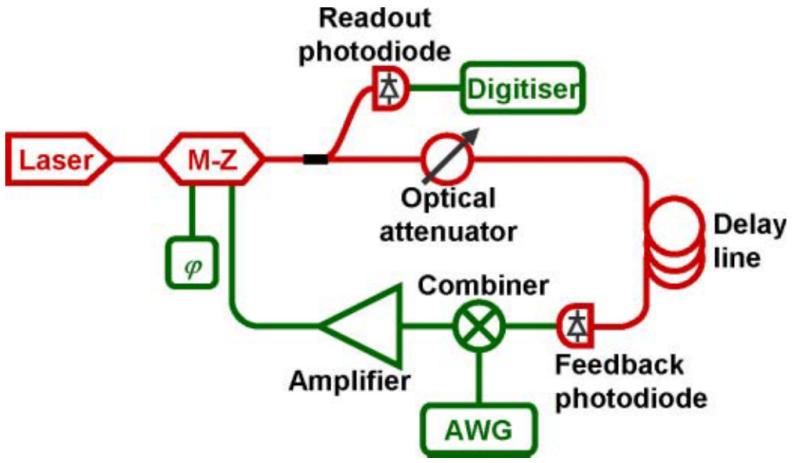

Figure 3.11: Scheme on the optoelectronic reservoir. taken from Y. Paquot *et al.* work [10]

More recently, free-space setup have been proposed to realize even larger network, with 2025 nodes made with a SLM, each neuron being a group of pixels on the SLM [128], with 16,384 nodes [129], or with an even larger number of nodes (up to 10^6 nodes) [130, 131], also realized thanks to a SLM.

An integrated photonic reservoir has also been proposed recently. This system is made of integrated optical waveguides, and integrated components, allowing to design a reservoir with 16 nodes. Each neuron can be either a nonlinear node (integrated micro-ring resonator), or a linear node (simple waveguide or integrated semiconductor amplifier). This system is completely passive, which leads to a fast reservoir computer with really low power consumption [132, 133, 134, 135].

3.3.2.2 Time-delay reservoir computing

The complexity of coupling a large set of photonic components motivated to use the time-delay reservoir approach to build a computational device. We report two main categories of photonic time-delay reservoir computers:

Optoelectronic time-delay reservoir computing

Two different research teams, composed of researchers from different research teams (ULB, UGhent, FEMTO-ST, VUB, IFC and IFISC) realized the first experimental time-delay reservoir computer using a Mach-Zehnder modulator as a physical node [10, 9, 136]. A scheme of their setup is shown in Fig. 3.11. This system is referred to as an optoelectronic reservoir computer since there is a conversion from optical to electronic power in the delay line.

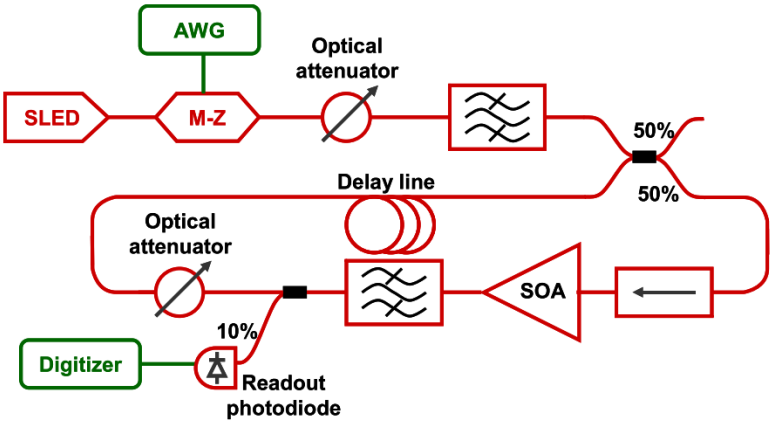

Figure 3.12: Scheme of the photonic reservoir. Taken from F. Duport *et al.* work [11]

This system was able to perform computation efficiently. But the intrinsic time constant of the electronic components produced low computational speed, (around 100 kHz). Further study of this setup have been performed, such as P. Antonik *et al.* studying the online computation of the output signal [137], or L. Larger *et al.* exploring the possibility to fasten the computation of such a system, reaching processing speed up to 500 MHz [16]. There has been some proposals to use faster components, such as photonic components, to perform computation at even higher speed.

Photonic time-delay reservoir computer

The main difference between the photonic time-delay reservoir and the optoelectronic reservoir lays in the nature of the signal in the feedback loop. As we saw previously, in the opto-electronic reservoir, the signal in the feedback is first generated optically, and then converted to an electronic signal. In the photonic reservoir, the signal in the feedback loop is optical from the beginning to the end. Different systems have been proposed. The first one was proposed by F. Duport *et al.* and is using a semiconductor optical amplifier (SOA) as a physical node [11].

A reservoir computer using an edge-emitting laser (EEL) as a physical node has also been reported and explored to process time signals in [12, 136] and more recently in [138], as well as an architecture using a semiconductor ring laser (SRL) [139].

Similar architectures are continuously proposed. For instance, integration on chip has been possible thanks to an integrated laser [140]. We can also report the use of a quantum cascade laser as a physical node [141]. These different architectures benefit from the time constants (direct modulation bandwidth and relaxation-oscillation time) of photonic components, and therefore can generally perform computation faster than the previously shown optoelectronic reservoir computer: as the dynamics of the system

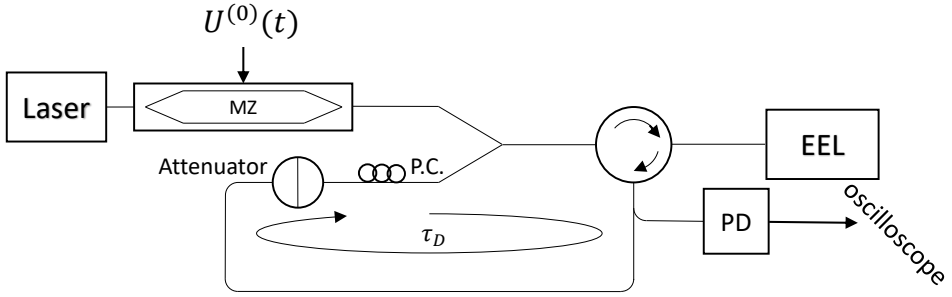

Figure 3.13: Scheme of the edge-emitting laser-based reservoir. Adapted from D. Brunner *et al.* work [136]

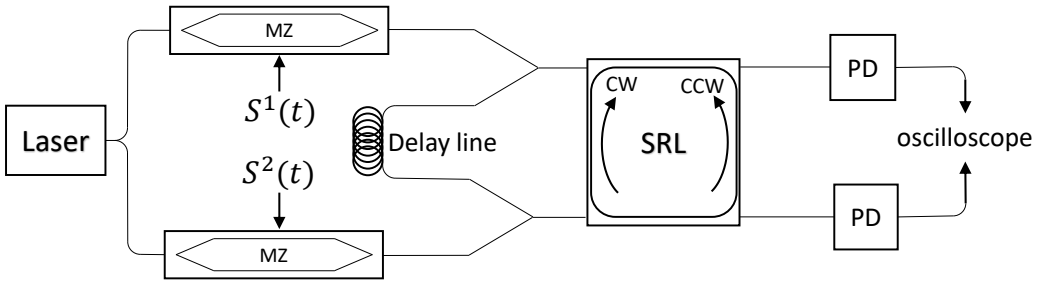

Figure 3.14: Scheme of the semiconductor ring laser-based reservoir. Adapted from R. Nguimdo *et al.* work [139]

is faster, the length of the delay-line can be reduced for a same number of nodes. L. Larger *et al.* have nevertheless realized successfully an experimental opto-electronic reservoir that was able to compute as fast as all-optical ones [16]. The system we will present in the next chapter uses a vertical-cavity surface-emitting laser (VCSEL) as a physical node. Such a system has been chosen to benefit from its specific polarization dynamics.

3.4 Tasks and metrics

Before presenting our new architecture, we will focus on the different tasks and metrics we will use in the next chapters to test the performance of our reservoir computer. We can split them in two categories. First the computational ability and the memory capacity, which are task-independent, allow evaluating the intrinsic performance of the system. Secondly all the other tasks such as Santa-Fe prediction task and the nonlinear channel equalization task, allow testing the performance of our architecture

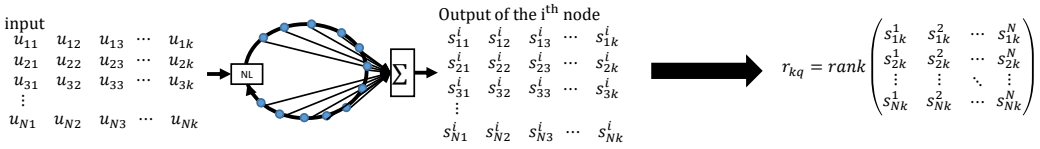

Figure 3.15: Measuring procedure of the kernel quality. N different input streams are sent in the reservoir computer. The response of each last input is recorded in a matrix. Adapted from L. Appeltant Ph. D. thesis [143]

on applied tasks that are presented below.

3.4.1 Computational ability

The computational ability measures the ability of the system to perform computation. This ability is influenced by two different factors: the kernel quality and the generalization property.

3.4.1.1 Kernel quality

The kernel quality measures the ability of the system to represent the different input streams properly. A reservoir computing system maps a problem from low-dimension space to one with a high dimensionality. This transformation should map different input streams to different states in the high-dimensional space. The kernel quality measures if the reservoir's response for different input streams are well separated, in other words how the reservoir contributes to simplify the classification. This has been originally introduced in [111] and a measurement procedure has been proposed in [142]. Let us suppose we fill a matrix with the states of the neurons of the reservoir for different input streams. If the reservoir separates properly the different streams, this matrix should be linearly separable.

To study the kernel quality on a reservoir of N nodes, we build N different input streams, each composed of k different random samples. For each stream, the $k-1$ first inputs are used to warm up the system, so that its original state does not impact the dynamics of the reservoir. Then, for each of the N input streams, the response of each node to the k^{th} input are ordered in a matrix, as illustrated in Fig. 3.15.

We finally compute the rank of the matrix previously made, and call that value r_{kq}. As explained previously, if the reservoir separates the inputs properly, the matrix rank should be maximal $r_{kq} = N$. The rank of the matrix should thus be as high as possible.

3.4.1.2 Generalization property

Having two inputs that are not identical does not mean that they are different: For instance, they can slightly differ because of the noise. Thus, these two inputs should be mapped by the reservoir closely in the high-dimensional space. The generalization property measures the ability of the system to consider these two non-identical inputs as close inputs. This is in fact the ability of the readout layer to read properly the states of the reservoir in order to be able to generalize the behavior learned during the training phase to the testing phase.

To study the generalization property of a reservoir computer with N nodes, we build N input streams with k inputs. The last l inputs are all identical, and the first $k-l$ are different. Only the response of the reservoir computer to the last l input are gathered to fill a matrix, as illustrated in Fig. 3.16. As for the kernel quality, we compute the rank of the matrix, and call that value r_{gp}. The first inputs are used to warm up the system, placing the system in a different state for each stream. The last l inputs being identical, the reservoir should map all the streams to a same state. That is why the rank of this matrix should remain as low as possible $r_{gp} = 0$.

3.4.1.3 Computational ability

As explained at the beginning of this section, the computational ability is linked to the kernel quality and the generalization property. It is given by the difference between the ranks of the matrices constructed in the two previous subsections:

$$r_c = r_{kq} - r_{gp} \tag{3.12}$$

This property is composed of two contradictory phenomena. We can easily imagine cases maximizing the kernel quality or minimizing the generalization property. In the first case, a chaotic system would map all the inputs to different states of the reservoir, and thus maximizing the kernel quality (*i.e.* $r_{kq} = N$). However, it is impossible to also map two similar inputs to the same state of the reservoir in this condition. This would thus minimize the generalization property (*i.e.* $r_{gp} = N$), and finally produce a

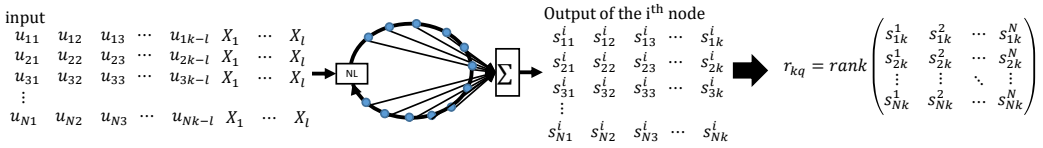

Figure 3.16: Measuring procedure of the generalization property. N different input streams are sent in the reservoir computer, before sending a same input series. The response of each last input is recorded in a matrix. Adapted from L. Appeltant Ph. D. thesis [143]

poor computational ability. On the other hand, it would be also easy to maximize the generalization property for sure, by rending the reservoir computing device insensitive to the input. In this case, two similar inputs would be mapped on the same state of the reservoir. But this is also true for two different inputs, which would result once again to a poor computational ability.

3.4.2 Memory capacity

We have explained previously that the time-delay reservoir computer is well designed to process temporal signals. There are many tasks that require to remember several consecutive inputs to produce the proper response. In order to learn the time dependency of the input data, the reservoir computer have to remember these values during a time longer than the round-trip of the feedback. There is thus a second task-independent property which is called memory capacity. It measures how well the system can remember the past inputs sent to the reservoir [97].

To compute the memory capacity, we generate a random signal $u(k)$ between 0 and 0.5, as the input of the reservoir at time k and we train it to reproduce the input signal delayed by i steps. We can compute the memory function for a given delay i by calculating the normalized correlation between the trained output of the reservoir $\hat{y}(k)$ and the delayed output $u(k-i)$:

$$m(i) = \mathrm{corr}(\hat{y}(k), u(k-i)). \tag{3.13}$$

$m(i)$ is taking its value in [0; 1]. It indicates how well the system is able to keep the data at a given delay. In Fig. 3.17, function $m(i)$ is computed for the VCSEL-based time-delay reservoir computing system, introduced in Chap. 4.

The memory capacity can then be obtained as follows:

$$\mu_c = \sum_{i=1}^{\infty} m(i) \tag{3.14}$$

It corresponds to the depth of memory reachable by the reservoir computer. If this value is too low, some tasks requiring several consecutive past inputs might not be satisfyingly processed by a reservoir computer.

3.4.3 The Sante Fe time series prediction

This first task is extracted from the Santa Fe Time Series Prediction and Analysis Competition led by the Santa Fe Institute in 1991 [144]. This competition aimed

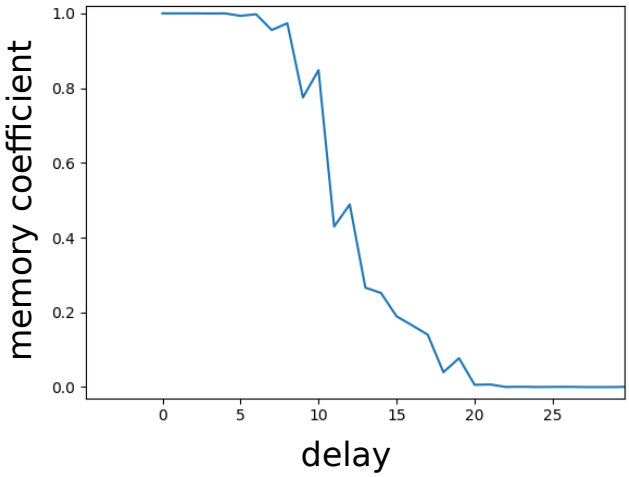

Figure 3.17: Exemple of memory function for VCSEL-based time-delay reservoir computer (numerical results presented in Chap. 4). This curve displays the different value of the memory coefficients, depending on the delay i.

at providing to researcher an overview of the new computer networks, and of their accuracy on analyzing data from different scientific fields. The data set we are using is the first time series proposed in this competition, made of the data of the chaotic fluctuation of a far-infrared laser. This series is presented in Fig. 3.18.

The goal of this task is, given the current state of the laser, to predict the next one. The difficulty on this task is due to the erratic drops of amplitude, which are poorly represented in the series, thus providing only a few instances of this power drops to train the reservoir computer correctly. However, the value of the next state of the laser is highly correlated to the value of the current state and does not requires a

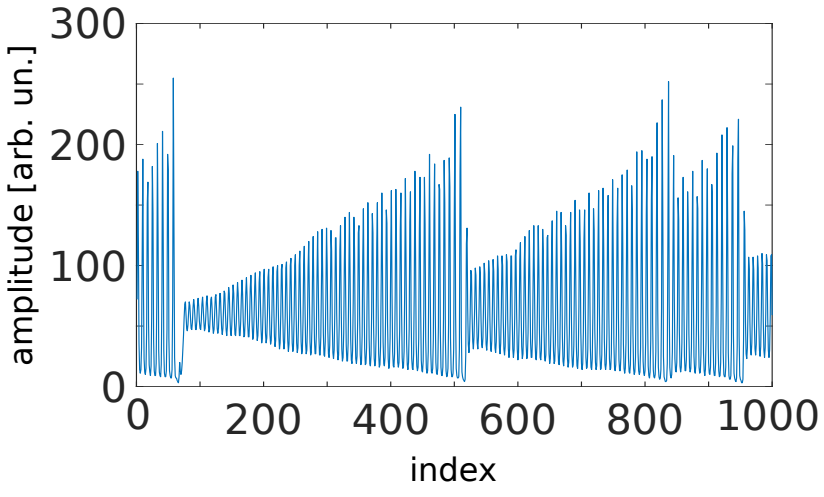

Figure 3.18: First thousand points of the Santa Fe time series

large amount of memory to be solved. This task is largely used to test performance of reservoir computers.

The error on this task is computed using the normalized mean square error (NMSE), which corresponds to the mean distance between the estimation of the reservoir and the expected response, normalized by the variance of the time series. Mathematically, this reads:

$$NMSE = \frac{1}{m} \frac{\sum_{i=1}^{m} (\hat{y}(i) - y(i))^2}{\sigma^2(y)}, \tag{3.15}$$

where m is the total number of points in the series, $\hat{y}$ is the trained reservoir output, y is the target signal, and $\sigma^2(y)$ is the variance of the target signal.

3.4.4 The Nonlinear channel equalization task

The other task studied in this thesis is the nonlinear channel equalization task, which is a problem typically encountered in telecommunication networks. Many physical communication channels exhibit nonlinear properties which induce distortion during the transmission, and a temporal shift due to reflections at different objects. The goal of this task is to reconstruct the original signal from the transmitted signal as illustrated in Fig. 3.19.

We will test two different nonlinear channels, which are presented below.

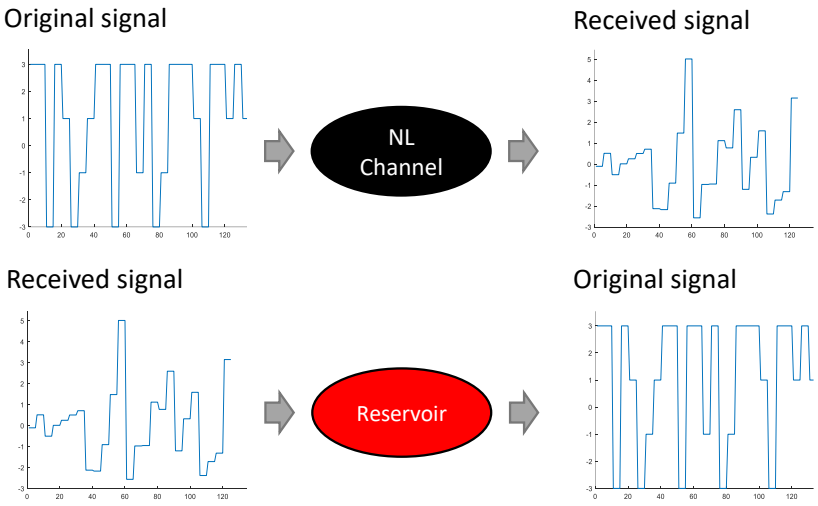

Figure 3.19: Principle of the nonlinear channel equalization task. The transmitted signal is distorted due to the nonlinear channel. This distorted signal is set as the input of the reservoir computer. The reservoir is trained to predict the original signal.

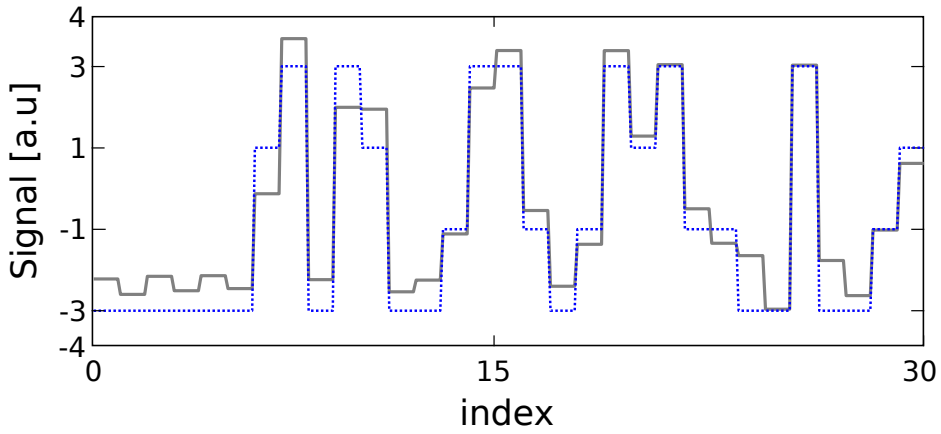

Figure 3.20: Example of wireless signal. The line in dotted blue is an example of signal at the input of the channel. The line in grey is the corresponding output of the channel.

3.4.4.1 WI-FI channel

The first channel presented is commonly used as a benchmark task for time-delay reservoir computer and has been presented in [145]. The input signal $d(n)$ is a sequence of symbols, independent and identically distributed among the values {-3; -1; 1; 3}. This signal is transmitted through a nonlinear channel, which can be modeled by a system linearly mixing consecutive inputs, followed by a memoryless nonlinear system. The linear part of the channel is given below:

$$\begin{aligned} q(i) &= 0.08d(i+2) - 0.12d(i+1) + d(i) + 0.18d(i-1) \\ &\quad -0.1d(i-2) + 0.091d(i-3) - 0.05d(i-4) \\ &\quad +0.04d(i-5) + 0.03d(i-6) + 0.01d(i-7). \end{aligned} \tag{3.16}$$

The signal is then modified by the nonlinearity given by:

$$u(i) = q(i) + 0.036q(i)^2 - 0.011q(i)^3 + v(n), \tag{3.17}$$

where $v(n)$ is a Gaussian noise. An example of signals is given in Fig. (3.20).

The linear part of the channel involves the inputs from the current step up to the $7th$ delayed step. That means memory capacity has to be at least 7 in order to process this task correctly. Moreover, it also involves two steps beyond the current one. These data have never been presented to the reservoir at the moment the input is being recovered. The system will have to somehow compensate this lack of information. The performance on this task is computed thanks to the symbol error rate

(SER): The number of miss-reconstructed symbols over the total number of symbols reconstructed.

3.4.4.2 Single mode optical fiber

The other channel studied in this thesis is one of the most used telecommunication channels in the current internet network: the single mode optical fiber SMF-28 made of silica [35]. We send a two-level pulse amplitude modulation (PAM) signal made of random bits in the fiber at a rate of 25 Gb/s. PAM modulation consists in encoding data in the amplitude of pulses, and is currently used for instance for fast Ethernet communication. This signal is filtered to take into account the rising time of the bit. An example of such a signal is given in Fig. 3.21.(a).

To simulate numerically the channel, we use the nonlinear Schrödinger equation [146]:

$$i\frac{\partial E(z,t)}{\partial z} = -i\frac{\alpha}{2}E(z,t) + \frac{\beta_2}{2}\frac{\partial^2 E(z,t)}{\partial t^2} - \gamma|E(z,t)|^2 E(z,t), \tag{3.18}$$

where $E(z,t)$ is the slowly varying envelop of the optical field, α is the attenuation of the fiber, β_2 is the second order coefficient of dispersion, and γ refers to the nonlinearity of the fiber. The values of the different parameters are chosen so that we simulate the SMF-28 fiber [147]: $\alpha = 0.2$ dB.km^{-1}, $\beta_2 = -21.4$ ps^2.km^{-1}, and $\gamma = 1.2$ W^{-1}.km^{-1}.

There are three different effects that make this task complex: First the attenuation that increases the impact of the noise on the signal, making it more difficult to distinguish the signal. The second one is the Kerr effect, which results from the nonlinear optical properties of the fiber and induces a change in the refractive index of the fiber depending on the optical signal. However, keeping a low amplitude for signals avoids triggering this effect. Using low power signals is thus the solution used nowadays in telecommunication networks to avoid nonlinear effects. We have thus used an amplitude of 4 mW at the input of the channel. The last effect is the chromatic dispersion, which is the one impacting the most the performance of the reservoir. It is responsible of the time-broadening of the bit. This means that the information of one bit are distributed on several steps of the input signals. Because of the chromatic dispersion, a large amount of memory is necessary.

The performance on this task is measured thanks to the bit error rate (BER), which is the number of miss-reconstructed bits over the total number of bits reconstructed.

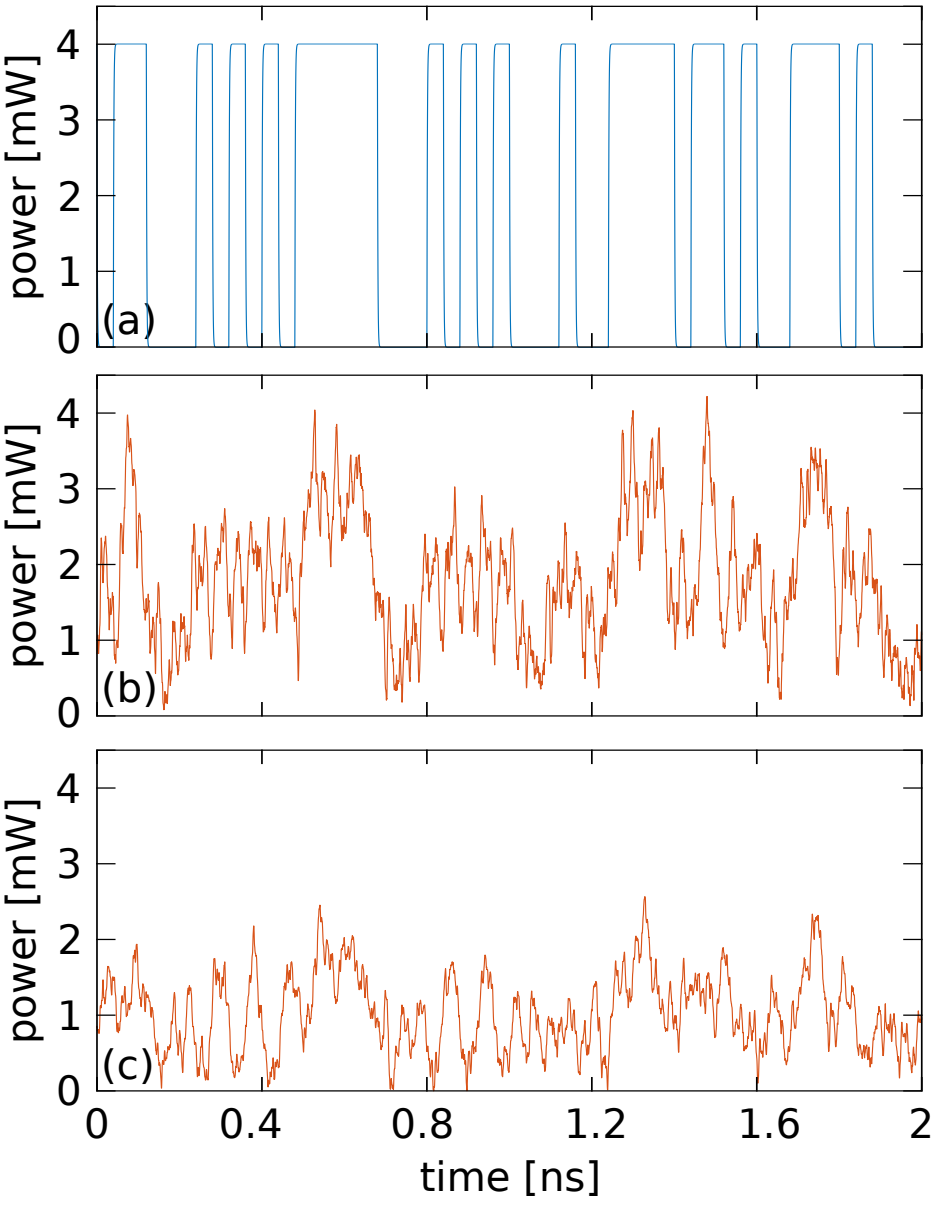

Figure 3.21: Example of optical signals. (a) Signal sent at the input of the fiber. (b) Received signal after 25 km of fiber. (c) Received signal after 50 km of fiber.

3.5 Conclusion

In this chapter, we have presented the basics of artificial neural networks and their different types of architectures and topologies. If the feedforward neural network is easy to train, it does not allow processing temporal signals due to the lack of memory. Creating loops inside the network allows keeping residual information in the network, and thus creating a memory effect. Nevertheless, it makes the training of the system more complex. Reservoir computing helps to tackle this problem, by considering a fixed recurrent neural network and by training only a readout layer with linear regression. The time-delay reservoir computing is specifically interesting as it allows creating experimental reservoir computer with a large number of virtual nodes, but only one physical node. In this paradigm, only one physical node is required, while the other neurons are timely distributed over a delay-line. Several tasks are used to test the performance of this architecture. We decided to keep the computational ability and the memory capacity to test the intrinsic capacity of the system, and the chaotic time series prediction and the nonlinear channel equalization as specific applied tasks.

In the next chapters, we will present a time-delay reservoir computer using a VCSEL as a physical node, and its computational performance. We will show that the specific properties of VCSEL can be used to enhance the performance and the speed of a time-delay reservoir computer.

4

Performance of VCSEL-based time-delay reservoir computing device on single task processing

I know there's a proverb which that says 'To err is human,' but a human error is nothing to what a computer can do if it tries.
Agatha Christie, *Hallowe'en Party*

Contents

4.1 Current performance of time-delay reservoir computing . . 62
4.2 Numerical simulations 63
4.2.1 Presentation of the model 64
4.2.2 Reservoir with an electric input 67
4.2.3 Reservoir with an optical input 71
4.3 Experimental results 86
4.3.1 Presentation of the experimental setup 86
4.3.2 Finding the operating point of the reservoir 89
4.3.3 Performance of the experimental system 91
4.3.4 Link between numerical and experimental results 98
4.4 Conclusion 99

The photonic time-delay reservoir computer has progressed significantly over the past few years regarding the processing of time-dependent signals. However, as presented in the previous chapter, this architecture still suffers from its "slow" processing time, since the different neurons are activated sequentially. This chapter aims at studying the performance of a time-delay reservoir computer made of a VCSEL. As presented in chapter 2, the VCSEL has several advantages compared to the classical semiconductor laser, such as higher modulation frequency and lower power consumption. We also aim at drawing benefits from its specific polarization dynamics to enhance the computational performance of the reservoir computer.

After a short summary of the different architecture of time-delay reservoir computing existing, and their performance in Sec. 4.1, we will present in detail our architecture and its simulated performance in Sec. 4.2.1. These numerical simulations have been realized in order to prepare the realization of an experimental setup, which performance are presented in Sec. 4.3, and confront the experimental results to the numerical simulations. We will finally capture the essential part of this work in Sec. 4.4.

Most of the results presented in this chapter have been published in peer-reviewed journals [17, 18].

4.1 Current performance of time-delay reservoir computing

As explained in Chap. 3, the first reference to a reservoir computer made of a single dynamical node was made by L. Appeltant *et. al.* in 2011 [8]. In their work, a Mackey-Glass oscillator is used to perform spoken digit recognition task with an error rate of 0.2 %. The suggested architecture performs well, but the processing speed is limited by the slow dynamics of the system. The same team proposed a year later an opto-electronic architecture based on the same working principle [9]. A Mach-Zehnder modulator is used to realize the nonlinear node. This system remains a reference in terms of performance. In their first work it has been used to recognize spoken digits, but also to predict the Sante Fe time series. The performance was comparable to their previous work concerning the speech recognition, but the speed of the system was increased by three order of magnitude thanks to the use of photonic components. The Santa Fe time series prediction was successfully performed with a NMSE of 1.2×10^{-4}. The same architecture has also been used by Y. Paquot *et. al.* to perform telecommunication task for the first time [10]. The system was able to recover experimentally WIFI signals with a symbol error rate of 10^{-4}. The opto-electronic reservoir has been recently optimized to be able to process information at gigabit per

second speed rate. The system was used to classify millions spoken digit words per second [16].

Simultaneously, other architectures of time-delay reservoir computer were reported. The first all-optical time-delay reservoir computer reported was made with a semiconductor optical amplifier [11]; it was performing WIFI channel equalization with a symbol error rate twice larger compared to the architecture previously introduced but operating twice faster. The same task has also been performed using a passive fiber cavity [148]. This architecture achieved an error rate of 10^{-5} both in numerical simulation and in experiment, which are the best performance on this task up to date, but at rather low computational speed.

The laser-based architecture was also proposed and is still under study as the use of laser allows to easily reach gigabit per second processing speed due to the fast modulation possibility. The first reservoir made of a conventional edge-emitting laser was presented in 2013 by D. Brunner *et. al.* [136], and was used for time series prediction and spoken digit recognition. This system has been further explored, and tested with several benchmarking tasks [12, 14, 149], such as exploring the memory capacity of the system, or testing the nonlinear channel equalization task.

The use of a semiconductor ring lasers has also been proposed by R. Nguimdo *et. al.* [139, 13, 150] to predict the Santa Fe time series. Different conditions of the two modes dynamics of the semiconductor ring laser were proposed to optimize the performance of the reservoir.

K. Takano *et. al.* demonstrated in 2018 the possibility to use photonic integrated circuit (PIC) made of an integrated DFB laser, a semiconductor amplifier and a feedback to perform Santa-Fe time series prediction [140].

4.2 Numerical simulations

Using a VCSEL as single dynamical node in a time-delay reservoir computer (TDRC) is motivated by the VCSEL intrinsic properties: (i) The VCSEL's high modulation speed can speed up the reservoir processing and (ii) the two-mode VCSEL polarization dynamics allows for the generation of more information per unit of time. In addition to that, the VCSEL is largely used for the data communication in the Internet, which would make a VCSEL-based reservoir computer suitable to perform telecommunication tasks and being seamlessly integrated with existing hardware. In this section, we present our VCSEL-based architecture, and the numerical analysis of the performance in the parameter space. Numerical simulations shall confirm our first insight, *i.e.* that

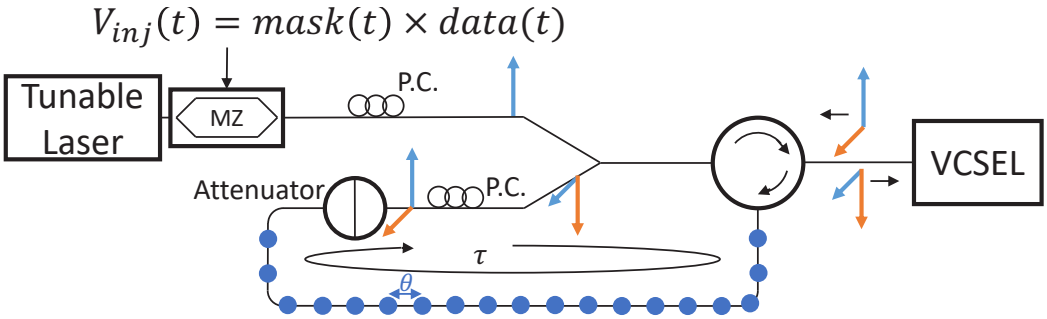

Figure 4.1: Scheme of the VCSEL-based reservoir computer taken from [17]

a VCSEL-based reservoir allows getting a faster computation device, while keeping (or even improving) the computational performance.

4.2.1 Presentation of the model

The architecture studied in this chapter is presented in Fig. 4.2. and is very similar to the one presented by K. Hicke *et al.* [12], except that an EEL is substituted by a VCSEL. The reservoir itself is made of the VCSEL and a feedback loop. In the loop, an attenuator and a polarization controller control the feedback strength and the polarization of the light at the output of the feedback, respectively. The number N of virtual nodes spread along the delay-line can be adjusted with the delay of the optical line τ. These two parameters fix the inter-delay θ between two consecutive virtual nodes such that: $\tau = N \times \theta$.

The system can be either injected or modulated electrically (via the pumping current). The optical input stage is composed of a master laser, and a Mach-Zehnder modulator to embed the data stream in the VCSEL dynamics.

In order to simulate our system, we consider the SFM model [60] with a feedback term and an optical injection term:

$$\begin{aligned}
\dot{E}_x &= \kappa(1+i\alpha)[(N-1)E_x+inE_y] - (\gamma_a+i\gamma_p)E_x \\
&\quad +\Phi_x(t)+\kappa A_{inj}(t)e^{(\omega_{inj}-\omega_0)t}+F_x(t), && (4.1)\\
\dot{E}_y &= \kappa(1+i\alpha)[(N-1)E_y-inE_x]+(\gamma_a+i\gamma_p)E_y \\
&\quad +\Phi_y(t)+F_y(t), && (4.2)\\
\dot{N} &= -\gamma_N[N-\mu+N(|E_x|^2+|E_y|^2)+in(E_yE_x^*-E_xE_y*)], && (4.3)\\
\dot{n} &= -\gamma_s n-\gamma_N[n(|E_x|^2+|E_y|^2+iN(E_yE_x^*-E_xE_y^*)], && (4.4)
\end{aligned}$$

where E_x and E_y are the slow-varying amplitude of the two orthogonal linearly polarized optical fields $LP_{x,y}$, N is the population difference between conduction and valence

bands. n is the population difference between the carrier densities with positive and negative spin values. μ is the injection current normalized to threshold. κ is the field decay rate, α is the linewidth enhancement factor, γ_N is the decay rate of the carrier population and γ_s is the decay rate which influences the mixing of carrier populations between the two different spins. γ_a and γ_p are used to model the linear dichroism and the linear birefringence of the active medium, respectively. $\omega_0 = 2\pi f \frac{c}{\lambda}$ is the angular frequency of the free-running laser (with λ the wavelength of the laser, and f the frequency of the electrical field), and η is the feedback strength (cf Eq. 2.2). The output of the Mach-Zehnder modulator A_{inj}, which corresponds to the injected optical field is calculated thanks to the following formula:

$$A_{inj}(t) = \sqrt{P_{inj}}/2 \times (1 + e^{iV(t)/V_\pi}), \tag{4.5}$$

where P_{inj} is the optical power of the tunable laser and $V(t)$ is the voltage relative to the input taken within $[-\pi V_\pi; \pi V_\pi]$. ω_{inj} is the angular frequency of the master laser. The electric input is made by modulating the bias current μ around its mean value. Hence, we can write $\mu(t) = \mu_0 + \gamma I(t)$, where μ_0 is the mean bias current, γ is a scaling factor, and $I(t)$ the current proportional to the input.

F_x and F_y are two Langevin noise sources modeling the spontaneous emission noise [151], and are given by:

$$F_x = \sqrt{\frac{\beta_{sp}}{2}} \left(\sqrt{N+n}\xi_1(t) + \sqrt{N-n}\xi_2(t) \right), \tag{4.6}$$

$$F_y = -i\sqrt{\frac{\beta_{sp}}{2}} \left(\sqrt{N+n}\xi_1(t) - \sqrt{N-n}\xi_2(t) \right), \tag{4.7}$$

where $\xi_1(t)$ and $\xi_2(t)$ are complex Gaussian white noise, and β_{sp} is the spontaneous emission rate. We first consider a deterministic case i.e. $\beta_{sp} = 0$.
Finally, $\Phi_x(t)$ and $\Phi_y(t)$ are the feedback terms. They can be expressed as follows:

$$\Phi_x(t) = \eta \left(\cos(\Theta) E_x(t-\tau) - \sin(\Theta) E_y(t-\tau) \right) e^{-i\omega_0 \tau}, \tag{4.8}$$

$$\Phi_y(t) = \eta \left(\sin(\Theta) E_x(t-\tau) + \cos(\Theta) E_y(t-\tau) \right) e^{-i\omega_0 \tau} \tag{4.9}$$

where η is the feedback strength and Θ is the polarization orientation of the delayed optical field induced by the polarization controller, with respect to the LP_x mode.

There are multiple tunable parameters, and therefore the dimension of the parameter space to explore becomes too large to be completely studied with fine resolution. We will first split the parameters in two categories: the internal parameters of the VCSEL, and the operating parameters, *i.e.* tunable and accessible by a user. We have split

VCSEL parameters	Values
κ	300 GHz
α	3
γ_a	-0.1 GHz
γ_p	6 GHz
γ_N	1 GHz
γ_s	50 GHz
λ	1550 nm
β_{sp}	10^{-12}

Table 4.1: Values of the VCSEL parameters.

them in the chart below:

VCSEL parameters	Operating parameters
κ	η
α	P_{inj}
γ_a	γ
γ_p	Θ
γ_N	$\theta = \frac{\tau}{N}$
γ_s	μ_0
ω_0	

Because we aim at building an experimental setup that corresponds to this simulated system, we will rather focus on exploring the operating parameters. Therefore, the VCSEL's internal parameters are fixed, with the commonly encountered values in the literature [151]. The values used for the VCSEL parameters are presented in Tab. 4.1.

The operating parameters have been chosen as the one that can be easily tuned experimentally. The bias current μ_0 can be set thanks to the power supply of the laser diode. The feedback strength η can be set thanks to an attenuator placed in the feedback loop, and the polarization orientation of the delayed optical field Θ can be adjusted thanks to a polarization controller also placed in the feedback loop. The optical power of the master laser P_{inj} is set with its power supply. Finally the delay between two nodes θ and the scaling factor γ can be adjusted while pre-processing the input signal.

We will also limit ourselves to only two different values for Θ:

- $\Theta = 0$: In this case, the polarization is maintained along the feedback. The main polarization mode of the VCSEL at the end of the feedback loop is injected parrallelly to the main emitted polarization mode. The depressed polarization

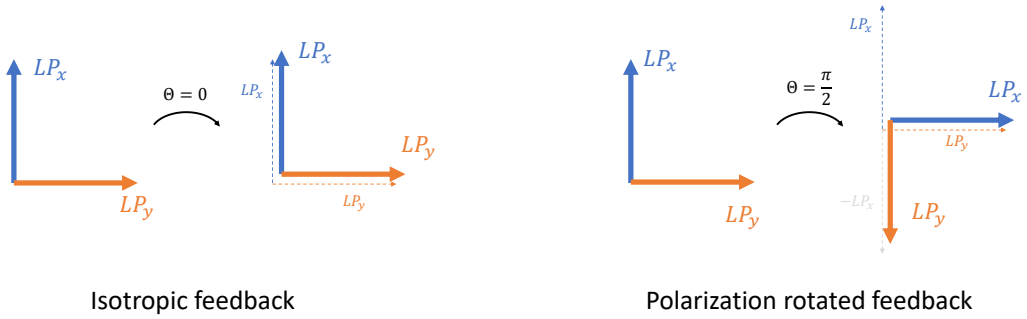

Figure 4.2: The two configurations of feedback. For isotropic feedback, the main polarization mode of the VCSEL at the end of the feedback loop is injected parrallely to the main emitted polarization mode, and so is the depressed polarization mode. For polarization rotated feedback, the polarization orientation is rotated perpendicularly during the feedback: the dominant VCSEL polarization mode LP_x at the end of the feedback loop is injected parrallelly to the depressed polarization mode LP_y, and the depressed polarization mode LP_y is injected to the opposite of the dominant polarization mode $-LP_x$.

mode at the end of the feedback loop is injected parrallelly to the depressed emitted polarization mode. This case is called isotropic feedback (IF) with the following expression:

$$\Phi_x(t) = \eta E_x(t-\tau)e^{-i\omega_0\tau}, \Phi_y(t) = \eta E_y(t-\tau)e^{-i\omega_0\tau}. \tag{4.10}$$

- $\Theta = \frac{\pi}{2}$: In this case, the polarization orientation is rotated perpendicularly in the feedback loop. The dominant VCSEL polarization mode LP_x at the end of the feedback loop is injected parrallelly to the depressed polarization mode LP_y, and inversely for the depressed polarization mode. This is what we refer as polarization rotated feedback (RF) and its mathematical expression reads:

$$\Phi_x(t) = -\eta E_y(t-\tau)e^{-i\omega_0\tau}, \Phi_y(t) = \eta E_x(t-\tau)e^{-i\omega_0\tau}. \tag{4.11}$$

This model has been used to perform numerical simulations, and the details of the numerical method are presented in Appendix A.

4.2.2 Reservoir with an electric input

We first study the performance of the reservoir with an electric input, with no optical injection. We examine the influence of the inter-delay θ between the virtual nodes, the bias current μ_0, the scaling factor γ and the feedback strength η. The results

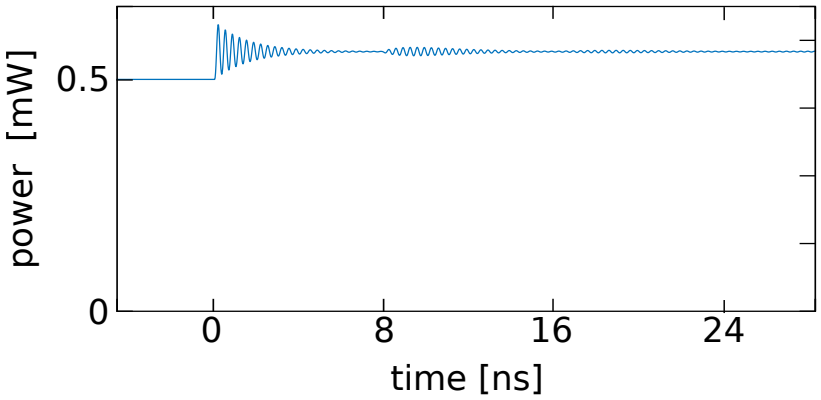

Figure 4.3: Temporal response of the system subitted to a step. The bias current is set at $\mu_0 = 1.5$ before $t = 0$ ns. At $t = 0$ ns, the bias current is set at $\mu = 1.55$. $\tau = 8$ ns, $\eta = 0.2$ GHz

presented in this part are preliminary, and not exhaustive since, as explained below, this electrical input method has not been selected.

4.2.2.1 Raw performance of the system

Before studying the performance of the system, to know how it responds to a step input current allows us to determine the range of time scales to explore and find a suitable operating point. The response to a step is given in Fig. 4.3, when the bias current μ changes from 1.5 to 1.55 at $t = 0$. The length of the feedback has been set at $\tau = 8$ ns. The feedback strength is chosen to be at $\eta = 0.2$ GHz. We can observe that the VCSEL oscillates towards a new steady state at $t = 0$ ns. The response oscillates with a frequency around 3 GHz until stabilizing. The response fades away after ~ 4 ns, and at $t = 8$ ns, we can see the influence of the feedback on the temporal response: an echo of the previous response is visible. To benefit from the transient dynamics of the system for our reservoir computer, we need to chose θ smaller than the time response of the dynamical system as explained in Chap. 3. The values of θ we explore are thus smaller than 0.3 ns.

Once we know more about the response time of the system, we will focus on the task independent performance metrics of the system, *i.e.* the computational ability and the memory capacity, to find the best operating point. We map the space of parameters (γ, θ) and (μ_0, η), to compute these two metrics. The maps showing the computational ability normalized by the number of nodes are provided in Fig. 4.4, for a number of neurons $N = 400$. Figure 4.4.(a) presents the computational ability depending on the scale factor γ, and the delay between nodes θ, with fixed $\mu_0 = 1.5$ and $\eta = 0.23$ GHz. The map shows an area in which the computational ability is close to 1: This provides an evidence that the system can perform computation properly. The best level of performance is achieved for an inter-delay around $\theta \sim 0.1$ ns, which is consistent with

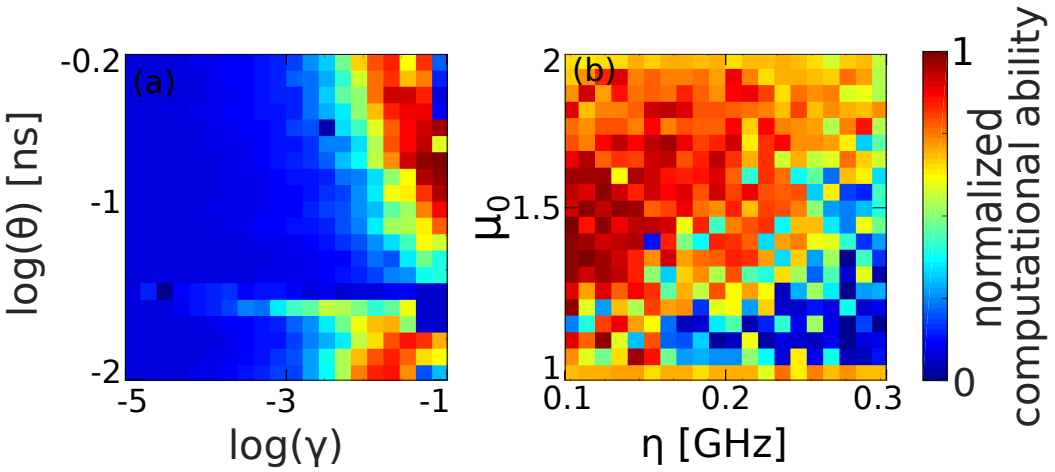

Figure 4.4: Computational ability of the system with electrical input depending on (a) the scaling factor γ and the delay between nodes θ, and (b) on the feedback strength η and the bias current μ_0. Computational ability has been normalized by the number of nodes.

with the fact that θ must be smaller than the typical time response of the system. The scaling factor has to be chosen around $\gamma \sim 0.1$. This provides an information about the required difference of amplitude to map differently two close inputs by the reservoir computer. We will thus fix $\theta = 0.2$ ns and $\gamma = 0.05$ to compute the second map presented in Fig. 4.4.(b), which explores the dependence of the computation ability on two other parameters: the bias current μ_0 and the feedback strength η. The area of best performance is larger while varying these parameters. There is still a smaller region providing even better performance for $\mu_0 \sim 1.5$ and $\eta \sim 0.15$. These results provide evidence that some parameters combinations are more suitable than others to perform computation. However, a proper reservoir computer not only needs to demonstrate good computational ability, but also a good memory capacity. The same method has been applied to compute the memory capacity, as shown in Fig. 4.5. The system is trained with 800 samples (reaching a satisfying trade-off between good learning and over-fitting), and the test is made on 1800 samples. We observe that depending on the scale factor and the delay between nodes, there is a region providing a memory capacity of 18. However, keeping the same values as previously ($\theta = 0.2$ ns and $\gamma = 0.05$) to compute the memory capacity depending on the feedback strength and the bias current provides a lower memory. In this case, the set of parameters providing the best memory capacity does not corresponds to the one giving the best computational ability. One might choose the parameters depending on the task that should be performed by the reservoir. If the tasks requires a large memory and the different inputs can be distinguished easily, then the memory capacity of the reservoir should be favored. On the contrary if the task requires a small memory capacity and the different inputs are close one from each other, the computational ability might be

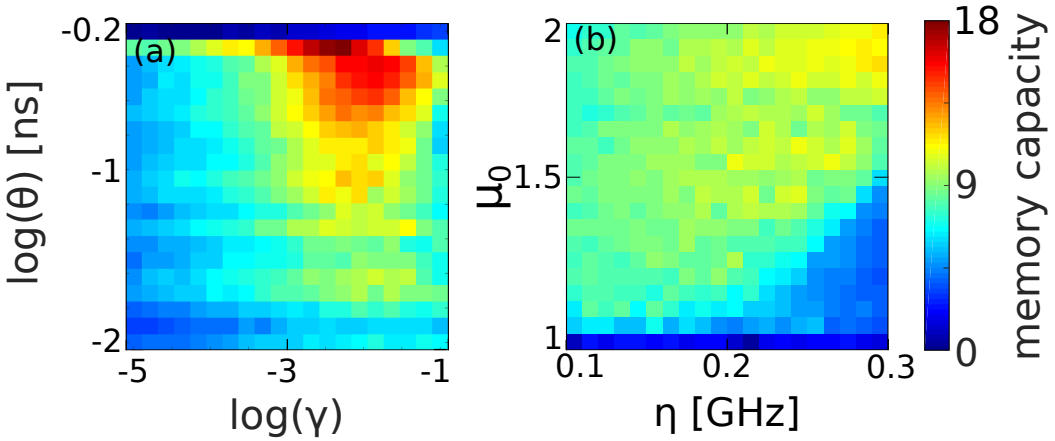

Figure 4.5: Memory capacity of the system with electrical input depending on (a) the scaling factor γ and the delay between nodes θ, and (b) on the feedback strength η and the bias current μ_0

a priority.

4.2.2.2 Applied performance of the system on the Santa-Fe prediction task

The maps presenting the performance for the Santa Fe tasks are depicted in Fig. 4.6. We used a training set with 3000 samples, and a testing set with 1000 samples. The maps have been computed only while sweeping η and μ_0. Two sets of parameters have been chosen:

- $\theta = 0.15$ ns and $\gamma = 0.05$, which maximize the computational ability (Fig. 4.6.(a)).

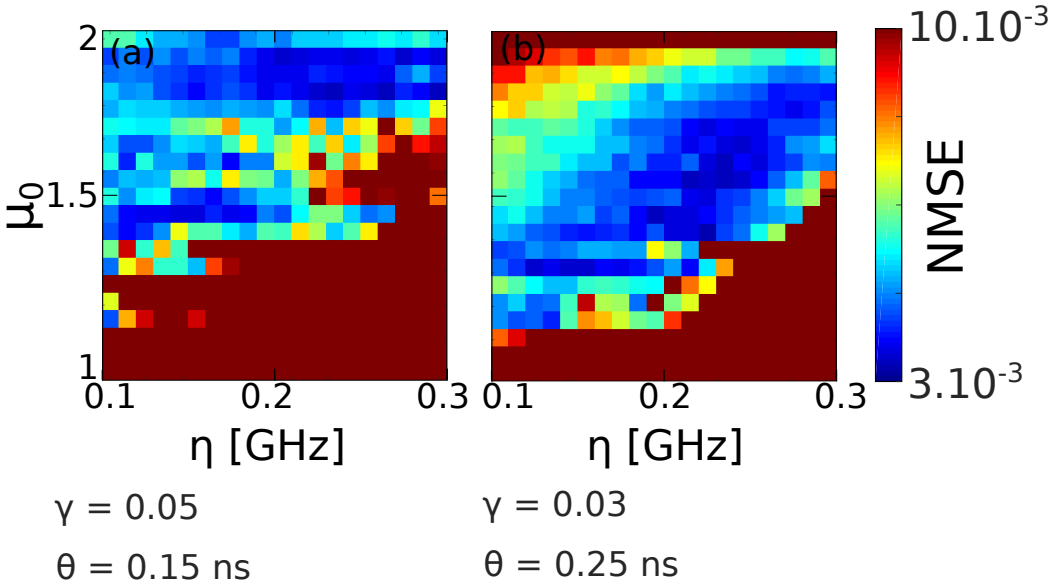

Figure 4.6: NMSE on Santa-Fe prediction task of the system with electrical input depending on on the feedback strength η and the bias current μ_0 for (a) $\theta = 0.15$ ns and $\gamma = 0.05$ the scaling factor γ, and (b) $\theta = 0.25$ ns and $\gamma = 0.03$.

- $\theta = 0.25$ ns and $\gamma = 0.03$, which maximize the memory capacity (Fig. 4.6.(b)).

We observe that in both cases, the system can exhibit its best performance, with a NMSE of 3×10^{-3}. However, it is still an order of magnitude higher (worse) than the performance obtained by the opto-electronic reservoir computer [9].

As explained at the beginning of this section, this input method has not been selected for our experimental setup, mainly because of speed reasons: the laser mount we will use for the experiment (TCLD-9 from Thorlabs) cannot achieve RF modulation beyond 600 MHz.

4.2.3 Reservoir with an optical input

This section presents the performance of the reservoir submitted to optical injection. From now on, the bias current μ is a fixed parameter. The scaling factor γ thus does not play any role. Except otherwise is stated, the injection is made with a zero detuning, hence $\omega_{inj} = \omega_0$

4.2.3.1 Dependence of the intrinsic performance of the system on operating parameters

We will first study the response of the system to a step of optical injection. Figure 4.7.(a) shows the response of the VCSEL with isotropic feedback. An optical step with an amplitude of $P_{inj} = 0.1$ mW is sent at $t = 0$ ns, inducing an oscillating behavior of the laser at 5 GHz. The oscillations are strongly damped, before reaching the new steady state. At $t = 8$ ns, we can observe the influence of the feedback: Echoes of the initial response which have larger amplitude with the optical input compared to the electric input. We can still distinguish the echo of the response after several roundtrip times. This is mainly because injecting the laser stabilizes its dynamics. The feedback strength can be thus set higher without destabilizing the VCSEL. Figure 4.7.(b) presents the response of the VCSEL with rotated feedback. We observe in this configuration that both polarization modes of the VCSEL are lasing, and both polarization modes show echoes of the step response, even if the optical injection is aligned with the main polarization mode. We have thus two choices to build the output layer: We can either train the reservoir with the total output power $|E_x^2| + |E_y^2|$, and having only one piece of information per node, or can measure separately the power of each polarization mode $|E_x^2|$ and $|E_y^2|$, which gives two pieces of information per node. In the second configuration, we build an output layer with twice more nodes, while keeping the same feedback duration τ. The echoes are damped more quickly compared to the isotropic feedback case. For both configurations, the response is faster compared to using an electric input, hence making possible to reduce the inter-delay θ between virtual nodes, and therefore to increase the processing speed.

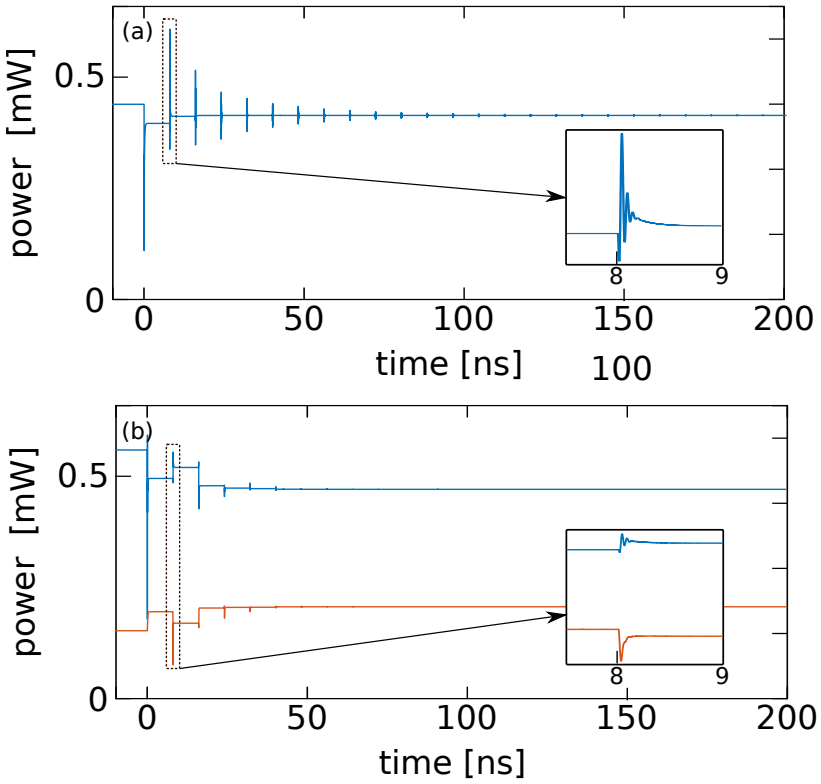

Figure 4.7: Temporal response of the system submitted to a step for the system with (a) isotropic feedback and (b) for the system with rotated feedback. The blue (red) line presents the power emitted by the dominant (depressed) polarization mode. There is no injected power before $t = 0$ ns. At $t = 0$ ns, the injected power is set at $P_{inj} = 0.1$ mW. $\tau = 8$ ns, $\eta = 30$ GHz. A zoom on the oscillating response is providing for both figures.

The study of the bifurcation diagram given in Fig. 4.8 adds information to the one gained from the analysis of the time response. The observed dynamical behavior is common for semiconductor laser submitted to feedback [45]: We observe the first Hopf

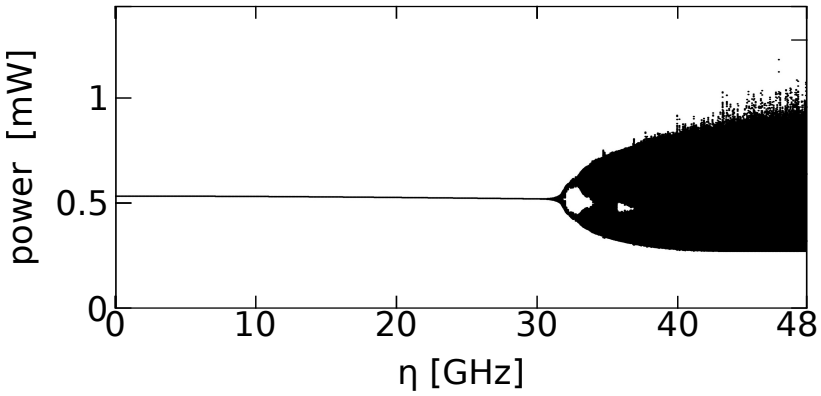

Figure 4.8: Bifurcation diagram of the reservoir computer with optical injection. The emitted power is measured while varying the feedback strength η. $P_{inj} = 0.1$ mW, $\tau = 8$ ns.

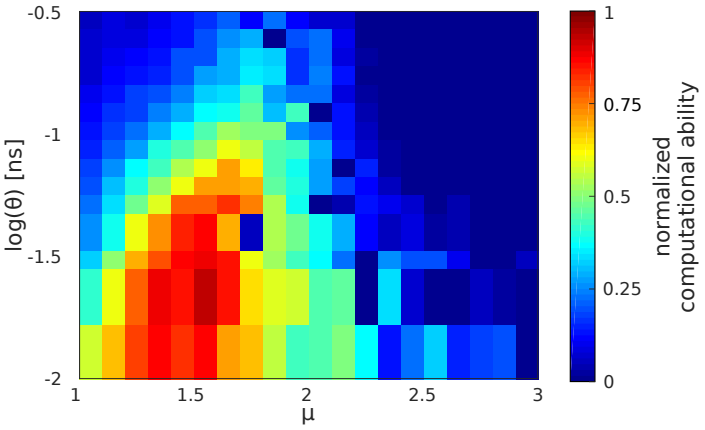

Figure 4.9: Computational ability plot as a function of the injection current μ, the node inter-delay θ for an injection power $P_{inj} = 0.1$ mW, and a feedback strength $\eta = 10$ GHz. Adapted from [17].

bifurcation point at $\eta \approx 32$ GHz, and successive bifurcations at higher feedback rates that lead to a chaotic dynamics. This information helps finding the operating point of the reservoir. As it has been demonstrated in 2012 by J. Dambre *et. al.* [152], the question for a dynamical system is not whether the system is able to perform computation, but rather what the parameters of the reservoir leading to the best performance are. This question has been studied: A dynamical system used as reservoir computing device performs better when it is set at the edge of the instabilities [153, 154]. Indeed, while getting closer to the edge of the instabilities, the response of the system shows more complex transient, while remaining stable. This complexity will contribute to better separating the states of the reservoir. Therefore, we assume that the best operating point will be found before, and near the first bifurcation (here for η close to 32 GHz).

We will now focus on the task-independent performance metrics of the reservoir. As these are not sensitive to the configuration of the output layer (*i.e.* using the total output power or the power of each polarization mode separately), we will only present the results obtained with the total output power. First, we present the computational ability. The results of this test as a function of the delay between nodes θ and of the bias current μ is presented in Fig. 4.9. The results are similar for the two feedback configurations, therefore only one map is given. The optical injected power is kept fixed at 0.1 mW, and the feedback strength is set at 10 GHz. The map highlights that there is a region of parameters that exhibits a better computational ability. As expected, this region is located for smaller values of the inter-delay. ($\theta \in$[0.01 ns, 0.04 ns]). This region is also located for a bias current close to the threshold current ($\mu \in$ [1.2, 1.5]). It appears that for smaller bias current, the VCSEL is more sensitive to the optical injection, which allows a better separation of the different inputs. Taking into

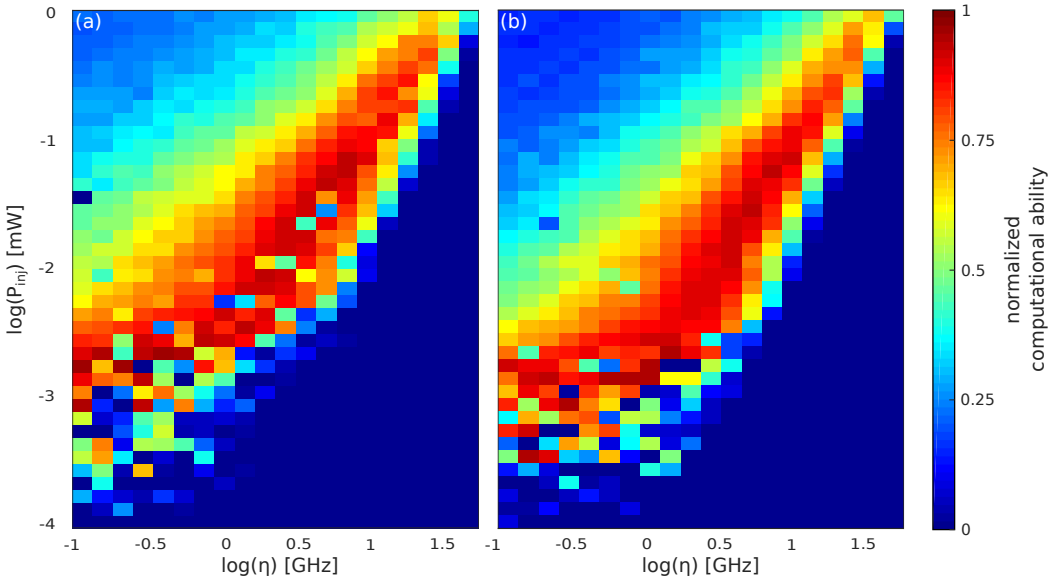

Figure 4.10: Computational ability as a function of the injection power P_{inj} and the feedback strength η. (a) Isotropic feedback configuration (b) Rotated feedback configuration. $\mu = 1.3$ and $\theta = 0.02$ ns. Adapted from [17].

account these results, we will keep for the rest of this work $\mu = 1.3$ and $\theta = 0.02$ ns.

The computational ability map as a function of the feedback strength and the injected power is given in Fig. 4.10. We observe that the results are similar, no matter the feedback configuration. The area region providing the best computational ability in the (η, P_{inj}) plane is large, which means this region is easily reachable experimentally.

We have also evaluated the memory capacity of the reservoir in the (η, P_{inj}) plane, keeping $\mu = 1.3$ and $\theta = 0.02$ ns. We chose to use 400 nodes in the output layer. The training is realized with 800 samples (reaching a satisfying trade-off between good learning and over-fitting), and the testing with 3,200 samples. The maps presenting the memory capacity are given in Fig. 4.11. If the difference of performance between the two feedback configurations is not significant, the impact of the feedback is more important on the memory capacity. The region giving the highest memory is globally obtained in the same region of the (η, P_{inj}) plane. However, the memory is twice higher with a rotated feedback (with a memory capacity of ~ 16) than with an isotropic feedback (with a memory capacity of ~ 8). We have not been able to clarify why the memory capacity is higher with the rotated feedback configuration. However, we assume this might be due to the dynamical response of the VCSEL which is different when using the rotated feedback in comparison with isotropic feedback. The two polarization modes "exchange information" via the carrier population in the laser in case of rotated feedback. This phenomenon being slower than the response of one polarization mode to optical injection, data last longer in the reservoir.

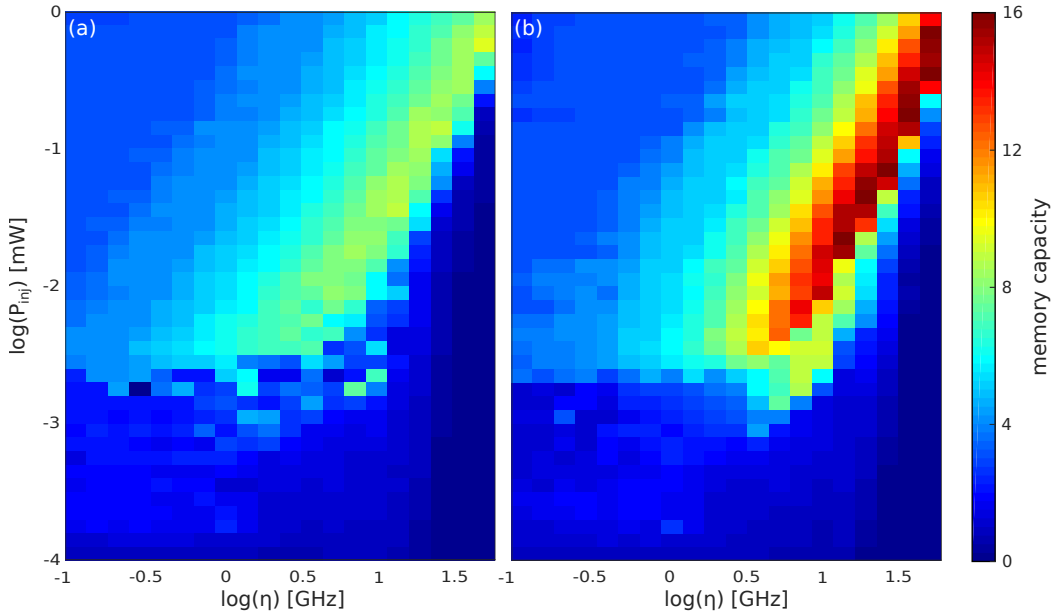

Figure 4.11: Memory capacity as a function of the injection power P_{inj} and the feedback strength η. (a) Isotropic feedback configuration (b) Rotated feedback configuration. $\mu = 1.3$ and $\theta = 0.02$ ns. Adapted from [17].

Moreover, the computational performance and the memory capacity of the system can be interpreted with the dynamics of the reservoir. The maps of task-independent performance are superimposed with the limit of chaos in Fig. 4.12. The dynamics

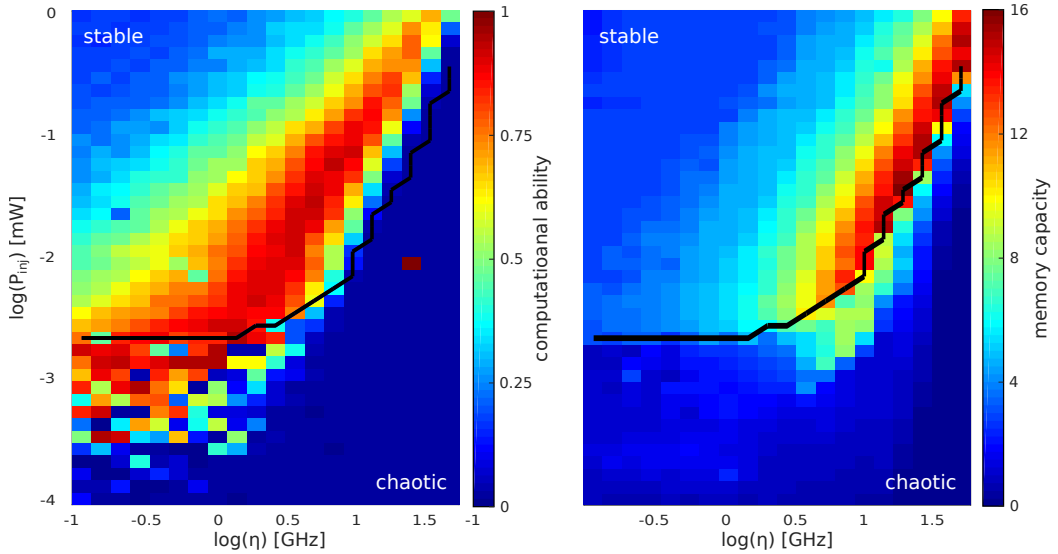

Figure 4.12: Comparison between the dynamics of the reservoir and its (a) computational ability and (b) memory capacity in case of rotated feedback, depending on the injection power P_{inj} and the feedback strength η. $\mu = 1.3$ and $\theta = 0.02$ ns. The black line shows the border between stable and chaotic dynamics.

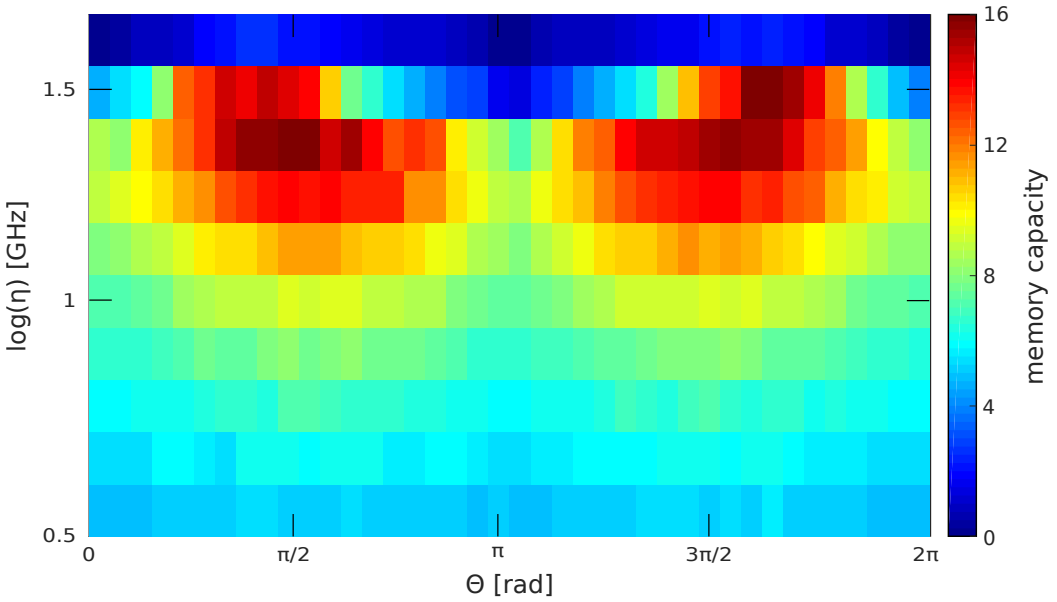

Figure 4.13: Memory capacity depending on the rotation of the feedback Θ and the feedback strength η. $P_{inj} = 0.1$ mW, $\mu = 1.3$ and $\theta = 0.02$ ns.

of the reservoir is compared with the computation ability in Fig. 4.12.(a), and with the memory capacity in case of rotated feedback in Fig. 4.12.(b). We observe that the region of parameters giving the best computational ability and the best memory capacity are really close to the edge of chaos, as discussed previously. The figure also allows identifying the parameters giving simultaneously the best memory capacity and the best computational ability. There is only a narrow region of parameters that leads to best performance for both computational ability and memory capacity, but it does not mean though that only this region will provide satisfactory performance on applied tasks.

4.2.3.2 Dependence of the memory capacity on VCSELs parameters

We finally realize additional simulations to assess the quality of the choice we have made at the beginning of this section.

We first perform a more systematic study of the influence of the rotation of the polarization on the memory capacity. The maps showing the performance is provided in Fig. 4.13. For this map, the injected power has been fixed to 0.1 mW. We notice that the region showing the highest memory capacity is centered around $\Theta = \pi/2$ and $\Theta = 3\pi/2$. On the contrary, the lowest memory capacity is obtained when $\Theta = 0$ or $\Theta = \pi$. This observation sustains our choice of studying the two feedback configurations, either isotropic or rotated feedback.

We also checked the influence of the frequency detuning on the memory capacity of the

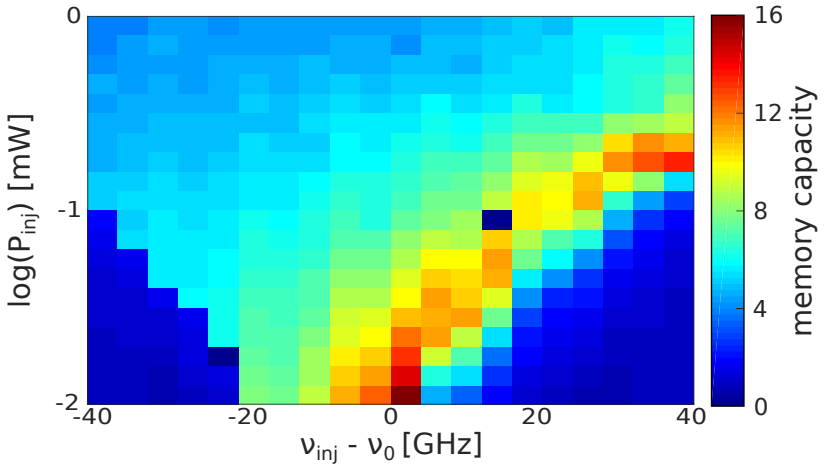

Figure 4.14: Memory capacity depending on the detuning $\Delta\nu$ and the injected power P_{inj}. $\eta = 10$ GHz, $\mu = 1.3$ and $\theta = 0.02$ ns.

reservoir, similarly to the work of J. Bueno *et. al.* on an EEL-baser time-delay reservoir computer [51]. The detuning $\Delta\nu = \nu_{inj} - \nu_0$ is the difference between the injected optical frequency and the VCSEL free-running frequency. The memory capacity depending on the detuning and the injected power in the case of rotated feedback is presented in Fig. 4.14. For this study, the feedback strength is fixed at 10 GHz. The map is closely related to the injection dynamics of the VCSEL. The region providing a memory capacity higher than one has the same shape as the injection locking region. The memory capacity is however higher at the limit of the region having a positive detuning. While injecting VCSEL, this limit is known to lead to a richer dynamics than the region of negative detuning values, which is characterized by a more stable dynamical response [155].

We finally study the influence of the parameters of the VCSEL on the memory capacity. For these simulations, all the parameters of the VCSEL are kept fixed at the values given in Tab. 4.1, except one which is analyzed. Only the results for rotated feedback are provided.

Figure 4.15 shows the different maps of memory capacity as a function of the feedback strength and of the injected power, for different values of α, the linewidth enhancement factor. This parameter quantifies the amplitude-phase coupling of the VCSEL. A higher value leads to a stronger coupling. Added to that a non-zero linewidth enhancement factor causes a chirp, *i.e.* the laser frequency gets modulated when modulating its amplitude [156]. We observe that each map is similar to the one presented in Fig 4.11. However, it seems that for a value of α about 2, the reservoir exhibits a higher memory capacity. The area providing the best memory capacity shifts to higher values of injected power while increasing α. This behavior can be interpreted as a consequence of the change of dynamics of the VCSEL with feedback. When increasing α, the

VCSEL destabilize more easily. The edge of chaos is then reached for lower values of the feedback strength and higher injected power.

The second VCSEL parameter being studied is γ_a. The maps are presented in Fig. 4.16. A positive value of γ_a leads to a lower threshold for the depressed polarization mode (LP_y) and inversely a negative value leads to a lower threshold for the dominant polarization mode (LP_x) [157]. The figure presents three of the memory capacity maps as a function of the feedback strength and the injected power for $\gamma_a = -0.5$ GHz (4.16.(a)), $\gamma_a = 0$ GHz (4.16.(b)) and $\gamma_a = 0.5$ GHz (4.16.(c)) (the value commonly used for γ_a is -0.1 GHz [151]). The last figure presents the best achievable memory capacity depending on γ_a. The region providing the best memory capacity remains the same while sweeping γ_a. The memory capacity is nevertheless higher when one polarization mode is strongly enhanced compared to the other ($\gamma_a = \pm 1$ GHz), or when both polarization modes have the same threshold ($\gamma_a = 0$ GHz). We also notice that the curve is approximately symmetric to 0, which is expected since the two polarization modes of the VCSEL play symmetrical roles in the dynamics.

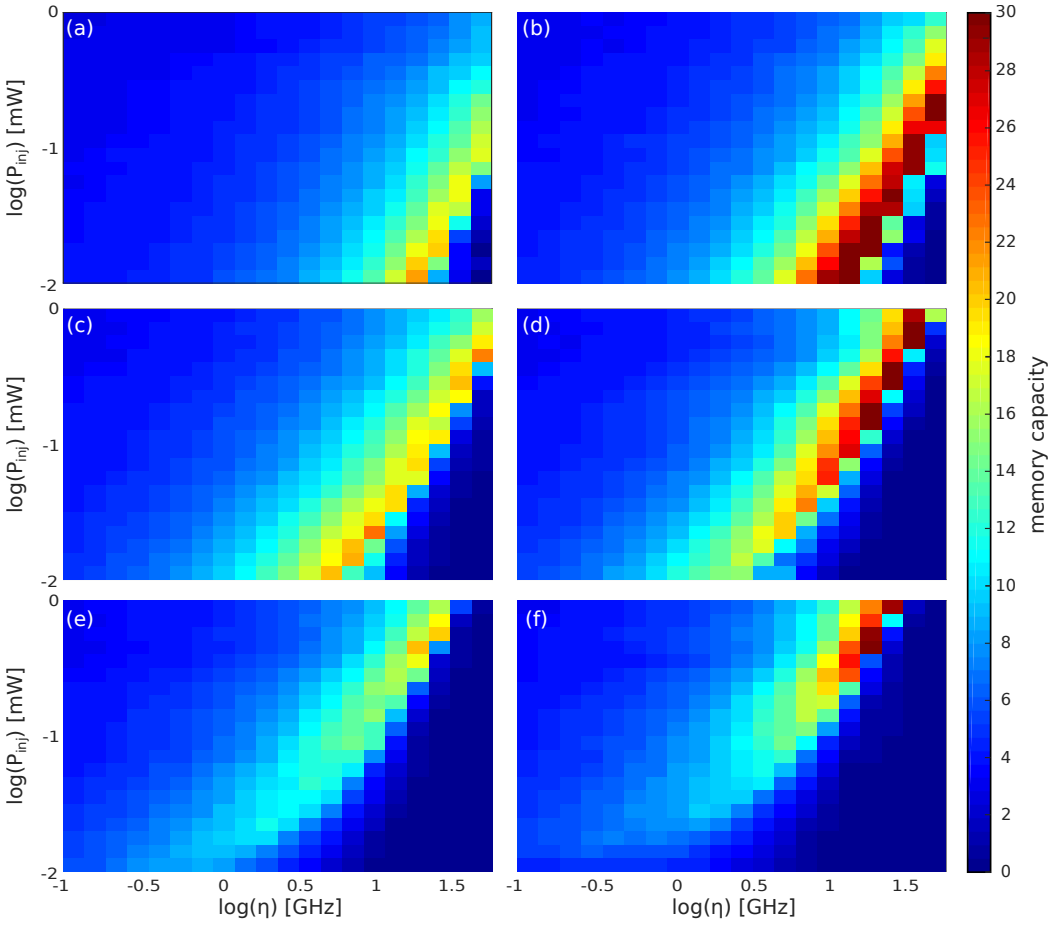

Figure 4.15: Memory capacity depending on the injection power P_{inj} and the feedback strength η for (a) $\alpha = 1$, (b) $\alpha = 2$, (c) $\alpha = 3$, (d) $\alpha = 4$, (e) $\alpha = 5$, (f) $\alpha = 6$. $\mu = 1.3$ and $\theta = 0.02$ ns.

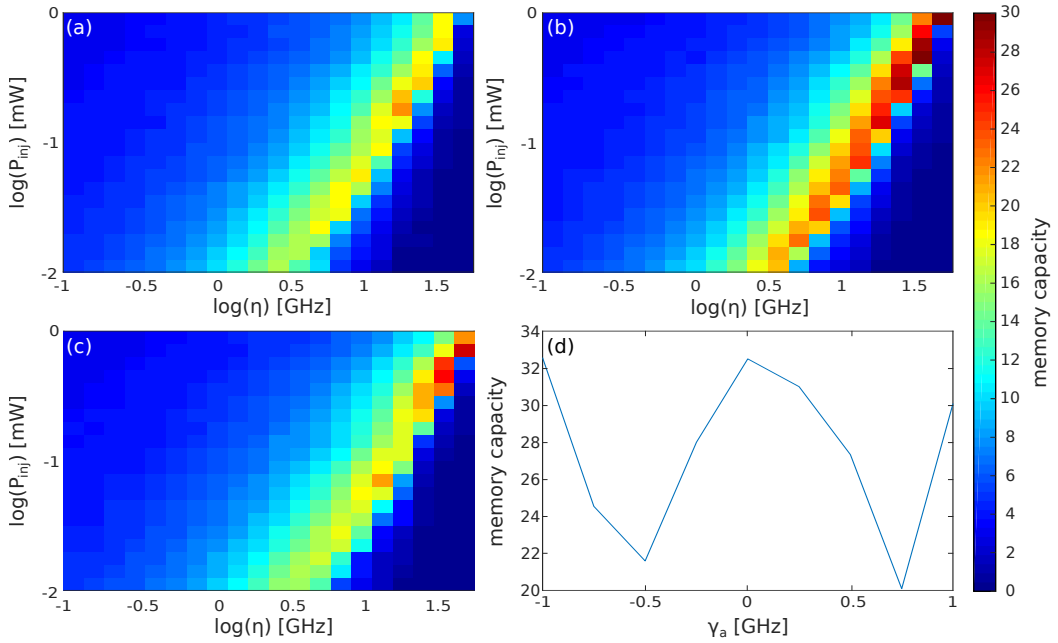

Figure 4.16: Memory capacity depending on the injection power P_{inj} and the feedback strength η for (a) $\gamma_a = -0.5$ GHz, (b) $\gamma_a = 0$ GHz, (c) $\gamma_a = 0.5$ GHz. $\mu = 1.3$ and $\theta = 0.02$ ns. (d) Best achievable memory capacity depending on γ_a

Finally, we study the influence of γ_p on the memory capacity. The results are presented in Fig 4.17. This parameter is directly related to the frequency difference between the two polarization modes (LP_x) and (LP_y), leading to a frequency difference of γ_p/π [157]. Figures 4.17.(a)-(f) present the maps of memory capacity for different values of γ_p, and Fig. 4.17.(g) presents the evolution of the best achievable memory capacity depending on γ_p. The memory capacity seems to oscillate while sweeping γ_p. However, the memory capacity tends to increase as γ_p increases. The memory capacity thus oscillates when sweeping γ_p, while globally increasing with γ_p.

4.2.3.3 Applied performance of the system

We will present in this section the performance of the reservoir on benchmarking tasks. Considering the numerical results already obtained, we will consider $\theta = 0.02$ ns and $\mu = 1.3$. The results will be presented depending on the feedback strength η and the injected power P_{inj}. We will also compare the performance of the reservoir when using either isotropic or rotated feedback configuration. We will test our reservoir computer with the Santa-Fe chaotic series prediction task. Yet the system is rather suitable to perform telecommunication tasks, as explained at the beginning of this section. This is why we also present the performance on nonlinear channel equalization task, using either the WIFI channel or the optical fiber channel.

We fist present the results for the Sante Fe time series prediction. We use separately

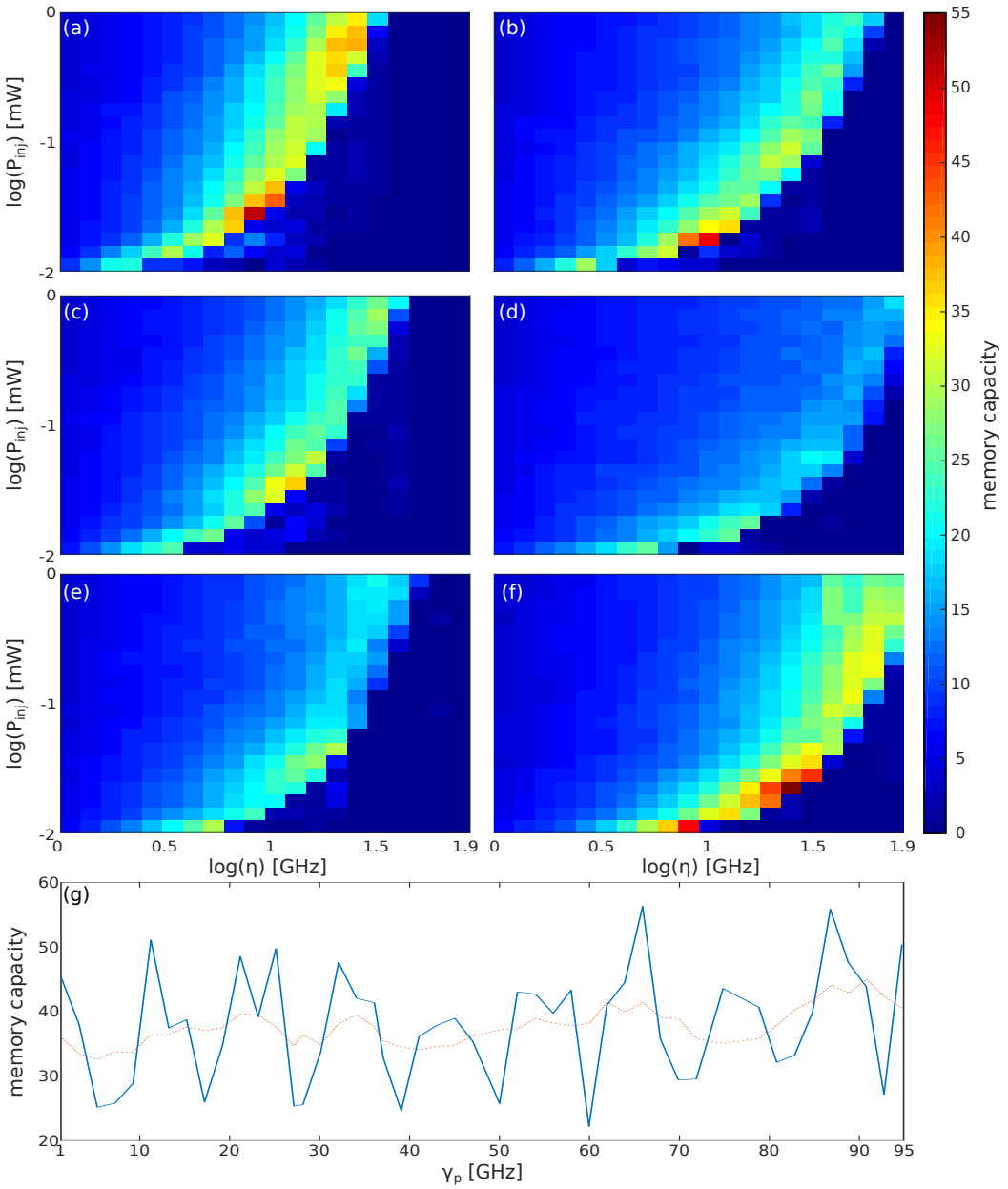

Figure 4.17: Memory capacity depending on the injection power P_{inj} and the feedback strength η for (a) $\gamma_p = 11$ GHz, (b) $\gamma_p = 21$ GHz, (c) $\gamma_p = 41$ GHz, (d) $\gamma_p = 50$ GHz, (e) $\gamma_p = 70$ GHz, (f) $\gamma_p = 87$ GHz. $\mu = 1.3$ and $\theta = 0.02$ ns. (f) Best achievable memory capacity depending on γ_p. The blue line corresponds to the real values, and the red dotted line corresponds to the moving average of the memory capacity.

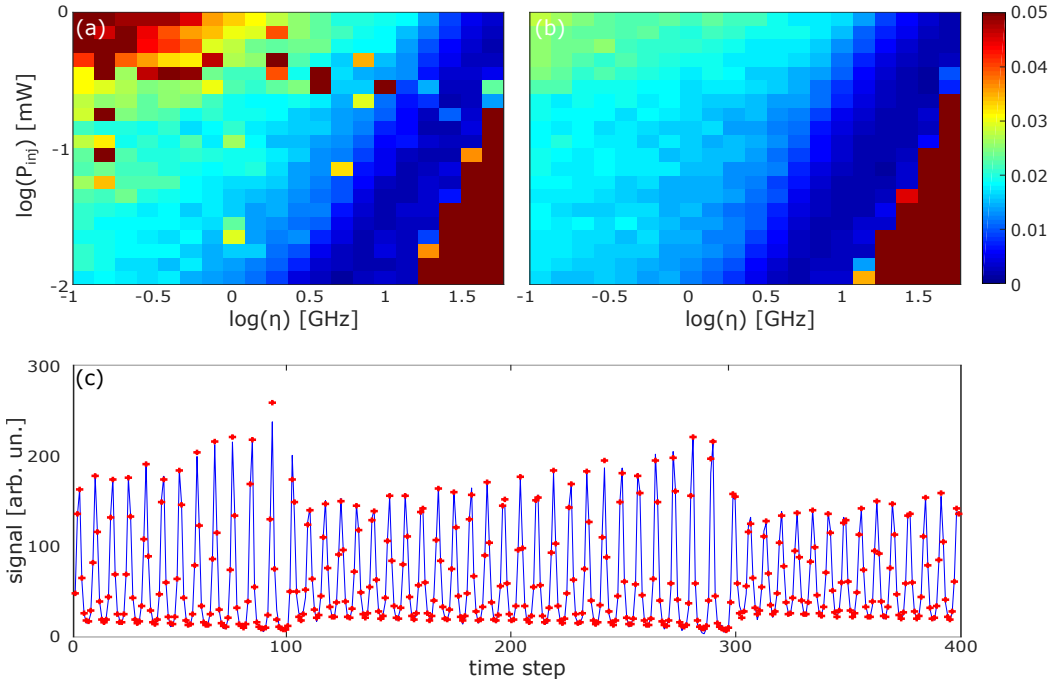

Figure 4.18: Sante Fe time series prediction (a) NMSE after prediction for isotropic injection. (b) NMSE after prediction for rotated injection. (c) Example of prediction of chaotic signal: the original signal(blue) and the predicted signal (red crosses). From [20]

the power of each polarization mode $|E_x^2|$ and $|E_y^2|$ as an output for the reservoir. Therefore, it allows having much information per node. The training is realized with 3,000 samples, and the testing is made with 1,000 samples, using 400 nodes (hence a computational speed of 25 MHz). The NMSE exhibited by the reservoir computer with both feedback configurations are given in Fig. 4.18. We observe that the shape of the region with the best NMSE is similar to the one providing the best computational ability. We are able to reach a NMSE of 5×10^{-3} with the isotropic feedback configuration. In the case of rotated feedback, we are able to decrease further the NMSE to 2×10^{-3}. Figure 4.18.(c) presents an example of prediction in that best case. It seems that the increase of memory capacity helps improving the performance of the reservoir. However, as this task does not require a lot of memory (the next value of the series being highly correlated to the current one), the NMSE is only divided by 2. We can highlight that this performance is the best achieved numerically with an all-optical reservoir computer with optical feedback [11], even if the opto-electronic reservoir is still more accurate [10].

As we design the system for solving telecommunication problems, we have tested the system with nonlinear channel equalization task and we will explore the influence of the feedback configuration on the performance. We assume that using the rotated feedback configuration should provide a better performance, similarly to our previous

observation. Nevertheless, we severely decreased the length of the feedback loop, using only 32 nodes (hence a computational speed of 1.56 GHz). This choice is made to meet the speed requirement of telecommunication networks. We used 20,000 samples to perform the testing since this value is a threshold beyond which the performance of the reservoir on this task does not significantly increase. We used 40,000 samples for the training to record significantly small error rate (up to 2.5×10^{-5}). The performance is presented in Fig. 4.19. We first use a signal without noise, and we study the influence of three different configurations:

- isotropic feedback using the total emitted power as a node state,
- rotated feedback using the total emitted power as a node state,
- rotated feedback using separately the emitted power of the two polarization modes. In this last configuration, there are twice more data available since each node is represented by two polarization states.

The maps of performance in the $\eta - P_{inj}$ plane in case of a SNR of 28 dB are depicted for the three different configurations in Figs. 4.19.(a)-(c). In each of the three cases, the region providing the best performance corresponds to the one with the best memory capacity. This observation is foreseen as this task requires a lot of memory (cf Sec. 3.4). However, we observe that the region showing the best performance is larger when using the rotated feedback than when using the isotropic feedback. It is even larger when using the two polarization modes separately. With the isotropic feedback, we can reach a minimum SER of 5×10^{-4}, and 1×10^{-4} is achievable with rotated feedback. Further improvement down to 1.5×10^{-5} is possible if training the reservoir computer is done with the two polarization modes separately. We have been able to divide by 5 the SER by optimizing the dynamics linked to the feedback, and to further divide the SER by 10 by exploiting the specificity of the two-modes dynamics of the VCSEL, doubling the number of virtual nodes with a fixed delay-line. The best achieved SER corresponds to state-of-the-art performance, and with the fastest computation speed so far (3.12 Gb/s versus 236 kb/s in for [10]).

This test is commonly realized when degrading the SNR of the received signal. We compare the best achievable SER with the three reservoir configurations as a function of this SNR in Fig. 4.19.(d). As the task gets more complex with a higher SNR, the best achievable SER increases as the SNR decreases. The conclusion drawn without noise remains unchanged: Using rotated feedback improves the performance of the reservoir and using the two polarization modes separately when analyzing the node states further improves the performance.

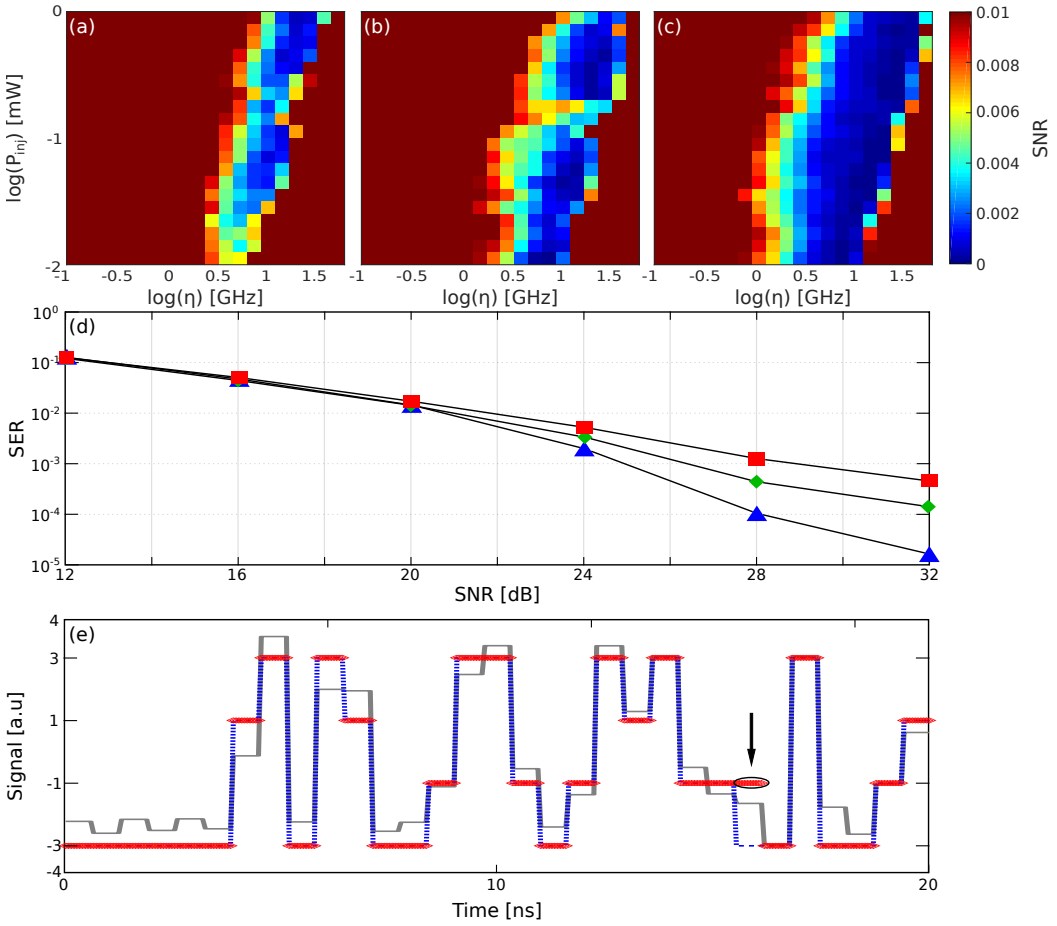

Figure 4.19: Nonlinear channel equalization. The performance of the reservoir is presented as a function of the feedback strength η and the injected power P_{inj} with (a) the isotropic feedback, (b) the rotated feedback configuration using the total emitted power $|E|^2$ as a node state, and (c) with the rotated feedback configuration using separately the emitted power of each polarization mode $|E_x|^2$ and $|E_y|^2$. (d) Symbol error rate for different signal-to-noise ratio. $\square$: single-mode system. $\diamond$: dual mode system using both $|E|^2$. $\triangle$: dual-mode system using $|E_x|^2$ and $|E_y|^2$. (e) Example of reconstruction of a signal with $SNR = 24$ dB: the signal sent in the channel (dotted blue), the non-linearly modified signal at the output of the channel (grey), the reconstructed signal (red). The arrow points to the single error in this data sequence. Adapted from [17]

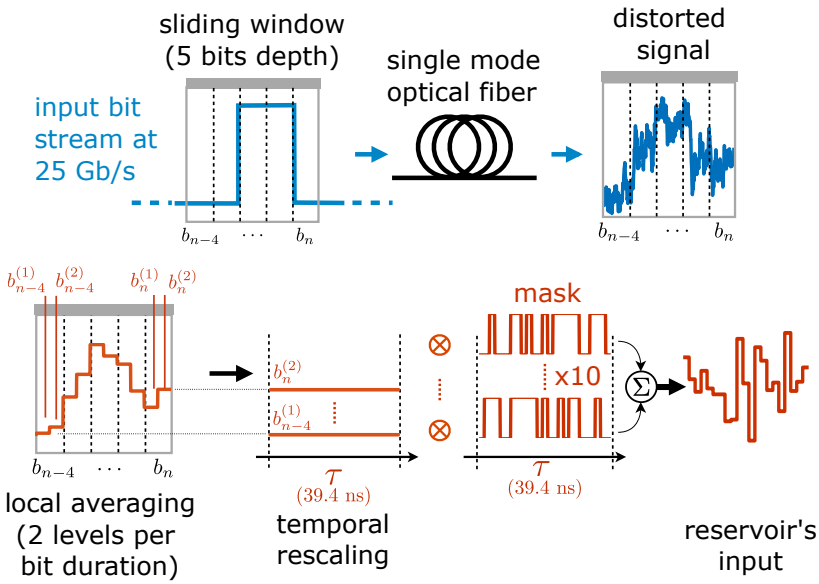

Figure 4.20: Illustration of the preprocessing method for the optical channel equalization, using 5 consecutive bits. The signal at the output of the fiber is averaged at twice the frequency of the input data stream, giving symbols $b_n^{(1)}$ and $b_n^{(2)}$ for each bit b_n. Each symbols is hold during the duration of the delay line τ. The 10 values $b_{n-4}^{(1)}$, $b_{n-4}^{(2)}$, to $b_n^{(1)}$ and $b_n^{(2)}$ are masked with a 10 different masks of N values (resulting in a global mask $10 \times N$ values) and used as an input of the reservoir to reconstruct b_{n-2}

We also tested the influence of different forms of noise in the reservoir: the spontaneous emission noise of the VCSEL β_{sp}, and the detection noise. We used $\beta_{sp} = 4.5 \times 10^{-4}$, and 8-bit quantization noise. In both cases, the performance of the reservoir is globally unchanged with respect to noiseless scenario. It seems that the training of the reservoir compensates the noise produced in the reservoir computer.

We finally changed the nonlinear channel to test our reservoir computer on the recovery of a signal being distorted by an optical fiber, as explained in Sec. 3.4. Considering the results on the compensation of the WIFI distortion, we only compare the performance of the reservoir with isotropic feedback and the one with rotated feedback and using separately the power of the two polarization modes of the VCSEL. Since the signal distortion introduced by the fiber is complex and tends to distribute the information of one bit in to several consecutive bits, the input signal is processed in order to feed the reservoir with the data from these several bits simultaneously, similarly to the method presented in [14]. An illustration of the method is presented in Fig. 4.20. For each bit, we associate two features values $b_n^{(1)}$ and $b_n^{(2)}$, which are the time-average values of the upper half and the lower half of the distorted signal for the duration of one bit. The input of the reservoir is realized by masking each feature value for three consecutive bits, therefore using 6 different masks (one per feature) made of N values,

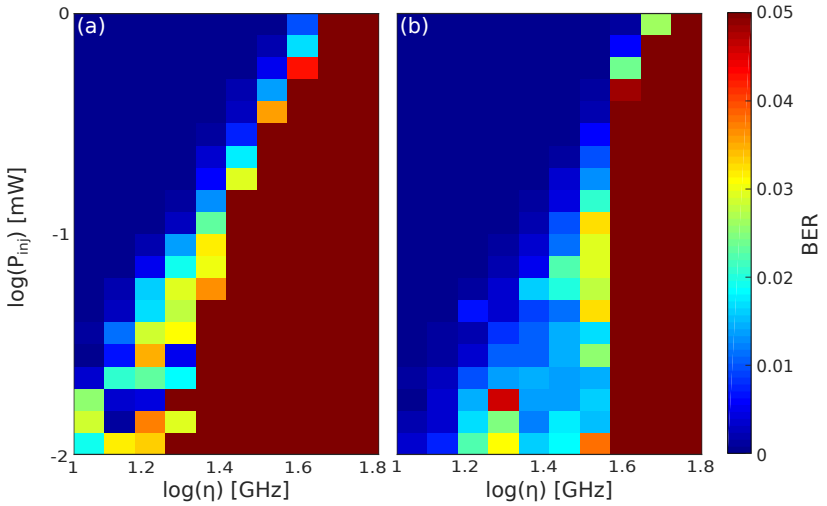

Figure 4.21: Nonlinear optical channel equalization. The BER of the reservoir is presented depending on the feedback strength η and the injected power P_{inj} with (a) the isotropic feedback configuration, (b) the rotated feedback configuration

which are then summed together. The masked input of the reservoir $J_{n-1}(t)$ at the step $n-1$ reads:

$$J_{n-1}(t) = \sum_{i=0}^{2} \left(b_{n-i}^{(1)} \times M_{2i}(t) b_{n-i}^{(2)} \times M_{2i+1}(t) \right), \tag{4.12}$$

where $M_i(t)$ is one of the 6 different masks.

We present in Fig. 4.21 the performance of the reservoir in recovering the signal after propagating over 25 km of fiber for the two configurations of feedback. The training has been performed using 20,000 samples and the testing with 40,000 samples. It appears that the reservoir is able to recover perfectly the signals without any error with both isotropic and rotated feedback. We nevertheless observe that the region providing zero error is larger in the case of rotated feedback than in the case of isotropic feedback. This observation is consistent with what we observed for the WIFI nonlinear channel equalization. However, this task is not complex enough to conclude for sure that the reservoir computer with rotated feedback brings better performance than with isotropic feedback.

We thus perform a more complex task by recovering a signal after 50 km of fiber. As previously, the training set is made of 20,000 samples, and the testing set of 40,000 samples. Figure 4.22.(a) presents the performance of the reservoir with isotropic feedback; we observe that the location of the area providing the best performance is similar to the one obtained when recovering WIFI signals. The best performance achieved with this configuration of feedback is a BER of 2×10^{-2}. For rotated feedback,

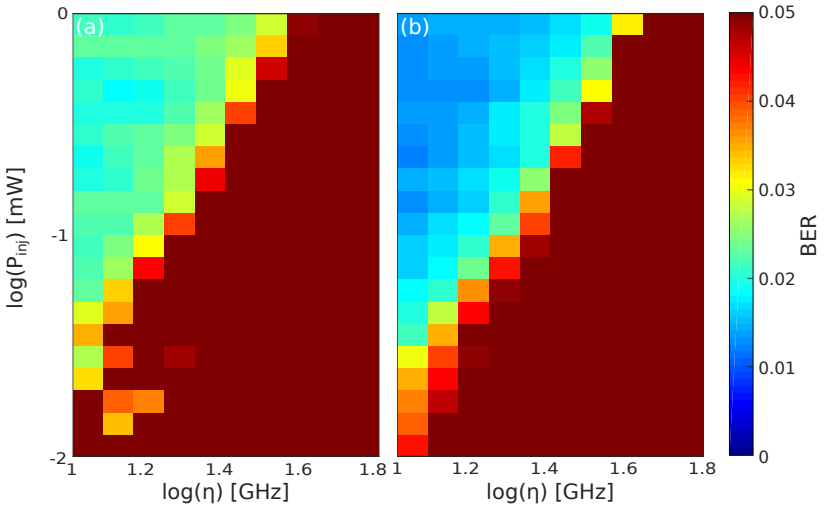

Figure 4.22: Nonlinear channel equalization. The BER of the reservoir is presented depending on the feedback strength η and the injected power P_{inj} with (a) the isotropic feedback configuration, (b) the rotated feedback configuration

the region providing the best BER is slightly shifted toward higher feedback strength (see in Fig 4.22.(b)). The best SER achieved with this configuration of feedback is 1.25×10^{-2}. The results obtained with this task lead to the same conclusion to that of the WIFI channel equalization task: polarization rotated feedback improves the performance of the reservoir.

4.3 Experimental results

The numerical simulations in the previous section 4.2.1 have been presented to motivate an experimental realization. The simulations help finding the best operating point for the experimental setup, and also bring insight into the experimental performance of the system.

In this section, we will detail the experimental setup and the components used, and then present the method used to test the experimental system. The experimental performance will be detailed as well as the comparison with the results obtained numerically.

Most of the results presented in this section have been published in [18].

4.3.1 Presentation of the experimental setup

We first present some pictures of the experimental setup in Fig. 4.23. These pictures

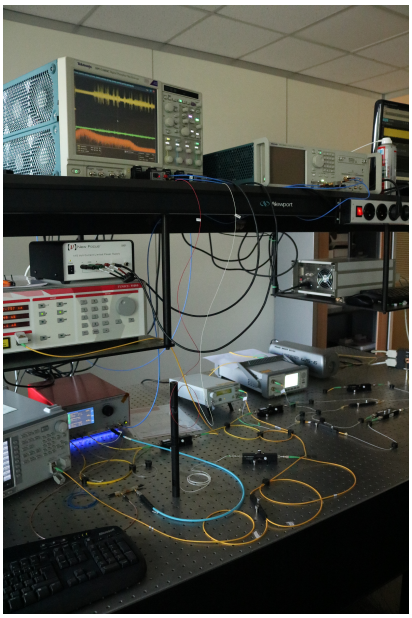

(a) Vertical view of the experimental setup. The oscilloscope and the AWG are on the shelf.

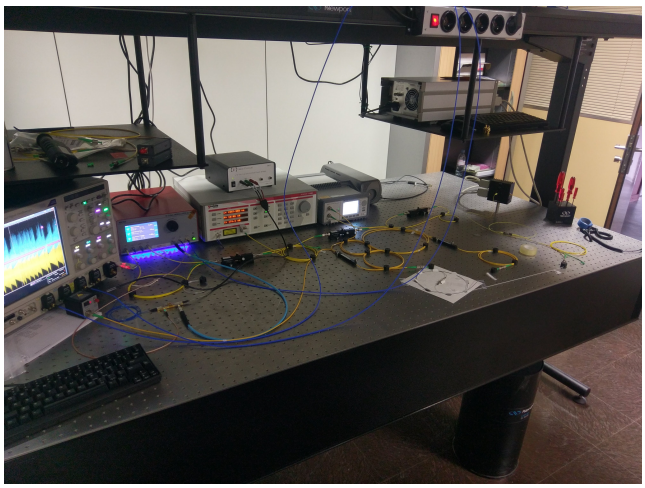

(b) Horizontal view of the setup. The reservoir and the input layer are fixed on the optical table.

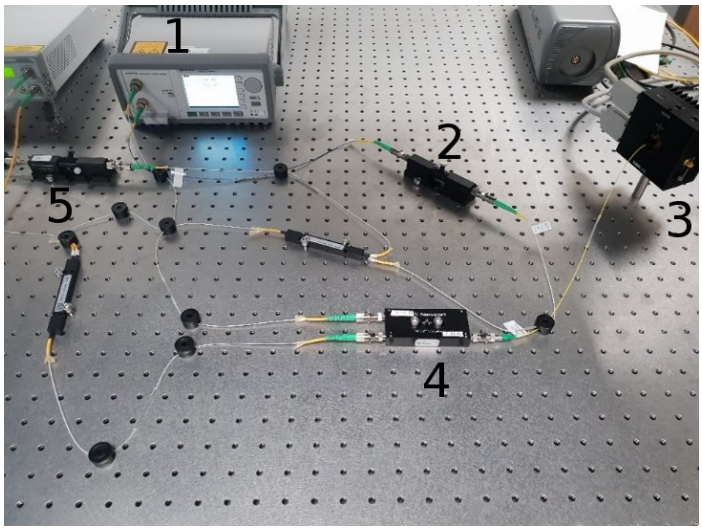

(c) Zoom on the reservoir computer. 1) Variable optical attenuator, 2) Polarization controller, 3) VCSEL, 4) circulator, 5) splitter

Figure 4.23: Pictures of the experimental setup

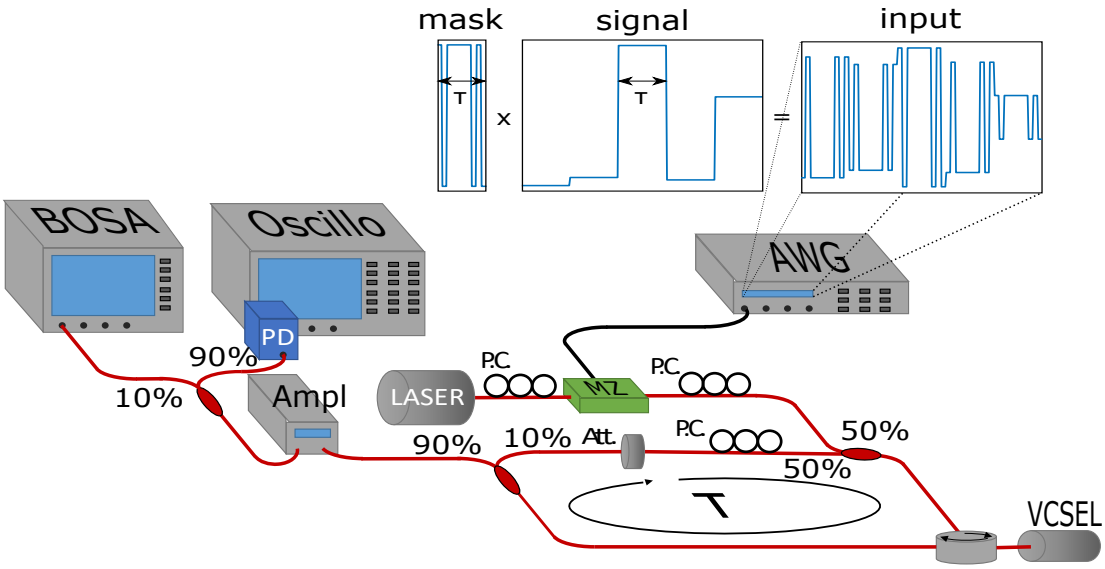

Figure 4.24: Scheme of the setup. The signal loaded in the AWG is made by multiplying the input signal by a mask. MZ: Mach-Zehnder madolator, P.C.: polarization Controller, AWG:Arbitrary Waveform Generator, att: attenuator, Oscillo: Oscilloscope, ampl: amplifier,PD: photodiode, BOSA: brilloin scattering optical spectrum analyser. Adaptated from [18]

show all the components used to realize the experiment. For the sake of clarity, the corresponding scheme is provided in Fig. 4.24.

The reservoir itself, presented in Fig. 4.23.(c), is composed of a VCSEL Raycan RC32xxx1-FFA emitting at 1550 nm and an optical feedback loop. Along the feedback loop, the light travels through an attenuator Keysight 81577A (att), that controls the feedback strength and a polarization controller (P.C.), that adjusts the polarization of the feedback and allows switching between the two different configurations: isotropic or rotated feedback. Because of the optical fiber already present in the packaging of the components used in the feedback loop, the optical delay line is minimum 11.7 m, then the delay-time is minimum 39 ns. This length is reached by cutting at the shortest the fibers of each component. The original length of the delay-line with the original length of fibers was 24 m (80 ns), hence we divided by two the length of the feedback during the shortening process. The length of the delay-line limits the processing speed at 25.6 MHz. According to the simulation realized in the previous section Sec. 4.2.1, the time separation θ between two nodes for this system has to be around 20 ps to provide the best performance. However due to the frequency limitation given by our oscilloscope and our modulator, we have chosen to set this value to $\theta = 100$ ps. This corresponds to the highest frequency we can record with our oscilloscope, *i.e.* a Tektronix DPO 71604C 16 GHz bandwidth, and the fastest modulation speed of our Mach-Zehnder modulator. This leads to $N = 390$ virtual nodes spread along the delay-line.

The input layer comprises a continuous tunable laser Yanista Tunics T100S. Its polarization is adjusted in order to be aligned with the principal modulation axis of a Lithium Niobate Mach-Zehnder modulator. An additional polarization controller (P.C.) is used to control the polarization of the injection. The input signals are numerically generated. The mask is composed of 390 different values (as much as the number of nodes). This mask is built by randomly generating values in {-1; 1}. This mask is then multiplied by the different input values. These signals are loaded in an Arbitrary Waveform Generator (AWG) Tektronix AWG 700002A and generated at 10 GSamples/s and sent to the RF port of the modulator.

The output layer has been modified compared to the numerically simulated system due to power constraints imposed by the low level of optical power emitted by the VCSEL. We thus add an EDFA-amplifier (ampl) in the output layer, to remain above the detection threshold of the electronic equipments. A photodiode (PD) Newport 1544-B 12 GHz bandwidth is connected to the oscilloscope, recording the signal at 50 GSamples/s. The fiber splitter between the feedback loop and the output layer yields 90% of the total power for the detection. The recorded signals are post-processed using a computer. The optical spectrum of the output layer is also measured thanks to a Brillouin scattering optical spectrum analyzer (BOSA). This device allows measuring the optical spectrum of the reservoir with a high resolution of 10 MHz.

4.3.2 Finding the operating point of the reservoir

Realizing a fiber based setup has several advantages, including the easy way of coupling the injecting laser, and connecting with the feedback loop. However, the polarization gets harder to tune, by comparison to a free space experiment, in which the polarization of the light remains fixed along the whole distance of propagation. In the fiber, the polarization rotates randomly and depends on the wavelength and on the room temperature. As a consequence, when we adjust the polarization properties in a fibered setup, we do not set the polarization at the point of the polarization controller, as it is done in free space setup, we rather set the polarization with the polarization controller to ensure that the polarization properties are the right one at the point of interest in the setup. For instance, in our setup, this point of interest is the input connection of the VCSEL. The polarization controllers are used to set properly the polarization properties of the feedback and the injecting laser so that the polarization is the desired one at the input of the VCSEL. There is then a second problem which is due to the fact that we cannot control the polarization properties in the fibered setup directly. This control has to be done thanks to the dynamical analysis: We adjust the polarization until the system exhibits the dynamic behavior corresponding to the desired configuration.

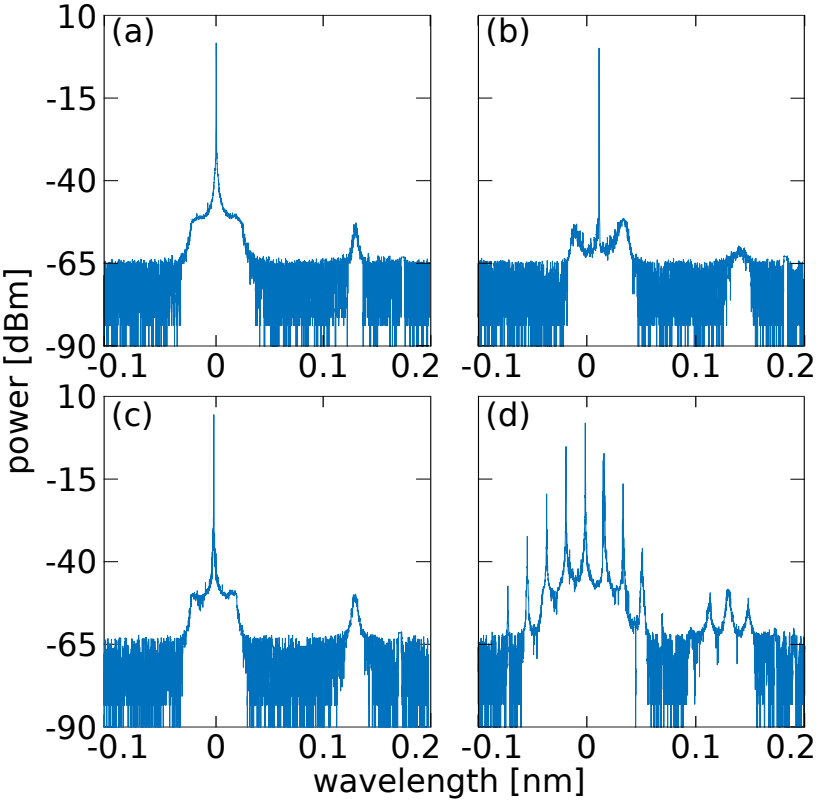

Figure 4.25: Experimental optical spectra in different conditions. (a) free running VCSEL, (b) System with feedback and injection (0.3 mW injection, 18 dB attenuation), (c) VCSEL with parallel feedback, 10 dB attenuation, (d) VCSEL with rotated feedback, 10 dB attenuation. From [18]

We first set the polarization properties of the feedback loop. This setting is done thanks to the optical spectrum that are recorded with the BOSA. Examples of spectrum are given in Fig. 4.25. The x-axis is centered on the wavelength of the main polarization mode of the free running VCSEL, at 1552.88 nm. Figure 4.25.(a) presents the optical spectrum of the free running VCSEL. The temperature of the VCSEL is controlled at 21°C, and the injection current is set at 4.5 mA, which corresponds to 1.5× the threshold current. In these conditions, we observe that the main polarization mode is lasing, and that the depressed polarization mode also emits a small amount of power. The ratio of emission between the two polarization modes is measured to be 54.23 dB, and the detuning between the two polarization modes is measured to be 16.4 GHz. The tuning of the feedback is done by setting the attenuator at the minimum, which is 10 dB in our case. In these conditions, the VCSEL exhibits totally different dynamics when setting isotropic or rotated feedback. We thus use the optical spectrum to adjust the feedback properties. The spectrum in the case of isotropic feedback is depicted in Fig. 4.25.(c). The peak corresponding to the dominant polarization mode of the VCSEL is narrower, and it exhibits two side modes separated from the main peak by a

frequency close to the relaxation oscillation of the VCSEL [158]. The spectrum of the system with rotated feedback is given in Fig. 4.25.(d). The VCSEL in this case exhibits several optical frequencies in the two polarization modes. The fact that the different peaks are equally separated is typical of the time-periodic dynamics of VCSELs. This means the first bifurcation has already been crossed. Once the polarization of the feedback is set, we can increase the feedback value to its best operating value. We set the total attenuation at 18 dB. According to the numerical results shown in Sec. 4.2.1, there is a best operating point for each value of the feedback and a corresponding injection power.

We then set the polarization of the input signal. This is done by sending a modulated input in the laser and tuning the polarization of the input signal to maximize the response of the VCSEL. We finally have to set the injection power P_{inj} and the detuning $\Delta\nu$. We concluded from the numerical results that the VCSEL needs to be locked to the master laser, at the edge of the parameter region leading to chaos. There are then two solutions two reach this operating point:

1. Set the injection power first and then sweep the detuning until destabilizing the VCSEL. We set the detuning at the smallest value producing a stable dynamics

2. Set the detuning and decrease the injection power until destabilizing the VCSEL. We choose the smallest value of injection strength producing the stable dynamics.

We choose the first option to set the parameter. We first set the injection power at $P_{inj} = 0.3$ mW (corresponding to 50 μW at the surface of the VCSEL), which leads to a detuning of $\Delta\nu = 1.05$ GHz. Figure 4.25.(b) shows the spectrum of the reservoir at its operating point. We observe that the VCSEL is locked on the master laser since the dominant polarization mode exhibits a narrow peak which is detuned with respect to the free running mode [159]. The power emitted by the depressed polarization mode is reduced.

We finally present experimental signals in Fig. 4.26. Figure 4.26.(a) presents an input signal. It is made by modulating the mask with the consecutive values in the input series. Figure 4.26.(b) presents the corresponding output of the reservoir. This complex response contains the states of the different nodes.

4.3.3 Performance of the experimental system

In this section, we will prove experimentally that the reservoir with rotated feedback performs better than the reservoir with isotropic feedback. This result will be proved

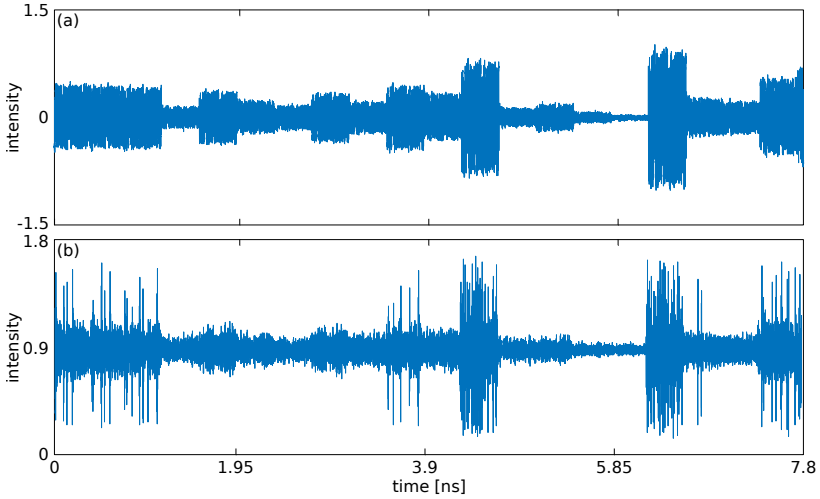

Figure 4.26: Experimental signals. (a) masked signal for the input of the reservoir computer. (b) corresponding response of the reservoir.

by testing the reservoir with several tasks, tuning the experimental setup following the method explained previously.

We have tested this result the Santa Fe time series prediction. We use the total emitted power of the VCSEL as the state for each node (*i.e.* $|E_x|^2 + |E_y|^2$), as we noticed that the low and noisy emitted power in the depressed polarization mode degrades the performance of the experiment. We use 6000 samples to train our system, performed with a linear regression. The 2992 other samples are used for testing. We realized the first test over 3 different trainings and testings for both feedback configurations. In these conditions, we successfully reach a NMSE of 1.9×10^{-2} with isotropic feedback. Performance is slightly better with rotated feedback, with a NMSE of 1.6×10^{-2}. This is also an order of magnitude lower than the results obtained with other laser-based time-delay reservoir computer [136]. An example of prediction is given in Fig. 4.27: the reservoir is able to predict the time series with only a small deviation from the target signal even for the small amplitude values, thus leading to a low relative error. As we explained in Chap. 3, this task is highly sensitive to the signal-to-noise ratio (SNR). Considering this fact, we assume that the performance we reach is related to the SNR we can achieve experimentally, which is estimated at about 12 dB. We have realized a larger study with additional training iterations to draw more precise statistics on the performance of the reservoir computer on the Santa Fe prediction task. The mask is different for each iteration. The results obtained over 50 realizations are presented in Fig. 4.28. We observe that for isotropic feedback, the reservoir is able to provide a NMSE between 0.01 and 0.06, with a mean NMSE at 0.036. The NMSE reached in the case of rotated feedback is lower, and is dispatched between 0.005 and 0.065, with a mean NMSE at 0.033. Even if the difference of performance is relatively small, the reservoir made with the rotated feedback configuration allows reaching a lower

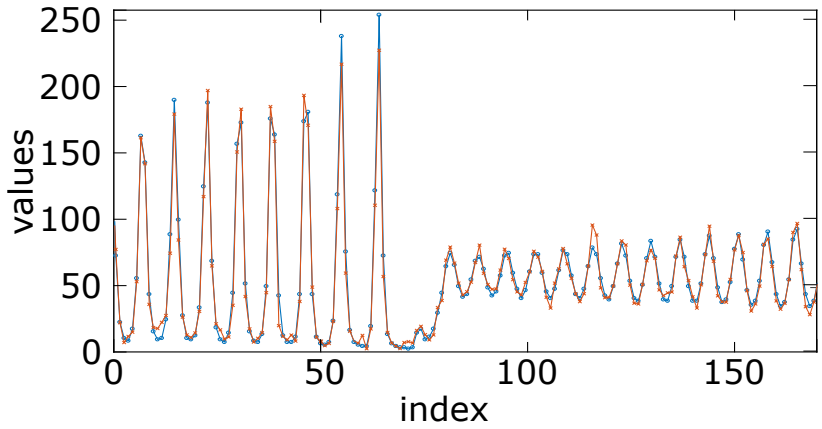

Figure 4.27: Example of Santa Fe series prediction: the original Santa-Fe series (blue line and circles), and the predicted series (red line and crosses). Adapted from [18]

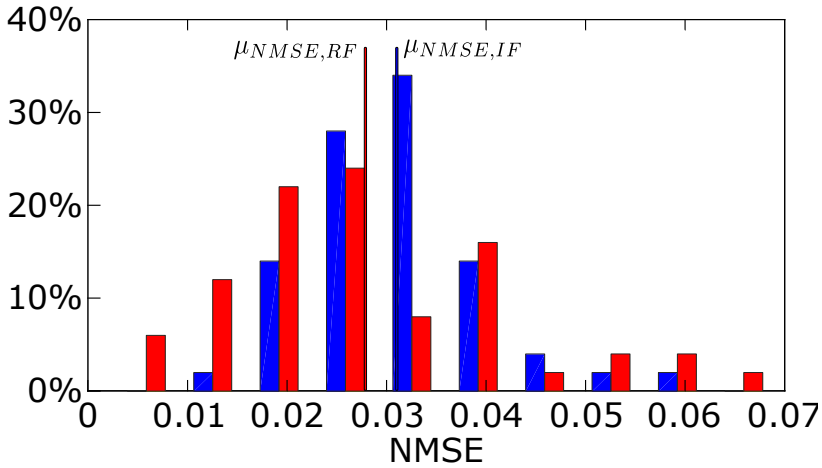

Figure 4.28: Histogram presenting the NMSE obtained with the reservoir with isotropic feedback configuration (blue) and rotated feedback configuration (red) on the Santa Fe prediction task over 50 repetitions. The mean values obtained with isotropic feedback ($\mu_{NMSE,IF}$) and with the rotated feedback ($\mu_{NMSE,RF}$) are represented with the thinner lines.

NMSE. We can also observe that in running a larger study, the NMSE is significantly higher than the first results obtained. This is mostly due to the fact that with further iterations, the statistics also takes into account the fluctuation of the dynamics of the system.

We have also tested our experimental setup with telecommunication tasks, which are more complex tasks. We first tried the recovery of WIFI signals. The training is realized with 10,000 samples, and the testing on 5,400 samples, using as previously the total emitted power by the VCSEL. The results over nine different trainings for each configuration of the feedback are presented on Fig. 4.33.(b). The mask is different for each iteration. The mean SER obtained with the rotated feedback configuration ($\mu_{SER,RF}$) is 1.5%, which is lower than the mean SER obtained with the isotropic configuration ($\mu_{SER,IF}$), that has been measured to be 1.9%.

Considering the low SNR we can reach and the small number of repetitions we have to compute the mean performance, these results have been statistically analyzed with a one-sided t-test with a significance level of $\alpha = 2.5\%$ to compare the averaged SER obtained from series of SER measurement realized in the isotropic ($\mu_{SER,IF}$) and polarization-rotated feedback ($\mu_{SER,RF}$) configuration, respectively. The null hypothesis H_0: $\mu_{SER,IF} = \mu_{SER,RF}$ is tested against the alternative hypothesis H_1: $\mu_{SER,RF} < \mu_{SER,IF}$. We first confirm the normality of the data using a Kolmogorov-Smirnov test [160] and then apply the t-test. We find that the statistics of interest computed from the data (and following a Student's distribution with 15 degrees of freedom) belongs to the rejection region of the test : $(-\infty, -2.131]$. As a result, we reject H_0 in favor of H_1 with significance level $\alpha = 2.5\%$. This implies that we have strong statistical evidence in this low-SNR situation that the polarization rotated feedback allows smaller SER in the nonlinear channel equalization task.

We also provide an example of reconstruction in Fig. 4.33.(a). It shows a sample of the target signal and the estimated signals, in a case exhibiting a SER of 1.1%. In this sample there is only one missreconstructed symbol.

As for the Santa Fe prediction task, we run a larger study, with more realizations to confirm the statistical analysis. The results are presented in Fig. 4.30. We observe that for isotropic feedback, the reservoir provides a SER between 0.015 and 0.04, with a mean SER at 0.0245. The SER reached in the case of rotated feedback is lower, and is scattered between 0.01 and 0.03, with a mean SER at 0.021. We observe that the difference between the SER obtained with the rotated feedback configuration and the one obtained with the isotropic feedback configuration is similar to the separation obtained in the previous study, even if the averaged performance is slightly worse. The reservoir with the rotated feedback configuration reaches a lower SER.

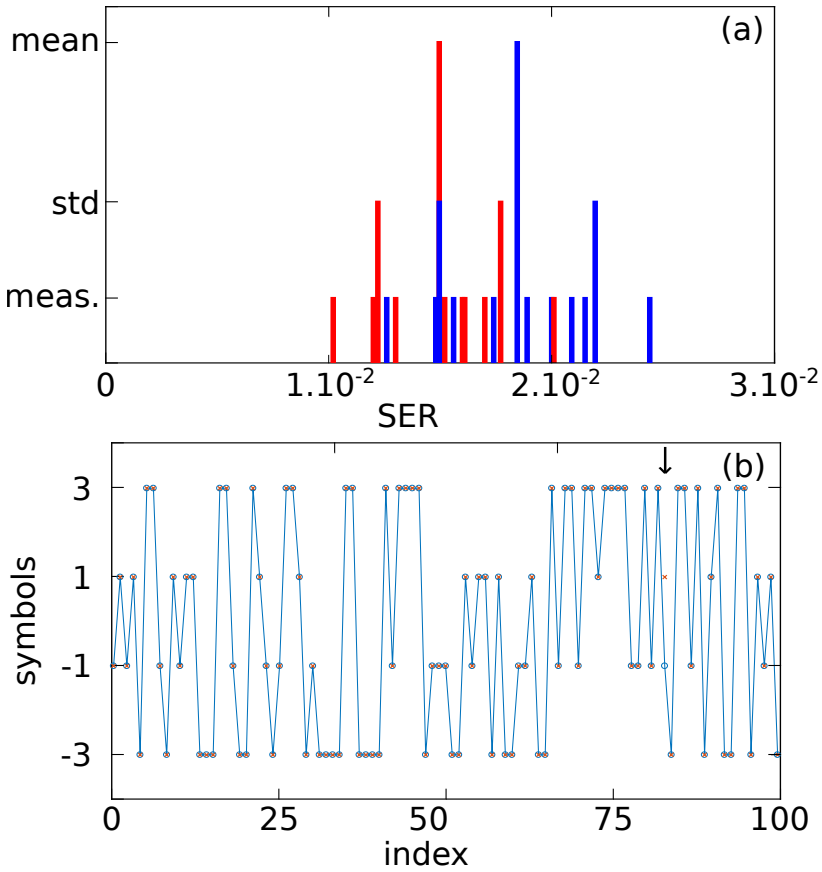

Figure 4.29: Results for channel equalization task. (a) Experimental results: The shortest strips shows the different SER obtained over different measurement series, the biggest strips shows the mean value, for the parallel feedback (blue) and the perpendicular feedback (red). (b) Experimental prediction for the channel equalization task: the target signal (blue lines and circles) and the predicted signal (red crosses) in case of polarization rotated feedback. arrow points out the error. Adapted from [18]

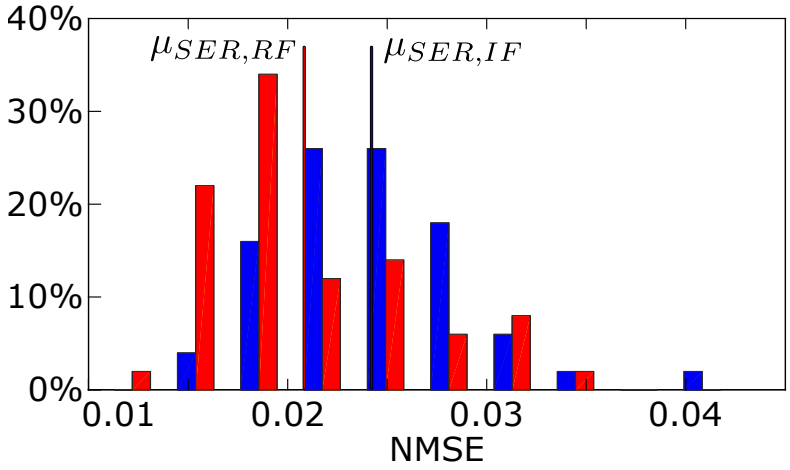

Figure 4.30: Histogram presenting the SER obtained with the reservoir with isotropic feedback configuration (blue) and rotated feedback configuration (red) on the wifi channel equalization task over 50 repetitions. The mean values obtained with isotropic feedback ($\mu_{SER,IF}$) and with the rotated feedback ($\mu_{SER,RF}$) are represented with the thinner lines.

Finally, we performed the optical telecommunication channel equalization with our reservoir in both feedback configurations. We still use the total emitted power as the state of one node, and we use 20,000 samples for the testing, and 5,380 for the testing. The signal has been preprocessed using the same method as the one used for the numerical simulations, using the data over 5 consecutive bits instead of 3 bits. The results over 50 realizations are presented in Fig. 4.31, for the equalization of 25 km and 50 km of fiber. The histogram showing the performance obtained when recovering the signal at the output of 25 km of fiber is presented in Fig. 4.31.(a). The system exhibits a BER between 10^{-4} and 1.4×10^{-3}, with a mean BER at 6×10^{-4}, in the case of the isotropic feedback configuration. For the rotated feedback configuration, the reservoir is able to recover the signal without any mistake. We conclude that the error provided in thus below 2×10^{-4}, as the testing is realized with 5380 samples. An example of prediction in this case is provided in Fig. 4.32. There is a real enhancement in rotating the polarization of the feedback. The performance of the recovery of a signal after 50 km is presented in Fig. 4.31.(b). The mean BER exhibited by the reservoir with a rotated feedback is at 7×10^{-3}, compared to 1.5×10^{-2} with isotropic feedback. The same conclusion therefore holds for the equalization of 50 km of fiber when compared to the equalization of 25 km of fiber and is even clearer. We also observe that the two histograms are clearly separated, which supports statistically the fact that the rotated feedback configuration enhances the performance of the reservoir.

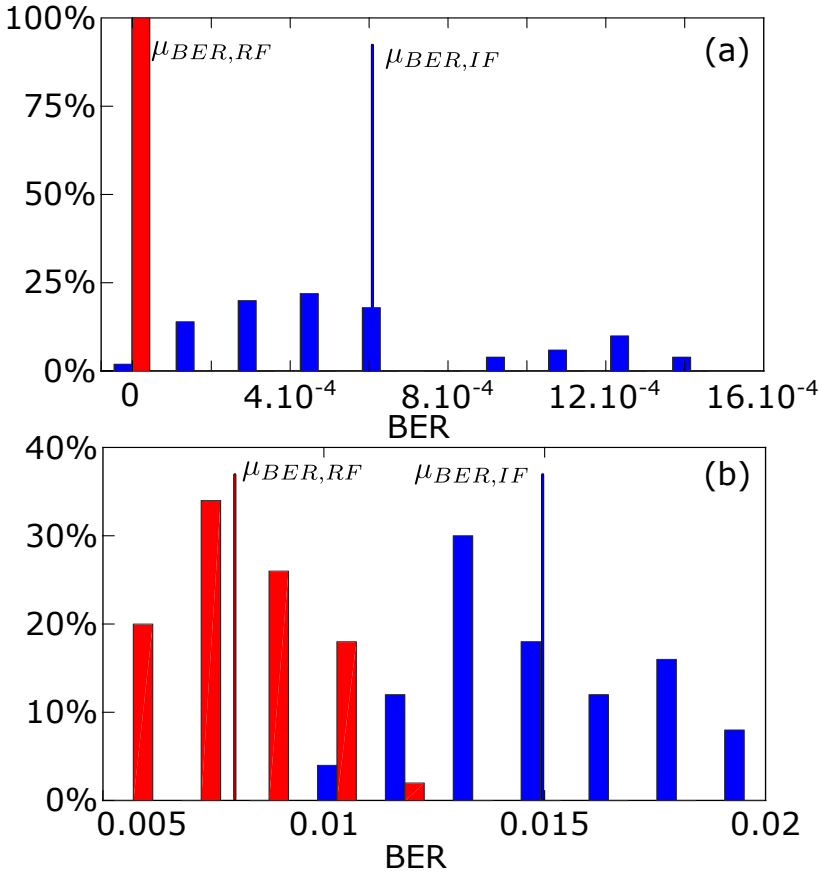

Figure 4.31: Histogram presenting the BER obtained with the reservoir with isotropic feedback configuration (blue) and rotated feedback configuration (red) on the optical channel equalization task over 50 repetitions using (a) 25 km of fiber and (b) 50 km of fiber. The mean values obtained with isotropic feedback ($\mu_{BER,IF}$) and with the rotated feedback ($\mu_{BER,RF}$) are represented with the thinner lines.

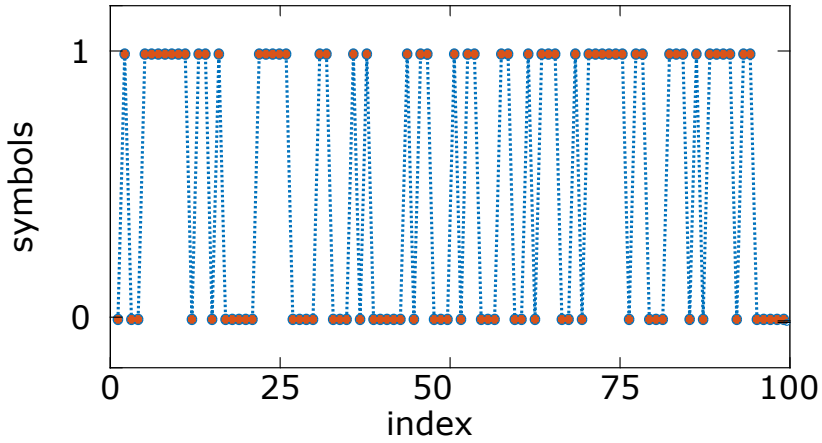

Figure 4.32: Experimental prediction for the optical channel equalization task for a 25 km-long fiber: the target signal (blue lines and circles) and the predicted signal (red crosses) in case of polarization rotated feedback.

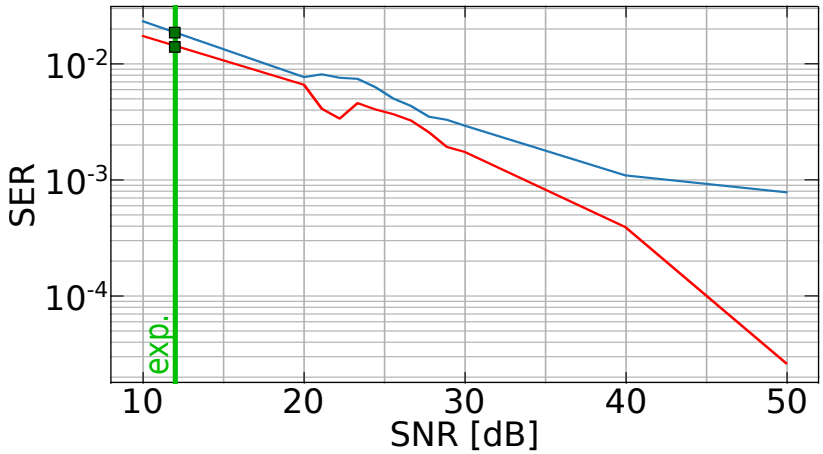

Figure 4.33: Histogram presenting the SER obtained depending on the level of noise in the output layer of the reservoir with the reservoir with isotropic feedback configuration (purple) and rotated feedback configuration (yellow) on the wifi channel equalization task over 50 repetitions. The mean values obtained with isotropic feedback ($\mu_{NMSE,IF}$) and with the rotated feedback ($\mu_{NMSE,RF}$) are represented with the thinner lines. Adapted from [18]

4.3.4 Link between numerical and experimental results

The numerical simulations have been realized taking into account the devices available to realize experimentally the reservoir computer. However, we notice that the performance obtained with the experimental setup is significantly lower than the theoretical prediction. This is mainly due to the lack of modeling of the many noise sources, especially the noise in the output layer, which is caused by the amplifier. We thus run other simulations to have an insight of the influence of the noise in the output layer of the reservoir. The performance on the WIFI channel equalization task is depicted in Fig. 4.33 depending on the noise in the output layer for both configurations of feedback. The first observation is expected: increasing the SNR in the output layer leads to a better performance of the reservoir computer. We presented in the last section that the SNR in our reservoir was around 12 dB which is really low. Yet if we compare the performance given by the numerical simulations at 12 dB and the experimental results, we notice that the results are matching. It provides supportive evidence of that the model we were using to produce the preliminary results is suitable to simulate the behavior of the experimental system.

We can also compare the performance obtained with the nonlinear optical channel equalization. Recovering the signal after 25 km of optical fiber seems to be an easy task. When considering the reservoir with polarization rotated feedback, both the simulated and experimental systems provide a perfect recovery of the signal. However, in the case of isotropic feedback, the experimental system shows a remaining error.

The comparison is more surprising when recovering the signal after 50 km of fiber: We observe that for both numerical and experimental results, the polarization rotated feedback case exhibits a better SER compared to the isotropic feedback case. However, with both configurations of feedback, the experimental results outperform the numerical results. We can think that, due to the complexity of the task, adding noise to the output of the reservoir simplifies the processing of the task.

4.4 Conclusion

To conclude, we have presented in this chapter the performance of a time-delay VCSEL based reservoir computer. We studied how to harness the polarization dynamics of the VCSEL to enhance the performance of a reservoir computing device. We first presented numerical simulations of the system, which brought a first insight of the intrinsic and applied performance of the reservoir. These results have been confirmed experimentally afterwards. Thanks to the experimental and numerical results, we have been able to prove that the rotated optical feedback configuration improves the computational performance of the reservoir, compared to other configurations of optical feedback, and that we can access twice more information for the same number of nodes with rotated feedback, improving further the performance of the reservoir. The model has finally been confronted to the experimental findings.

We have studied in this chapter how to use the specific polarization dynamics to enhance the performance of the reservoir. However, we could imagine that we would also take advantage of the two-mode dynamics of the VCSEL to speed up the processing. This point will be discussed in the next chapter.

5

Performance of VCSEL-based time-delay reservoir computing device on multi-task processing

- Tu sens quelque chose de bizarre toi ?

- Bizarre, peut-être pas. Je dirais plutôt cocasse ou simplement inattendu, voire impromptu, quoiqu'un tantinet insolite disons-le, dans la mesure du saugrenu, tout en étant singulièrement fantasque, presque excentrique si l'on y songe, et qui sait ? Extravagant en diable...

- Caracole ! Alain Damasio, *La Horde du Contrevent*

Contents

5.1 Time-delay reservoir and dual task processing 102

5.2 Numerical simulations 103

5.2.1 Presentation of the new model 103

5.2.2 Memory properties of the system 106

5.2.3 Applied performance of the system 109

5.3 Experimental results 114

5.3.1 Presentation of the complete experimental setup 115

5.3.2 Preparing the setup to perform computation 119

5.3.3 Experimental performance 120

5.3.4 Comparison numerical and experimental results 126

5.4 Conclusion 126

We detailed until now how to perform computation of a single task with a VCSEL-based time-delay reservoir computer. The main conclusion is that we can get benefits from the polarization dynamics of the VCSEL to improve the computational performance of the reservoir device.

However, we can also imagine using the multimode polarization dynamics to perform several tasks simultaneously (one task per mode for instance). We will study more in depth this possibility in this chapter.

The results presented in this section have been published in [19].

5.1 Time-delay reservoir and dual task processing

The idea of using the multimode dynamics for optical computing is relatively novel and has been studied theoretically with only few photonic device. The first architecture reported performing two tasks simultaneously was a time-delay reservoir computer using an edge emitting laser as a physical node [136]. Two tasks are injected simultaneously in the reservoir by modulating the bias current of the laser, and injecting a modulated optical beam in the cavity. The experimental setup was able to recognize two series of spoken digit recognition with an error rate of 0.014% for the task injected optically and 0.64% for the task injected electrically.

In 2015, R. NGuimdo *et al.* proposed a reservoir computer using a semiconductor ring laser as a physical node [13]. Each task is processed by either the clockwise or counterclockwise mode of the laser. The system is used to perform either the Santa Fe prediction task (best NMSE at 4×10^{-2}) or the nonlinear channel equalization (best SER at 10^{-3}). That work also studies the influence of coupling the two modes through the feedback on the computational performance of the reservoir. They concluded that coupling the two modes creates interferences between the two tasks, and therefore decreases the performance.

Even more recently, it has been reported a time-delay reservoir computing architecture performing two tasks simultaneously, using two longitudinal modes of a semiconductor laser [161]. This system has been used to perform in parallel two Santa Fe prediction tasks, each task being encoded in a different longitudinal mode of the laser. This system is able to reach a NMSE below 0.01.

We will thus present in this chapter our proposal to perform multi-tasking using the multimode dynamics of the VCSEL.

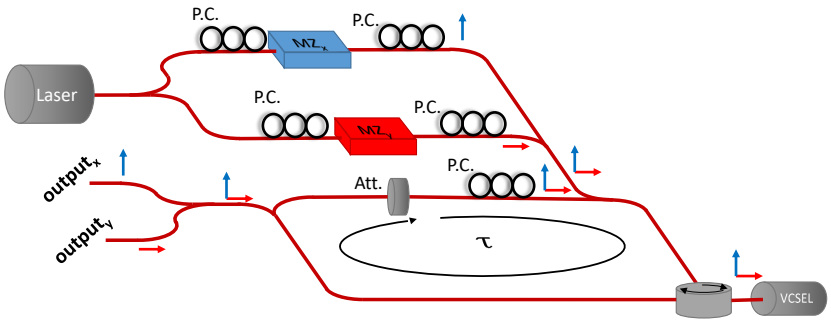

Figure 5.1: Scheme of the setup. The dominant (depressed) polarization mode is represented by the blue (orange) arrow. The polarization controller in the feedback loop preserves the polarization state along the fiber. The ones in the input layer are used to align the polarization of both signals with the dominant and depressed polarizations of the VCSEL. MZ: Mach-Zehnder modulator, P.C.: polarization controller, att.: attenuator

5.2 Numerical simulations

We will in this section present the new model and the numerical performance of the reservoir computing system performing simultaneously two tasks.

5.2.1 Presentation of the new model

The system we are now considering is presented in Fig. 5.1. We consider a system identical to the one of the previous chapter. The reservoir is still composed of the VCSEL and a delay line. The output layer also remains the same: the powers of each polarization mode of the VCSEL are recorded separately. The input layer is however slightly different. The power emitted by the master laser is split in two, in order to be modulated by two Mach-Zehnder separately. The two Mach-Zehnder modulators are fed with the input data of two different tasks. The polarization of each signal at the output of the Mach-Zehnder modulator is finally aligned with each polarization mode of the VCSEL. We use the SFM model with two terms of injection and one term of feedback to simulate this system:

$$\begin{aligned}
\dot{E}_x &= \kappa(1+i\alpha)[(N-1)E_x+inE_y] - (\gamma_a+i\gamma_p)E_x \\
&\quad +\Phi_x(t)+\kappa A_{inj_x}(t)e^{(\omega_{inj}-\omega_0)t}, && (5.1)\\
\dot{E}_y &= \kappa(1+i\alpha)[(N-1)E_y-inE_x]+(\gamma_a+i\gamma_p)E_y \\
&\quad +\Phi_y(t)+\kappa A_{inj_y}(t)e^{(\omega_{inj}-\omega_0)t}, && (5.2)\\
\dot{N} &= -\gamma_N[N-\mu+N(|E_x|^2+|E_y|^2)+in(E_yE_x^*-E_xE_y*)], && (5.3)\\
\dot{n} &= -\gamma_s n-\gamma_N[n(|E_x|^2+|E_y|^2+iN(E_yE_x^*-E_xE_y^*)], && (5.4)
\end{aligned}$$

VCSEL parameters	values
κ	300 GHz
α	3
γ_a	-0.1 GHz
γ_p	6 or 50 GHz
γ_N	1GHz
γ_s	10 GHz or ∞
λ	1550 nm

Table 5.1: Values of the VCSEL parameters.

The injected optical field $A_{inj_{x,y}}$ corresponding to the task T_i can be expressed as:

$$A_{inj_{x,y}} = \sqrt{P_{inj_{x,y}}}/2 \times (1 + e^{iS_{x,y}(t)+\Phi_0}) \tag{5.5}$$

where $P_{inj_{x,y}}$ is the power of the tunable laser modulated in the Mach-Zehnder modulator $MZ_{x,y}$ and $S_{x,y}(t)$ is the normalized signal of the input used in the respective modulator, Φ_0 is the bias voltage of the modulator.

We will test our reservoir with rotated and isotropic feedback configurations, as done in the previous chapter. However, R. Nguimdo *et al.* proved in his work that crossing the modes of the laser along the feedback (and therefore increasing the mixing of the two tasks) reduces the performance of the reservoir. We thus assume that the isotropic feedback should provide better performance than the rotated feedback here.

We will keep the same values for the parameters of the VCSEL as in Sec. 4.2.1 except for the decay rate influencing the mixing of the two carrier populations with different spin γ_s, and the birefringence of the active layer γ_p. Indeed, we want to infer the influence of the coupling of the two polarization modes inside the VCSEL and therefore choose different values of these two parameters. γ_p can take its value in {6 GHz; 50 GHz}, and γ_s in {10 GHz; ∞}. As explained in the previous chapter, a lower value of γ_p reduces the frequency difference between the two polarization modes of the VCSEL, and thus increases the coupling between the two polarization modes. A higher value for γ_s leads to a lower coupling between the two polarization modes. Taking $\gamma_s = \infty$ is equivalent to having $\dot{n} = n = 0$, which means having two polarization modes not coupled through spin-flip relaxation mechanisms. A summary of the parameters of the VCSEL used for the simulations is presented in Tab. 5.1.

We will also study in this chapter the influence of the injected power in the main polarization mode P_{inj_x}, the injected power in the depressed polarization mode P_{inj_y}, and the feedback strength η. Since we already presented the performance of the reservoir depending on the injected power and on the feedback strength, we will rather present the influence of the ratio between the two injection powers P_{inj_y}/P_{inj_x}.

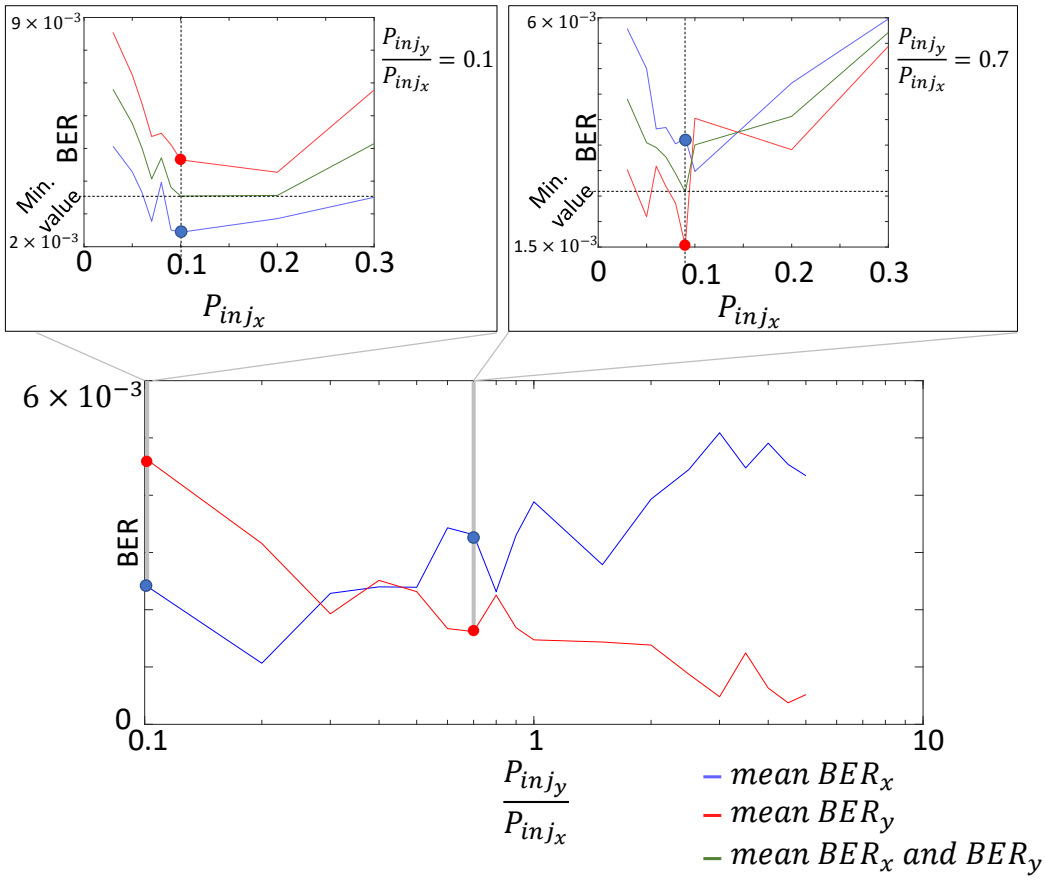

Figure 5.2: Method used to produce the figures. For each value of the ratio of infected power $\frac{P_{inj_y}}{P_{inj_x}}$, we look for minimizing the mean of the BER of both tasks T_x and T_y. We take the values of the BER and report them in the next figures.

However, as this parameter may impact on the best operating point of the reservoir when varying the injected power and the feedback strength, we run each simulation with a sweep of both η and P_{inj_x}. The value of P_{inj_y} is fixed by the ratio. The best performance is kept and reported in our figures. We consider that the best performance corresponds to the one maximizing the performance on both tasks simultaneously. The method is illustrated in Fig. 5.2.

We assume that as the inter-delay θ between virtual nodes, and the bias current μ is relative to the dynamics of the VCSEL. Processing two tasks instead of one will not change the values of these two parameters that leads to the best operating point. Hence, we keep $\theta = 0.02$ ns and $\mu = 1.3$ as found in the previous chapter.

Since processing two tasks simultaneously is more complex, we will choose to use separately the emitted power of each polarization mode $|E_x|^2$ and $|E_y|^2$ to maximize the number of features for the training. The training is realized by building the state matrix S with the optical power of the two polarization modes $|E_x|^2$ and $|E_y|^2$ for

each neuron, as follows:

$$S = \begin{bmatrix} |E_{x,1}^{(1)}|^2 & \cdots & |E_{x,N}^{(1)}|^2 & |E_{y,1}^{(1)}|^2 & \cdots & |E_{y,N}^{(1)}|^2 \\ \vdots & \vdots & \vdots & \vdots & \vdots & \vdots \\ |E_{x,1}^{(i)}|^2 & \cdots & |E_{x,N}^{(i)}|^2 & |E_{y,1}^{(i)}|^2 & \cdots & |E_{y,N}^{(i)}|^2 \\ \vdots & \vdots & \vdots & \vdots & \vdots & \vdots \\ |E_{x,1}^{(N_t)}|^2 & \cdots & |E_{x,N}^{(N_t)}|^2 & |E_{y,1}^{(N_t)}|^2 & \cdots & |E_{y,N}^{(N_t)}|^2 \end{bmatrix}, \tag{5.6}$$

where N_t is the size of the training set, $|E_{x,j}^{(i)}|^2$ corresponds to the optical power of the main polarization mode measured at the j^{th} node corresponding to the i^{th} input, and $|E_{y,j}^{(i)}|^2$ corresponds to the optical power of the depressed polarization mode measured at the j^{th} node corresponding to the i^{th} input. We then perform two linear regressions using the same matrix S for both processed tasks T_x and T_y. This also ensures using the useful data in both polarization modes, since they are mutually coupled, and thus each polarization mode of the VCSEL contains information on both tasks. The equations for the linear regressions are $S \times \omega_x = b_{T_x}$ and $S \times \omega_y = b_{T_y}$ where ω_i is the vector containing the readout layer weights obtained from linear regression, and b_{T_i} is the vector containing the target output of the task T_i.

5.2.2 Memory properties of the system

As done in the previous chapter, we first checked the task independent properties of the system. Since the computational ability measures how well the system is able to separate the input in the parameter space, we assume that the computational ability remains the same while processing two tasks since the input method does not change, and we rather focus our study on the memory capacity. As we are processing two tasks, we now define the memory capacity per input signal. Two independent signals are injected in the reservoir and the two memory capacity tasks consists in estimating each of the two delayed input signal. We use for this test 400 neurons, hence a delay line of 8 ns. We used 1000 samples for the training set, and 3000 for the testing set. We first present in Fig. 5.3 an example of memory capacity corresponding to the two signals injected in each polarization mode of the VCSEL in case of an isotropic feedback configuration. We observe that the region leading to the best memory capacity is roughly the same for the two polarization modes of the VCSEL. The two regions are also similar to the region we observed in the previous chapter (Sec. 4.2.1) in case of single-task processing. We nevertheless observe that with a ratio of injected power $P_{inj_y}/P_{inj_x} = 2$, the memory capacity reached in the depressed polarization mode is higher (~ 11) compared to the one achieved in the dominant polarization mode (~ 7). Considering the fact that the dependency of the performance of the reservoir on η and

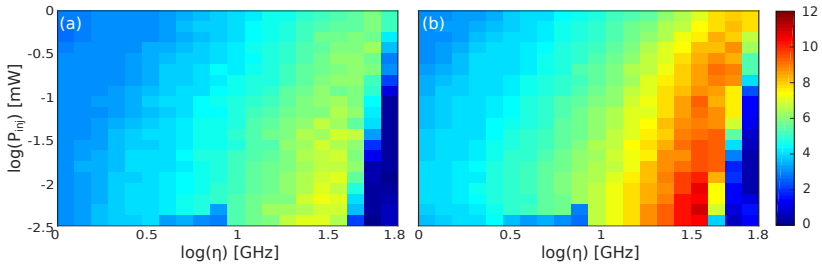

Figure 5.3: Memory capacity of (a) the task injected in the dominant polarization mode and (b) the task injected in the depressed polarization mode, provided by the system with isotropic feedback configuration plot as a function of the feedback strength η and the injected power in the dominant polarization mode P_{inj_x}. $P_{inj_x}/P_{inj_x} = 2$, $\gamma_s = 10$ GHz, $\gamma_p = 50$ GHz.

on P_{inj_x} is similar to the case of single task processing, we will focus on the study of the memory capacity depending on the ratio of injected power P_{inj_y}/P_{inj_x}. We will show that the difference of memory capacity between the two injected tasks is related to this ratio.

The memory capacity of the reservoir with isotropic feedback configuration as a function of the injection ratio is presented in Fig. 5.4. This figure also presents the influence of the coupling between the two polarization modes through the parameters γ_s and γ_p. It appears that the memory split between the two tasks is sensitive to this ratio. Furthermore, we identified two different tendencies. In the case of a small frequency splitting between the two polarization modes of the VCSEL ($\gamma_p = 6$ GHz), the memory is higher in the task T_x when the injection power is higher in the dominant mode ($P_{inj_y}/P_{inj_x} < 1$). The memory then gets higher in the task T_y when more power is injected in the depressed polarization mode than in the dominant one. This is due to a polarization switching that occurs at the crossing point. In the case of a larger frequency spacing between both polarization modes, no polarization switching is observed, and the memory capacity remains the highest in the depressed polarization mode. The memory in task T_x decreases as the injection ratio increases. Linking the two polarization modes through γ_s also slightly decreases the overall memory capacity of the system. It seems that both tasks are cross-talking. Increasing the injected power in the depressed polarization mode thus acts as increasing the perturbations in the dominant one. This is the reason why with a higher value for γ_s, the total memory capacity is higher as there is a decrease in the coupling between the two polarization modes. Therefore, each mode reaches higher memory capacity. We finally observe that the memory capacity in each polarization mode is lower than the one exhibited by the reservoir processing only one task. The total memory capacity seems to be shared when using the two polarization modes.

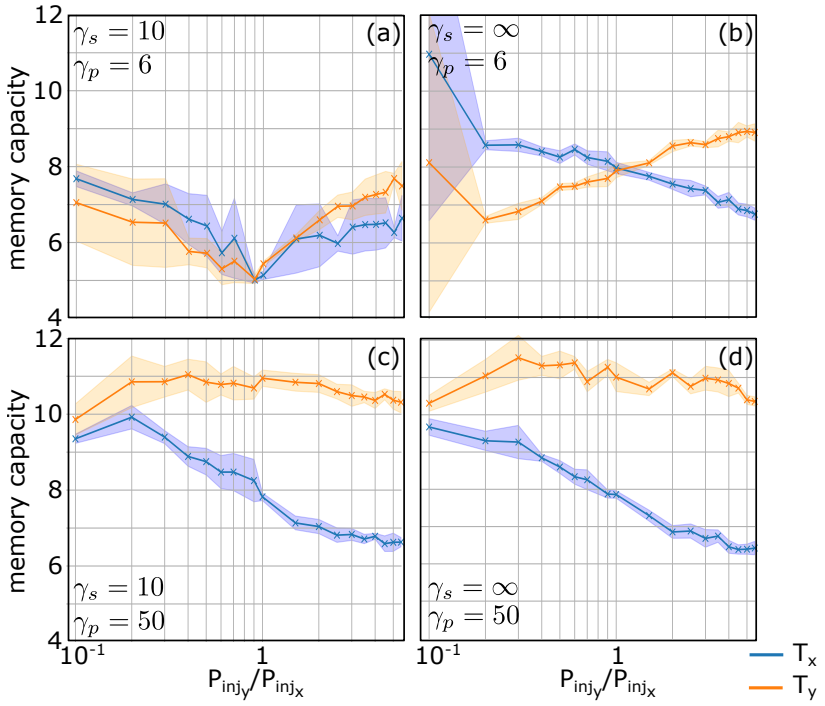

Figure 5.4: Best memory capacity of the system with isotropic feedback configuration plot as a function of the injection ratio between the two polarization modes, for different set of parameters of the VCSEL. The blue (orange) line corresponds to the memory of the task injected in the dominant (depressed) polarization mode of the VCSEL. The light color corresponds to the standard deviation. Parameters are (a) $\gamma_s = 10$ GHz,$\gamma_p = 6$ GHz, (b) $\gamma_s = \infty, \gamma_p = 6$ GHz, (c) $\gamma_s = 10$ GHz, $\gamma_p = 50$ GHz, (d) $\gamma_s = \infty, \gamma_p = 50$ GHz

We also run the same study in the case of rotated feedback configuration. The memory capacity is presented in Fig. 5.5. We can draw similar conclusions to the one found for the isotropic feedback case. Linking the two polarization modes through γ_s still slightly decreases the overall memory capacity of the system, and a larger frequency spacing allows reaching higher memory capacity. However, contrary to the isotropic feedback case, the two curves of the memory capacity of the tasks T_x and T_y intersect when using a VCSEL having a larger frequency spacing between its polarization modes (*i. e.* with a larger γ_p). Finally, we observe that, similarly to processing a single task, the system exhibits a higher memory capacity in the case of rotated feedback than in the case of isotropic feedback. For instance, if we compare the performance of the system using a VCSEL with $\gamma_p = 6$ GHz and $\gamma_s = 10$ GHz, the reservoir exhibits a memory capacity up to 23 in the case of rotated feedback, compared to 14 in the case of isotropic feedback.

It can be thought that there is a contradiction with the work realized on the semiconductor ring laser [13]. However, there is none: having a higher memory capacity does not ensure that the reservoir will perform better on an applied task. That is what we

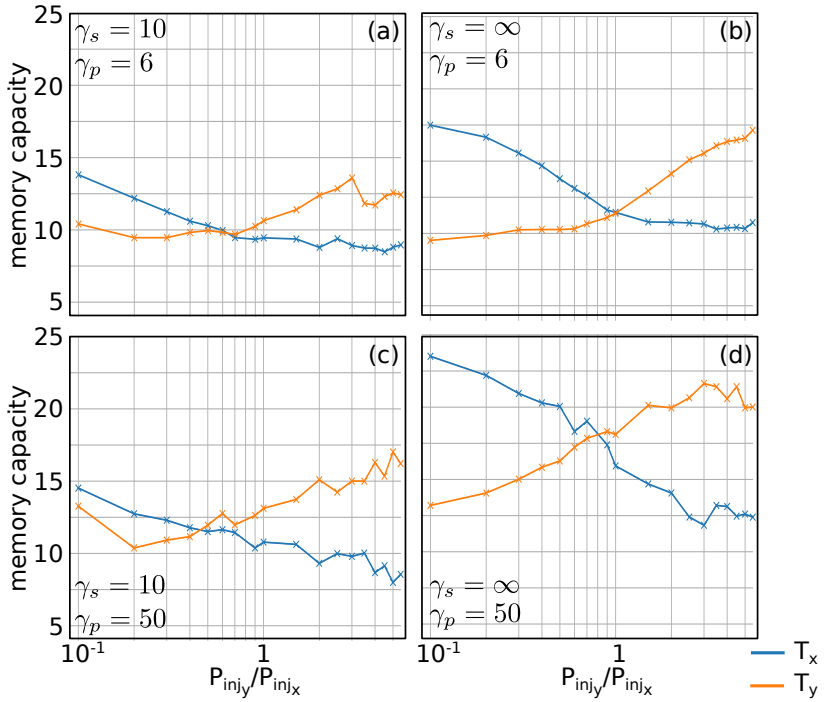

Figure 5.5: Best memory capacity of the system with rotated feedback configuration plot as a function of the injection ratio between the two polarization modes, for different set of parameters of the VCSEL. The blue (orange) line corresponds to the memory of the task injected in the dominant (depressed) polarization mode of the VCSEL. Parameters are (a) $\gamma_s = 10$ GHz, $\gamma_p = 6$ GHz, (b) $\gamma_s = \infty, \gamma_p = 6$ GHz, (c) $\gamma_s = 10$ GHz, $\gamma_p = 50$ GHz, (d) $\gamma_s = \infty, \gamma_p = 50$ GHz

will show in the next section.

5.2.3 Applied performance of the system

Following the test of the memory capacity, we benchmarked our reservoir with the nonlinear channel equalization. We first tested the WIFI channel equalization. For this task, we reduced the number of neurons to 32, which leads to a feedback length of 0.64 ns. This allows a cumulated bitrate of 6.25 Gb/s. We used for this task 20,000 symbols for the testing set, and 40,000 for the training. The two series of symbols drawn for the two tasks T_x and T_y are different, but the binary mask remains the same. As for the memory capacity, we performed this task for either isotropic or rotated feedback configuration, in order to verify if the conclusion drawn with the semiconductor ring laser is also valid with the VCSEL. We present in Fig. 5.6 an example of reconstruction of two signals simultaneously. The recovery has been performed when injecting the two polarization modes of the VCSEL with similar input amplitudes $P_{inj_x} = P_{inj_y}$. In these conditions, the SER reached for each task is at 5×10^{-3}. Both samples of the processed signals only show one error. The confusion

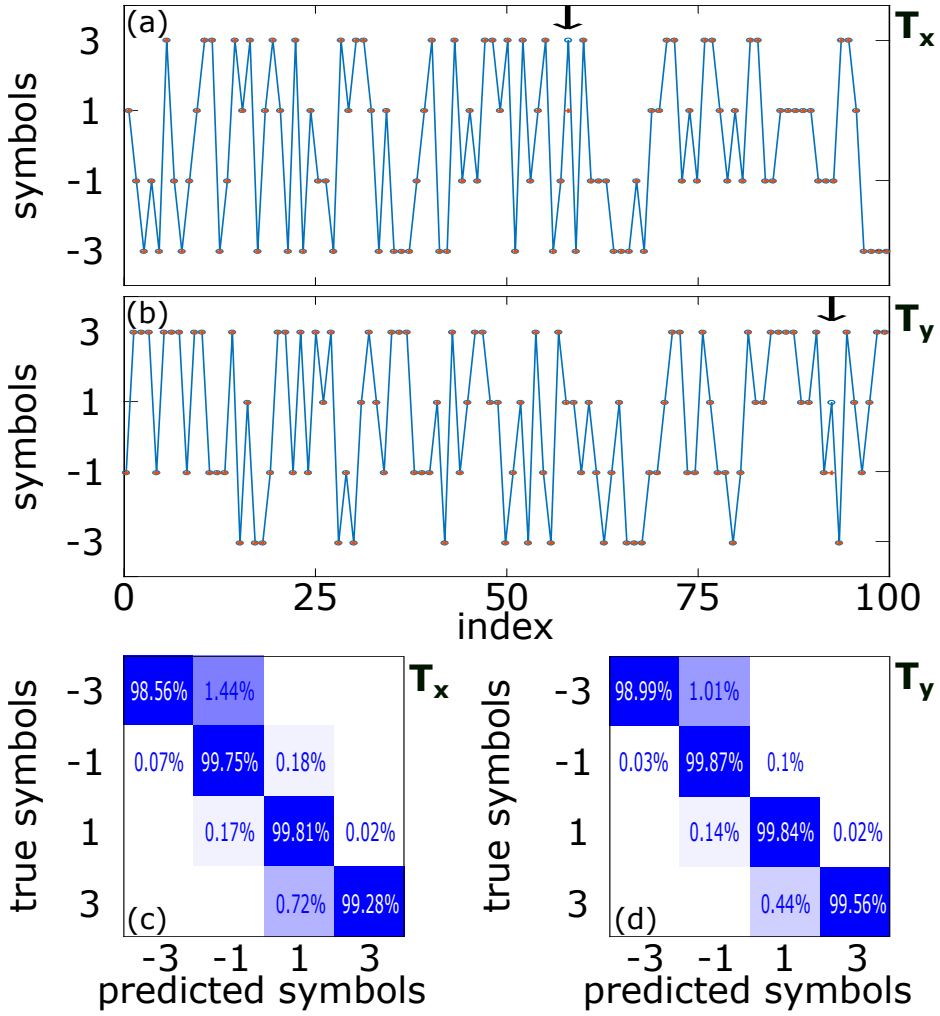

Figure 5.6: Example of performance on nonlinear channel equalization for two different signals injected in the two different polarization modes of the VCSEL. Parameters are $\gamma_p = 6$, $\gamma_s = \infty$, $P_{inj_y}/P_{inj_x} = 1$. (a)-(b) Example of symbols reconstruction on the task injected in the dominant polarization mode (a) and in the depressed polarization mode (b). The blue circles correspond to the original signal and the red crosses to the predicted signal. The arrows point out the errors. (c) confusion matrix of the task injected in the dominant polarization mode (LP_X). (d) confusion matrix of the task injected in the depressed polarization mode (LP_Y).

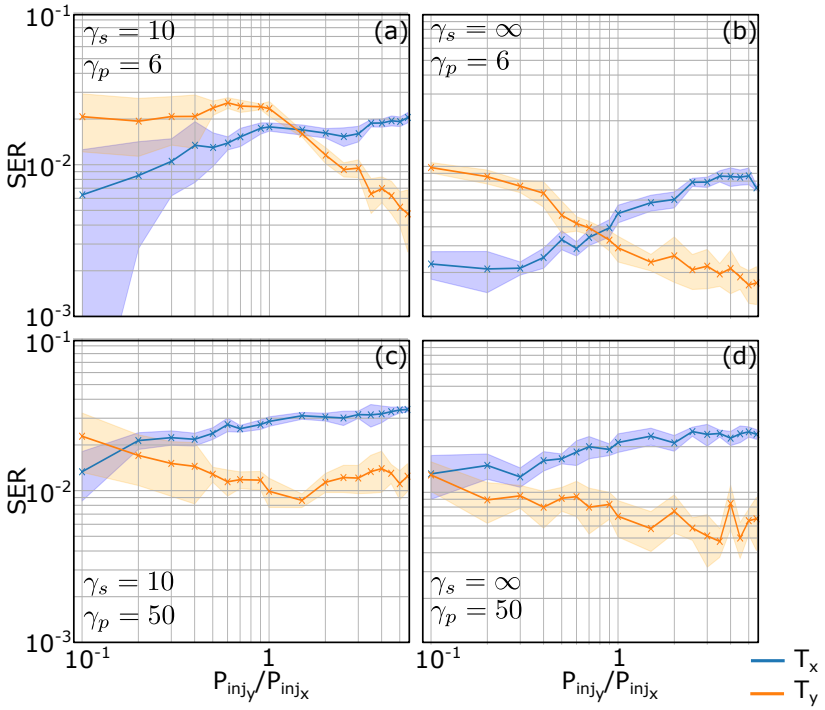

Figure 5.7: Best SER on the nonlinear channel equalization task of the system with isotropic feedback configuration plot as a function of the injection ratio between the two polarization modes, for different set of parameters of the VCSEL. The blue (orange) line corresponds to the SER of the task injected in the dominant (depressed) polarization mode of the VCSEL. The light color corresponds to the standard deviation. Parameters are (a) $\gamma_s = 10, \gamma_p = 6$, (b) $\gamma_s = \infty, \gamma_p = 6$, (c) $\gamma_s = 10, \gamma_p = 50$, (d) $\gamma_s = \infty, \gamma_p = 50$

matrices show that the error made in the reconstruction are equally distributed on the four symbols. Moreover, when an error is made, the estimated symbol is at a distance 2 from the desired output, *i.e.* the predicted symbol is just above or below the target output.

The performance of the reservoir computing device with rotated feedback is presented in Fig. 5.7. In the same figure we analyze the impact of different parameters on the performance since these parameters influence the coupling between the polarization modes. Some conclusions are similar to the observations made previously: (i) The ratio of injections P_{inj_y}/P_{inj_x} plays an important role on how the performance is distributed between the two tasks and (ii) the influence of γ_s is also similar. Increasing the value of γ_s, (*i.e.* reducing the dependency between LP_x and LP_y) improves the averaged performance of the reservoir computer. For a small value of γ_p, there is still the reversal of performance between the two tasks when $P_{inj_y}/P_{inj_x} = 1$, due to the polarization switching of the VCSEL.

However, the influence of γ_p on this task differs from what we concluded regarding

the memory capacity. Narrowing the frequency splitting between the two polarization modes indeed improves the computational performance, contrary to the observation made for the memory capacity. This tells us that the memory capacity is not the prime factor impacting the computational performance of the system. When enlarging the frequency splitting, the nonlinear operation made by the VCSEL on the input stream is less suitable for this task and prevents one from maintaining good computational performance.

We also observe an upper level of performance that cannot be overcome, even by increasing the injection ratio between the two polarization modes. In the best performance case (Fig. 3.20.b), we are not able to further improve the SER below 2×10^{-3} for a single-task operation with the sets of parameters under consideration. We have to choose either which task has the best level of performance (in our case with a SER at 2×10^{-3}), or have both tasks with a similar, but lower, level of performance (SER at 5×10^{-3}).

We also processed two WIFI channel recovery with the reservoir made with rotated feedback. The performance is presented in Fig. 5.8. γ_s and γ_p play the same role for the reservoir with rotated feedback as for the reservoir with isotropic feedback. However, as for the memory capacity, the polarization rotated feedback yields a polarization switching for a larger value of γ_p. We also observe that the performance of the reservoir made with polarization-rotated feedback is lower than the performance obtained with isotropic feedback. For instance, when using a VCSEL with $\gamma_p = 6$ GHz and $\gamma_s = \infty$ (which corresponds to the case providing the best performance for both configurations of feedback), we are able to reach a mean BER of 5×10^{-3} with the rotated feedback, compared to 3×10^{-3} with isotropic feedback. We reach the same conclusion as the one presented in [13].

We also tested our reservoir with the optical channel equalization. Since we demonstrated that the reservoir computer reaches better performance with isotropic feedback, we have only performed this task with this configuration of feedback. We first present the results for the recovery of signals distorted after 25 km of fiber, for the different sets of parameters of the VCSEL under consideration. For this task, we used 20,000 samples for the training, and 40,000 for the testing. Performance is presented in Fig. 5.9. It seems that we can tune the splitting of performance between the two processed tasks by changing the ratio of injection P_{inj_y}/P_{inj_x}. This can be mainly observed when the two polarization modes are strongly linked through the spin relaxation parameter γ_s and the birefringence parameter γ_p. As for the WIFI channel equalization, increasing this ratio improves the performance on task T_y, lowering the performance of task T_x. A polarization switching is observed for a ratio of injection $P_{inj_y}/P_{inj_x} = 1$, leading to a reversal of the best processed task. Moreover, similarly to the previously tested

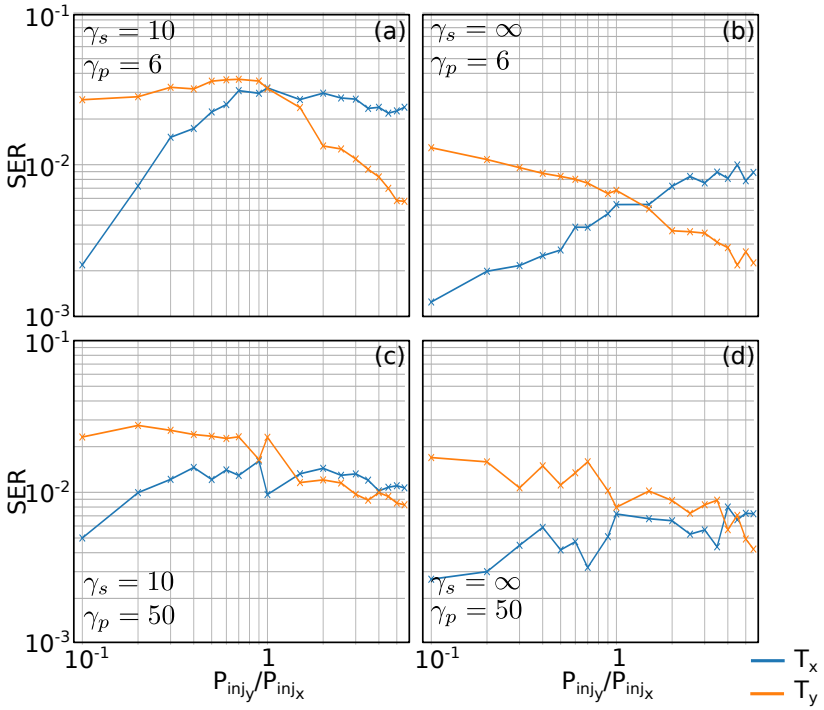

Figure 5.8: Best SER on the nonlinear channel equalization task of the system with rotated feedback as a function of the injection ratio between the two polarization modes, for different set of parameters of the VCSEL. The blue (orange) line corresponds to the SER of the task injected in the dominant (depressed) polarization mode of the VCSEL. Parameters are (a) $\gamma_s = 10, \gamma_p = 6$, (b) $\gamma_s = \infty, \gamma_p = 6$, (c) $\gamma_s = 10, \gamma_p = 50$, (d) $\gamma_s = \infty, \gamma_p = 50$

task, reducing the nonlinear effects coupling the two polarization modes enhances the mean performance of the reservoir computer. However, it appears that, similarly to the single-task operation, recovering a 25 km-distortion is an easy task, and does not allow for discriminating the different cases. The reservoir is indeed able to recover the two processed signals without any mistake in most of the parameter cases.

We thus tested our reservoir with the recovery of signals distorted after 50 km of fiber. The testing and the training are realized in the same conditions as previously. The performance is presented in Fig. 5.10. Since the task is more complex, we can better observe the influence of the different parameters. We notice that, as previously, an improvement of the mean performance is visible when increasing γ_p or γ_s. However, the difference of performance is less pronounced than for the processing of WIFI channel equalization. The averaged performance is a BER of $\sim 2.5\%$ for each set of parameters. The ratio of injection power P_{inj_y}/P_{inj_x} controls the splitting of performance in most of the presented cases, except in the case $\gamma_p = 50$ GHz and $\gamma_s = \infty$, which corresponds to the situation for which the nonlinear effects coupling the two polarization modes are the weakest. In this scenario, the two tasks provide similar BER for each value of

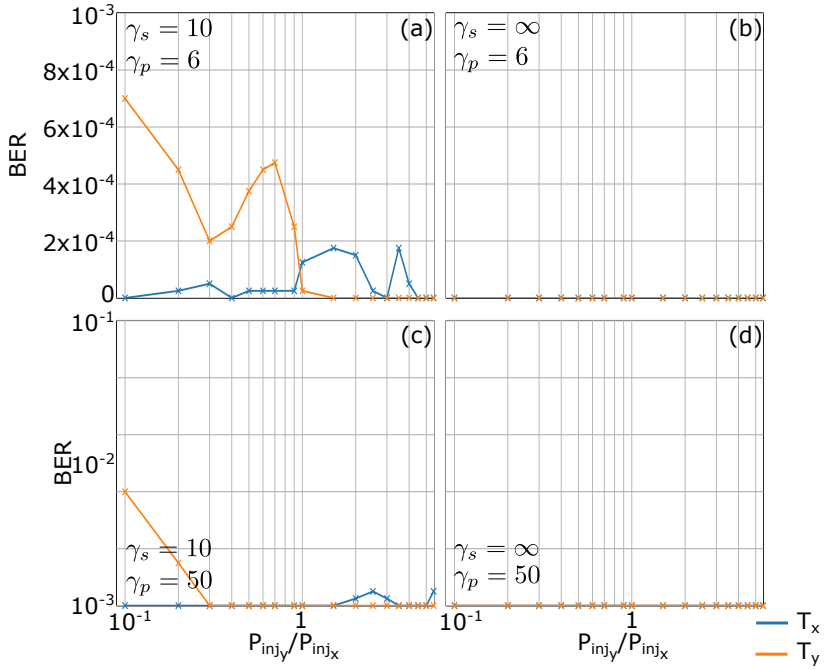

Figure 5.9: Best BER on the nonlinear optical channel equalization task after 25 km of fiber as a function of the injection ratio between the two polarization modes, for different set of parameters of the VCSEL. The blue (orange) line corresponds to the BER of the task injected in the dominant (depressed) polarization mode of the VCSEL. Parameters are (a) $\gamma_s = 10$ GHz, $\gamma_p = 6$ GHz, (b) $\gamma_s = \infty, \gamma_p = 6$ GHz, (c) $\gamma_s = 10$ GHz, $\gamma_p = 50$ GHz, (d) $\gamma_s = \infty, \gamma_p = 50$ GHz

P_{inj_y}/P_{inj_x}. For the other set of parameters, we still observe that one task is better processed than the other one, and that it exists a crossing point in the performance curve, leading to an exchange of the best processed task. This point still corresponds physically to a polarization switching of the VCSEL.

5.3 Experimental results

Considering that we are not able to choose the internal parameters of the VCSEL, this section will rather focus on proving that we are indeed able to perform two tasks simultaneously with an experimental VCSEL-based reservoir, and that we are able to tune the split of performance between the two tasks by changing the ratio of injected power P_{inj_y}/P_{inj_x}.

In this section, we will first present the experimental setup, before explaining how we set up the different parameters of the reservoir. We will finally present the performance obtained with our architecture.

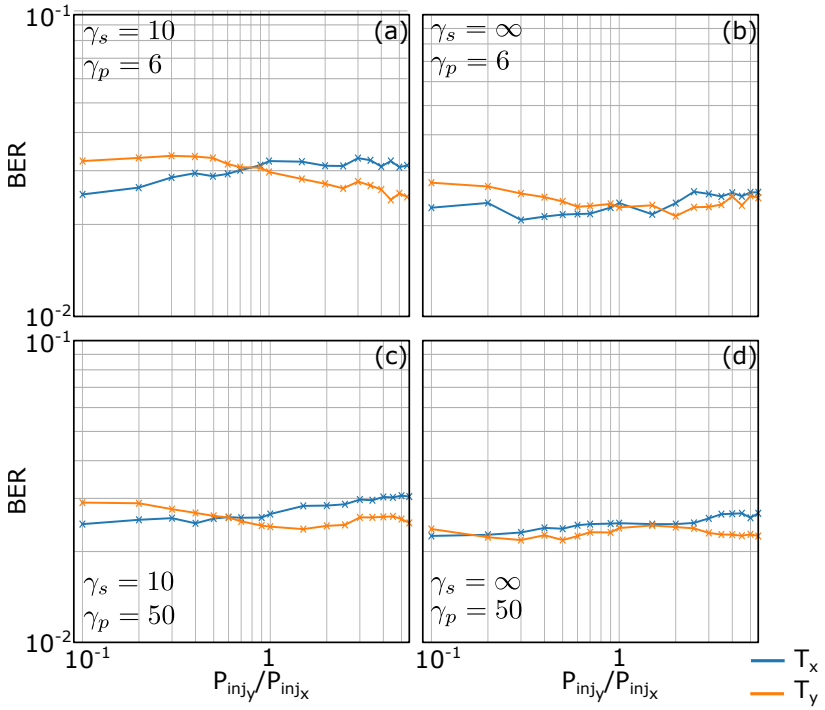

Figure 5.10: Best BER on the nonlinear optical channel equalization task after 50 km of fiber as a function of the injection ratio between the two polarization modes, for different set of parameters of the VCSEL. The blue (orange) line corresponds to the BER of the task injected in the dominant (depressed) polarization mode of the VCSEL. Parameters are (a) $\gamma_s = 10$ GHz, $\gamma_p = 6$ GHz, (b) $\gamma_s = \infty, \gamma_p = 6$ GHz, (c) $\gamma_s = 10$ GHz, $\gamma_p = 50$ GHz, (d) $\gamma_s = \infty, \gamma_p = 50$ GHz

5.3.1 Presentation of the complete experimental setup

The setup we use is structurally similar to the one presented in the previous chapter (Sec. 4.3). The reservoir remains the same. Only the input and the output layers have been changed to be able to process two tasks in parallel. The reservoir itself is the same as the one we have previously studied in Sec. 4.3: It comprises a VCSEL (Raycan) as a physical node, which emits light at 1552.75 nm for the dominant linear polarization mode (LP_x) and at 1552.89 nm for the depressed polarization mode (LP_y). The bias current of the VCSEL is set at 4.5 mA, which corresponds to 1.5 times the threshold current. The feedback loop is made of a SMF-28 single mode fiber (standard telecommunication fiber) resulting in a delay-line of $\tau = 39.4$ ns. As only one calculation step can be performed per round-trip, this length limits the processing speed to 25.65 MHz per task, thus 51.3 MHz for two tasks. To optimize our use of the VCSEL dynamics, we set the inter-nodes delay $\theta = 0.04$ ns according to simulations run in the previous chapter (Sec. 4.2.1) and to the frequency limitation of the experimental components (*i.e.* oscilloscope, arbitrary waveform generator and modulators). We use

for the training and testing of the reservoir only one every two nodes separated by $2\theta = 0.08$ ns due to the memory limitation of the computer performing the training, thus leading to consider $N = 492$ nodes instead of $N = 984$. This choice was made as it speeds up the reservoir's training without impeding the performance. This choice also does not reduce the connectivity between the neurons as the delay between nodes is still shorter than the time required by the VCSEL to restabilize experimentally. There is also a polarization controller (P.C.) to control the optical polarization along the feedback loop. Finally, an optical attenuator Keysight 81577A (Att.) is used to control the feedback strength. According to the results obtained in the previous section (cf Fig. 5.3), there is an optimum operating point for each value of the feedback strength while varying the injection power. This is why we set the feedback attenuation η to 17 dB, to guarantee that enough power is injected to find this best operating point.

The input layer is primarily composed of an arbitrary waveform generator (AWG) AWG700002A from Tektronix, a tunable laser Tunics T100S from Yanista, and two Mach-Zehnder modulators ($\mathrm{MZ}_{x,y}$) with a bandwidth of 12.5 GHz. Both modulators are working in their linear regime. The light emitted by the tunable laser is split in two different beams and sent in the two different modulators. The two different masked input streams, corresponding to the two tasks $T_{x,y}$ to be processed are used to drive both modulators, and are generated by the AWG at a symbol rate of 25 GS/s for each stream. The output power of the modulator is controlled by an optical attenuator built inside each modulator. This allows an independent control of the injected power $P_{inj_{x,y}}$ for the two tasks $T_{x,y}$. At the modulators output, the optical polarization of the input stream containing T_x is aligned with the main polarization mode (LP_x) of the VCSEL, and the one of the input stream containing T_y with the depressed polarization mode (LP_y). An example of input streams is given in Fig. 5.13.(a). Both beams are then recombined and sent in the reservoir computer. Pictures of the setup are presented in Fig. 5.11. The corresponding scheme is presented in Fig. 5.12.

The response of the reservoir is recorded at the output layer: The signal is first amplified with an erbium-doped fiber amplifier (EDFA) from Lumibird. Then, the two polarization modes of the VCSEL are separated and recorded with two photodiodes Newport 1544-B 12 GHz bandwidth, connected to an oscilloscope Tektronix DPO 71604C 16 GHz bandwidth with two channels at 50 GS/s. Examples of the experimental time series recorded for each polarization mode of the VCSEL are given in Fig. 5.13.(b). The signal-to-noise ratio (SNR) has been experimentally measured to be 21 dB.

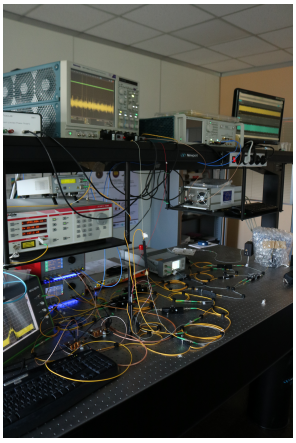

(a) Vertical view of the experimental setup. The oscilloscope and the AWG are on the shelf.

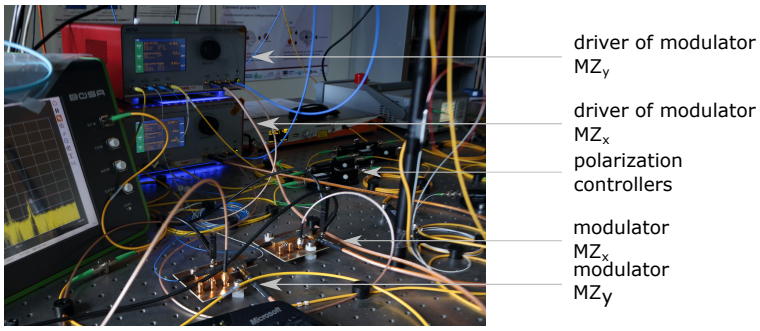

(b) Zoom on the input layer. We can distinguish the two modulators on the foreground, and the modulators drivers with the polarization controllers used to set the polarization in the input layer in the background

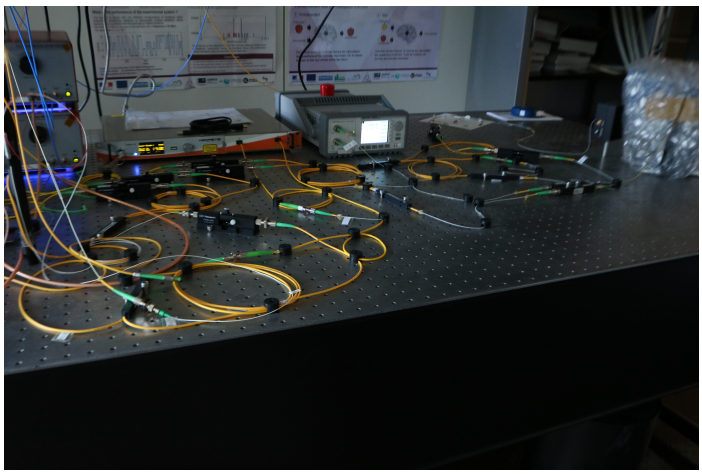

(c) Horizontal view of the optic table. We observe on the left the input layer, and the reservoir on the right of the picture.

Figure 5.11: Pictures of the experimental setup

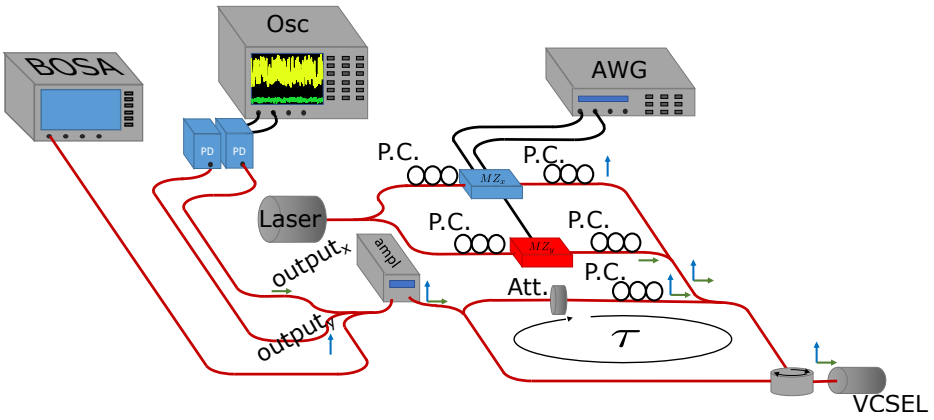

Figure 5.12: Scheme of the experiment. The two masked signals are sent on the two modulators. Each input signal is aligned with a different polarization mode of the VCSEL. The blue and orange arrows show the polarization of the light in the setup. MZ: Mach-Zehnder modulator, P.C.: polarization controller, AWG: arbitrary waveform generator, Att: attenuator, Osc: Oscilloscope, ampl: amplifier, PD: photodiode.

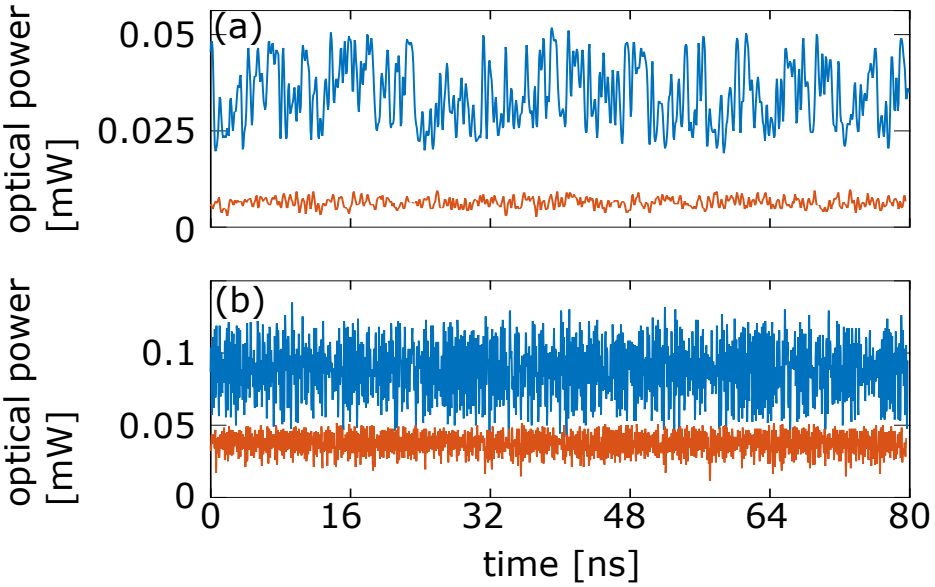

Figure 5.13: Example of experimental signals. (a) Example of two input streams generated by the AWG. The blue line corresponds to the input stream injected in the dominant polarization mode (LP_x), and the red line to the stream injected in the depressed polarization mode (LP_y) of the VCSEL (b) Example of signals recorded at the output of the reservoir computing system. The blue line corresponds to the response of the dominant polarization mode (LP_x), and the red line to response of the depressed polarization mode (LP_y) of the VCSEL.

5.3.2 Preparing the setup to perform computation

Since we want to process two tasks simultaneously, there are more parameters to set before being able to perform computation. As explained at the beginning of this section, we only perform computation with isotropic feedback. We set the polarization of the feedback as explained in the previous chapter (Sec. 4.3). Added to that, we observe that there is an optimal operating point for each value of feedback strength as soon as we inject enough power in the reservoir (cf. Fig. 5.3). The attenuation in the feedback loop is thus set to 18 dB, to ensure that we can inject enough power from the master laser.

We lastly set the master laser. We provide again the optical spectrum of the VCSEL with optical feedback in Fig. 5.14.(a). The VCSEL is lasing at 1552.72 nm, the wavelength of its dominant polarization mode. The dominant mode LP_x of the VCSEL has a spectral width of 5.72 GHz with an attenuation of 17 dB in the feedback loop. The two smaller side peaks are induced by the undamped relaxation oscillations of the VCSEL [158], which frequency is measured at 3.73 GHz.

The wavelength of this laser is set to 1552.82 nm so that its wavelength is equally separated from the frequencies of the main and depressed polarization modes of the VCSEL, as presented in Fig. 5.14.(b). By doing so, we ensure that, having the same power in both linear polarization modes at the output of the modulators, the power is equally distributed among the two linear polarization modes of the injected VCSEL. Shifting the frequency of the master laser to one of the polarization modes of the VCSEL leads to a more efficient optical injection in this mode, and therefore enhances the response of this mode at the expense of the response of the other mode, for which the optical injection is reduced.

We then align the linear polarization at the output of the two modulators with each polarization of the VCSEL. The alignment is realized by turning on the output of only one modulator and setting the injection power to a rather high value (around 4 mW). An arbitrary signal is sent on the RF port of the modulator. We then turn the optical polarization of this input until maximizing the amplitude response of the VCSEL. Once the polarization of the first input is set, we adjust the polarization of the second input similarly. We observe that in these conditions (Fig. 5.14.(b)) , the VCSEL is emitting light only in its dominant mode, and exhibits wave-mixing dynamics.

When modulating the master laser, its spectrum broadens and overlaps the two wavelengths of the VCSEL as shown in Fig. 4.25.(c)-(d). This allows the VCSEL to react to the master laser, and to respond according to the modulated input. This response also broadens the spectra of the two polarization modes of the VCSEL. The

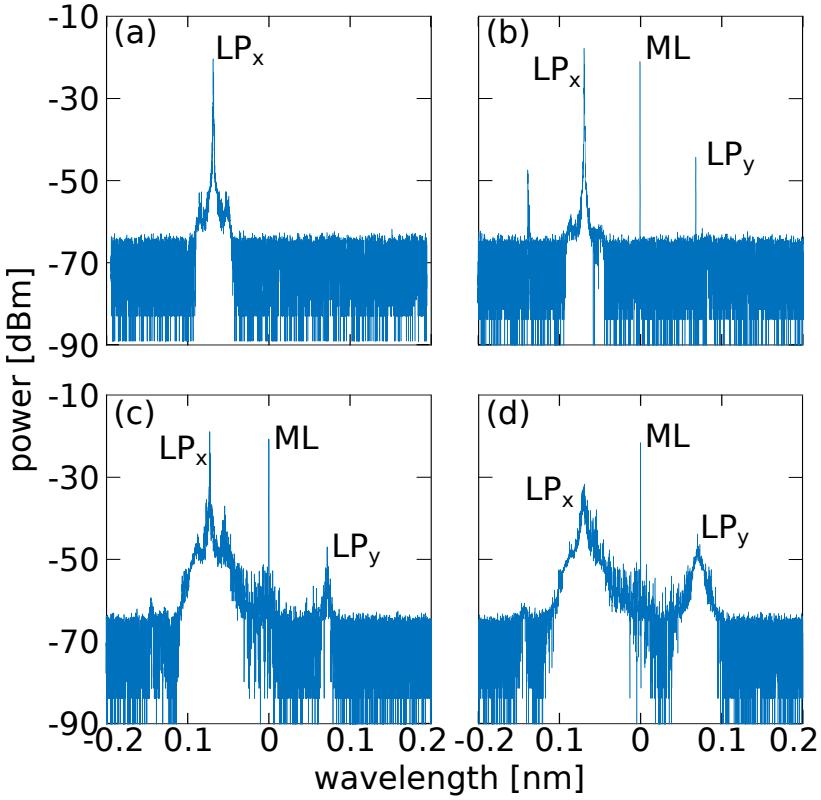

Figure 5.14: Optical spectra of the system under different operation conditions. LP_x: dominant polarization mode, LP_y: depressed polarization mode, ML: master laser. (a) VCSEL with isotropic feedback, $\eta = 17$ dB. (b) reservoir computer with optical injection on both polarization mode without modulation, $P_{inj_x} = P_{inj_y} = 0.08$ mW, $\eta = 17$ dB, (c) reservoir computer with optical injection on both polarization mode with modulation, $P_{inj_x} = P_{inj_y} = 0.08$ mW, $\eta = 17$ dB, (d) reservoir computer with optical injection on both polarization mode with modulation, $P_{inj_x} = 0.08$ mW, $P_{inj_y} = 0.4$ mW $\eta = 17$ dB.

spectral width of the dominant polarization mode LP_x detuned from the modulated input by 9.45 GHz. We observe also that injecting more power in the depressed mode LP_y forces lasing in the depressed mode despite that mode is not lasing when the VCSEL is free-running.

The experimental finding of the best operating point is then realized similarly to the numerical method. Given a value for the ratio of injected power P_{inj_y}/P_{inj_x}, we sweep the value of P_{inj_x} and keep the value for which the reservoir computer exhibits its best performance, as presented in Fig. 5.2.

5.3.3 Experimental performance

We tested our device with the nonlinear channel equalization task. We use for the state of one node the optical power of the two polarization modes of the VCSEL

separately, since we perform the training of the simulated system. We fill only one state matrix to perform the training of the two different tasks (cf 5.2). As for the numerical simulations, the two tasks processed by the reservoir consist of two different signals drawn randomly. The masks used are the same for both tasks.

We first present the results of the WIFI channel equalization, where we use 12,000 samples for the training set, and 13,380 for the testing. Figure 5.15 presents an example of the dependency on the injected power P_{inj_x}, of the performance of the reservoir on the WIFI channel equalization, for a fixed ratio $P_{inj_y}/P_{inj_x} = 3$. We observe that the performance on both tasks performed simultaneously is influenced by the injected power. Moreover, there is an optimal power of injection, which provides the best performance of the reservoir. In this case, the lowest mean BER reached is at 4%, obtained for an injected power in the dominant mode of 0.1 mW (hence a total injected power of 0.13 mW).

We studied the variation of this best averaged performance. The results are presented in Fig. 5.16 and show the performance on both tasks with the ratio of injection. The performance on task T_x decreases and the one on task T_y increases while increasing the injection ratio. For a ratio lower than 0.7, task T_x is better performed than task T_y. The trend is reversed for a ratio greater than 0.7. This inversion can be explained by a polarization switching induced in the VCSEL by the optical injection. The reservoir is able to exhibit a best SER for the task T_x of 2.5% when the dominant mode is

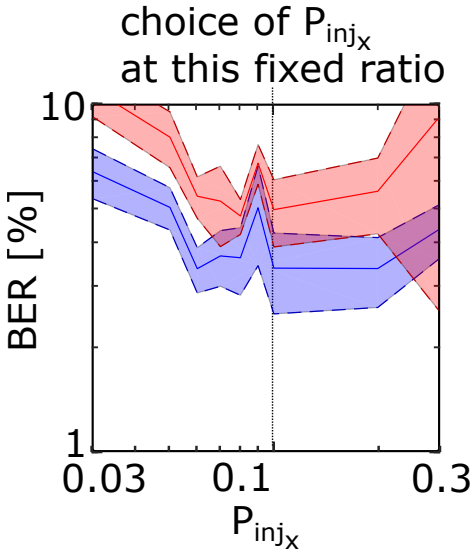

Figure 5.15: Performance on wifi channel equalization task as a function of the injection power in the main polarization mode P_{inj_x} for a fixed ratio of injection power $\frac{P_{inj_y}}{P_{inj_x}}$ at 0.3. The blue curve corresponds to the performance of the task T_x and the red one to the performance of the task T_y. The dotted line corresponds to the choice of P_{inj_x} reported in figures 5.16 for this specific case.

strongly injected. In this case, the SER reached for task T_y is at 8.5%. The reservoir reaches a mean SER of 4%. The ratio of injected power in the polarization modes can thereby be used to easily choose the splitting of performance between the two performed tasks. The reservoir is able to reach a SER really close to the one obtained for a single task when the dominant mode of the VCSEL is strongly injected. However, the overall performance of the reservoir is lower when processing two tasks instead of one, although the difference is not very significant.

We confirm this behavior of the reservoir by performing the nonlinear optical channel equalization task for two lengths of fiber, 25 km and 50 km. We processed this task as we did for the single task operation. The input of the reservoir is realized using a sliding window of 5 bits (cf Sec. 4.20). We perform the training using 20,000 samples, and the testing with 5,380 samples.

We first present the influence of the injected power on the performance of both tasks T_x and T_y in Fig. 5.17. On this figure, the injection ratio P_{inj_y}/P_{inj_x} is fixed to 0.3. We can observe that there is an optimal injected power that yields the best mean performance at $P_{inj_x} = 0.09$ mW for 25 km and at $P_{inj_x} = 0.2$ mW for 50 km. We will only report this best value in the figures of the next section.

The results for the channel equalization after 25 km of propagation in the fiber are presented in Fig. 5.18.(a). We observe that the performance on tasks T_x and T_y varies with the injection ratio P_{inj_y}/P_{inj_x}. If this ratio is smaller than 2, Task T_x is better performed than Task T_y. When this ratio is greater than 2, the trend is

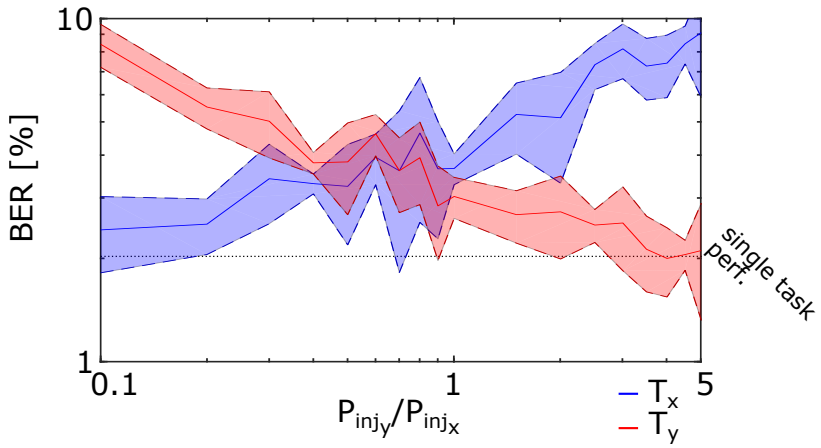

Figure 5.16: Performance on wifi channel equalization task as a function of the ratio of injection P_{inj_y}/P_{inj_x}. The blue curve corresponds to the performance of the task T_x, and the red curves corresponds to the performance of the task T_y. The lighter area shows the standard deviation of the performance. The dotted line shows the performance of the reservoir performing the single task.

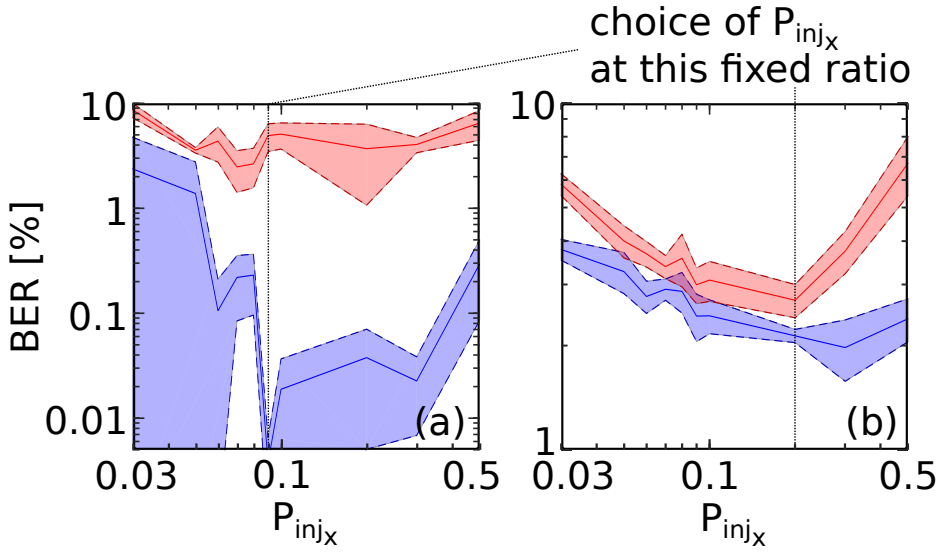

Figure 5.17: Performance on nonlinear optical channel equalization task as a function of the injection power in the main polarization mode P_{inj_x} for a fixed ratio of injection power $\frac{P_{inj_y}}{P_{inj_x}}$ at 0.3. (a) Performance for a distortion due to 25 km of optical fiber. (b) Performance for a distortion due to 50 km of optical fiber. The blue curve corresponds to the performance of the task T_x and the red one to the performance of the task T_y. The dotted line corresponds to the choice of P_{inj_x} reported in figures 5.18 and 5.19 for this specific case.

reversed, and the task T_y is better performed. We can explain this phenomenon by a polarization switching in the VCSEL output induced by optical injection. This phenomenon therefore increases the SNR of the task T_y injected in the depressed polarization mode. The system is able to provide a BER of 0.04 % for the task T_x, when the dominant mode is strongly injected (with an injection ratio P_{inj_y}/P_{inj_x} of 0.2). The other task is processed with lower performance in this case, with a BER of 1.6 %. When the ratio of power is greater than 0.5, the average performance of the reservoir reaches a threshold of performance with a BER of 0.35 %. The ratio of injected power in the polarization modes can thereby be used to easily choose the splitting of performance between the two performed tasks. When processing a single nonlinear channel equalization task, the reservoir computer exhibits a BER of 0.06 %, as presented in the previous chapter. This is comparable to the performance obtained on task T_x when the dominant mode is strongly injected. However, as we observed with the WIFI channel equalization, processing two tasks instead of one limits the averaged performance of the system.

Considering that the input of the reservoir is strongly preprocessed, we analyze the impact of the nonlinear transformation induced by our VCSEL based reservoir on the task, by comparing it to a stand-alone linear regression (a *linear classifier*). Towards this end, the linear classifier is operated in the same conditions as the reservoir

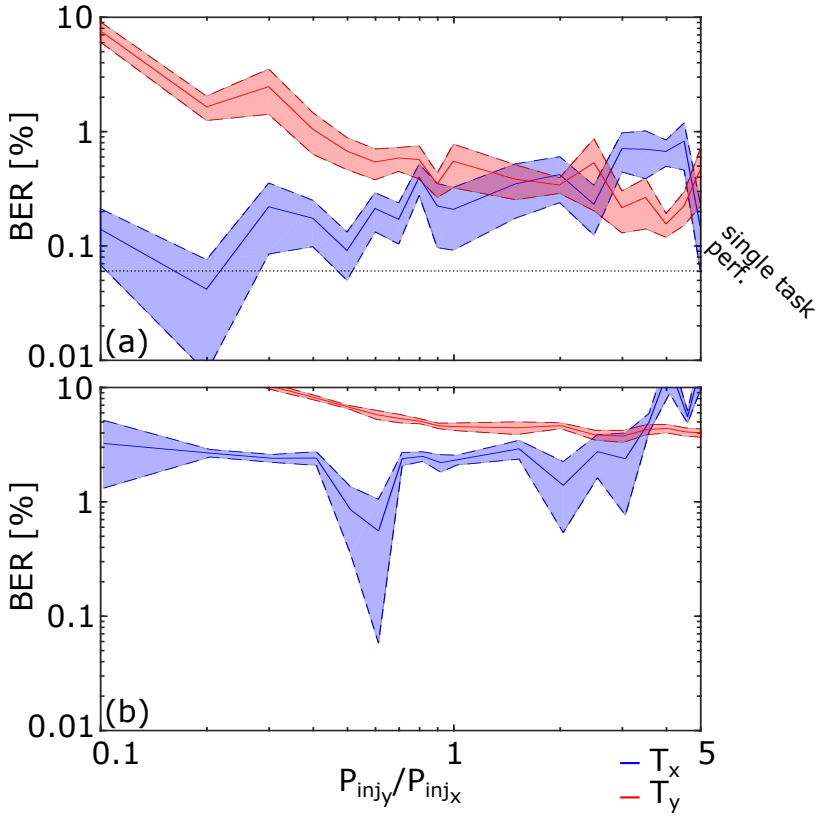

Figure 5.18: Performance on nonlinear optical channel equalization task after 25 km of optical fiber as a function of the ratio of injection P_{inj_y}/P_{inj_x}. The blue curves correspond to the performance of the task T_x, and the red curves corresponds to the performance of the task T_y for (a) the reservoir computer and (b) the linear classifier. The lighter area shows the standard deviation of the performance. The dotted line shows the performance of the reservoir performing the single task.

computer: One classifier is used to process the two tasks with the same number of neurons and similar injection power ratio to the one injected in the photonic reservoir computer. We use also the same input features (two masked signals, using a mask having the same size, and preprossing each input signal in the same manner as for the photonic reservoir) with identical sizes for the training and testing sets (20,000 samples for training and 5,380 for testing). Finally, similar SNR conditions are considered. To meet this last condition, since the experimental VCSEL introduces additional noise, we added white noise to the input signal to achieve 21 dB before performing a stand-alone linear regression. With these similar operating conditions, a stand-alone linear regression provides a BER slightly lower than 1 %, and the mean BER of the two tasks is ~ 3.2 % in the best operating point identified in our experiment (*i.e.* for a ratio in the range of 0.6 to 3). The reservoir computer is thus able to improve the performance on the two tasks by approximately one order of magnitude.

We also provide results on the dual channel equalization after propagating 50 km

in the single mode fiber. Since the distortion of the signal is more pronounced, the mean performance of the reservoir computer is expected to be lower than the one after a 25 km transmission. The performance of the reservoir computer is given in Fig. 5.19.(a). We still observe a similar trend: The polarization switching of the VCSEL appears for a ratio of injection $P_{inj_y}/P_{inj_x} \sim 1$ and the best achieved BER for one task is at 1.6 %. The best mean performance is at 2.2 %, achieved for a ratio of injection at 0.7. The system performing this single task exhibits a BER of 1.5 %, which is still comparable to the performance of task T_x when the dominant mode is strongly injected, even if processing two tasks simultaneously slightly decreases the mean performance of the system, when compared to processing a single task.

The performance of the stand-alone linear regression (linear classifier) is presented in Fig. 5.19.(b). The test has been realized with the same condition as the one used for the reservoir computer. The linear classifier is achieving a BER of 7.5 % as a best performance. When both processed signals are balanced, the linear classifier exhibits

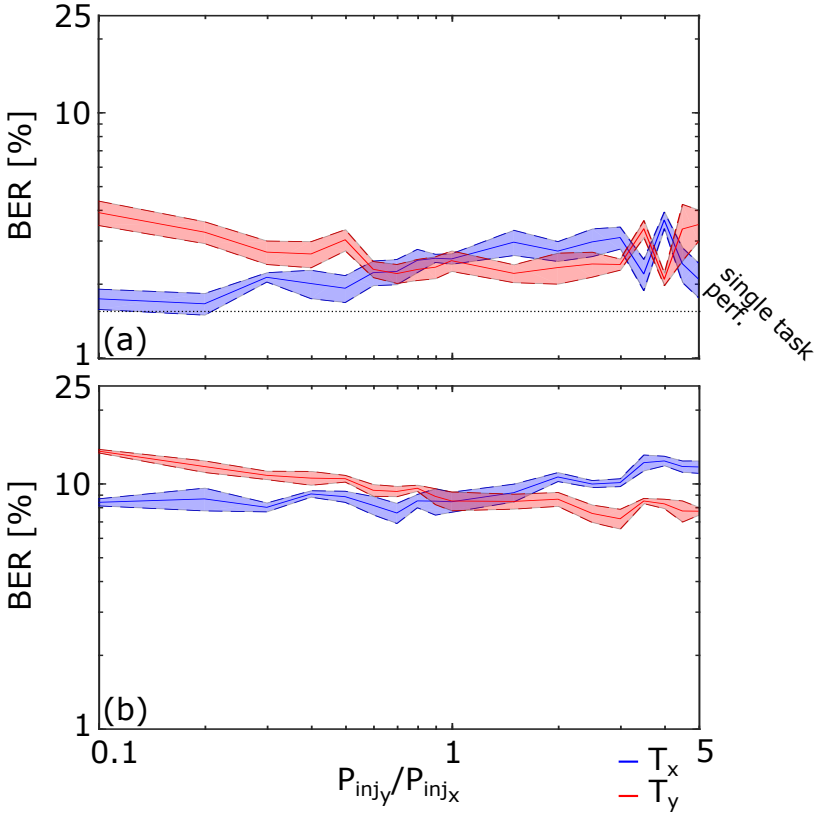

Figure 5.19: Performance on nonlinear optical channel equalization task after 50 km of optical fiber as a function of the ratio of injection P_{inj_y}/P_{inj_x}. The blue curves corresponds to the performance of the task T_x, and the red curves corresponds to the performance of the task T_y for (a) the reservoir computer and (b) the linear classifier. The lighter area shows the standard deviation of the performance. The dotted line shows the performance of the reservoir performing the single task.

its best mean performance, with a mean BER at 8.4 %. Using the nonlinear effects in our VCSEL-based photonic reservoir computer in similar SNR conditions thus provides a significant benefit, allowing to improve by a factor 5 the performance on the signal recovery task.

5.3.4 Comparison numerical and experimental results

We presented in this chapter the numerical and experimental performance of our reservoir architecture on several tasks. As we explained previously, the frequency difference between the two polarization modes of the VCSEL we use is at 17.4 GHz, which leads to $\gamma_p = 54.7$ GHz. Our reservoir is then close to $\gamma_p = 50$ GHz, and we suppose that $\gamma_s = 10$ GHz as it is a standard value that we can find in the literature.

We observe that the performance obtained numerically without noise and experimentally are closer in the dual task processing case than in the single task processing case. When comparing the SER obtained on the WIFI channel equalization task, the numerical results predicts a mean SER of 1.8%. The experiment provides a SER of 4%, which only differs by a factor 2. This might be due to the perturbation induced by the injection of two different data streams in the reservoir. As explained in Sec. 5.2, both tasks are cross talking and therefore each task can be seen as a perturbation for the other one. Thus, increasing the ratio of injected power P_{inj_y}/P_{inj_x} increases the perturbations in the reservoir, and the influence of the noise in the output layer is largely reduced in the dual task processing scenario.

Same conclusions can be drawn from the nonlinear optical channel equalization task. For a 25 km-distortion, the experimental reservoir exhibits a mean SER of 4×10^{-4}, to compare with a mean SER of 0 for the simulated system. These results are really close when we take into account that the lowest detectable SER is at 2×10^{-4}, due to the size of the training set. A SER of 4×10^{-4} is equivalent to only two errors made during the testing. For a 50 km-distortion, the experimental reservoir and simulated system exhibit similar SER, about 2.5×10^{-2}. As we explained, the good match between the numerical and experimental performance is justified since processing two tasks simultaneously greatly reduces the impact of the noise in the output layer on the performance of the reservoir.

5.4 Conclusion

We demonstrated in this chapter how to use the polarization dynamics of the VCSEL to process simultaneously two tasks. This possibility has been first explored numerically,

and we found that the performance of the reservoir is influenced by the way we couple the two polarization modes either by a suitable choice of the internal parameters of the VCSEL or by rotating the polarization along the feedback loop. We also showed that we can tune the performance of each task by changing the ratio of injection power between the two tasks. These numerical simulations help to get an insight into the upper limit for the performance of the reservoir. The mean SER reached by the reservoir on the WIFI channel equalization is between 4×10^{-3} and 2×10^{-2}, and the mean BER for the optical channel equalization is between 4×10^{-3} and 3.5×10^{-2} for 25 km of fiber and about 2.2×10^{-2} for 50 km of fiber, depending on the parameters used for the VCSEL.

We then tested the performance of the experimental reservoir computer and have been able to reproduce the same trends. We can use the ratio of injection power to tune the performance of each task, and the reservoir exhibits similar performance experimentally compared to the numerical results: a mean SER of 4×10^{-2} for the WIFI signal recovery, a mean BER of 0.3 % for the optical signal recovery with a 25 km-distortion, and a mean BER of 3 % for a 50 km-distortion. This error rate has been achieved when processing the signal at a processing speed of 51.3 Mb/s (because of the feedback length).

We observed yet that the performance reached while processing two tasks simultaneously are slightly lower than the performance obtained while processing a single task. A trade-off is needed therefore between the overall performance and the processing speed of the data. It is interesting also to note that the speed of the experimental system could be increased by reducing the length of the delay-line, which was not possible with our setup.

6

Conclusion and perspectives

Stuff your eyes with wonder, he said, live as if you'd drop dead in 10 seconds. See the world. It's more fantastic than any dream made or paid for in factories.

Ray Bradbury, *Fahrenheit 451*

Contents

6.1 Summary of the dissertation 130

6.2 Perspective for future work 131

Through this thesis, we discussed the possibility to realize a photonic reservoir computing device, made of telecommunication components. The architecture we proposed is within the framework of time-delay reservoir computer using a VCSEL as physical neuron and single mode silica fiber to realize the feedback loop. The study of this system has been realized both numerically and experimentally. More specifically, we studied the possible use of the polarization dynamics of the VCSEL to enhance the computational performance of the photonic reservoir.
In this chapter, we propose a summary of this thesis, and more specifically of the main results presented in this dissertation. We will then present the possible perspectives of this work.

6.1 Summary of the dissertation

In Chapter 2, we have presented the basics of the physics of semiconductor lasers. We first remind that a laser is composed of three main elements: a gain medium to amplify light, a cavity to be wavelength selective, and a pump to compensate for the losses. A laser can be realized with semiconductor materials, which allows realizing small and cheap components. We can distinguish lasers emitting light from the edge (EEL) and lasers emitting from the surface (VCSEL). This last kind of laser has several advantages which makes it largely used in different fields, such as telecommunication networks, in biology or in smartphones. A semiconductor laser can exhibit different dynamics while submitted to feedback or injection. It can exhibit steady state, oscillating dynamics or chaotic dynamics. The dynamics of a laser can also be modified while modulating the optical injected beam. This complex dynamics is already used, to mimic natural phenomena, or to process signals for instance.

In Chapter 3, we have presented the basic knowledge of reservoir computing. We first introduce the artificial neural network, and the two main topologies of network: the feedforward and the recurrent neural network. Due to its training complexity, the reservoir computing paradigm has been proposed. This paradigm consists in using a fixed recurrent neural network, and training only a readout layer thanks to simple regression algorithm. In reservoir computing, we focused more specifically on the time-delay reservoir computing. This architecture is composed of a single physical neuron with a feedback loop, along which virtual neurons are distributed. We presented several examples of reservoir computing device, using mechanical electronic or photonic components. We finally presented tasks that are commonly used to benchmark reservoir computing devices: memory capacity and computational ability that are task independent, and the Santa-Fe time series prediction and the nonlinear channel equalization.

In Chapter 4, we have presented the performance of our reservoir computing device processing a single task. We first introduced our architecture made of a VCSEL and single mode silica fiber, based on time-delay reservoir computing paradigm. We used the spin-flip model (SFM) to simulate the system and explore the space of parameters of the system by either injecting the input electrically or optically. We also explored the influence of the polarization of the optical feedback. We drew two main conclusions: (i) the input injected optically leads to better and faster performance, and (ii) using polarization-rotated optical feedback allows doubling the memory capacity of the reservoir computer, hence potentially reaching better performance on applied tasks. The experimental confirmation of this last observation has been detailed, after presenting the experimental setup. We finally compared the numerical and experimental performance of the reservoir computer and have been able to demonstrate that both are consistent if we take into account the level of noise in the output layer. This also allowed showing that this level of noise greatly impact the performance of the reservoir computer.

In Chapter 5, we finally explored the performance of our proposed architecture processing two tasks simultaneously. We adapted the model of the previous chapter to be able to inject the two tasks: each task is injected in a different polarization mode of the VCSEL. We tested the influence of the nonlinear coupling between the two polarization modes via the polarization of the feedback, the spin relaxation, and the birefringence parameter on the memory capacity of the reservoir, and on its performance when processing telecommunication tasks. We have been able to prove that coupling these two polarization modes decreases the performance of the reservoir, implying also that isotropic feedback provides better performance in this case. We also proved that the ratio of the injection power between the two polarization modes can be used to tune the splitting of performance between the two processed tasks. This last conclusion has also been demonstrated experimentally. We finally compared the performance of the numerical and experimental systems. We prove thanks to this observation that while processing two tasks, the level of noise in the output layer does not play a significant role, contrary to what is concluded from the processing of a single task.

6.2 Perspective for future work

We presented in this thesis the performance of a photonic time-delay reservoir computer based on the VCSEL dynamics.

However, the training and the testing have been realized offline, meaning that all the

inputs are sent at once, and the output is recorded in one measurement and processed in a single process. A study focused on processing signals online can be interesting. Online processing consists in processing the inputs one at a time and adapting the learned weights online. This is closer to the use of the reservoir computing in real conditions. However, due to the processing speed of photonic components, the online application of the weights to produce the final output remains a technical challenge. Such an approach has been proposed using an optical integrator and a high-speed Mach-Zehnder modulator, for a reservoir made with an EEL [162]. Applying a similar technique to our architecture can be interesting. Adding an adaptation of the weights to take into account the ageing process of the components could also be an interesting study.

Another interesting study would be to improve the experimental setup to reduce the length of the feedback loop in order to assess if the setup is able to process signals at the data rate predicted numerically (about 3 Gb/s).

We observed in this dissertation that the SNR is a crucial issue in the experiment, due to the low emitted power of the VCSEL. Replacing the VCSEL with a more powerful one (emitting about 2 mW when biased near the threshold) would also help reaching significantly better SNR and might thus improve the overall performance of the system. Even though such a VCSEL emitting at 1550 nm does not exist yet, we could test the impact of a higher emitted power with a VCSEL emitting at 1310 nm or 850 nm. One might also expect that a powerful VCSEL at 1550 nm could be developed in the next few years.

We also focus our work on a specific architecture. We could imagine a time-delay based architecture, cascading VCSELs instead of using only one. This would change the overall dynamics of the reservoir computer. By adding a new physical device, we can hope to improve the memory capacity of the system, and therefore to be able to process more complex tasks, such as recovery of signal distorted by a longer fiber (several hundreds of kilometers).

Bibliography

[1] G. M. D. T. Forecast, "Cisco visual networking index: global mobile data traffic forecast update, 2017–2022," *Update*, vol. 2017, p. 2022, 2019.

[2] T. Chouard, "Legacy of a universal mind," *Nature*, vol. 482, no. 7386, pp. 455–455, 2012.

[3] D. Ciregan, U. Meier, and J. Schmidhuber, "Multi-column deep neural networks for image classification," in *2012 IEEE conference on computer vision and pattern recognition*, pp. 3642–3649, IEEE, 2012.

[4] D. Amodei, S. Ananthanarayanan, R. Anubhai, J. Bai, E. Battenberg, C. Case, J. Casper, B. Catanzaro, Q. Cheng, G. Chen, *et al.*, "Deep speech 2: End-to-end speech recognition in english and mandarin," in *International conference on machine learning*, pp. 173–182, 2016.

[5] D. Jurafsky, *Speech & language processing*. Pearson Education India, 2000.

[6] A. Lugnan, A. Katumba, F. Laporte, M. Freiberger, S. Sackesyn, C. Ma, E. Gooskens, J. Dambre, and P. Bienstman, "Photonic neuromorphic information processing and reservoir computing," *APL Photonics*, vol. 5, no. 2, 2020.

[7] D. Brunner and I. Fischer, "Reconfigurable semiconductor laser networks based on diffractive coupling," *Optics Letters*, vol. 40, no. 16, p. 3854, 2015.

[8] L. Appeltant, M. C. Soriano, G. Van Der Sande, J. Danckaert, S. Massar, J. Dambre, B. Schrauwen, C. R. Mirasso, and I. Fischer, "Information processing using a single dynamical node as complex system," *Nature Communications*, vol. 2, no. 1, pp. 466–468, 2011.

[9] L. Larger, M. C. Soriano, D. Brunner, L. Appeltant, J. M. Gutierrez, L. Pesquera, C. R. Mirasso, and I. Fischer, "Photonic information processing beyond Turing: an optoelectronic implementation of reservoir computing," *Optics Express*, vol. 20, no. 3, p. 3241, 2012.

[10] Y. Paquot, F. Duport, A. Smerieri, J. Dambre, B. Schrauwen, M. Haelterman, and S. Massar, "Optoelectronic reservoir computing," *Scientific Reports*, vol. 2, pp. 1–6, 2012.

[11] F. Duport, B. Schneider, A. Smerieri, M. Haelterman, and S. Massar, "All-optical reservoir computing," *Optics Express*, vol. 20, no. 20, p. 22783, 2012.

[12] K. Hicke, M. Escalona, D. Brunner, M. C. Soriano, I. Fischer, and C. R. Mirasso, "Information processing using transient dynamics of semiconductor lasers subject to delayed feedback," *IEEE Journal of Selected Topics in Quantum Electronics*, vol. 19, no. 4, p. 1501610, 2013.

[13] R. Modeste Nguimdo, G. Verschaffelt, J. Danckaert, and G. Van Der Sande, "Simultaneous computation of two independent tasks using reservoir computing based on a single photonic nonlinear node with optical feedback," *IEEE Transactions on Neural Networks and Learning Systems*, vol. 26, no. 12, pp. 3301–3307, 2015.

[14] A. Argyris, J. Bueno, and I. Fischer, "Photonic machine learning implementation for signal recovery in optical communications," *Scientific Reports*, no. April, pp. 1–13, 2017.

[15] J. B. Héroux, N. Kanazawa, and D. Nakano, "Delayed Feedback Reservoir Computing with VCSEL," pp. 594–602, 2018.

[16] L. Larger, A. Baylón-Fuentes, R. Martinenghi, V. S. Udaltsov, Y. K. Chembo, and M. Jacquot, "High-speed photonic reservoir computing using a time-delay-based architecture: Million words per second classification," *Physical Review X*, vol. 7, no. 1, 2017.

[17] J. Vatin, D. Rontani, and M. Sciamanna, "Enhanced performance of a reservoir computer using polarization dynamics in VCSELs," *Optics Letters*, vol. 43, p. 4497, sep 2018.

[18] J. Vatin, D. Rontani, and M. Sciamanna, "Experimental reservoir computing using VCSEL polarization dynamics," *Optics Express*, vol. 27, p. 18579, jun 2019.

[19] J. Vatin, D. Rontani, and M. Sciamanna, "Experimental realization of dual task processing with a photonic reservoir computer," *APL Photonics*, vol. 5, no. 8, p. 086105, 2020.

[20] J. Vatin, D. Rontani, and M. Sciamanna, "High-Speed All-Optical Reservoir Computing Using VCSEL Polarization Dynamics," *2018 European Conference on Optical Communication (ECOC)*, pp. 1–3, sep 2018.

[21] J. Vatin, D. Rontani, and M. Sciamanna, "Reservoir computing using vcsel polarization dynamics," in *The European Conference on Lasers and Electro-Optics*, p. cb_10_4, Optical Society of America, 2019.

[22] J. Vatin, D. Rontani, and M. Sciamanna, "Polarization dynamics of vcsels improves reservoir computing performance," in *International Conference on Artificial Neural Networks*, pp. 180–183, Springer, 2019.

[23] "Laser | signification, définition dans le dictionnaire anglais de cambridge," 2020.

[24] A. Einstein, "Strahlungs-emission und-absorption nach der quantentheorie, 17 jul 1916," 1916.

[25] T. H. Maiman and et al., "Stimulated optical radiation in ruby.," *Nature*, vol. 187, pp. 493—-494, 1960.

[26] A. Javan, W. R. Bennett Jr, and D. R. Herriott, "Population inversion and continuous optical maser oscillation in a gas discharge containing a he-ne mixture," *Physical Review Letters*, vol. 6, no. 3, p. 106, 1961.

[27] R. N. Hall, G. E. Fenner, J. Kingsley, T. Soltys, and R. Carlson, "Coherent light emission from gaas junctions," *Physical Review Letters*, vol. 9, no. 9, p. 366, 1962.

[28] G. P. Agrawal and N. K. Dutta, *Semiconductor lasers*. Springer Science & Business Media, 2013.

[29] H. Kroemer, "A proposed class of hetero-junction injection lasers," *Proceedings of the IEEE*, vol. 51, no. 12, pp. 1782–1783, 1963.

[30] Z. I. Alferov, V. Andreev, D. Garbuzov, Y. V. Zhilyaev, E. Morozov, E. Portnoi, and V. Trofim, "Investigation of the influence of the alas-gaas heterostructure parameters on the laser threshold current and the realization of continuous emission at room temperature," *Sov. Phys. Semicond*, vol. 4, no. 9, pp. 1573–1575, 1971.

[31] H. Soda, K.-i. Iga, C. Kitahara, and Y. Suematsu, "Gainasp/inp surface emitting injection lasers," *Japanese Journal of Applied Physics*, vol. 18, no. 12, p. 2329, 1979.

[32] M. Ogura, W. Hsin, M.-C. Wu, S. Wang, J. R. Whinnery, S. Wang, and J. J. Yang, "Surface-emitting laser diode with vertical gaas/gaalas quarter-wavelength multilayers and lateral buried heterostructure," *Applied physics letters*, vol. 51, no. 21, pp. 1655–1657, 1987.

[33] J. Jewell, A. Scherer, S. McCall, Y.-H. Lee, S. Walker, J. Harbison, and L. Florez, "Low-threshold electrically pumped vertical-cavity surface-emitting microlasers," *Electronics Letters*, vol. 25, no. 17, pp. 1123–1124, 1989.

[34] "Optoelectronic next raycan," 2007.

[35] P. J. Winzer, D. T. Neilson, and A. R. Chraplyvy, "Fiber-optic transmission and networking: the previous 20 and the next 20 years [Invited]," *Optics Express*, vol. 26, no. 18, p. 24190, 2018.

[36] C. K. Kao and M. S. Maklad, "High-strength optical preforms and fibers with thin, high-compression outer layers," Jan. 6 1981. US Patent 4,243,298.

[37] E. Desurvire, J. R. Simpson, and P. Becker, "High-gain erbium-doped traveling-wave fiber amplifier," *Optics letters*, vol. 12, no. 11, pp. 888–890, 1987.

[38] A. L. Birkbeck, R. A. Flynn, M. Ozkan, D. Song, M. Gross, and S. C. Esener, "Vcsel arrays as micromanipulators in chip-based biosystems," *Biomedical Microdevices*, vol. 5, pp. 47–54, Mar 2003.

[39] T. Svensson, M. Andersson, L. Rippe, S. Svanberg, S. Andersson-Engels, J. Johansson, and S. Folestad, "Vcsel-based oxygen spectroscopy for structural analysis of pharmaceutical solids," *Applied Physics B*, vol. 90, pp. 345–354, Feb 2008.

[40] M. Grabherr, H. Moench, and A. Pruijmboom, "Vcsels for optical mice and sensing," *VCSELs, Springer Series in Optical Sciences, Volume 166. ISBN 978-3-642-24985-3. Springer-Verlag Berlin Heidelberg, 2013, p. 521*, vol. 166, pp. 521–, 10 2013.

[41] B. Pesach and Z. Mor, "Projectors of structured light," June 10 2014. US Patent 8,749,796.

[42] A. Lipson, "Low cost small size lidar for automotive," Nov. 28 2017. US Patent 9,831,630.

[43] J. Ohtsubo, *Semiconductor lasers: stability, instability and chaos*, vol. 111. Springer, 2012.

[44] G. H. M. van Tartwijk and D. Lenstra, "Semiconductor lasers with optical injection and feedback," *Quantum and Semiclassical Optics: Journal of the European Optical Society Part B*, vol. 7, pp. 87–143, apr 1995.

[45] R. Tkach and A. Chraplyvy, "Regimes of feedback effects in 1.5-µm distributed feedback lasers," *Journal of Lightwave Technology*, vol. 4, no. 11, pp. 1655–1661, 1986.

[46] T. Simpson, J.-M. Liu, A. Gavrielides, V. Kovanis, and P. Alsing, "Period-doubling route to chaos in a semiconductor laser subject to optical injection," *Applied Physics Letters*, vol. 64, no. 26, pp. 3539–3541, 1994.

[47] S. Kobayashi and T. Kimura, "Injection locking characteristics of an algaas semiconductor laser," *IEEE Journal of Quantum Electronics*, vol. 16, no. 9, pp. 915–917, 1980.

[48] T. Simpson, J. Liu, and A. Gavrielides, "Bandwidth enhancement and broadband noise reduction in injection-locked semiconductor lasers," *IEEE Photonics Technology Letters*, vol. 7, no. 7, pp. 709–711, 1995.

[49] H. Chen, J. Liu, and T. Simpson, "Response characteristics of direct current modulation on a bandwidth-enhanced semiconductor laser under strong injection locking," *Optics communications*, vol. 173, no. 1-6, pp. 349–355, 2000.

[50] T. Simpson, J. Liu, K.-F. Huang, and K. Tai, "Nonlinear dynamics induced by external optical injection in semiconductor lasers," *Quantum and Semiclassical Optics: Journal of the European Optical Society Part B*, vol. 9, no. 5, p. 765, 1997.

[51] J. Bueno, D. Brunner, M. C. Soriano, and I. Fischer, "Conditions for reservoir computing performance using semiconductor lasers with delayed optical feedback," *Optics Express*, vol. 25, no. 3, p. 2401, 2017.

[52] M. Shimizu, F. Koyama, and K. Iga, "Polarization characteristics of mocvd grown gaas/gaalas cbh surface emitting lasers," *Japanese journal of applied physics*, vol. 27, no. 9R, p. 1774, 1988.

[53] J. Martin-Regalado, J. Chilla, J. Rocca, and P. Brusenbach, "Polarization switching in vertical-cavity surface emitting lasers observed at constant active region temperature," *Applied physics letters*, vol. 70, no. 25, pp. 3350–3352, 1997.

[54] G. Verschaffelt, K. Panajotov, J. Albert, B. Nagler, M. Peeters, J. Danckaert, I. Veretennicoff, and H. Thienpont, "Polarisation switching in vertical-cavity surface-emitting lasers: from experimental observations to applications," *OPTOELECTRONICS REVIEW*, no. 3, pp. 257–268, 2001.

[55] A. Jansen van Doorn, M. Van Exter, and J. Woerdman, "Elasto-optic anisotropy and polarization orientation of vertical-cavity surface-emitting semiconductor lasers," *Applied physics letters*, vol. 69, no. 8, pp. 1041–1043, 1996.

[56] M. Van Exter, A. J. van Doorn, and J. Woerdman, "Electro-optic effect and birefringence in semiconductor vertical-cavity lasers," *Physical Review A*, vol. 56, no. 1, p. 845, 1997.

[57] M. Virte, K. Panajotov, H. Thienpont, and M. Sciamanna, "Deterministic polarization chaos from a laser diode," *Nature Photonics*, vol. 7, no. 1, p. 60, 2013.

[58] K. D. Choquette, D. Richie, and R. Leibenguth, "Temperature dependence of gain-guided vertical-cavity surface emitting laser polarization," *Applied physics letters*, vol. 64, no. 16, pp. 2062–2064, 1994.

[59] B. Ryvkin, K. Panajotov, A. Georgievski, J. Danckaert, M. Peeters, G. Verschaffelt, H. Thienpont, and I. Veretennicoff, "Effect of photon-energy-dependent loss and gain mechanisms on polarization switching in vertical-cavity surface-emitting lasers," *JOSA B*, vol. 16, no. 11, pp. 2106–2113, 1999.

[60] M. San Miguel, Q. Feng, and J. V. Moloney, "Light-polarization dynamics in surface-emitting semiconductor lasers," *Phys. Rev. A*, vol. 52, pp. 1728–1739, Aug 1995.

[61] J. Dennis, *The Bird in the Waterfall: A Natural History of Oceans, Rivers and Lakes*. Harper-Collins Publishers, 1996.

[62] C.-H. Uy, D. Rontani, and M. Sciamanna, "Vectorial extreme events in vcsel polarization dynamics," *Optics Letters*, vol. 42, no. 11, pp. 2177–2180, 2017.

[63] D. R. Solli, C. Ropers, P. Koonath, and B. Jalali, "Optical rogue waves," *Nature*, vol. 450, no. 7172, pp. 1054–1057, 2007.

[64] A. K. Dal Bosco, D. Wolfersberger, and M. Sciamanna, "Extreme events in time-delayed nonlinear optics," *Optics letters*, vol. 38, no. 5, pp. 703–705, 2013.

[65] É. Mercier, A. Even, E. Mirisola, D. Wolfersberger, and M. Sciamanna, "Numerical study of extreme events in a laser diode with phase-conjugate optical feedback," *Physical Review E*, vol. 91, no. 4, p. 042914, 2015.

[66] F. Baronio, B. Frisquet, S. Chen, G. Millot, S. Wabnitz, and B. Kibler, "Observation of a group of dark rogue waves in a telecommunication optical fiber," *Physical Review A*, vol. 97, no. 1, p. 013852, 2018.

[67] H. M. Smith, "Synchronous flashing of fireflies," *Science*, vol. 82, no. 2120, pp. 151–152, 1935.

[68] M. R. Tinsley, S. Nkomo, and K. Showalter, "Chimera and phase-cluster states in populations of coupled chemical oscillators," *Nature Physics*, vol. 8, no. 9, pp. 662–665, 2012.

[69] A. M. Hagerstrom, T. E. Murphy, R. Roy, P. Hövel, I. Omelchenko, and E. Schöll, "Experimental observation of chimeras in coupled-map lattices," *Nature Physics*, vol. 8, no. 9, pp. 658–661, 2012.

[70] E. A. Martens, S. Thutupalli, A. Fourrière, and O. Hallatschek, "Chimera states in mechanical oscillator networks," *Proceedings of the National Academy of Sciences*, vol. 110, no. 26, pp. 10563–10567, 2013.

[71] C.-H. Uy, L. Weicker, D. Rontani, and M. Sciamanna, "Optical chimera in light polarization," *APL Photonics*, vol. 4, no. 5, p. 056104, 2019.

[72] P. A. Rutecki, "Neuronal excitability: voltage-dependent currents and synaptic transmission," *Journal of clinical neurophysiology*, vol. 9, no. 2, pp. 195–211, 1992.

[73] R. FitzHugh, "Mathematical models of threshold phenomena in the nerve membrane," *The bulletin of mathematical biophysics*, vol. 17, no. 4, pp. 257–278, 1955.

[74] F. Ponulak and A. Kasinski, "Introduction to spiking neural networks: Information processing, learning and applications.," *Acta neurobiologiae experimentalis*, vol. 71, no. 4, pp. 409–433, 2011.

[75] H.-T. Peng, G. Angelatos, T. F. de Lima, M. A. Nahmias, A. N. Tait, S. Abbaslou, B. J. Shastri, and P. R. Prucnal, "Temporal information processing with an integrated laser neuron," *IEEE Journal of Selected Topics in Quantum Electronics*, vol. 26, no. 1, pp. 1–9, 2019.

[76] J. Robertson, T. Deng, J. Javaloyes, and A. Hurtado, "Controlled inhibition of spiking dynamics in vcsels for neuromorphic photonics: theory and experiments," *Optics Letters*, vol. 42, no. 8, pp. 1560–1563, 2017.

[77] T. Deng, J. Robertson, Z. Wu, G. Xia, X. Lin, X. Tang, Z. Wang, and A. Hurtado, "Stable propagation of inhibited spiking dynamics in vertical-cavity surface-emitting lasers for neuromorphic photonic networks," *IEEE Access*, vol. 6, pp. 67951–67958, 2018.

[78] S. Xiang, A. Wen, and W. Pan, "Emulation of spiking response and spiking frequency property in vcsel-based photonic neuron," *IEEE Photonics Journal*, vol. 8, no. 5, pp. 1–9, 2016.

[79] T. Erneux and S. Barbay, "Two distinct excitable responses for a laser with a saturable absorber," *Physical Review E*, vol. 97, no. 6, p. 062214, 2018.

[80] C. R. Mirasso, P. Colet, and P. García-Fernández, "Synchronization of chaotic semiconductor lasers: Application to encoded communications," *IEEE Photonics Technology Letters*, vol. 8, no. 2, pp. 299–301, 1996.

[81] M. Sciamanna and K. A. Shore, "Physics and applications of laser diode chaos," *Nature photonics*, vol. 9, no. 3, pp. 151–162, 2015.

[82] L. M. Pecora, T. L. Carroll, G. A. Johnson, D. J. Mar, and J. F. Heagy, "Fundamentals of synchronization in chaotic systems, concepts, and applications," *Chaos: An Interdisciplinary Journal of Nonlinear Science*, vol. 7, no. 4, pp. 520–543, 1997.

[83] R. Roy and K. S. Thornburg Jr, "Experimental synchronization of chaotic lasers," *Physical Review Letters*, vol. 72, no. 13, p. 2009, 1994.

[84] A. Argyris, D. Syvridis, L. Larger, V. Annovazzi-Lodi, P. Colet, I. Fischer, J. Garcia-Ojalvo, C. R. Mirasso, L. Pesquera, and K. A. Shore, "Chaos-based communications at high bit rates using commercial fibre-optic links," *Nature*, vol. 438, no. 7066, pp. 343–346, 2005.

[85] A. Uchida, K. Amano, M. Inoue, K. Hirano, S. Naito, H. Someya, I. Oowada, T. Kurashige, M. Shiki, S. Yoshimori, K. Yoshimura, and P. Davis, "Fast physical random bit generation with chaotic semiconductor lasers," *Nature Photonics*, vol. 2, pp. 728–732, Dec 2008.

[86] A. Argyris, S. Deligiannidis, E. Pikasis, A. Bogris, and D. Syvridis, "Implementation of 140 gb/s true random bit generator based on a chaotic photonic integrated circuit," *Optics express*, vol. 18, no. 18, pp. 18763–18768, 2010.

[87] N. Oliver, M. C. Soriano, D. W. Sukow, and I. Fischer, "Dynamics of a semiconductor laser with polarization-rotated feedback and its utilization for random bit generation," *Optics letters*, vol. 36, no. 23, pp. 4632–4634, 2011.

[88] M. Virte, E. Mercier, H. Thienpont, K. Panajotov, and M. Sciamanna, "Physical random bit generation from chaotic solitary laser diode," *Optics express*, vol. 22, no. 14, pp. 17271–17280, 2014.

[89] G. Bouchez, C.-H. Uy, B. Macias, D. Wolfersberger, and M. Sciamanna, "Wideband chaos from a laser diode with phase-conjugate feedback," *Optics letters*, vol. 44, no. 4, pp. 975–978, 2019.

[90] C. H. Pua, W. Y. Chong, and H. Ahmad, "Instantaneous response of wide area intrusion sensor with long haul monitoring capability," *IEEE Photonics Technology Letters*, vol. 25, no. 23, pp. 2255–2258, 2013.

[91] Y. Zhang, M. Zhang, W. Jin, H. Ho, M. Demokan, X. Fang, B. Culshaw, and G. Stewart, "Investigation of erbium-doped fiber laser intra-cavity absorption sensor for gas detection," *Optics Communications*, vol. 234, no. 1, pp. 435 – 441, 2004.

[92] V. Girardeau, C. Goloni, O. Jacquin, O. Hugon, M. Inglebert, and E. Lacot, "Nonlinear laser dynamics induced by frequency shifted optical feedback: application to vibration measurements," *Applied optics*, vol. 55, no. 34, pp. 9638 – 9638, 2016.

[93] W. S. McCulloch and W. Pitts, "A logical calculus of the ideas immanent in nervous activity," *The bulletin of mathematical biophysics*, vol. 5, pp. 115–133, Dec 1943.

[94] F. Rosenblatt, "Principles of neurodynamics (new york: Spartan)," 1962.

[95] D. E. Rumelhart, G. E. Hinton, and R. J. Williams, "Learning representations by back-propagating errors," *nature*, vol. 323, no. 6088, pp. 533–536, 1986.

[96] T. D. Sanger, "Optimal unsupervised learning in a single-layer linear feedforward neural network," *Neural Networks*, vol. 2, no. 6, pp. 459 – 473, 1989.

[97] H. Jaeger, "A tutorial on training recurrent neural networks , covering BPPT , RTRL , EKF and the " echo state network " approach," *ReVision*, vol. 2002, pp. 1–46, 2005.

[98] I. Sutskever, *Training recurrent neural networks*. University of Toronto Toronto, Canada, 2013.

[99] E. M. Izhikevich, *Dynamical systems in neuroscience*. MIT press, 2007.

[100] A. L. Hodgkin and A. F. Huxley, "A quantitative description of membrane current and its application to conduction and excitation in nerve," *The Journal of Physiology*, vol. 117, no. 4, pp. 500–544, 1952.

[101] P. Y. Ma, B. J. Shastri, T. F. De Lima, A. N. Tait, M. A. Nahmias, and P. R. Prucnal, "All-optical digital-to-spike conversion using a graphene excitable laser," *Optics Express*, vol. 25, no. 26, pp. 33504–33513, 2017.

[102] T. Van Vaerenbergh, M. Fiers, J. Dambre, and P. Bienstman, "Simplified description of self-pulsation and excitability by thermal and free-carrier effects in semiconductor microcavities," *Physical Review A*, vol. 86, no. 6, p. 063808, 2012.

[103] A. Van Schaik, "Building blocks for electronic spiking neural networks," *Neural networks*, vol. 14, no. 6-7, pp. 617–628, 2001.

[104] Y. V. Pershin and M. Di Ventra, "Experimental demonstration of associative memory with memristive neural networks," *Neural networks*, vol. 23, no. 7, pp. 881–886, 2010.

[105] T. Van Vaerenbergh, M. Fiers, P. Mechet, T. Spuesens, R. Kumar, G. Morthier, B. Schrauwen, J. Dambre, and P. Bienstman, "Cascadable excitability in microrings," *Optics express*, vol. 20, no. 18, pp. 20292–20308, 2012.

[106] A. N. Tait, M. A. Nahmias, B. J. Shastri, and P. R. Prucnal, "Broadcast and weight: an integrated network for scalable photonic spike processing," *Journal of Lightwave Technology*, vol. 32, no. 21, pp. 4029–4041, 2014.

[107] O. Bichler, D. Querlioz, S. J. Thorpe, J.-P. Bourgoin, and C. Gamrat, "Extraction of temporally correlated features from dynamic vision sensors with spike-timing-dependent plasticity," *Neural Networks*, vol. 32, pp. 339–348, 2012.

[108] L. F. Abbott and S. B. Nelson, "Synaptic plasticity: taming the beast," *Nature neuroscience*, vol. 3, no. 11, pp. 1178–1183, 2000.

[109] J. J. Wade, L. J. McDaid, J. A. Santos, and H. M. Sayers, "Swat: a spiking neural network training algorithm for classification problems," *IEEE Transactions on Neural Networks*, vol. 21, no. 11, pp. 1817–1830, 2010.

[110] J. H. Lee, T. Delbruck, and M. Pfeiffer, "Training deep spiking neural networks using backpropagation," *Frontiers in neuroscience*, vol. 10, p. 508, 2016.

[111] W. Maass, T. Natschläger, and H. Markram, "Real-time computing without stable states: A new framework for neural computation based on perturbations," *Neural Computation*, vol. 14, no. 11, pp. 2531–2560, 2002.

[112] M. Lukoševičius and H. Jaeger, "Reservoir computing approaches to recurrent neural network training," *Computer Science Review*, vol. 3, no. 3, pp. 127–149, 2009.

[113] H. Jaeger and H. Haas, "Harnessing Nonlinearity: Predicting Chaotic Systems and Saving Energy in Wireless Communication," *Science*, vol. 304, no. 5667, pp. 78–80, 2004.

[114] H. Jaeger, "Short term memory in echo state networks. gmd-report 152," in *GMD-German National Research Institute for Computer Science (2002), http://www. faculty. jacobs-university. de/hjaeger/pubs/STMEchoStatesTechRep. pdf*, Citeseer, 2002.

[115] P. Antonik, M. Haelterman, and S. Massar, "Online Training for High-Performance Analogue Readout Layers in Photonic Reservoir Computers," *Cognitive Computation*, vol. 9, no. 3, pp. 297–306, 2017.

[116] R. Penrose, "A generalized inverse for matrices," in *Mathematical proceedings of the Cambridge philosophical society*, vol. 51, pp. 406–413, Cambridge University Press, 1955.

[117] C. Fernando and S. Sojakka, "Pattern Recognition in a Bucket," pp. 588–597, 2003.

[118] M. Le Berre, E. Ressayre, A. Tallet, H. M. Gibbs, D. L. Kaplan, and M. H. Rose, "Conjecture on the dimensions of chaotic attractors of delayed-feedback dynamical systems," *Phys. Rev. A*, vol. 35, pp. 4020–4022, May 1987.

[119] D. Brunner, B. Penkovsky, B. A. Marquez, M. Jacquot, I. Fischer, and L. Larger, "Tutorial: Photonic neural networks in delay systems," *Journal of Applied Physics*, vol. 124, no. 15, 2018.

[120] J. Nakayama, K. Kanno, and A. Uchida, "Laser dynamical reservoir computing with consistency: an approach of a chaos mask signal," *Optics Express*, vol. 24, no. 8, p. 8679, 2016.

[121] K. Nakajima, H. Hauser, T. Li, and R. Pfeifer, "Information processing via physical soft body," *Scientific Reports*, vol. 5, pp. 1–11, 2015.

[122] K. Caluwaerts, J. Despraz, A. Işçen, A. P. Sabelhaus, J. Bruce, B. Schrauwen, and V. SunSpiral, "Design and control of compliant tensegrity robots through simulation and hardware validation," *Journal of The Royal Society Interface*, vol. 11, no. 98, p. 20140520, 2014.

[123] N. D. Nikolic, S. Häusler, N. W. Singer, and W. Maass, "Temporal dynamics of information content carried by neurons in the primary visual cortex," in *Advances in Neural Information Processing Systems*, pp. 1041–1048, MIT Press, 2007.

[124] M. S. Kulkarni and C. Teuscher, "Memristor-based reservoir computing," in *Proceedings of the 2012 IEEE/ACM International Symposium on Nanoscale Architectures*, NANOARCH '12, (New York, NY, USA), p. 226–232, Association for Computing Machinery, 2012.

[125] J. Torrejon, M. Riou, F. A. Araujo, S. Tsunegi, G. Khalsa, D. Querlioz, P. Bortolotti, V. Cros, K. Yakushiji, A. Fukushima, H. Kubota, S. Yuasa, M. D. Stiles, and J. Grollier, "Neuromorphic computing with nanoscale spintronic oscillators," *Nature*, vol. 547, pp. 428–431, Jul 2017.

[126] G. Tanaka, T. Yamane, J. B. Héroux, R. Nakane, N. Kanazawa, S. Takeda, H. Numata, D. Nakano, and A. Hirose, "Recent advances in physical reservoir computing: A review," *Neural Networks*, vol. 115, pp. 100–123, 2019.

[127] J. Pauwels, G. V. der Sande, A. Bouwens, M. Haelterman, and S. Massar, "Towards high-performance spatially parallel optical reservoir computing," in *Neuro-inspired Photonic Computing* (M. Sciamanna and P. Bienstman, eds.), vol. 10689, pp. 7 – 12, International Society for Optics and Photonics, SPIE, 2018.

[128] J. Bueno, S. Maktoobi, L. Froehly, I. Fischer, M. Jacquot, L. Larger, and D. Brunner, "Reinforcement learning in a large-scale photonic recurrent neural network," *Optica*, vol. 5, p. 756, jun 2018.

[129] P. Antonik, N. Marsal, and D. Rontani, "Large-Scale Spatiotemporal Photonic Reservoir Computer for Image Classification," *IEEE Journal of Selected Topics in Quantum Electronics*, vol. 26, pp. 1–12, jan 2020.

[130] M. Rafayelyan, J. Dong, Y. Tan, F. Krzakala, and S. Gigan, "Large-scale optical reservoir computing for spatiotemporal chaotic systems prediction," *arXiv preprint arXiv:2001.09131*, 2020.

[131] S. Maktoobi, L. Froehly, L. Andreoli, X. Porte, M. Jacquot, L. Larger, and D. Brunner, "Diffractive coupling for photonic networks: How big can we go?," *IEEE Journal of Selected Topics in Quantum Electronics*, vol. 26, pp. 1–8, Jan 2020.

[132] K. Vandoorne, P. Mechet, T. Van Vaerenbergh, M. Fiers, G. Morthier, D. Verstraeten, B. Schrauwen, J. Dambre, and P. Bienstman, "Experimental demonstration of reservoir computing on a silicon photonics chip," *Nature Communications*, vol. 5, pp. 1–6, 2014.

[133] A. Katumba, M. Freiberger, P. Bienstman, and J. Dambre, "A Multiple-Input Strategy to Efficient Integrated Photonic Reservoir Computing," *Cognitive Computation*, vol. 9, no. 3, pp. 307–314, 2017.

[134] S. Sackesyn, C. Ma, J. Dambre, and P. Bienstman, "An enhanced architecture for silicon photonic reservoir computing," in *Cognitive Computing 2018-Merging Concepts with Hardware*, pp. 1–2, 2018.

[135] F. Denis-Le Coarer, M. Sciamanna, A. Katumba, M. Freiberger, J. Dambre, P. Bienstman, and D. Rontani, "All-Optical Reservoir Computing on a Photonic Chip Using Silicon-Based Ring Resonators," *IEEE Journal of Selected Topics in Quantum Electronics*, vol. 24, pp. 1–8, nov 2018.

[136] D. Brunner, M. C. Soriano, C. R. Mirasso, and I. Fischer, "Parallel photonic information processing at gigabyte per second data rates using transient states," *Nature Communications*, vol. 4, pp. 1364–1367, 2013.

[137] P. Antonik, M. Haelterman, and S. Massar, "Brain-Inspired Photonic Signal Processor for Generating Periodic Patterns and Emulating Chaotic Systems," *Physical Review Applied*, vol. 7, no. 5, pp. 1–16, 2017.

[138] K. Harkhoe and Van der Sande, "Task-Independent Computational Abilities of Semiconductor Lasers with Delayed Optical Feedback for Reservoir Computing," *Photonics*, vol. 6, p. 124, dec 2019.

[139] R. M. Nguimdo, G. Verschaffelt, J. Danckaert, and G. Van der Sande, "Fast photonic information processing using semiconductor lasers with delayed optical feedback: Role of phase dynamics," *Optics Express*, vol. 22, no. 7, p. 8672, 2014.

[140] K. Takano, C. Sugano, M. Inubushi, K. Yoshimura, S. Sunada, K. Kanno, and A. Uchida, "Compact reservoir computing with a photonic integrated circuit," *Optics Express*, vol. 26, no. 22, p. 29424, 2018.

[141] R. M. Nguimdo and T. Erneux, "Enhanced performances of a photonic reservoir computer based on a single delayed quantum cascade laser," *Opt. Lett.*, vol. 44, pp. 49–52, Jan 2019.

[142] V. Vapnik, "Statistical learning theory. john wiley&sons," *Inc., New York*, 1998.

[143] L. Appeltant, J. Danckaert, I. Fischer, and G. V. D. Sande, "Reservoir Computing based on Delay-dynamical Systems Joint PhD Vrije Universiteit Brussel and Universitat de les Illes Balears," no. May, 2012.

[144] N. A. Gershenfeld and A. S. Weigend, "The Future of Time Series: Forecasting the Future and Understanding the Past," *Time Series Prediction: Forecasting the Future and Understanding the Past*, pp. 1–70, 1993.

[145] V. Mathews and J. Lee, "Adaptive algorithms for bilinear filtering," *Proceedings of SPIE - The International Society for Optical Engineering*, vol. 2296, no. 1, pp. 317–327, 1994.

[146] G. P. Agrawal, "Nonlinear fiber optics," in *Nonlinear Science at the Dawn of the 21st Century* (P. L. Christiansen, M. P. Sørensen, and A. C. Scott, eds.), (Berlin, Heidelberg), pp. 195–211, Springer Berlin Heidelberg, 2000.

[147] K. Hammani, B. Kibler, C. Finot, P. Morin, J. Fatome, J. M. Dudley, and G. Millot, "Peregrine soliton generation and breakup in standard telecommunications fiber," *Optics Letters*, vol. 36, no. 2, p. 112, 2011.

[148] Q. Vinckier, F. Duport, A. Smerieri, K. Vandoorne, P. Bienstman, M. Haelterman, and S. Massar, "High-performance photonic reservoir computer based on a coherently driven passive cavity," *Optica*, vol. 2, no. 5, pp. 438–446, 2015.

[149] A. Argyris, J. Cantero, M. Galletero, E. Pereda, C. R. Mirasso, I. Fischer, and M. C. Soriano, "Comparison of Photonic Reservoir Computing Systems for Fiber Transmission Equalization," *IEEE Journal of Selected Topics in Quantum Electronics*, vol. 26, no. 1, pp. 1–9, 2019.

[150] R. M. Nguimdo, G. Verschaffelt, J. Danckaert, and G. Van der Sande, "Reducing the phase sensitivity of laser-based optical reservoir computing systems," *Optics Express*, vol. 24, no. 2, p. 1238, 2016.

[151] J. Martin-Regalado, F. Prati, M. San Miguel, and N. B. Abraham, "Polarization properties of vertical-cavity surface-emitting lasers," *IEEE Journal of Quantum Electronics*, vol. 33, no. 5, pp. 765–783, 1997.

[152] J. Dambre, D. Verstraeten, B. Schrauwen, and S. Massar, "Information processing capacity of dynamical systems," *Scientific Reports*, vol. 2, 2012.

[153] R. Legenstein and W. Maass, "Edge of chaos and prediction of computational performance for neural circuit models," *Neural Networks*, vol. 20, no. 3, pp. 323–334, 2007.

[154] L. Grigoryeva, J. Henriques, L. Larger, and J. P. Ortega, "Optimal nonlinear information processing capacity in delay-based reservoir computers," *Scientific Reports*, vol. 5, pp. 1–11, 2015.

[155] F. Denis-Le Coarer, A. Quirce, P. Pérez, A. Valle, L. Pesquera, M. Sciamanna, H. Thienpont, and K. Panajotov, "Injection locking and polarization switching bistability in a 1550 nm vcsel subject to parallel optical injection," *IEEE Journal of Selected Topics in Quantum Electronics*, vol. 23, no. 6, pp. 1–10, 2017.

[156] C. Henry, "Theory of the linewidth of semiconductor lasers," *IEEE Journal of Quantum Electronics*, vol. 18, no. 2, pp. 259–264, 1982.

[157] C. Masoller and N. B. Abraham, "Low-frequency fluctuations in vertical-cavity surface-emitting semiconductor lasers with optical feedback," *Physical Review A*, vol. 59, pp. 3021–3031, apr 1999.

[158] R. Lang and K. Kobayashi, "External optical feedback effects on semiconductor injection laser properties," *IEEE Journal of Quantum Electronics*, vol. 16, no. 3, pp. 347–355, 1980.

[159] K. Panajotov, I. Gatare, A. Valle, H. Thienpont, and M. Sciamanna, "Polarization- and transverse-mode dynamics in optically injected and gain-switched vertical-cavity surface-emitting lasers," *IEEE Journal of Quantum Electronics*, vol. 45, no. 11, pp. 1473–1481, 2009.

[160] N. L. Johnson, S. Kotz, and N. Balakrishnan, *Continuous Univariate Distributions*. Wiley-Interscience, 5 1995. Ed. 2, Vol. 2.

[161] K. Harkhoe and G. V. D. Sande, "Delay-Based Reservoir Computing Using Multimode Semiconductor Lasers: Exploiting the Rich Carrier Dynamics," *IEEE Journal of Selected Topics in Quantum Electronics*, vol. 25, no. 6, p. 1, 2019.

[162] F. Duport, A. Smerieri, A. Akrout, M. Haelterman, and S. Massar, "Fully analogue photonic reservoir computer," *Scientific Reports*, vol. 6, no. October 2015, pp. 1–12, 2016.

[163] A. J. Roberts, "Modify the Improved Euler scheme to integrate stochastic differential equations," 2012.

A

Appendix 1: Code deployment on CPU cluster

A.0 Computation method used for numerical simulations

We have simulated the VCSEL model presented in Sec. 4.2.1 using a C++ code to ensure a fast and efficient integration of differential equations integration. The integration is made with a second order of Runge-Kutta method (RK2). This method is the best trade between the numerical accuracy, the possibility to take into account the noise in the equations and a stable numerical simulations for small integration step. The Heun method [163] which is derivated from the RK2 method ensure that the statistic properties of the Langevin terms are properly included when integrating the stochastic differential equations. This code has been optimized and prepared to run on CPU clusters, using the vectorization properties of the processor. This C++ execution is embedded in a Python code which is easier to use to perform matrix computation, when we train and test the reservoir computer, and this step is not critical in terms of computation time.

The code is then deployed on the different CPUs of the cluster to test in parallel multiples sets of parameters. An illustration of the simulation method is presented in Fig. A.1.

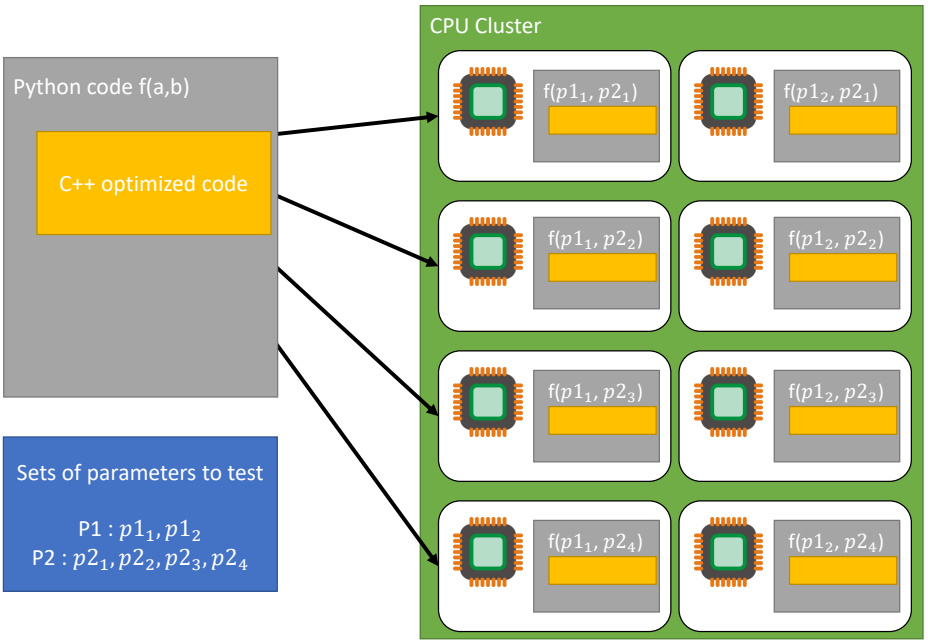

Figure A.1: Principle of the numerical simulation method. The C++ code is embedded in an Python environment. The same code is run on each CPU of the cluster using a different set of parameters

B

Appendix 2: Résumé de la thèse en français

Le but de cette thèse est donc de réaliser un dispositif de calcul composé de composants photoniques, qui vise à être utilisé pour des applications de télécommunication, impliquant d'atteindre une vitesse de calcul rapide. Notre défi sera d'utiliser principalement des composants de télécommunication pour réaliser ce réservoir, tels que le laser à cavité verticale à émission de surface (VCSEL), et la fibre optique monomode. Il semble que ce laser spécifique présente une dynamique de polarisation intéressante que nous voulons exploiter pour obtenir les meilleures performances de calcul possibles. Nous réaliserons le système sur la base de simulations numériques et de tests expérimentaux. Chaque concept est d'abord exploré numériquement pour choisir les composants correctement et trouver le meilleur ensemble de paramètres qui conduise à un dispositif de calcul efficace. Cela permet d'explorer plus de paramètres rapidement, et d'avoir un aperçu du rôle de chaque paramètre sur les propriétés de fonctionnement du système. Les données pertinentes trouvées numériquement sont exploitées pour construire le dispositif expérimental correspondant, et pour valider l'hypothèse numérique de manière expérimentale. Dans cette thèse, nous ne visons pas à créer de nouvelles dynamiques mais plutôt à exploiter ces dynamiques connues pour effectuer des calculs avec des performances optimales.

Ce manuscrit peut être divisé en deux grandes parties. Nous présentons tout d'abord dans les chapitres 2 et 3 les bases théoriques nécessaires pour comprendre les résultats présentés dans les chapitres 4 et 5.

Dans le chapitre 2, nous présentons les bases de la physique des lasers à semiconducteurs. Nous rappelons tout d'abord qu'un laser est composé de trois éléments

principaux : un milieu de gain pour amplifier la lumière, une cavité pour être sélectif en longueur d'onde, et une pompe pour compenser les pertes. Un laser peut être réalisé avec des matériaux semi-conducteurs, ce qui permet de réaliser des composants petits et bon marché. On peut distinguer les lasers émettant de la lumière depuis le bord (EEL) et les lasers émettant depuis la surface (VCSEL). Ce dernier type de laser présente plusieurs avantages qui le rendent largement utilisé dans différents domaines, tels que les réseaux de télécommunication, la biologie ou les smartphones. Un laser à semi-conducteur peut présenter des dynamiques différentes lorsqu'il est soumis à une rétroaction ou à une injection. Il peut présenter une dynamique stable, oscillante ou chaotique. La dynamique d'un laser peut également être modifiée en modulant le faisceau optique injecté. Cette dynamique complexe est déjà utilisée, pour imiter des phénomènes naturels ou pour traiter des signaux par exemple.

Dans le chapitre 3, nous présentons les connaissances de base du calcul de réservoir. Nous présentons d'abord le réseau de neurones artificiels, et les deux principales topologies de réseau : le réseau de neurones à propagation vers l'avant et le réseau de neurones récurrent. En raison de la complexité de son entrainement, le paradigme du reservoir computing a été proposé. Ce paradigme consiste à utiliser un réseau neuronal récurrent fixe, et à entrainer uniquement une couche de lecture en sortie grâce à un algorithme de régression simple. Au sein du reservoir computing, nous nous sommes concentrés plus particulièrement sur le reservoir computing à retard. Cette architecture est composée d'un seul neurone physique avec une boucle de rétroaction, le long de laquelle sont distribués des neurones virtuels. Nous présentons plusieurs exemples de dispositif de reservoir computing, utilisant des composants mécaniques, électroniques ou photoniques, ainsi que des exemples de reservoir à retard, incluant le reservoir opto-électronique qui est la première réalisation de ce type d'architecture. Enfin, nous présentons des tâches qui sont couramment utilisées pour évaluer les dispositifs de calcul de réservoir : la capacité de mémoire et la capacité de calcul qui sont indépendantes de la tâche, et la prédiction de la série temporelle Santa-Fe et l'égalisation non linéaire des canaux.

Au chapitre 4, nous présentons les performances de notre dispositif de calcul de réservoir traitant une seule tâche. Nous présentons d'abord notre architecture composée d'un VCSEL et d'une fibre optique monomode en silice, basée sur le paradigme du reservoir à retard. Nous avons utilisé le modèle spin-flip (SFM) pour simuler le système et explorer l'espace des paramètres du système en injectant l'entrée soit électriquement soit optiquement. Nous avons également exploré l'influence de la polarisation de la rétroaction optique. Nous avons tiré deux conclusions principales : (i) l'injection optique de l'entrée conduit à de meilleures et plus rapides performances, et (ii) l'utilisation de la rétroaction optique avec rotation de polarisation permet de doubler

la capacité mémoire du reservoir, et donc d'atteindre potentiellement de meilleures performances sur des tâches applicatives. Nous détaillons la confirmation expérimentale de cette dernière, après avoir présenté le montage expérimental. Plus précisément, nous avons été en mesure grâce à notre reservoir expérimental d'obtenir un taux d'erreur à 1.5% lors de l'égalisation de canal WIFI, et de récupérer parfaitement un signal transmis par fibre optique. Nous avons finalement comparé les performances numériques et expérimentales de notre système et avons pu démontrer que les deux sont similaires si nous prenons en compte le niveau de bruit dans la couche de sortie. Cela a également permis de montrer que ce niveau de bruit a un impact important sur les performances du reservoir.

Dans le chapitre 5, nous explorons les performances de l'architecture que nous proposons traitant deux tâches simultanément. Nous avons adapté le modèle du chapitre précédent pour pouvoir injecter les deux tâches : chaque tâche est injectée dans un mode de polarisation différent du VCSEL. Nous avons testé l'influence du couplage non linéaire entre les deux modes de polarisation via la polarisation de la rétroaction, la relaxation du spin et le paramètre de biréfringence sur la capacité mémoire du réservoir et sur ses performances lors du traitement des tâches de télécommunication. Nous avons pu prouver que le couplage de ces deux modes de polarisation diminue les performances du réservoir, ce qui implique également que la rétroaction isotrope fournit de meilleures performances dans ce cas. Nous avons également prouvé que le rapport de la puissance d'injection entre les deux modes de polarisation peut être utilisé pour régler la répartition des performances entre les deux tâches traitées. Cette dernière conclusion a également été démontrée expérimentalement. Nous avons enfin comparé les performances des systèmes numériques et expérimentaux. Nous prouvons grâce à cette observation que, lors du traitement de deux tâches, le niveau de bruit dans la couche de sortie ne joue pas un rôle significatif, contrairement à ce que l'on conclut du traitement d'une seule tâche.

Perspectives :

Nous avons présenté dans cette thèse les performances d'un reservoir à retard photonique utilisant la dynamique du VCSEL. Cependant, l'entrainement de ce dernier été réalisés hors ligne, ce qui signifie que toutes les entrées sont envoyées en même temps, et que la sortie est enregistrée dans une mesure et traitée dans un processus unique. Une étude axée sur le traitement des signaux en ligne peut être intéressante. Le traitement en ligne consiste à traiter les entrées une à une et à adapter les poids en temps réel. Cette méthode est plus proche de l'utilisation d'un reservoir en conditions réelles. Cependant, en raison de la vitesse de traitement des composants photoniques, l'ajustement des poids en temps réel pour produire le résultat final reste un défi technique. Une telle approche a été proposée en utilisant un intégrateur optique

et un modulateur Mach-Zehnder à grande vitesse, pour un réservoir réalisé avec un laser émettant par la tranche. L'application d'une technique similaire à notre architecture peut être intéressante. L'ajout d'une adaptation des poids pour prendre en compte le processus de vieillissement des composants pourrait également être une étude intéressante.

Une autre étude intéressante consisterait à améliorer le dispositif expérimental pour réduire la longueur de la boucle de rétroaction afin d'évaluer si le dispositif est capable de traiter les signaux au débit de données prévu numériquement (environ 3 Gb/s). Nous avons observé dans cette thèse que le SNR est une question cruciale dans l'expérience, en raison de la faible puissance émise par le VCSEL. Remplacer le VCSEL par un autre plus puissant (émettant environ 2 mW lorsqu'il est polarisé près du seuil) permettrait également d'atteindre un SNR nettement meilleur et pourrait ainsi améliorer les performances globales du système. Même si une telle VCSEL émettant à 1550 nm n'existe pas encore, nous pourrions tester l'impact d'une puissance émise plus élevée avec une VCSEL émettant à 1310 nm ou 850 nm. On pourrait également s'attendre à ce qu'un VCSEL plus puissant émettant à 1550 nm soit développé dans les prochaines années.

Nous concentrons également nos travaux sur une architecture spécifique. Nous pourrions imaginer une architecture à délai, en cascadant les VCSEL au lieu d'en utiliser qu'un seul. Cela modifierait la dynamique globale de l'architecture. En ajoutant un nouveau dispositif physique, nous pouvons espérer améliorer la capacité mémoire du système, et donc être en mesure de traiter des tâches plus complexes, comme la récupération de signaux déformés par une fibre plus longue (plusieurs centaines de kilomètres).